BOSTON UNIVERSITY

GRADUATE SCHOOL OF ARTS AND SCIENCES

Dissertation

COMPUTATIONAL STUDIES OF THERMAL AND QUANTUM PHASE TRANSITIONS APPROACHED THROUGH NON-EQUILIBRIUM QUENCHING

by

CHENG-WEI LIU

Submitted in partial fulfillment of the

requirement for the degree of

Doctor of Philosophy

2015

Approved by

First Reader

Anders W. Sandvik, Ph.D.
Professor of Physics

Second Reader

Anatoli Polkovnikov, Ph.D.
Professor of Physics

To my parents and family, thank you all for your unconditional supports.

Acknowledgments

First and foremost, I would like to thank my major advisor Professor Anders Sandvik and also Professor Anatoli Polkovnikov, who basically serves as my second advisor on collaborating projects during this period of time. I sincerely thank their patience, numerous discussions, immense and broad knowledge, and excellent guidance. It is my upmost honor working with them, words simply can not fully express my gratitude. I feel really privileged to have the rare chance to work closely with two excellent professors, whose research areas also match my interests so nicely. This period of time at BU is absolutely the most intellectually-rewarding period in my life so far.

I would also like to thank Professor A. Peter Young at University of California, Santa Cruz, for collaborating on the 3D spin-glass project and numerous stimulating discussions along the way. I also thank Professor Ribhu Kaul at University of Kentucky for inspiring discussions while he visited BU.

I sincerely thank Professor Richard Averitt, Professor Tulika Bose, Professor Robert Carey, Professor Claudio Chamon, and Professor Shyamsunder Erramilli for serving on my preliminary oral committee and final PhD committee. I appreciate their time giving me comments and advising on my dissertation.

I am thankful to current and former group members: Dr. Thomas Lang, Dr. Arnab Sen, Dr. Hidemaro Suwa, Dr. Songbo Jin, Dr. Ying Tang, Adam Iaizzi, and Na Xu, and visiting scholar Dr. Pablo Serna from Spain, I really enjoy all the discussions we have had during official group meetings and unofficial off-line chat. I especially thank Adam for carefully reading my thesis draft before its completion. I am also grateful to CMT group's post-doc researchers: Dr. Luca D'Alessio, Dr. Michael Kolodrubetz, and Dr. Paul Krapivsky, for countless discussions during this period of time. I have learned a lot from them.

I would also like to thank BU Research Computing Services scientific analyst Katia Oleinik.

She has provided generous support and very helpful consultancy on GPU computing. I am very grateful to our computer resources manager Goan Hu in our Physics Department, who has provided excellent supports and always responds promptly to all kinds of computer issues. In addition, I am grateful to Physics Department graduate program coordinator Mirtha Cabello, thank her for the constant patience in helping all of the graduate students and making our department such a warm place.

Overall, I would like to thank all of the members in the CMT group, from faculty members, post-doc fellows, to graduate students, thank you all for creating an academically vibrant environment and making this corner a great place to do condensed matter physics research.

Finally, I sincerely thank my family back home. Every piece of my achievement is made possible because of all of your unconditional supports.

COMPUTATIONAL STUDIES OF THERMAL AND QUANTUM PHASE TRANSITIONS APPROACHED THROUGH NON-EQUILIBRIUM QUENCHING

(Order No.)

CHENG-WEI LIU

Boston University Graduate School of Arts and Sciences, 2015

Major Professor: Anders W. Sandvik, Ph.D., Professor of Physics

ABSTRACT

Phase transitions and their associated critical phenomena are of fundamental importance and play a crucial role in the development of statistical physics for both classical and quantum systems. Phase transitions embody diverse aspects of physics and also have numerous applications outside physics, e.g., in chemistry, biology, and combinatorial optimization problems in computer science. Many problems can be reduced to a system consisting of a large number of interacting agents, which under some circumstances (e.g., changes of external parameters) exhibit collective behavior; this type of scenario also underlies phase transitions.

The theoretical understanding of equilibrium phase transitions was put on a solid footing with the establishment of the renormalization group. In contrast, non-equilibrium phase transition are relatively less understood and currently a very active research topic. One important milestone here is the Kibble-Zurek (KZ) mechanism, which provides a useful framework for describing a system with a transition point approached through a non-equilibrium quench process.

I developed two efficient Monte Carlo techniques for studying phase transitions, one is for classical phase transition and the other is for quantum phase transitions, both are under

the framework of KZ scaling.

For classical phase transition, I develop a non-equilibrium quench (NEQ) simulation that can completely avoid the critical slowing down problem. For quantum phase transitions, I develop a new algorithm, named quasi-adiabatic quantum Monte Carlo (QAQMC) algorithm for studying quantum quenches. I demonstrate the utility of QAQMC quantum Ising model and obtain high-precision results at the transition point, in particular showing generalized dynamic scaling in the quantum system.

To further extend the methods, I study more complex systems such as spin-glasses and random graphs. The techniques allow us to investigate the problems efficiently. From the classical perspective, using the NEQ approach I verify the universality class of the 3D Ising spin-glasses. I also investigate the random 3-regular graphs in terms of both classical and quantum phase transitions. I demonstrate that under this simulation scheme, one can extract information associated with the classical and quantum spin-glass transitions without any knowledge prior to the simulation.

Contents

List of Tables

List of Figures

List of Abbreviations

APT	adiabatic perturbation theory
DMRG	density matrix renormalization group
ED	exact diagonalization
FSS	finite-size scaling
MC	Monte Carlo
NEQ	non-equilibrium quench
NEQMC	non-equilibrium quantum Monte Carlo
NP	non-polynomial
PQMC	projector quantum Monte Carlo
QA	quantum annealing
QAA	quantum adiabatic algorithm
QAQMC	quasi-adiabatic quantum Monte Carlo
QMC	quantum Monte Carlo
RG	renormalization group
RSB	replica symmetry breaking
SA	simulated annealing
SSE	stochastic series expansion
SG	spin glass
SW	Swendsen-Wang
TFIM	transverse-field Ising model

Chapter 1

Introduction

Phase transitions and their associated critical phenomena have been a main theme and an actively studied research area in the development of statistical physics. The occurrence of phase transitions comes from the interactions between the individual constituents of the system. The strengths of the interactions can be controlled by some parameter λ. Different strengths corresponding to different values of λ will result in different phases, therefore the term "phase transition." The framework for equilibrium phase transitions has been well established since the development of renormalization group [2, 3], however, the non-equilibrium counterpart is relatively less completed despite some important achievement [4], therefore will be the focus of this dissertation. In either equilibrium or non-equilibrium, usually the Hamiltonians of this type of interacting systems can not be solved exactly, except for a few examples such as 2D Ising mode [5] and 1D transverse-field Ising model [6], therefore computational techniques, especially unbiased Monte Carlo simulation has provided a major tool to investigate this class of problems.

Throughout this dissertation we will mainly use Monte Carlo simulation techniques to investigate several phase transition problems of spins systems. In Ch. 2 and 3, the focus will be on the developments of two numerical techniques for studying phase transitions. In these two chapters we use classical and quantum ferromagnetic systems to demonstrate the techniques, which are under the framework of non-equilibrium dynamics. Then we will apply these techniques to investigate the phase transitions of more complex systems such as spin-glasses and random graphs. It will be shown that, in many circumstances, the non-equilibrium simulation methods will be more efficient than the equilibrium counterpart and allow us to obtain important information that is traditionally difficult to obtain through

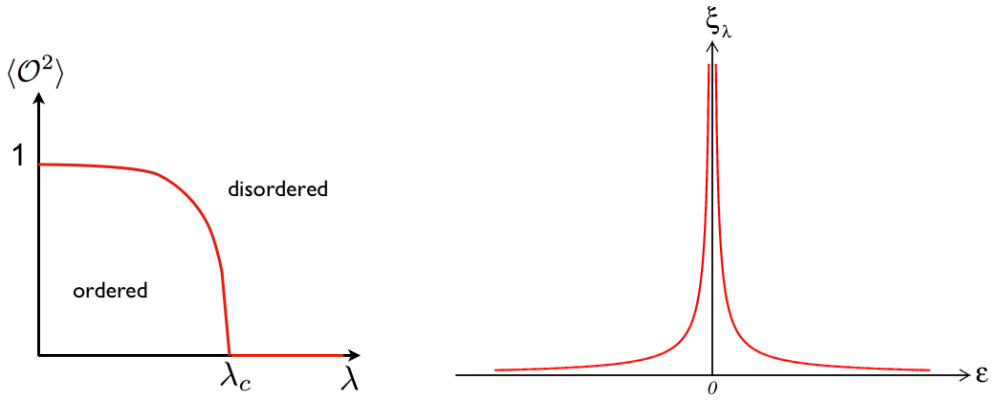

(a) (b)

Figure 1.1: The order parameter as a function of tuning parameter λ (a). For the second-order phase transition, the order parameter is 0 when $\lambda > \lambda_c$, and begins to grow when $\lambda \leq \lambda_c$. It should be noted that the curve only illustrates the behavior of the thermodynamic limit, in terms of finite-size systems the curves will be rounded and the order parameter is not strictly zero in the disordered phase [7], more specific examples will be discussed in Sec. 1.1.2 and 1.1.3. The correlation length ξ_λ as a function of the reduced distance from the critical point, $\varepsilon = |\lambda - \lambda_c|/\lambda_c$ (b). As the figure illustrates, close to and exactly at λ_c, the correlation length and therefore the relaxation time τ_{rel} will diverge. The divergence of the relaxation time is the root cause of *critical slowing-down* [8] since the system needs infinitely long time to relax to its equilibrium state.

equilibrium approaches.

1.1 Equilibrium phase transitions and finite-size scaling

In this dissertation we will focus on second-order phase transitions, with the transition characterized by a tuning parameter λ and a transition point λ_c. In classical (thermal) phase transitions, the tuning parameter is the temperature T, and in $T = 0$ quantum phase transitions, λ is a parameter of the Hamiltonian. One characteristic feature of second-

order phase transitions is that, around the critical point λ_c, physical quantities such as the correlation length, ξ_λ, the order parameter, $\mathcal{O}$, and the fluctuations of the order parameter χ, will grow in terms of a power-law of ε, as illustrated in Fig. 1.1:

$$\begin{aligned} \xi_\lambda &\sim \varepsilon^{-\nu}, \\ \mathcal{O} &\sim \varepsilon^{\beta}, \\ \chi &\sim \varepsilon^{-\gamma}, \end{aligned} \tag{1.1}$$

where $\varepsilon \equiv |\lambda - \lambda_c|/\lambda_c$ is the reduced distance from the critical point, ν is the correlation length exponent, β the order parameter exponent, γ is the exponent that governs the divergence of the fluctuation in the order parameter.

Another important quantity is the relaxation time τ_{rel}:

$$\tau_{\text{rel}} \sim \xi_\lambda^z, \tag{1.2}$$

where z is the dynamic exponent. The divergence of the correlation length ξ_λ results in the divergence of the relaxation time, which implies that the time required for the system to relax to the equilibrium configuration will effectively become infinitely long. This critical slowing-down [8] problem has posed an enormous obstacle in the field of computational physics for almost four decades, especially when the system under study has a large value of z, such as highly frustrated systems or spin-glasses. We will demonstrate that based on the techniques to be discussed in Ch. 2 and 3, a non-equilibrium approach that completely circumvents the critical slowing-down can be taken to study this type of hard problems.

1.1.1 Finite-size scaling

In this subsection we briefly review the argument of standard equilibrium finite-size scaling *ansatz*, which will pave the way for the dynamic finite-size scaling to be discussed in Sec. 1.2.2

Despite the correlation length ξ_λ diverging at the critical point λ_c, as illustrated in Fig. 1.1, in terms of finite-size system, ξ_λ is bounded by the linear size of the system L since it can not grow beyond the system size. Therefore, around λ_c, the quantities Eqs. (1.3) and (1.2) can be written in terms of finite-size as:

$$\begin{array}{rcccc} \xi_\lambda & \sim & L, & & \\ \varepsilon & \sim & \xi_\lambda^{-1/\nu} & \sim & L^{-1/\nu}, \\ \mathcal{O} & \sim & \varepsilon^{\beta} & \sim & L^{-\beta/\nu}, \\ \chi & \sim & \varepsilon^{-\gamma} & \sim & L^{\gamma/\nu}, \\ \tau_{\mathrm{rel}} & \sim & \xi_\lambda^{z} & \sim & L^{z}. \end{array} \tag{1.3}$$

More importantly, the correlation length ξ_λ is a characteristic length scale that separates two different phases: when $\xi_\lambda \ll L$ the system is in the disordered phase, i.e., $\varepsilon \gg 1$; when $\xi_\lambda \sim L$ the system enters into the ordered phase, i.e., $\varepsilon \to 0$. In this sense, the ratio ξ_λ/L provides a universal gauge to measure how far/close the system is from the transition. Therefore the physical quantities A can be written as:

$$A(\lambda, L) = L^{\kappa/\nu} G(\xi_\lambda/L), \tag{1.4}$$

$$= L^{\kappa/\nu} G\big((\lambda - \lambda_c) L^{1/\nu}\big), \tag{1.5}$$

where the term $L^{\kappa/\nu}$ describes the size-dependent behavior, and the function $G(\xi_\lambda/L)$ is a dimension-less universal function around the transition. Eq. (1.5) indicates that if one graphs the quantity $A(\lambda, L)L^{-\kappa/\nu}$ versus $(\lambda - \lambda_c)L^{1/\nu}$, what appears will be an universal function G regardless of the system sizes, this phenomenon is called *scaling collapse*, as we will illustrate more in the following two subsections.

The finite-size scaling expression Eq. (1.4) is especially interesting when applied to the order parameter of the system, $\mathcal{O}$:

$$\langle \mathcal{O}^2 \rangle = L^{-2\beta/\nu} F(\xi_\lambda / L). \tag{1.6}$$

We can further decompose the scaling of the order parameter as follows: When the system is very far away from the transition and is in the disordered phase, the order parameter should vanish as the system size grows, since in the thermodynamic limit it should be strictly zero, as illustrated in the Fig. (1.1) (a). In this regime one can expect:

$$\langle \mathcal{O}^2 \rangle \sim \frac{1}{L^d}, \quad \text{when} \quad \varepsilon \gg 1, \tag{1.7}$$

where d is the dimension of the system.

When λ moves toward λ_c, the order should begin to develop for finite-size systems, although $\langle \mathcal{O}^2 \rangle$ should still be strictly zero on the disordered side in the thermodynamic limit. Furthermore, when λ is still far away but gradually moves closer to λ_c, the correlation length should also grow gradually. In this regime the domain size of the system can be described by $a \sim O(1)$, which is of the order of 1 lattice spacing. In this sense, the scaling function in Eq. (1.6) can be further written as:

$$\langle O^2 \rangle = \begin{cases} L^{-2\beta/\nu} a^{-d+2\beta/\nu} f_1(\xi_\lambda / L), & |\lambda - \lambda_c| \simeq 1 \\ L^{-d} f_2(a/\xi_\lambda), & \lambda - \lambda_c \gg 1 \quad \text{(disordered side)} \end{cases} \tag{1.8}$$

where the factor $a^{-d+2\beta/\nu}$ in the first line of Eq. (1.8) is introduced as the *engineering dimension* [6] to compensate for the discrepancy between the canonical dimension L^{-d} of $\langle \mathcal{O}^2 \rangle$, and its scaling dimension $L^{-2\beta/\nu}$, in any practical purpose the factor is of $O(1)$ and will be implicitly suppressed for simplicity. The expressions of Eq. (1.8) can be viewed as two limits of a single function $\tilde{F}(\xi_\lambda/L, a/\xi_\lambda)$: When $|\lambda - \lambda_c| \simeq 1$ around the transition, $\xi_\lambda \gg a$ and the function $\tilde{F}$ reduces to f_1. When $\lambda - \lambda_c \gg 1$ on the disordered side, $\xi_\lambda \ll L$ and the function is dominated by the second argument, therefore reduces to f_2. Between these two limits, the two scaling functions should smoothly connect to each other, and the

most natural and straightforward form is a power-law, hence Eq. (1.8) can be explicitly written as:

$$\langle O^2\rangle = \begin{cases} L^{-2\beta/\nu} f_1\big((\lambda-\lambda_c)L^{1/\nu}\big), & |\lambda-\lambda_c| \simeq 1 \\ L^{-2\beta/\nu}\big((\lambda-\lambda_c)L^{1/\nu}\big)^{-x} = L^{-d}\big((\lambda-\lambda_c)^{-1}\big)^{x}, & \lambda-\lambda_c \gtrsim 1 \\ L^{-d} f_2\big((\lambda-\lambda_c)^{-1}\big), & \lambda-\lambda_c \gg 1 \end{cases} \tag{1.9}$$

where the exponent x can be obtained by demanding the powers on L of these two scaling regimes be equal:

$$L^{-2\beta/\nu}\big((\lambda-\lambda_c)L^{1/\nu}\big)^{-x} = L^{-d}.$$

Therefore, we have

$$x = \nu d - 2\beta. \tag{1.10}$$

Note that f_1 and f_2 work in their own respective regimes, and the region of the power-law form is where both f_1 and f_2 applicable. We will demonstrate this dual scaling behavior in Sec. 1.1.2 for classical system and in Sec. 1.1.3 for quantum system. In Sec. 1.2.2, it will be shown that similar dual scaling behavior can be found in non-equilibrium scenario.

1.1.2 Example: classical Ising model

In this subsection, we use classical 2D Ising model to demonstrate the equilibrium finite-size scaling outlined in Sec. 1.1.1. The Hamiltonian of the 2D Ising model can be written as:

$$\mathcal{H} = -J\sum_{\langle i,j\rangle}\sigma_i\sigma_j, \tag{1.11}$$

where the indices $\langle i,j\rangle$ represent the nearest-neighbor spin pairs , $J>0$ is the ferromagnetic interaction, and the Ising spins take value $\sigma_i = +1 \text{or} -1$. The phase diagram of the model

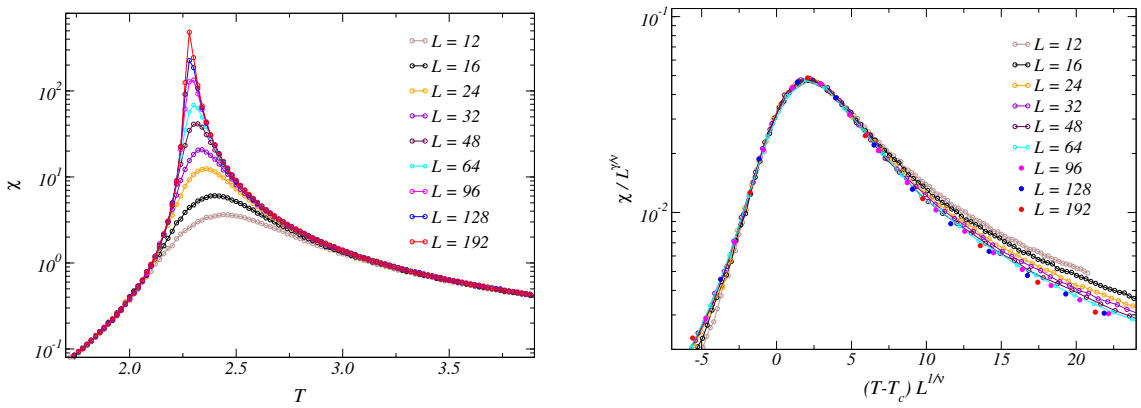

(a) (b)

Figure 1.2: Results for the classical 2D Ising model. The susceptibility as a function of temperature for different sizes (a). The peak of χ, which is shifting due to finite-size effect, corresponds to the transition point. According to Eq. (1.13), after rescaling the susceptibility by graphing rescaled χ versus the reduced distance from the transition point, all curves collapse to an universal curve (b). When the sizes are small, deviations from the universal behaviors are still detectable, however, as system size grows, it is clear that the curve will eventually converge to a size-independent scaling form. To alleviate the critical slowing-down problem around T_c, the efficient Swendsen-Wang cluster algorithm [9] was used to generate the data.

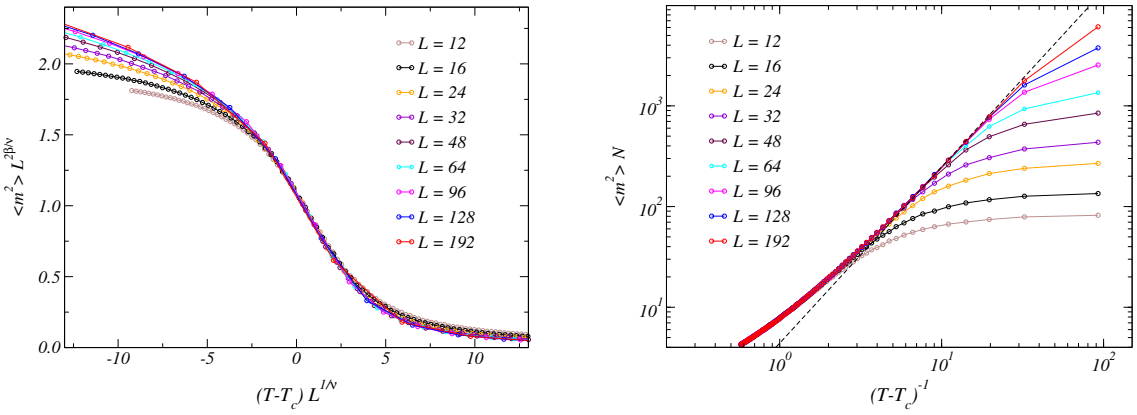

(a) (b)

Figure 1.3: Results for the 2D classical Ising model. The dual scaling behavior of the order parameter, the magnetization squared $\langle m^2 \rangle$, is shown. The f_1 scaling, critical scaling , depicts the scaling collapse when the temperature is around the transition point T_c (a). The f_2 scaling, disordered scaling, describes the behavior when the temperature is much higher than T_c (b). Note that these two figures come from the same data set. In f_2 scaling, the left region corresponds to where the temperature is much higher than T_c, and the right region is where close to the transition. The middle region shows a clear power-law behavior, the dashed line draws the power-law with the power predicted by Eq. (1.10).

is illustrated by Fig. 1.1(a) with λ representing the temperature T and the order parameter $\mathcal{O}$ stands for the magnetization $\langle m \rangle = (1/N)\sum_i \sigma_i$. The solution to the 2D Ising model in equilibrium is known exactly by the Onsager solution [5], $T_c/J = 2/\ln(1+\sqrt{2})$, $\beta = 1/8$, $\nu = 1$, and $\gamma = 7/4$, therefore it provides a solid testing ground for the theory.

The susceptibility of a ferromagnetic system such as the Ising model can be derived from $\chi = \big(\partial\langle m\rangle/\partial h\big)\big|_{h\to 0}$:

$$\chi = \frac{N}{T}\big(\langle m^2\rangle - \langle |m|\rangle^2\big), \tag{1.12}$$

which can be interpreted as the fluctuation in the order parameter. The second term in the parenthesis of Eq. (1.12) takes the absolute value to account for the fact that the symmetry is not broken in finite-size systems, and therefore $-m_0$ and m_0 are equally likely in the ordered phase. According to the finite-size scaling Eq. (1.5), the susceptibility should scale as:

$$\chi = L^{\gamma/\nu} f\big((T - T_c)L^{1/\nu}\big). \tag{1.13}$$

This means that after rescaling χ properly, one should see an universal behavior as illustrated in Fig. 1.2(b).

Now we turn the attention to the scaling of the order parameter $\langle m^2\rangle$. According to Eq. (1.9), $\langle m^2\rangle$ should show dual scaling behavior, depending on how far away the system is from the transition point T_c, the scaling behavior should be reflected as either f_1 or f_2 scaling. Fig. 1.3 illustrates this dual scaling behavior. More importantly, in f_2 scaling, a power-law regime between the regime $T \gg T_c$ and the regime that is around the transition $T \gtrsim T_c$ is clearly shown, the power predicted (drawn as the dashed line) by Eq. (1.10) shows very good agreement with the data.

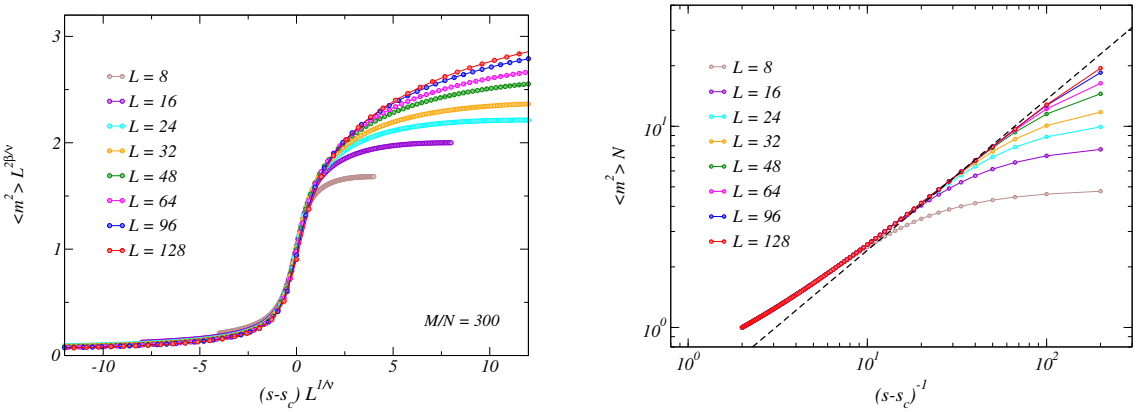

(a) (b)

Figure 1.4: For 1D TFIM. The dual scaling behavior of the order parameter, magnetization squared $\langle m_z^2 \rangle$, is shown. The f_1 scaling, critical scaling , depicts the scaling collapse when the tuning parameter s is around the critical point $s_c = 1/2$ (a). Strong finite-size effect can also be observed. The f_2 scaling, disordered scaling, described the behavior when s is far away from s_c (b). Same as in Fig. 1.3, the figures of these two panels come from the same data set. In f_2 scaling, the left region corresponds to where the s is relatively far away from s_c, and the right region is where it is close to the transition. Again, the middle region shows a clear power-law behavior, the dashed line shows the power-law with the power predicted by Eq. (1.10).

1.1.3 Example: quantum Ising model (transverse-field Ising model)

In this subsection, we use the quantum Ising model, also known as the transverse-filed Ising model (TFIM), to demonstrate the same dual scaling behavior described by Eq. (1.9), which we have observed in the classical Ising model. The Hamiltonian can be written as

$$\mathcal{H} = -s \sum_{\langle i,j \rangle} \sigma_i^z \sigma_j^z - (1-s) \sum_i \sigma_i^x, \tag{1.14}$$

where $\langle i, j \rangle$ stands for nearest-neighbor spin paris as in the classical Ising model Eq. (1.11), s is the tuning parameter $s \in [0, 1]$, and σ_z, σ_x are Pauli matrices. Note that given the notation

used in Eq. (1.14), the parameter λ mentioned previously could be defined as $\lambda \equiv 1 - s$. Here we are only interested in zero temperature $T = 0$ quantum phase transition, therefore there is no thermal fluctuation. However, the non-commuting property of σ_i^z and σ_i^x results in quantum fluctuations, which can be controlled by the parameter s. When $s = 0$, the system is in a strongly fluctuating state that can be described (in the σ^z basis) by an equal superposition eigenstate:

$$|\Psi_0\rangle = \prod_i \frac{|\uparrow\rangle_i + |\downarrow\rangle_i}{\sqrt{2}}, \tag{1.15}$$

where $|\uparrow\rangle$ stands for single-spin up state and $|\downarrow\rangle$ stands for single-spin down state. When $s = 1$, the system reduces to the classical Ising model and the system will exhibit a perfect ferromagnetic order since it is at $T = 0$. The 1D TFIM can be solved exactly [6], due to its mapping to a $(1+1)$ classical solvable Ising system [10], therefore the exponents are the same as the 2D Ising model: $\beta = 1/8, \nu = 1$, and the critical point at which the system undergoes a transition from a disordered phase to a ferromagnetic phase as $s : 0 \to 1$ is $s_c = 1/2$.

Here we focus on the order parameter, the z-component magnetization defined as: $m_z = (1/N)\sum_i \sigma_i^z$. According to Eq. (1.9), the same scaling as we saw in the classical case will be expected, as illustrated in Fig. 1.4. The SSE-based (stochastic series expansion [11, 12]) projector quantum Monte Carlo algorithm for TFIM [13] is used to carry out the simulations. The length of the operator sequence used was $M/N = 300$.

1.2 Phase transitions approached through non-equilibrium quench

Whether classical or quantum systems, as a general principle, one can slowly change the tuning parameter λ that controls the phase of the system in order to achieve "adiabatic

change" (or "quasi-static change" for the classical systems.) However, this idea no longer holds when λ is tuned toward the transition point, because the relaxation time will eventually diverge at the critical point, as discussed in Sec. 1.1. The first attempt to get around this problem is the Kibble-Zurek (KZ) arguments, [14,15] which originally focused on quantitatively relating defect formation (e.g., the typical defect size and the density of defects) to the rate of change (the quench velocity) of a parameter of the system (such as the temperature, external fields, etc.). The KZ mechanism and extensions of it have successfully been used to describe out-of-equilibrium physics at both classical and quantum phase transitions, for a general review, see Ref. [16]. In Sec. 1.2.1 we outline the general ideas and basic scalings associated with KZ. In Sec. 1.2.2, based on KZ argument, we derive the generalized dynamic finite-size scaling, and also the non-equilibrium version of the dual scaling behavior analogous to the equilibrium case Eq. (1.8). This non-equilibrium dual scaling behavior will be tested and verified in various systems throughout this dissertation.

1.2.1 Kibble-Zurek mechanism

We consider a system with critical point λ_c and whose transition can be described by Fig. 1.1. When this system is quenched at some finite velocity to the neighborhood of λ_c by starting from some initial value $\lambda_i > \lambda_c$ and ending at some final value $\lambda_c \leq \lambda < \lambda_i$, if the rate of change is sufficiently slow the system evolves adiabatically toward its equilibrium state that is controlled by λ. Small deviations from adiabaticity (the quasi-adiabatic regime) can be described by adiabatic perturbation theory. In contrast, if the evolution is fast (the quench velocity is high), excitations lead to a large density of defects and the adiabatic description breaks down. The KZ mechanism provides a natural way to distinguish these perturbative and non-perturbative regimes.

According to the arguments of KZ, for the quasi-adiabatic picture to be valid, the time τ_{q} that the system is allowed to take to approach the final point λ must be at least of the order of the relaxation time τ_{rel} associated with the system's microscopic dynamical properties at

that parameter λ. As mentioned in Eq. (1.2), the relaxation time is simply related to the equilibrium spatial correlation length ξ_λ as

$$\tau_{\rm rel} \sim \xi_\lambda^z,$$

which defines the dynamic exponent z. This exponent depends on the equilibrium universality class of the phase transition, as well as the stochastic dynamics imposed on the system (or, alternatively, one can consider Hamiltonian dynamics, e.g., in quantum systems). Thus, for a linear quench with velocity v, the criterion for staying adiabatic is obtained by requiring for the total quench time τ_q:

$$\tau_{\rm q} \sim |\lambda_i - \lambda|/v \sim \tau_{\rm rel} \sim \xi_\lambda^z \sim |\lambda - \lambda_c|^{-z\nu}, \tag{1.16}$$

where ν is the equilibrium correlation-length exponent.

Another way to interpret the above relationship is to consider the *remaining* time τ of a quench which has reached $\lambda > \lambda_c$ after starting out at some $\lambda_i > \lambda$ and which is to continue all the way down to λ_c. Then, for a given τ, or equivalently, for given velocity v, the relation

$$\tau = |\lambda - \lambda_c|/v \sim |\lambda - \lambda_c|^{-z\nu} \tag{1.17}$$

defines the value of parameter λ at which the system falls out of the adiabatic evolution and essentially freezes, not being able to evolve significantly for the remainder of the quench process. This should hold independently of the initial value λ_i if it is sufficiently away from λ. From this relation we can also extract the velocity (the KZ velocity)

$$v_c(\lambda) \sim |\lambda - \lambda_c|^{1+z\nu}, \tag{1.18}$$

at which the system falls out of adiabaticity at the value λ. Thus, it is, in the thermodynamic limit, not possible to stay adiabatic all the way down to λ_c. An alternative derivation of this result has been derived in Ref. [17], where we consider the continuous quench as a series of infinitesimal quenches.

We can also write down the spatial length-scale ξ_v associated with a given velocity, i.e., the correlation length reached at the point where the infinite system freezes and cannot follow the instantaneous equilibrium state. Since $\xi_v \sim \xi_\lambda$ for the quasi-adiabatic evolution and $\xi_\lambda \sim |\lambda - \lambda_c|^{-\nu}$ at the point of freezing, Eq. (1.18) gives

$$\xi_v \sim v^{-1/(z+1/\nu)}. \tag{1.19}$$

For a finite system the maximum length scale is L, i.e., $\xi_v \leq L$, and the characteristic velocity separating the adiabatic and non-adiabatic responses then has an lower bound, which is simply obtained, according to standard arguments in finite-size scaling theory [3], by replacing the largest length-scale for the infinite system by L. In this case that means $\xi_v \to L$ in (1.19). Thus, a system of linear size L will remain adiabatic all the way down to λ_c, provided that the quench velocity is of the order of the size-dependent KZ velocity given by

$$v_c(L) \sim L^{-(z+1/\nu)}. \tag{1.20}$$

When the velocity is below this characteristic value, the non-adiabatic response of the system is very small and can be treated perturbatively. In contrast, when the velocity exceeds $v_c(L)$ the quasi-adiabaticity breaks down and the response of the system corresponds to non-adiabatic dynamics which is non-perturbative in v.

It should be pointed out that it is in general not possible to assign an exact value to $v_c(L)$ (and all the other quantities defined above), as Eq. (1.20) only indicates a proportionality and the change between the quasi-adiabatic and non-perturbative regime normally takes place in the form of a smooth cross-over. Throughout this thesis we will use extensive MC simulations to extract scaling functions of the form $f(v/v_c)$ describing the dynamic approach to the critical point for several classical and quantum models and dynamic schemes, from which the cross-over scale can be readily read-off. In addition to the KZ scale, we will also investigate and quantify another higher-velocity (diabatic) cross-over scale v_a related to a size-independent microscopic (lattice) scale a, as will be discussed in the Sec. 1.2.5.

1.2.2 Dynamic finite-size scaling

It is well known in equilibrium physics, as outlined in Sec. 1.1, that systems show universal finite-size scaling behavior in the neighborhood of the transition λ_c. Physical quantities can then be described by a non-singular scaling function $g(L/\xi_\lambda)$ and a universal power of the system size according to Eq. (1.4)

$$A(L,\lambda) = L^{\kappa/\nu} g(L/\xi_\lambda) = L^{\kappa/\nu} G[(\lambda-\lambda_c)L^{1/\nu}],$$

where κ is an exponent depending on the universality class of the transition and the quantity A. This general equilibrium form was initially hypothesized based on observations and has now been rigorously demonstrated through the renormalization group [2,3]. We here discuss how the KZ mechanism introduced in Sec. 1.2.1 can be incorporated into finite-size scaling forms for systems undergoing quench dynamics.

In a non-equilibrium setup, which we here first take to be a linear quench toward the critical point, the scaling argument L/ξ_v, with ξ_v defined in Eq. (1.19) should enter in addition to the equilibrium argument L/ξ_λ. Equivalently, as is clear from the definitions in Sec. 1.2.1, we can also consider the velocity ratio $v/v_c(L)$. We use it to write down an ansatz in terms of a function depending on the two scaling arguments;

$$\begin{aligned} A(\lambda,L,v) &= L^{\kappa/\nu} f(L/\xi_\lambda, v/v_c) \\ &= L^{\kappa/\nu} F\big[(\lambda-\lambda_c)L^{1/\nu}, vL^{z+1/\nu}\big]. \end{aligned} \tag{1.21}$$

The above expression captures the basic essence of the dynamic finite-size scaling, later in Sec. 1.2.5 a more detailed description depending on the velocity regime will be discussed.

1.2.3 Linear quench protocol

Clearly, Eq. (1.21) reduces to the standard equilibrium finite-size scaling ansatz in the limit $v \to 0$. When $v \neq 0$ the framework allows us to study the response of the system away

from the adiabatic limit. For a system with a known value of transition λ_c, one can carry out a quench process from the disordered phase, $\lambda_i > \lambda_c$ to λ_c, hence eliminating the first argument in the universal function in Eq. (1.21);

$$A(\lambda_c, L, v) = L^{\kappa/\nu} F(vL^{z+1/\nu}). \tag{1.22}$$

This scaling form is analogous to the equilibrium form Eq. (1.4) and is easy to study the size and velocity dependences of physical quantities at the transition point, using data-collapse techniques familiar from conventional finite-size scaling.

Applying Eq. (1.22) with the exponent $\kappa = -2\beta$ for the order parameter $\mathcal{O}$, we expect scaling at λ_c to be

$$\langle \mathcal{O}^2 \rangle = L^{-2\beta/\nu} F\big(vL^{z+1/\nu}\big). \tag{1.23}$$

1.2.4 Nonlinear quench protocols

The simple scaling hypothesis discussed above has also been generalized to non-linear protocols, where the critical point is approached according to an arbitrary power-law of the time t measured with respect to the final time τ_q [18]:

$$\lambda - \lambda_c = v(\tau_q - t)^r, \tag{1.24}$$

where the physical interpretation of v is the velocity as above for a linear quench ($r = 1$), the acceleration (up to an important factor 2) for a quadratic quench ($r = 2$), etc. (and for simplicity we will refer to v as the "velocity" in a generalized sense.) For a sudden quench ($r = 0$), v should be regarded as the amplitude of the change in λ.

The generalized critical velocity for arbitrary r (including non-integer) can be easily found by following the same arguments as in Sec. 1.2.1;

$$v_c(L) \sim L^{-(zr+1/\nu)}. \tag{1.25}$$

In Ref. [17], we provide an alternative derivation of this result based on a time-discretized quench, which also gives some information on how the unknown prefactor above depends on the exponents involved.

The order parameter Eq. (1.23) with Eq. (1.25) becomes

$$\langle \mathcal{O}^2 \rangle = L^{-2\beta/\nu} F\big(vL^{zr+1/\nu}\big). \tag{1.26}$$

1.2.5 Complete scaling form for the order parameter

When the quench velocity becomes very high, one can imagine that the order parameter after the quench to λ_c remains close to its value at λ_i. According to the equilibrium argument discussed in Sec. 1.1, since λ_i is in the disordered phase and the correlation length has a finite value there, one expects, for sufficiently large L,

$$\langle \mathcal{O}^2 \rangle \sim L^{-d}, \tag{1.27}$$

where d is the number of dimensions; Thus, in the high-velocity limit, $\langle \mathcal{O}^2 \rangle$ should depend on the initial value λ_i and scale as L^{-d}.

When the velocity decreases one can expect the order of the system to develop gradually, and as long as the KZ correlation length ξ_v is much smaller than the system size L the order parameter should still depend on L with the trivial power above. With the scaling form (1.26), this behavior implies that the function F in this regime must reduce to a power law of the argument $vL^{z+1/\nu}$;

$$\langle \mathcal{O}^2 \rangle \sim L^{-2\beta/\nu} \big(vL^{zr+1/\nu}\big)^{-x}, \tag{1.28}$$

and this exponent can be obtained by demanding this to be proportional to L^{-d}, i.e.,

$$x = \frac{d - 2\beta/\nu}{zr + 1/\nu}. \tag{1.29}$$

Thus, there is an intermediate universal scaling regime where

$$\langle \mathcal{O}^2 \rangle \sim L^{-d} v^{-x}. \tag{1.30}$$

Finally, when the velocity is decreased further and approaches $v_c(L)$, the assumption $\xi_v \ll L$ no longer holds. One would then expect deviations from the power-law form and a cross-over to a regime where Eq. (1.26) tends toward the corresponding L-dependent equilibrium value at λ_c, i.e., the standard finite-size behavior scaling,

$$\langle \mathcal{O}^2 \rangle \sim L^{-2\beta/\nu}, \tag{1.31}$$

sets in. This cross-over from the v-dependent power-law to this equilibrium form is smooth and contained in the function F in Eq. (1.26).

To incorporate all these different asymptotics in different velocity regimes, it is useful to introduce a short-range length scale a, which is of the order of one lattice spacing, and, therefore, can be set to 1 for any practical purpose. This non-trivial factor a is essential for defining the *engineering dimension* [6], $a^{-d+2\beta/\nu}$, which compensates for the discrepancy between the scaling dimension $L^{-2\beta/\nu}$ of $\langle \mathcal{O}^2 \rangle$ and its canonical dimension L^{-d}. The short-range length scale sets the size-independent upper limit $v \sim v_a$ beyond which the power-law behavior Eq. (1.30) should break down;

$$v_a \sim a^{-(zr+1/\nu)}. \tag{1.32}$$

More explicitly, based on the above discussion one cannot expect Eq. (1.26) to be able to describe all situations with a single scaling function F, and this function should actually be replaced by two different scaling functions in different regimes of (v, L), namely,

$$\langle \mathcal{O}^2 \rangle = \begin{cases} L^{-2\beta/\nu} a^{-d+2\beta/\nu} f_1(vL^{zr+1/\nu}), & v < v_a \\ L^{-d} f_2(a^{-(zr+1/\nu)} v^{-1}), & v > v_c(L), \end{cases} \tag{1.33}$$

where f_1 and f_2 are different scaling functions, valid in their own associated velocity regions. More generally, the above two scaling functions can be described by a single common universal form with two arguments, i.e.,

$$\langle \mathcal{O}^2 \rangle \sim L^{-2\beta/\nu} a^{-d+2\beta/\nu} G(vL^{zr+1/\nu}, a^{-(zr+1/\nu)}/v). \tag{1.34}$$

However, it is in practice easier to analyze its two limiting forms (1.33) with single scaling arguments.

In the velocity regime $v \ll v_c(L)$, the system should be perturbative in v, while in the opposite limit when $v \gg v_a$, the system can be described by perturbation in $1/v$. As we will demonstrate in later chapters, there is a wide region, $v_c(L) < v < v_a$, over which f_1 and f_2 are both applicable. This corresponds to the regime where both perturbative descriptions (in v and $1/v$) have broken down and have been replaced by a universal power-law behavior, expressed as Eq. (1.28) and (1.30) for f_1 and f_2, respectively.

The basic idea is that by quenching the system to λ_c with different velocities (or generalized velocity for $r \neq 1$), one can generally observe cross-over behaviors at $v \sim v_c(L)$ as well as at $v \sim v_a$ between perturbative and non-perturbative regimes. The velocities $v_c(L)$ and v_a separate different forms of the size dependencies of the order parameter. The characteristic velocity v_a separates the velocity independence, $\langle \mathcal{O}^2 \rangle \sim L^{-d}$, from the power-law form $\langle \mathcal{O}^2 \rangle \sim L^{-d} v^{-x}$ for $v_c(L) < v < v_a$, and then another characteristic velocity $v_c(L)$ separates this behavior from the critical equilibrium scaling form $\langle \mathcal{O}^2 \rangle \sim L^{-2\beta/\nu}$ for $v < v_c(L)$.

Although it is not necessary but numerically convenient, we can also assume that the function f_1 in Eq. (1.33) can be written as a series expansion of $vL^{z+1/\nu}$ in its perturbative regime, and, as was pointed out above, f_2 should depend on λ_i and can be written as a series expansion in $1/v$ in its perturbative regime. In their non-perturbative regimes both functions reduce to the same power law form (just expressed in two different ways). We therefore expect the following forms to hold in the three different scaling regimes:

$$\langle \mathcal{O}^2 \rangle = \begin{cases} L^{-2\beta/\nu} \sum\limits_n c_n (vL^{zr+1/\nu})^n, & v \lesssim v_c(L) \\ L^{-d} \left(\frac{1}{v}\right)^x, & v_c(L) \ll v \ll 1 \\ L^{-d} \sum\limits_n c_n (1/v)^n, & v \gtrsim 1 \end{cases} \tag{1.35}$$

where we have explicitly set $a = 1$ and, therefore, $v_a = 1$. Through this dissertation, we will refer to the velocity regime $v \lesssim v_c(L)$ as the quasi-adiabatic regime, $v_c(L) \ll v \ll 1$ as

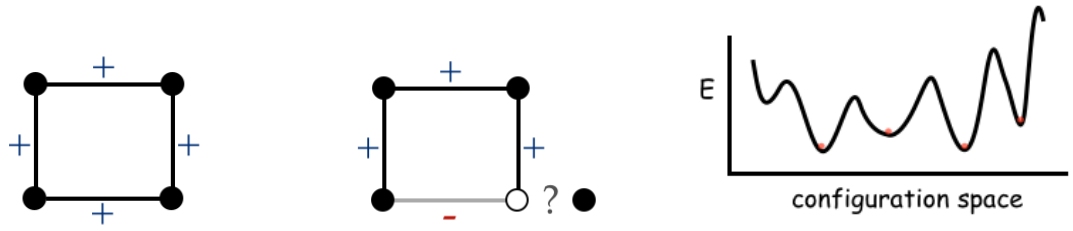

(a) (b) (c)

Figure 1.5: A 4-spin system with all ferromagnetic Ising interactions has a unique ground state configuration (a). A system with both ferromagnetic and antiferromagnetic interactions that is "frustrated" and has degenerate ground state due to the competing orders (b). Generally speaking, a frustrated system is usually associated with a rough energy landscape in the configuration space because many different configurations would have the same energy (c).

the universal scaling regime, and $v \gtrsim 1$ as the diabatic regime. The asymptotic form in the universal scaling regime $v_c(L) \ll v \ll 1$ corresponds to the power-law behavior, Eq. (1.30), that both scaling functions f_1 and f_2 converge to.

1.3 Introduction to spin-glass systems

In the previous two sections, we have introduced systems in which the spin-spin interactions $\sigma_i \sigma_j$ are isotropic. Another class of systems, spin-glasses, can be though of as introducing anisotropy into the interactions. The simplest modification can be described by:

$$\mathcal{H} = -\sum_{\langle i,j \rangle} J_{ij}\, \sigma_i \sigma_j, \tag{1.36}$$

where $\langle i, j \rangle$ can be beyond nearest-neighbor spin pairs, and the interactions J_{ij} generally are random in both magnitude and sign. For demonstration purpose, in this section we will only consider $J_{ij} = \pm 1$ spin-glasses, also known as bimodal spin-glasses, where $J_{ij} = +1(-1)$

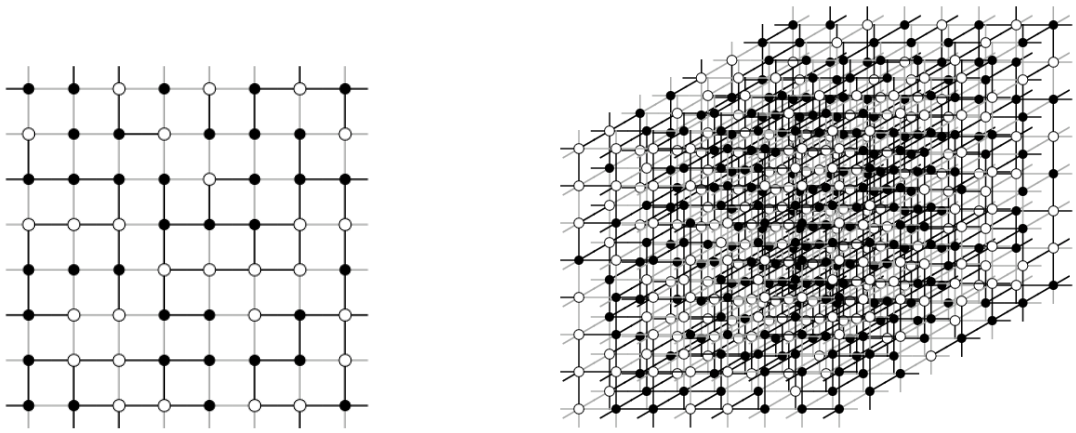

(a) (b)

Figure 1.6: Illustrations of the 2D (a) and 3D (b) bimodal spin-glasses in which the interactions are randomly assigned, $J_{ij} = +1$ or -1, both systems are highly frustrated. A classical 2D system is known to have spin-glass transition at $T = 0$ [19, 20]. A classical 3D system instead has a finite transition temperature $T_c \approx 1.10(1)$ [21].

stands for (anti-)ferromagnetic interaction. When the interactions are all ferromagnetic, as we have illustrated in Sec. 1.1.2 for the classical Ising model, the ground state configuration has an unique configuration (apart from the spin-inversion configuration), as illustrated in Fig. 1.5(a). However, when some of the interactions are replaced by anti-ferromagnetic ones, the ground state configuration is no longer unique due to the competing interactions that result in degenerate ground state, also known as "frustration," as illustrated in Fig. 1.5(b). As one can imagine, when the system becomes larger and larger, or the dimension increases as illustrated in Fig. 1.6, the degree of frustration will increase dramatically. Therefore, frustrations usually bring a rough energy landscape to the system in the configuration space, because many different configurations would result in the same or similar energy level, as illustrated in Fig. 1.5(c). Furthermore, except for a few special cases that will be mentioned below, most spin-glass systems are too complicated to be solved exactly, therefore, numerical techniques, especially unbiased Monte Carlo simulation, have served as the major tool to investigate this type of systems.

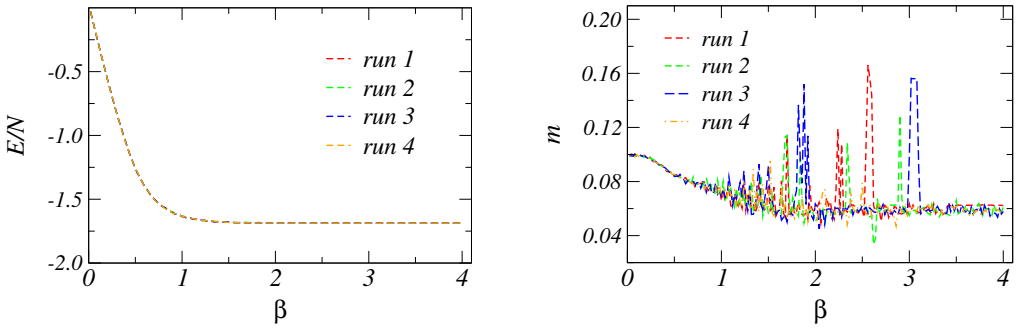

(a) (b)

Figure 1.7: Four independent runs for a realization of 3D bimodal Ising spin-glass of size $L = 4$. The energy per site,E/N, as a function of the inverse temperature $\beta = 1/T$ (a). The magnetization, $m = (1/N)\sum_i \sigma_i$, as a function of the inverse temperature (b). These two panels show that below some temperature β_c, the system shows degenerate configurations since the energies are the same while the magnetizations are different.

When the system is at some high temperature, the thermal fluctuation dominates over spin-spin interactions; however, when the temperature decreases, the thermal fluctuation diminishes and eventually the system exhibits the rough energy landscape, i.e., spin-glass phase. Therefore at some temperature there is a spin-glass transition. For 2D bimodal spin-glass systems, it was found that the transition temperature is zero [19, 20]. However, 3D system has a finite transition temperature, $T_c \approx 1.10(1)$ [21].

Fig. 1.7 further depicts the highly degenerate behavior in the spin-glass phase. Four independent simulations were carried out for a given realization of the 3D bimodal Ising spin-glass cube of linear size $L = 4$. While the energies are the same for these four independent runs, the magnetizations show clear distinctions when the temperature is below some value, indicating the degenerate configurations in the spin-glass phase.

The highly disordered configuration, as illustrated in Fig. 1.6, suggests that the magnetization is not ideal for characterizing the spin-glass phase, since different locations in the system may have different preferred magnetic orientations, which may result in a small

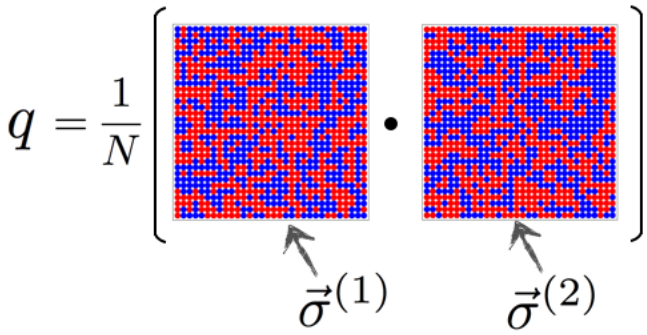

Figure 1.8: The illustration of EA order parameter defined in Eq. (1.37), which can be though of as the overlap between two configurations obtained respectively by two independent simulations for the same spin-glass realization.

overall magnetization. Therefore another order parameter defined below, called Edwards-Anderson (EA) order parameter, had ben proposed by Parisi [22] to describe the spin-glass phase:

$$q = \frac{1}{N} \sum_i \sigma_i^{(1)} \sigma_i^{(2)}, \tag{1.37}$$

where $\vec{\sigma}^{(1)}$ and $\vec{\sigma}^{(2)}$ are two "replica," namely, the configurations from two independent simulations. One can think of q as computing the overlap between these two replicas, as illustrated by Fig. 1.8.

The 2D and 3D bimodal spin-glass systems mentioned above are to this day too complicated to solve analytically. Nevertheless, currently there are two special types of spin-glasses that can be solved exactly, both being amenable to a mean-field description, and in the classical (thermal) description both are effectively at the upper critical dimension $d_{\rm uc} = 6$ in the sense of conversion between N and L through $L = N^{1/d}$ [23].

The first exactly solvable spin-glass model was the Sherrington-Kirkpatrick (SK) model [24], which is the fully-connected model described by the same Hamiltonian Eq. (1.36), with $\langle i, j \rangle$ standing for all possible spin pairs. One example of SK model with $N = 16$ spins is

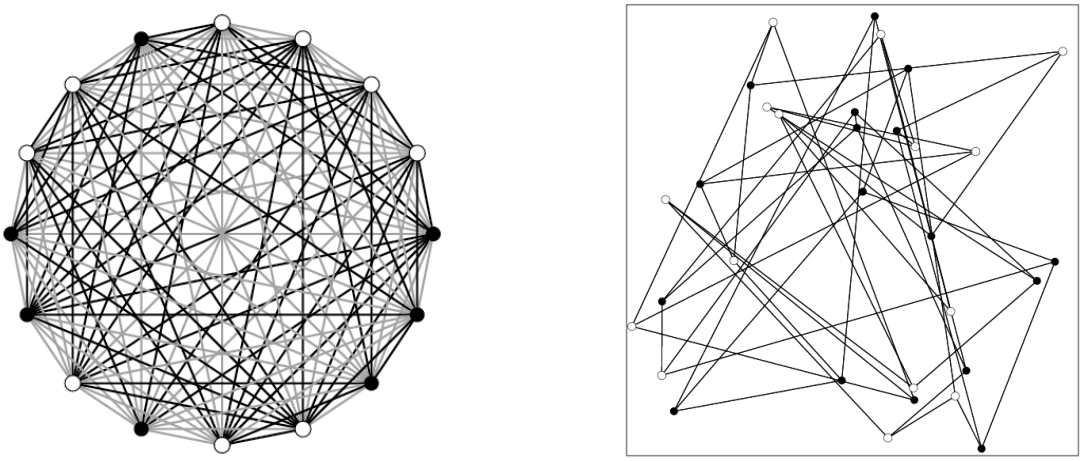

(a) (b)

Figure 1.9: Two examples of exactly solvable spin-glasses. SK model with $N = 16$ spins (a), in which the interactions exist between all possible spin pairs with magnitude J_{ij} being Gaussian-distributed at mean 0 and variance $1/N$, i.e., $J_{ij} \sim \mathcal{N}(0, 1/N)$. An antiferromagnetic 3-regular random graph with $N = 32$ spins (b). "3-regular" means the connectivity is 3 for every spin, and each spin is interacting with 3 other spins individually through the isotropic AF interactions, i.e., $J_{ij} = -1$ isotropically. However, due to loops of odd lengths, the system is highly frustrated. Both systems (a) and (b) are at the upper critical dimension $d_{\text{uc}} = 6$ in terms of the classical (thermal) scaling.

illustrated in Fig. 1.9(a).

The second type of exactly solvable spin-glasses, which employs a cavity method with replica symmetry breaking (RSB) [25–29], is the antiferromagnetic Potts model on a random graph that has finite connectivity. In this dissertation we will specifically only consider the case which has connectivity = 3 for every spin, also known as 3-regular random graphs, as illustrated in Fig. 1.9(b). Although the interaction is isotropic in this case, $J_{ij} = -1$, due to large number of loops of odd lengths, the system is highly frustrated and shows a spin-glass phase. This type of spin-glass systems is interesting in another aspect duo to its connection to numerous combinatorial optimizations and satisfiability problems [26, 27, 30].

Most importantly, we will demonstrate in different chapters of this dissertation that the non-equilibrium dynamic finite-size scaling described in Sec. 1.2 still holds at the spin-glass transitions. We will specifically use several spin-glass systems mentioned in this section to demonstrate this idea from the perspective of both classical and quantum transitions.

1.4 Organizations of the rest of the dissertation

In the following six chapters, we demonstrate the idea of approaching either the classical or quantum phase transition through non-equilibrium quench (NEQ) processes on different systems, using the formalism outlined in Sec. 1.2.

The following three chapters 2, 3, and 4 establish and demonstrate the ideas of NEQ on benchmark systems. The applications of NEQ with different protocols on classical and quantum systems, and how to independently extract static and dynamic critical exponents will be discussed in detail. Based on this approach we also present an efficient method to study disordered and frustrated systems, which will be the focus of chapters 5, 6, and 7. The organization of the chapters is summarized in Fig. 1.10.

In Ch. 2, we apply NEQ to the Ising model in two-dimension as well as higher dimensions. We obtain high-precision numerical estimate of various dynamic exponents associated with different types of dynamics. In Ch. 3, we demonstrate the idea of non-equilibrium quench on quantum Ising model. Along these lines we also develop a new quantum Monte Carlo algorithm called the *quasi-adiabatic quantum Monte Carlo* (QAQMC) algorithm. It should be noted that despite its name, the utility of QAQMC can actually be carried out in the regime far away from quasi-adiabatic limit, as we will discuss in Ch. 4, in which we also discuss the distinct difference between simulation-time quantum annealing and imaginary-time quantum annealing that is implemented via QAQMC algorithm. In Ch. 5, we apply NEQ to study a disordered system, namely, 3-regular random graphs with ferromagnetic interactions, in terms of classical and quantum phase transitions, respectively. The system,

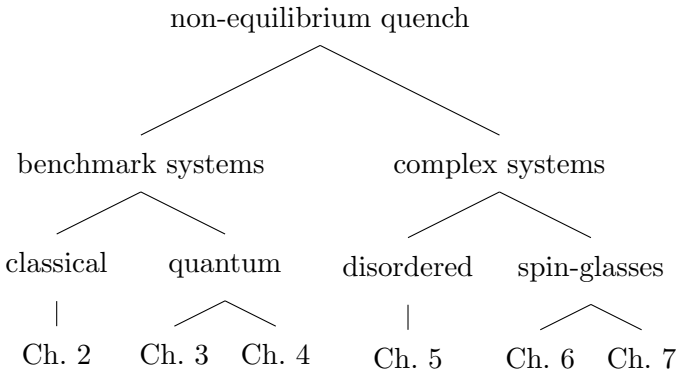

Figure 1.10: Structural organization of the thesis.

being disordered, provides an intermediate bridge for us to go from clean systems such as the Ising model studied in Chapters 2 and 3 to more complex systems such as spin-glasses discussed in Chapters 6 and 7. In Ch. 6, we apply NEQ to study 3-regular random graphs with anti-ferromagnetic interactions. The system is disordered and frustrated, i.e., a spin-glass system. The interest in this system arises because of its spin-glass properties in physics as well as its correspondence to the MaxCut problem of graph partitioning in information science, combinatorial optimization in engineering, and the complexity analysis in quantum computing and adiabatic quantum algorithm. In Ch. 7, we look at the quench performance on classical 3D spin-glasses with different microscopic interaction types, e.g., bimodal and Gaussian. Despite the notorious and severe critical slowing-down problem, the static properties and exponents of the model with different microscopic interaction types have been thoroughly studied and found to be in the same static universality class. However, the dynamic universality is still controversial and unsettled to this date. We therefore use the quench method to solve this problem.

Chapter 2

Classical phase transitions approached through non-equilibrium quench

2.1 Introduction

Phase transitions and critical phenomena have formed a dominant theme in statistical physics for a long time and new aspects are still subject to active research. This is not only because of the importance and elegance of the fundamental aspect of many-body systems in the original setting of condensed-matter physics, but also thanks to diverse applications to various complex systems in other areas of physics, as well as in chemistry, biology, and even in economics and social sciences. Any system with collective behavior resulting from a large number of interacting particles (or "agents") can be described by methods of statistical physics, and phase transitions often are important features of such systems.

A fundamental aspect of phase transitions is the scale invariance emerging upon approaching a critical point, which leads to universal scaling behavior independent of microscopic characteristics. The theoretical understanding of universality in equilibrium statistical mechanics is well established in terms of the renormalization group (RG). [2] Attempts have also been made to generalize this formalism as well as general scaling hypotheses to non-equilibrium phase transitions and dynamic critical scaling, [4, 14–16, 31–37] but the understanding here is much less complete. Since many important systems are far from equilibrium, deeper understanding of criticality and scaling behavior under such conditions is called for.

In this chapter we report progress in characterizing dynamical critical scaling at classical (thermal) phase transitions. We discuss a scaling hypothesis for a very general class of

quench (or annealing) protocols in which a function with a single dynamic exponent (along with the standard equilibrium exponents) describes the changes from adiabatic to diabatic evolution. To test the scaling forms we study phase transitions in classical Ising models, using Monte Carlo (MC) simulations with both single-spin and cluster updates.

2.1.1 Kibble-Zurek Mechanism

Our approach is based on extensions of the Kibble-Zurek (KZ) arguments, [14, 15] which originally focused on quantitatively relating defect formation (e.g., the typical defect size and the density of defects) to the rate of change (the quench velocity) of a parameter of the system (such as the temperature, external fields, etc.). The KZ mechanism and extensions of it have successfully been used to describe out-of-equilibrium physics at both classical [14, 15, 32] and quantum phase transitions [31, 33, 34, 37–40] (for a general review, see, e.g., Ref. [16]).

We consider a system with critical temperature T_c. When this system is quenched to the neighborhood of T_c by starting from some initial temperature $T_i > T_c$ and ending at some final temperature $T_c \leq T < T_i$, if the rate of change is sufficiently slow the system evolves adiabatically toward its equilibrium state at temperature T. (More accurately, we should refer to this limit as the quasi-static limit when we are dealing with an open system. We will here use the term adiabatic in the generalized sense.) Small deviations from adiabaticity (the quasi-adiabatic regime) can be described by adiabatic perturbation theory (as has been demonstrated explicitly for quenches of quantum systems at zero temperature, [37, 41] and one can anticipate direct analogues for classical quenches). In contrast, if the evolution is fast (the quench velocity is high), excitations lead to a large density of defects and the adiabatic description breaks down. The KZ mechanism provides a natural way to distinguish these perturbative and non-perturbative regimes.

According to the arguments of KZ, for the quasi-adiabatic picture to be valid, the time τ_{q}

that the system is allowed to take to approach the final temperature T must be at least of the order of the relaxation time $\tau_{\rm rel}$ associated with the system's microscopic dynamical properties at that temperature. The relaxation time is simply related to the equilibrium spatial correlation length ξ_T according to

$$\tau_{\rm rel} \sim \xi_T^z, \tag{2.1}$$

which defines the dynamic exponent z. This exponent depends on the equilibrium universality class of the phase transition, as well as the stochastic dynamics imposed on the system (or, alternatively, one can consider Hamiltonian dynamics, e.g., in quantum systems). Thus, for a linear quench with velocity v, the criterion for staying adiabatic is obtained by requiring for the total quench time τ_q:

$$\tau_{\rm q} \sim |T_i - T|/v \sim \tau_{\rm rel} \sim \xi_T^z \sim |T - T_c|^{-z\nu}, \tag{2.2}$$

where ν is the equilibrium correlation-length exponent.

Another way to interpret the above relationship is to consider the *remaining* time τ of a quench which has reached temperature $T > T_c$ after starting out at some $T_i > T$ and which is to continue all the way down to T_c. Then, for a given τ, or equivalently, for given velocity v, the relation

$$\tau = |T - T_c|/v \sim |T - T_c|^{-z\nu} \tag{2.3}$$

defines the temperature T at which the system falls out of the adiabatic evolution and essentially freezes, not being able to evolve significantly for the remainder of the quench process. This should hold independently of the starting temperature T_i if it is sufficiently above T. From this relation we can also extract the velocity (the KZ velocity)

$$v_{\rm KZ}(T) \sim |T - T_c|^{1+z\nu}, \tag{2.4}$$

at which the system falls out of adiabaticity at temperature T. Thus, it is, in the thermodynamic limit, not possible to stay adiabatic all the way down to T_c. In Ref. [17], we

present an alternative derivation of this result, where we consider the continuous quench as a series of infinitesimal quenches.

We can also write down the spatial length-scale ξ_v associated with a given velocity, i.e., the correlation length reached at the point where the infinite system freezes and cannot follow the instantaneous equilibrium state. Since $\xi_v \sim \xi_T$ for the quasi-adiabatic evolution and $\xi_T \sim |T - T_c|^{-\nu}$ at the point of freezing, Eq. (2.4) gives

$$\xi_v \sim v^{-1/(z+1/\nu)}. \tag{2.5}$$

For a finite system the maximum length scale is L, i.e., $\xi_v \leq L$, and the characteristic velocity separating the adiabatic and non-adiabatic responses then has an lower bound, which is simply obtained, according to standard arguments in finite-size scaling theory, [3] by replacing the largest length-scale for the infinite system by L. In this case that means $\xi_v \to L$ in (2.5). Thus, a system of linear size L will remain adiabatic all the way down to T_c, provided that the quench velocity is of the order of the size-dependent KZ velocity given by

$$v_{KZ}(L) \sim L^{-(z+1/\nu)}. \tag{2.6}$$

When the velocity is below this characteristic value, the non-adiabatic response of the system is very small and can be treated perturbatively. In contrast, when the velocity exceeds $v_{KZ}(L)$ the quasi-adiabaticity breaks down and the response of the system corresponds to non-adiabatic dynamics which is non-perturbative in v.

It should be pointed out that it is in general not possible to assign an exact value to $v_{KZ}(L)$ (and all the other quantities defined above), as Eq. (2.6) only indicates a proportionality and the change between the quasi-adiabatic and non-perturbative regime normally takes place in the form of a smooth cross-over (although we will also demonstrate an interesting exception, where the break-down of the quasi-adiabatic regime is sudden). We will here use extensive MC simulations to extract scaling functions of the form $f(v/v_{\mathrm{KZ}})$ describing the dynamic approach to the critical point for several models and dynamic schemes, from

which the cross-over scale can be readily read-off. In addition to the KZ scale, we will also investigate and quantify another, higher-velocity (diabatic) cross-over scale v_a related to a size-independent microscopic (lattice) scale a.

2.1.2 Dynamic exponents

As we have seen in the discussion above, the dynamic scaling will naturally involve the dynamic exponent z of a given combination of model and imposed MC dynamics (updating scheme for the system configurations). For Metropolis dynamics [42], in which N single-spin flip attempts define a unit of time in updating the system configurations, many works have been devoted to extracting the value of z (which in the case of Metropolis dynamics we will often call z_{M}) for the 2D Ising model, e.g., Refs. [43–46]. The values obtained are typically close to 2.2, with $z_{\mathrm{M}} = 2.1667(5)$, obtained in Ref. [45], often quoted as the most reliable result. The relatively large dynamic exponent implies that the Metropolis algorithm suffers rather severely from critical slowing-down [8] when the system is close to its critical point—the collective critical clusters persist for long times when updated only gradually by single-spin flips. Despite the critical slowing-down issue, Metropolis dynamics is still indispensable in its own right due to its close correspondence to relaxation processes due to local couplings to the environment in experiment systems [47]. Moreover, the Metropolis algorithm is very widely applicable to simulations even of very complex many-body systems. Even though there is no experimental counterpart of cluster updates, efficient cluster updates such as the Swendsen-Wang (SW) [9] and Wolff algorithms [48] have been very important to reduce or eliminate the inefficiency caused by critical slowing down in simulations. However, unlike the Metropolis scheme, the applicability in practice of these algorithms is restricted to a smaller number of models.

For SW updates of the 2D Ising model, where the system is subdivided into clusters and each cluster is flipped with probability 1/2, the nature of the dynamic scaling is still somewhat controversial. Values for the dynamic exponent have typically fallen in the range $z_{\mathrm{SW}} =$

$0.2 \sim 0.35$, [49–52] but in some works it was instead proposed that the characteristic time diverges not as a power L^z but logarithmically, which would imply $z_{\mathrm{SW}} = 0$. [53] For the 3D Ising model the exponent is not known very precisely, with results typically falling in the range $z_{\mathrm{SW}} = 0.44 \sim 0.75$ [51, 52, 54].

In the Wolff algorithm, which can be regarded as an improvement over the SW algorithm, clusters are constructed one at a time and always flipped. It is therefore normally more likely to flip large clusters [54]. The value of the dynamic exponent was estimated at $z_{\mathrm{W}} \approx 0.3$ for the 2D Ising model, and in the range $z_{\mathrm{W}} \sim 0.28$ to 0.44 for the 3D Ising model [52, 54].

2.1.3 Aims and outline of the chapter

We here explore dynamic critical scaling in MC simulations of the Ising model, primarily in two dimensions but with some results also for higher dimensions. We change the temperature linearly or nonlinearly as a function of MC time and focus on the approach to the critical point. When such a quench becomes extremely slow (and perhaps is more properly referred to as annealing), the scheme described above is known as *simulated annealing*. [55]

While ideas of how to incorporate insights from the KZ mechanism or similar considerations into simulated annealing processes have been discussed previously [56–58], the goal of these works has normally been to maximize the efficiency of the process of finding the global energy minimum of a system (optimizing the annealing schedule), or to reach the finite-temperature equilibrium distribution as fast as possible. Also, simulated annealing was studied to analyze the interplay between the KZ mechanism and coarsening dynamics [59, 60]. In our work presented here, the objective is instead to study the scaling behavior when the transition point is approached in systems of different size and at different velocities.

The basic idea is to generalize the standard finite-size scaling techniques, where scaling functions depend on the ratio L/ξ_T, to finite-velocity scaling where L/ξ_v should enter in a similar way. Our main aim is to establish benchmarks for dynamical critical scaling,

especially the form of the scaling functions describing quenches to T_c, for a prototypical model system and the above mentioned most commonly used MC updating schemes. Some aspects of this kind of generalized KZ scaling have already been reported, e.g., in quantum systems where similar scaling behavior applies, [33, 37, 40] in some classical systems based on effective dynamical Ginzburg-Landau models [32]. Here we propose different ways to analyze data and provide a more complete characterization of the scaling behaviors in the entire velocity range.

We study basic classical Ising models described by the generic Hamiltonian

$$H = -J \sum_{\langle i,j \rangle} \sigma_i \sigma_j, \tag{2.7}$$

where the coupling is ferromagnetic, $J > 0$, and the spins take values $\sigma_i = \pm 1$. The site pairs $\langle i, j \rangle$ normally correspond to nearest neighbors (and we then impose periodic boundary conditions) but we will also consider the fully-connected model (i.e., all site pairs are included in the summation). We discuss the two-dimensional (2D) case in Sec. 2.3 and discuss the three-dimensional (3D) and fully connected cases in Sec. 2.4. For the dynamics, we use single-spin flips accepted according to the Metropolis algorithm [42] as as well as two different cluster algorithms; those of Swendsen-Wang [9] and Wolff. [48]

The rest of the chapter is organized as follows: In Sec. 2.2 we discuss details of the dynamic scaling of the order parameter for linear and generalized non-linear power-law protocols through which the system is quenched to the critical point. We also discuss the use of different scaling functions applicable in the low-velocity (quasi-adiabatic) and high-velocity (diabatic) regimes, as well as in the regime (a universal scaling regime) connecting these behaviors. In Sec. 2.3 we demonstrate the application of the dynamic scaling ansatz using simulation data obtained with the three different MC updating schemes for the 2D Ising model. In Sec. 2.5 we summarize our main conclusions and discuss potential further applications. An alternative derivation of the KZ velocity is provided in Ref. [17], where we also briefly discuss optimized protocols given finite time resources for quenching. In

Sec. 2.4 we demonstrate dynamic scaling with SW and Wolff cluster updates for the 3D and fully-connected Ising models.

2.2 Dynamic Finite-Size Scaling

It is well known in equilibrium physics that systems show universal finite-size scaling behavior in the neighborhood of the critical temperature T_c. Physical quantities can then be described by a non-singular scaling function $g(L/\xi_T)$ and a universal power of the system size according to the form

$$A(L,T) = L^{\kappa/\nu} g(L/\xi_T) = L^{\kappa/\nu} G[(T-T_c)L^{1/\nu}], \tag{2.8}$$

where κ is an exponent depending on the universality class of the transition and the quantity A. This general equilibrium form was initially hypothesized based on observations and has now been rigorously demonstrated through the renormalization group. [2, 3]

We here discuss how the KZ mechanism introduced in Sec. 2.1.1 can be incorporated into finite-size scaling forms for systems undergoing quench dynamics.

2.2.1 Generalized KZ finite-size scaling

In a non-equilibrium setup, which we here first take to be a linear quench toward the critical point, the scaling argument L/ξ_v, with ξ_v defined in Eq. (2.5) should enter in addition to the equilibrium argument L/ξ_T. As is clear from the definitions in Sec. 2.1.1, we can also consider the velocity ratio $v/v_{KZ}(L)$. We use it to write down an ansatz in terms of a function depending on the two scaling arguments;

$$\begin{aligned} A(T,L,v) &= L^{\kappa/\nu} f(L/\xi_T, v/v_{KZ}) \\ &= L^{\kappa/\nu} F\big[(T-T_c)L^{1/\nu}, vL^{z+1/\nu}\big]. \end{aligned} \tag{2.9}$$

This generalized scaling ansatz has been justified in quantum systems in the slow limit using adiabatic perturbation theory, [38] and it has also been demonstrated in the case of

quantum phase transitions in imaginary-time dynamics. [33,37] However, except for several works by Zhong and collaborators (where an $L \to \infty$ formalism was mostly adopted from the outset) [61] and Chandran *et al.* [32] the classical counterpart has not, to our knowledge, been investigated as extensively as the quantum case.

2.2.2 Linear quench protocol and procedures

Clearly, Eq. (2.9) reduces to the standard equilibrium finite-size scaling ansatz in the limit $v \to 0$. When $v \neq 0$ the framework allows us to study the response of the system away from the adiabatic limit. For a system with a known value of T_c, one can carry out a quench process from a high temperature, $T_i > T_c$ to T_c, hence eliminating the first argument in the universal function in (2.9);

$$A(T_c, L, v) = L^{\kappa/\nu} F(vL^{z+1/\nu}). \tag{2.10}$$

This scaling form is very similar to the equilibrium form (2.8) and is easy to study the size and velocity dependence of physical quantities at the transition point, using data-collapse techniques familiar from conventional finite-size scaling.

The main purpose of the work reported here is to justify the generalized scaling ansatz (2.10) at $T = T_c$ by testing it in detail for classical phase transitions and investigating its range of applicability. We present several benchmark cases showing that the ansatz works extremely well. Below we will also extend Eq. (2.10) by introducing yet another scaling argument v/v_a, where v_a is related to a microscopic scale. One can then observe scaling over the entire velocity range $v \in [0, \infty]$.

Theoretically, any temperature higher than T_c can be used as the initial temperature (or one can start below T_c from an ordered state, but here we will only consider $T_i > T_c$) but in practice a higher temperature implies that it is easier to generate an equilibrated configuration before the quench process begins (which would be particularly important when studying spin glasses or related systems with very slow equilibration close to T_c). The

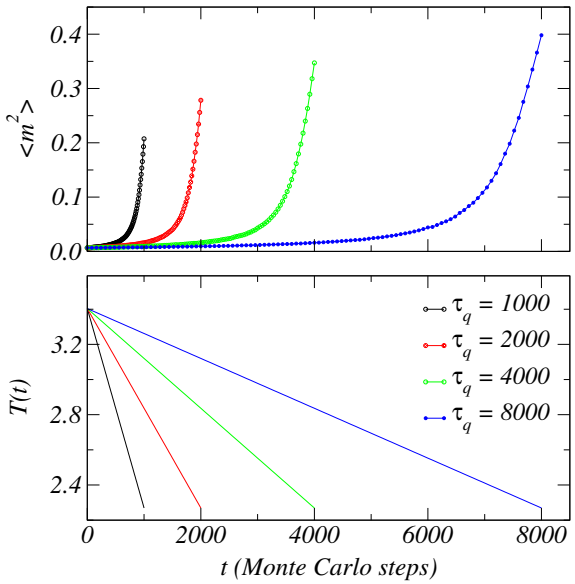

Figure 2.1: Illustration of linear quenches of the 2D Ising model. A system of size $L = 32\times32$ was equilibrated at the initial temperature $T_i = 1.5T_c$ and was thereafter linearly quenched to T_c. The quench velocity was $v = 0.5T_c/\tau_q$, where τ_q is the total quench time. Here one unit of time is defined as one MC step consisting N attempts to flip randomly selected spins using the standard Metropolis probability. Shown are the temperature (bottom panel) and the magnetization squared (top panel) versus time for different total quench times. We will focus our studies here on the scaling of $\langle m^2 \rangle$ at the final point.

details of the diabatic dynamics will also of course depend on T_i, but for slower velocities the results should become independent of the initial condition.

Knowing the exact value of T_c prior to the simulation is not a necessary condition for this approach to work, since one can also track, e.g., the order parameter or the Binder cumulant [62] in non-equilibrium simulations and locate T_c by various scaling techniques similar to equilibrium finite-size scaling. We demonstrated this recently for a quantum model. [37] However, for purpose of demonstrating dynamic scaling at classical transitions under different dynamic schemes, we will here use the known values of T_c for the systems of interest.

For obtaining the results presented in this chapter, we typically started with an equilibrated configuration at an initial temperature $T_i = 1.5T_c$ and performed an MC quench process carrying the system to its critical point. The quench velocity in the linear case can therefore be written as $v = 0.5T_c/\tau_q$, where τ_q is the total quench time in units of MC steps. We note that one unit of time in MC simulations normally corresponds to an extensive number of spin flips (but we will also consider a case, with Wolff dynamics, where this is not true). The precise definition of the time unit depends on the dynamics used.

Typical examples of linear quench processes are illustrated in Fig. 2.1 with results for the magnetization squared (which will be the only physical quantity studied in this chapter);

$$m^2 = \left(\frac{1}{N} \sum_{i=1}^{N} \sigma_i \right)^2 . \tag{2.11}$$

In this case the exponent $\kappa = -2\beta$ in Eq. (2.10) and we expect scaling at T_c according to

$$\langle m^2 \rangle = L^{-2\beta/\nu} F\big(vL^{z+1/\nu}\big), \tag{2.12}$$

provided v is sufficiently small (and we will discuss how small that is below). Note that the process stops at T_c and there is no waiting time after that to relax the system further (which would introduce yet another time scale, which one can certainly consider but we do not include it here). Only a single measurement of m^2 is carried out after the system has reached T_c and the brackets $\langle \dots \rangle$ in Eq. (2.12) represent the ensemble average over different quenches with different equilibrated starting configurations. Typically, we calculated averages on the basis of thousands of such independent MC runs.

The initial configuration at $T = T_i$ was equilibrated and sampled before the start of each run using cluster updates (to be discussed further below) to ensure statistically independent starting configurations for each quench process. For studying slow dynamics it is strictly not necessary to equilibrate the initial configuration, since one can expect the system to become memoryless for slow enough quenches when approaching T_c. However, we here also study the fast limit and want the system to reduce to the equilibrium at T_i when $v \to \infty$. We therefore always equilibrate.

2.2.3 Nonlinear quench protocols

The simple scaling hypothesis discussed above has also been generalized to non-linear protocols, where the critical point is approached according to an arbitrary power-law of the time t measured with respect to the final time τ_q, [18] [1]

$$T - T_c = v(\tau_q - t)^r, \tag{2.13}$$

where v is the velocity as above for a linear quench ($r = 1$), the acceleration (up to a factor 2) for a quadratic quench ($r = 2$), etc. (and for simplicity we will refer to v as the velocity, regardless of the power r). For a sudden quench ($r = 0$) v should be regarded as the amplitude of the change in T (and with this definition note that there is no waiting time after the quench, which is another time-scale that could be added but we do not consider here). As in the linear case, for all r we use $T_i = 1.5T_c$ and express v in units of T_c as $v = 0.5T_c/\tau_q^r$, where τ_q is the total quench time.

The generalized critical "velocity" for arbitrary r (including non-integer) can be easily found by following the same arguments as in Sec. 2.1.1;

$$v_{KZ}(L) \sim L^{-(zr+1/\nu)}. \tag{2.14}$$

In [17] we provide an alternative derivation of this result based on a time-discretized quench, which also gives some information on how the unknown prefactor above depends on the exponents involved.

The magnetization scaling form (2.12) with (2.14) becomes

$$\langle m^2 \rangle = L^{-2\beta/\nu} F\big(vL^{zr+1/\nu}\big). \tag{2.15}$$

We will study mainly $r = 1$ quenches but also discuss some results for $r = 1/2$ and $r = 2$. Protocols for approaching the critical point very slowly, in particular with negative r, have also been investigated recently. [32]

[1] In Ref. [18], the protocol was defined as $T - Tc = v(\tau_q - t)^r/r!$. For simplicity, we here leave out $1/r!$.

2.2.4 Complete scaling form for the order parameter

For a given system size we can access a wide range of velocities (the highest $v < \infty$ corresponding to carrying out a single MC step) and we can therefore examine very different response regimes of the system. When the quench velocity becomes very high, our procedures ensure that the magnetization squared after the quench to T_c remains close to its value at the initial temperature T_i. Since the correlation length has a finite value there, one expects, for sufficiently large L,

$$\langle m^2 \rangle = \frac{1}{N^2} \sum_{\langle i,j \rangle} \langle \sigma_i \sigma_j \rangle = \frac{1}{N} \sum_j \langle \sigma_0 \sigma_j \rangle \sim L^{-d}, \tag{2.16}$$

where d is the number of dimensions; here $d = 2$ except in Sec. 2.4, where we also consider $d = 3$ and infinite dimensionality (in which case L is defined by $L = N^{1/d}$ with d the upper critical dimension). Thus, in the high-velocity limit, $\langle m^2 \rangle$ should depend on the initial temperature T_i and scale as L^{-d}.

When the velocity decreases one can expect the order of the system to develop gradually, and as long as the KZ correlation length ξ_v is much smaller than the system size L the magnetization squared should still depend on L with the trivial power above. With the scaling form (2.15), this behavior necessarily implies that the function F in this regime must reduce to a power law of the argument $vL^{z+1/\nu}$;

$$\langle m^2 \rangle \sim L^{-2\beta/\nu} \left(vL^{zr+1/\nu} \right)^{-x}, \tag{2.17}$$

and this exponent can be obtained by demanding this to be proportional to L^{-d}, i.e.,

$$x = \frac{d - 2\beta/\nu}{zr + 1/\nu}. \tag{2.18}$$

Thus, there is an intermediate universal scaling regime where

$$\langle m^2 \rangle \sim L^{-d} v^{-x}. \tag{2.19}$$

Note that this is not consistent with the high-velocity limit for fixed L, where, as discussed above, $\langle m^2 \rangle$ must converge to a constant times L^{-d} (without any remaining v dependence).

The power law written as Eq. (2.17) should instead hold for arbitrary large values of $vL^{z+1/\nu}$, as long as L is sufficiently large. Below we will discuss in detail the cross-overs between the power law and the ultimate high-v limit for any L.

Finally, when the velocity is decreased further and approaches $v_{KZ}(L)$, the assumption $\xi_v \ll L$ no longer holds. One would then expect deviations from the power-law form and a cross-over to a regime where Eq. (2.15) tends toward the corresponding L-dependent equilibrium value of at T_c, i.e., the standard finite-size behavior scaling,

$$\langle m^2 \rangle \sim L^{-2\beta/\nu}, \tag{2.20}$$

sets in. This cross-over from the v-dependent power-law to this equilibrium form is smooth and contained in the function F in Eq. (2.15).

To incorporate all these different asymptotics in different velocity regimes, it is useful to introduce a short-range length scale a, which is of the order of one lattice spacing, and, therefore, can be set to 1 for any practical purpose. This non-trivial factor a is essential for defining the *engineering dimension*, [6] $a^{-d+2\beta/\nu}$, which compensates for the discrepancy between the scaling dimension $L^{-2\beta/\nu}$ of $\langle m^2 \rangle$ and its canonical dimension L^{-d}. The short-range length scale sets the size-independent upper limit $v \sim v_a$ beyond which the power-law behavior (2.19) should break down;

$$v_a \sim a^{-(zr+1/\nu)}. \tag{2.21}$$

More explicitly, based on the above discussion one cannot expect Eq. (2.15) to be able to describe all situations with a single scaling function F, and this function should actually be replaced by two different scaling functions in different regimes of (v, L), namely,

$$\langle m^2 \rangle = \begin{cases} L^{-2\beta/\nu} a^{-d+2\beta/\nu} f_1(vL^{zr+1/\nu}), & v < v_a \\ L^{-d} f_2(a^{-(zr+1/\nu)} v^{-1}), & v > v_{KZ}(L), \end{cases} \tag{2.22}$$

where f_1 and f_2 are different scaling functions, valid in their own associated velocity regions. More generally, the above two scaling functions can be described by a single common

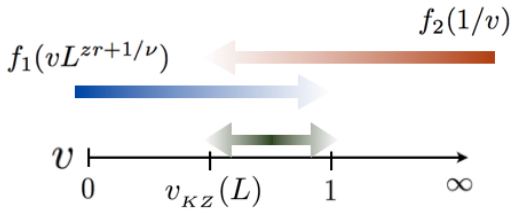

Figure 2.2: Illustration of the dual-scaling behavior outlined in Eq. (2.22) and Eq. (2.24). The first scaling function f_1 covers from quasi-adiabatic limit up to a high-velocity cut-off, $v_a \sim \mathcal{O}(1)$, and the second scaling function f_2 covers from the ultra-high velocity limit down to a low-velocity cut-off, $v_{KZ}(L)$. The middle region is where both functions apply and both functions reduce to a simple power-law behavior, therefore we call it universal power-law region.

universal form with two arguments, i.e.,

$$\langle m^2 \rangle \sim L^{-2\beta/\nu} a^{-d+2\beta/\nu} G(vL^{zr+1/\nu}, a^{-(zr+1/\nu)}/v). \tag{2.23}$$

However, it is in practice easier to analyze its two limiting forms (2.22) with single scaling arguments.

In the velocity regime $v \ll v_{KZ}(L)$, the system should be perturbative in v, while in the opposite limit when $v \gg v_a$ the system can be described by perturbation in $1/v$. As we will demonstrate below with numerical data, there is a wide region, $v_{KZ}(L) < v < v_a$, over which f_1 and f_2 are both applicable. This corresponds to the regime where both perturbative descriptions (in v and $1/v$) have broken down and have been replaced by a universal power-law behavior, expressed as Eq. (2.17) and (2.19) for f_1 and f_2, respectively. Fig. 2.2 illustrates the idea.

The basic idea that we are pursuing throughout this chapter is that by quenching the system with different velocities (or generalized velocity for $r \neq 1$), one can generally observe cross-over behaviors at $v \sim v_{KZ}(L)$ as well as at $v \sim v_a$ between perturbative and non-perturbative regimes. The velocities $v_{KZ}(L)$ and v_a separate different forms of the size dependencies of the magnetization squared (which is the quantity we focus on here, but

one of course expects analogous behaviors in other quantities). The characteristic velocity v_a separates the velocity independence, $\langle m^2 \rangle \sim L^{-d}$, from the power-law form $\langle m^2 \rangle \sim L^{-d} v^{-x}$ for $v_{KZ}(L) < v < v_a$, and then another characteristic velocity $v_{KZ}(L)$ separates this behavior from the critical equilibrium scaling form $\langle m^2 \rangle \sim L^{-2\beta/\nu}$ for $v < v_{KZ}(L)$.

The above forms Eq. (2.22) can be used to analyze numerical data by dividing $\langle m^2 \rangle$ by the appropriate power of L appearing on the right-hand side and graphing the result versus the argument of the scaling function. The data should then collapse onto the scaling function in the region of (v, L) where it holds; hence the scaling function is obtained. The first scaling form f_1, which requires the knowledge of critical exponents, is analogous to the equilibrium scaling at T_c. The second scaling f_2, requires no knowledge of the critical exponents.

Although it is not necessary, we can also assume that the function f_1 in Eq. (2.22) can be written as a series expansion of $vL^{z+1/\nu}$ in its perturbative regime, and, as was pointed out above, f_2 should depend on T_i and can be written as a series expansion in $1/v$ in its perturbative regime. In their non-perturbative regimes both functions reduce to the same power law form (just expressed in two different ways). We therefore expect the following forms to hold in the three different scaling regimes:

$$\langle m^2 \rangle = \begin{cases} L^{-2\beta/\nu} \sum_n c_n (vL^{zr+1/\nu})^n, & v \lesssim v_{KZ}(L) \\ L^{-d} \left(\frac{1}{v}\right)^x, & v_{KZ}(L) \ll v \ll 1 \\ L^{-d} \sum_n c_n (1/v)^n, & v \gtrsim 1 \end{cases} \tag{2.24}$$

where we have explicitly set $a = 1$ and, therefore, $v_a = 1$. In the following, we will refer to the velocity regime $v \lesssim v_{KZ}(L)$ as the quasi-adiabatic regime, $v_{KZ}(L) \ll v \ll 1$ as the universal scaling regime, and $v \gtrsim 1$ as the diabatic regime. The asymptotic form in the universal scaling regime $v_{KZ}(L) \ll v \ll 1$ corresponds to the power-law behavior, Eq. (2.19), that both scaling functions f_1 and f_2 converge to. Note again that, in practice, the highest velocity in our simulations corresponds to one MC step, i.e., $v = (T_i - T_c)/\tau_q^r$ with $\tau_q = 1$, which is of the order 1 with our chosen initial temperature.

Normally the cross-overs between the different regimes in Eq. (2.24) are completely smooth,

which we will demonstrate in the next section for Metropolis and SW dynamics in the 2D Ising model. Remarkably, however, in the case of the Wolff cluster algorithm we will show that the power-law regime is absent and the cross-over between the two perturbative regimes is not smooth. Instead, in the thermodynamic limit both the quasi-adiabatic and diabatic scaling behaviors break down discontinuously at specific values of the scaled velocity. In this sense the Ising model with Wolff dynamics undergoes a dynamic phase transition.

2.3 Simulation Results

In this section we demonstrate the application of dynamic finite-size scaling using the standard 2D Ising model on the square lattice. We discuss results using Metropolis dynamics in Sec. 2.3.1, SW dynamics in Sec. 2.3.2, and Wolff dynamics in Sec. 2.3.3. The exact value of T_c and the critical exponents are known exactly from the Onsager solution: [5] $T_c/J = 2/\ln(1+\sqrt{2})$, $\nu = 1$ and $\beta = 1/8$. This system therefore provides a good testing ground for our techniques. For all the quench processes we consider in the following we start with an initial temperature $T_i = 1.5T_c$, using the value of T_c quoted above, and then quench the system exactly to the critical point, at which observables are computed (and note again that there is no further waiting at T_c; a single measurement of $\langle m^2 \rangle$ is obtained after each quench). The quench process for given parameters is repeated thousands of times with different equilibrated starting configurations in order to obtain god statistical precision.

The focus here will be how the system responds to the dynamics when crossing the two characteristic velocities defined in the previous section, v_a and $v_{KZ}(L)$, and how the cross-over behaviors emerge in the dynamic scaling. As shown explicitly in the scaling forms discussed above, the scaling naturally involves the dynamic exponent z. Since the 2D Ising equilibrium critical exponents are all known exactly, the dynamic scaling allows one to extract z independently (and note that this exponent depends on the dynamics imposed and is not known exactly for any of the schemes we use). In practice we here do this by

optimizing a data collapse (onto one of the unknown scaling functions, which the process yields) with z as the only adjustable parameter.

2.3.1 Metropolis dynamics

Typical linear quench processes using Metropolis dynamics have been shown in Fig. 2.1. Fig .2.3 further demonstrates a typical scenario of a linear quench with Metropolis dynamics from an initial temperature T_i to T_c.

We here follow the convention that one unit of time is defined as $N = L^2$ attempts of flipping a randomly selected spin with the acceptance probability $p = \min[1, \mathrm{e}^{-\Delta E/T}]$, where ΔE is the change in energy after flipping the spin. For convenience we will give velocities in units of T_c, i.e., with the above T_i we define $v = 0.5/\tau_q^r$ for total quench time τ_q in units of MC steps. To demonstrate the insensitivity of the scaling to T_i, we will also present a test of this assumption. We first discuss the linear quenches and then present some results also for $r = 1/2$ and $r = 2$ non-linear protocols according to Eq. (2.13).

Linear quench

Data sets for different system sizes in linear-quench simulations at different velocities are analyzed collectively in Fig. 2.4 (a), using the scaling procedure appropriate when the first scaling form in Eq. (2.22) applies. Scaling collapse giving the function f_1 is observed all the way from the adiabatic regime, crossing over into universal power-law scaling, which persists up to arbitrarily large values of the KZ scaled velocity $vL^{z+1/\nu}$ when increasingly large L is used (pushing the diabatic cross-over further to the right). As we discussed in Sec. 2.2, the scaling behavior allows one to determine the dynamic exponent by carrying out a fitting procedure in which the value of z is adjusted to give the optimal fit to all the data included, which we quantify using the standard χ^2 per degree of freedom (dof). We here use two different functional forms to describe the function f_1 in the fitting procedure,

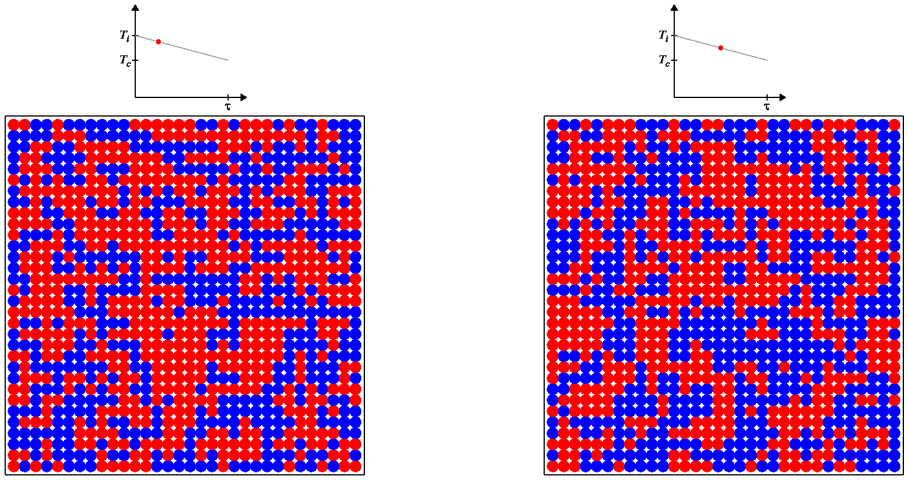

(a)

(b)

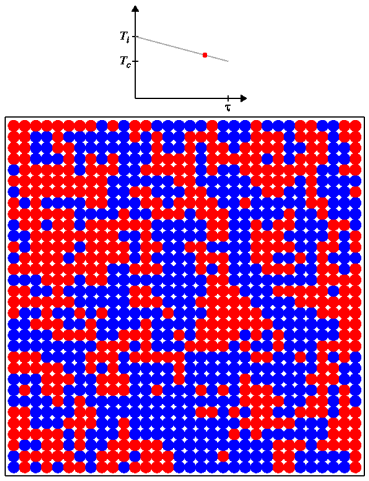

(c)

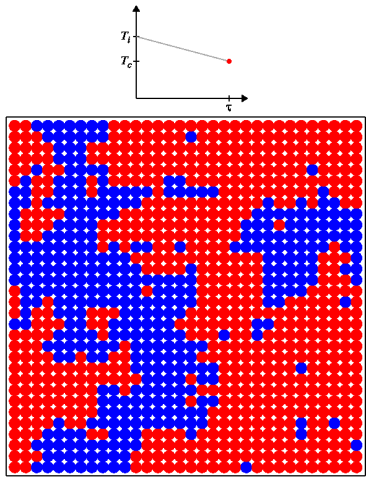

(d)

Figure 2.3: Illustration of a linear quench process on 2D Ising model with Metropolis dynamics. Shown are 25% (a), 50% (b), 75% (c), and 100% (d), through the quench process. At T_c (d), a percolating cluster spanning the entire system is clearly observed. In this demonstration, a total quench time $\tau_q = 3000$ Monte Carlo steps is used on a 32×32 square lattice.

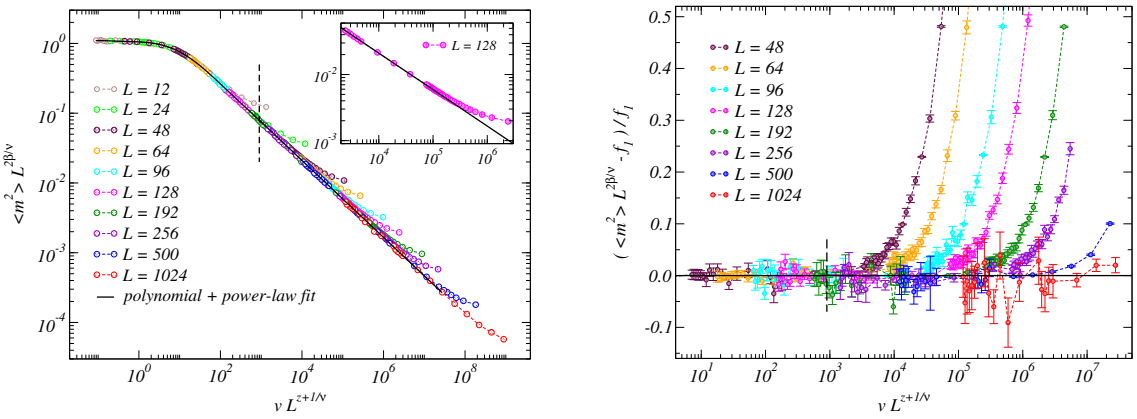

Figure 2.4: (a) The squared magnetization scaled by $L^{2\beta/\nu}$ after linear quenches to T_c, using Metropolis dynamics for 2D Ising models of different sizes. The collapsed data correspond to the first scaling form, f_1, in Eq. (2.22). The expected three different regimes corresponding to different asymptotics can be clearly distinguished; (left) approach to the equilibrium critical scaling in the quasi-adiabatic regime $v \lesssim v_{KZ}(L)$, (center) power-law scaling in the universal regime $v_{KZ}(L) \ll v \ll 1$, and (right-most points for each L) deviations from the scaling function in the diabatic regime $v \gtrsim 1$. The vertical dashed line shows the point separating the two fitting windows used in the optimization of the data collapse (varying z); to the left the fitted function approximating f_1 in the quasi-adiabatic regime is a high-order polynomial, and to the right a pure power law (straight line) given by Eq. (2.18) is used to account for the universal scaling behavior. The diabatic tails for each L were not included in the fits. The dynamic exponent used in scaling the x-axis was adjusted to obtain the overall best simultaneous fits of the data in the quasi-adiabatic and scaling regimes, which resulted in $z_M = 2.172(3)$ with the goodness of the fit, $\chi^2/\mathrm{dof} \approx 1.0$. Error bars for the data points are all smaller than the symbol sizes. The inset shows details of the $L = 128$ data in the region where the behavior crosses over from universal scaling to diabatic. (b) The difference between the fitted function $f_1(vL^{z+1/\nu})$ and the scaled magnetization squared, $\langle m^2 \rangle L^{2\beta/\nu}$ (same data as in panel (a)). The vertical line shows the point separating the two fitting windows. The points deviating significantly from the horizontal line correspond to diabatic behavior and those points were systematically excluded in the fitting procedure.

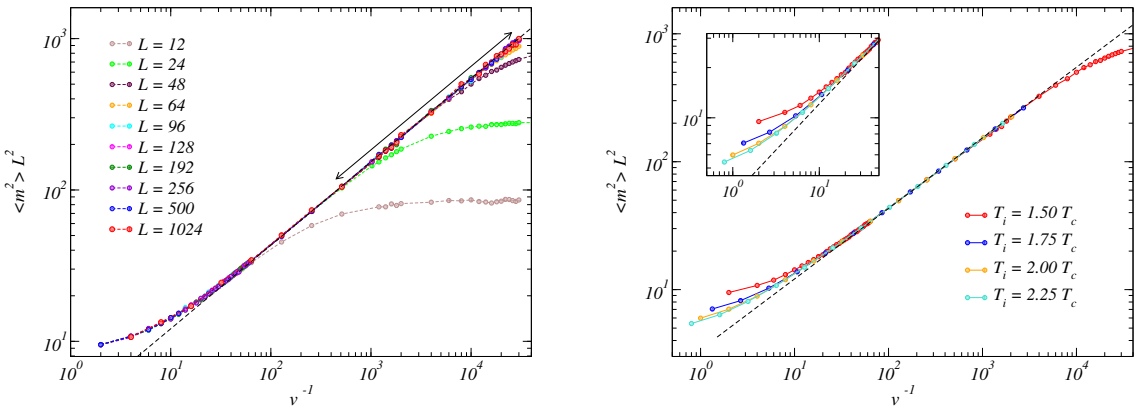

Figure 2.5: (a) Data collapse producing the second scaling function, f_2, in Eq. (2.22) for linear Metropolis-quenches with different system sizes. Here the left region corresponds to the diabatic regime, while straight-line form corresponds to the universal power-law scaling regime. The points deviate from the common function f_2 in the L-dependent quasi-adiabatic regime. The dashed line shows the slope expected with the dynamic exponent extracted in Fig. 2.4. As will be discussed in Sec. 2.3.1, the line with arrow indicates the region selected for the linear fit after taking log-log, we consider sizes $L \geq 192$. The linear fit gives the slope $x_{r_1} = 0.550(3)$, with $\chi^2/\text{dof} \approx 1.0$, which implies $z_M = 2.17(1)$, consistent with the result obtained in Fig. 2.4 of f_1 scaling. (b) Data graphed according to the second scaling function, f_2, in Eq. (2.22) for linear Metropolis quenches on $L = 48$ system with different initial temperatures. As expected, f_2 nominally depends on the initial temperature only in the diabatic regime. The inset shows more details of the data in the region where the data converge to common curve.

as in the first two lines of Eq. (6.7), in two non-overlapping windows of the scaling argument $vL^{z+1/\nu}$. The "plateau and shoulder" in Fig. 2.4 correspond to the quasi-adiabatic regime $v \lesssim v_{KZ}(L)$ and we use a high-order polynomial fit in this window. For practical purposes, to minimize the order of the polynomial required, we fit to the log-log data instead of the original data. The second window corresponds to the universal scaling regime characterized by $v_{KZ}(L) \ll v \ll 1$, where we use a pure power-law fit (a straight-line fit on the log-log scale).

The point separating the two fitting windows is chosen such that χ^2 computed individually in each window is statistically good. High-v data are excluded for each L when they deviate from the common curve (in which case they will also ruin the goodness of the fit, thus allowing for systematic exclusion of diabatic data). There are of course scaling corrections expected, as in standard finite-size scaling of equilibrium data, but for the Ising model these are relatively small. [63] We obtain good fits by considering system sizes $L \geq 12$. The statistical error of z is computed by repeating the data-collapse procedure many times with Gaussian noise added to the MC data (with standard deviation given by the corresponding error bars of the data). This procedure gives $z_M = 2.172(3)$, which is in good agreement with values previously obtained, e.g., in Refs. [44, 45].

Fig. 2.4 (b) further illustrates the optimization procedure in the form of the deviation of the two-piece fitting function $f_1(vL^{z+1/\nu})$ from the MC data for $\langle m^2 \rangle L^{2\beta/\nu}$. Statistically, the data points fully obey the scaling collapse except for those corresponding to the diabatic $v \gtrsim 1$ regime (which are excluded from the fits).

Note that the purpose of parametrizing the scaling function and carrying out fits is only to provide a convenient way to define the goodness of the data collapse. As long as the imposed functional form is capable of reproducing the scaling function to within the precision set by the error bars of the data (which is self-consistently tested by the statistical soundness of the fit quantified by χ^2), this procedure in no way distorts or biases the data collapse.

We discuss the diabatic regime next. Data collapse according to the second of Eqs. (2.22) is shown in Fig. 2.5 (a). The dashed line in Fig 2.5 (a) is drawn according the the value of x given by the result of z from Fig 2.4 (a). However, independently, the power-law behavior corresponding to the straight line allows one to estimate the dynamic exponent in a straight-forward manner through this kind of analysis, given the relation between the power (slope) x and z in Eq. (2.18). The advantage of this procedure is that the rescaling of the data does not involve any critical exponents at all. As we will discuss in more detail in Sec. 2.3.1, using linear fit after taking log-log, we obtain $x_{r_1} = 0.550(3)$, which implies $z_M = 2.17(1)$, this is consistent with the result obtained by f_1 scaling.

Note again that the linear regions in Figs. 2.4 (a) and 2.5 (a) correspond to the same data points, falling within the universal scaling regime, with just two different ways of expressing the middle line of Eq. (2.24), as stated according to Eq. (2.19) or as in Eq. (2.17) by moving the appropriate power of L to the left.

As discussed in Sec. 2.2, the initial temperature T_i at which the system is equilibrated before the quench process begins should only have a nominal effect on the scaling. We normally use $T_i = 1.5T_c$, but to demonstrate the insensitivity of the scaling to the initial temperature we show in Fig. 2.5 (b) results for a fixed system size and several values of T_i. As expected, there are differences in the diabatic regime, where in the $v \to \infty$ limit the results converge to the equilibrium at T_i. Beyond this regime, at lower velocities the data quickly converge to a common curve in the universal scaling regime. The convergence to a pure power law is somewhat faster for higher T_i, but it should be noted that the simulation time increases with T_i, which implies that, for purposes of extracting the dynamic exponent by fitting a straight line, there is some trade-off between the faster convergence to the power law and the longer simulation time. In cases where the initial equilibration may be challenging close to T_c, e.g., in frustrated systems (especially glasses) where cluster algorithms cannot be used, one may also want to start at a high T_i in order to ensure good initial equilibration.

Non-linear quenches

As we pointed out in Sec. 2.2, the KZ scaling scheme is not restricted to linear protocols. Eq. (2.22) incorporate nonlinear quench scenarios through the exponent r in the definition (2.13) of the more general protocol. These expressions provide a simple way to separate the quench process from the underlying stochastic dynamics (updating scheme); the former is characterized by the parameter r and the latter by the dynamic exponent z. Since in the non-equilibrium scaling relations only the combination zr enters, changing the exponent r has an effect similar to manipulating the dynamical exponent, which potentially can be useful for optimization and other purposes. Here we just focus on testing the applicability of scaling with $r \neq 1$.

In Fig. 2.6 (a), bottom panel, we show results of a "constant acceleration" quadratic quench with $r = 2$, in which case the the characteristic quantity (2.14) stands for a critical acceleration separating a perturbative and non-perturbative regimes, in analogy with the earlier discussion of the linear quench. The scaling collapse works very well, apart from the expected ultra-high acceleration limit where a break-down again is expected (and the deviations can be analyzed in terms of a different scaling function, as we will do below). The dynamic scaling also holds when the parameter r is a non-integer number corresponding to a non-analytic protocol, as it should, based on the derivations of the KZ scaling in [17] (while the applicability for non-integer r is less clear from other generalizations considered for $r \neq 1$ [18]). We demonstrate this with results of a square-root quench, $r = 1/2$, in the top panel of Fig. 2.6 (a).

As shown in Fig. 2.6 (b), scaling collapse also works very well in the diabatic limit of both these nonlinear quench protocols. A cross-over of the function f_2 to the universal scaling regime is observed as in the $r = 1$ case. Most importantly, the power-law behavior is clearly observed. One can again use the power-law regime in the f_2 scaling to estimate the power x, which can then be translated to z according to Eq. (2.18). Using linear fit

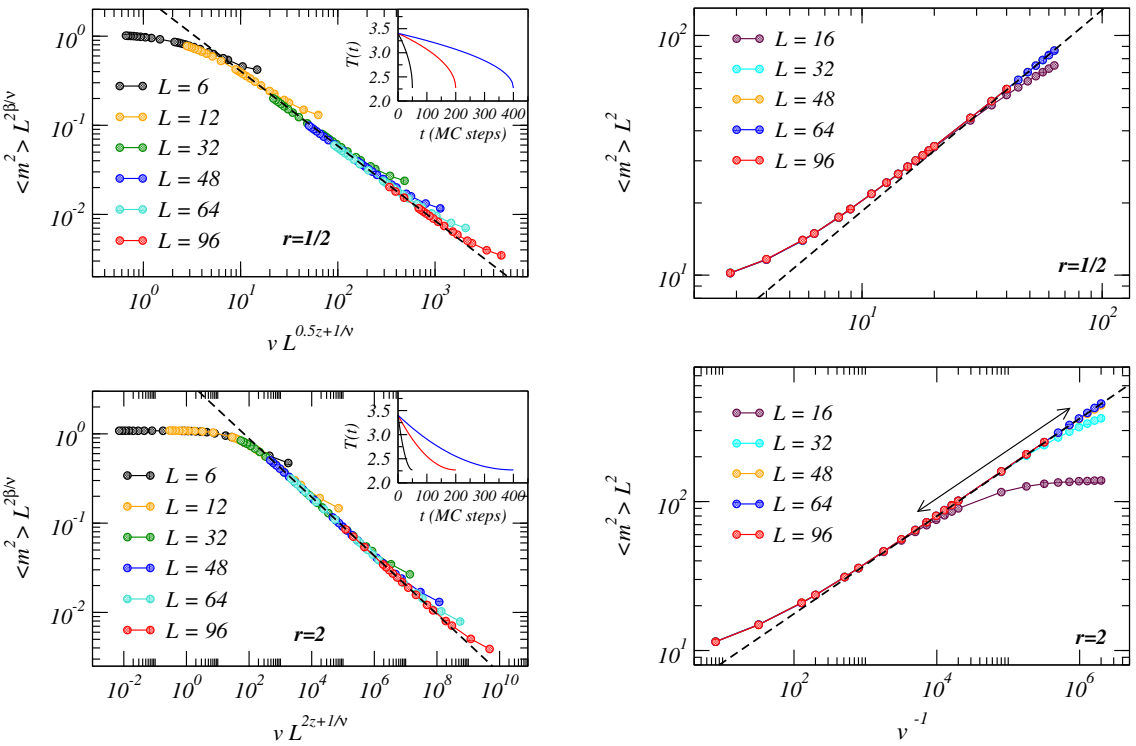

(a) (b)

Figure 2.6: (a) Data collapse in non-linear quenches to T_c with Metropolis dynamics of the 2D Ising model. The top and bottom panels are for $r = 1/2$ and $r = 2$, respectively, and v is expressed in units of T_c according to the definition (2.13) of the protocols with $T_i = 1.5T_c$. The data are analyzed and graphed in the same way as the linear quenches in Fig. 2.4 (a). The dashed lines show the slopes expected according to Eq. (2.18) with the dynamic exponent extracted in Fig. 2.4 (a). The insets shows examples of the protocols used. (b) Data collapse in the diabatic and universal scaling regimes for non-linear Metropolis quenches, with the top and bottom panels for protocols with $r = 1/2$ and $r = 2$, respectively. The dashed lines show the slopes expected according to Eq. (2.18) with the dynamic exponent extracted in Fig. 2.4 (a). As we will discuss in Sec. 2.3.1, the line in $r = 2$ panel indicates the region selected for linear fit after taking log-log, we consider sizes $L \geq 48$. The linear fit yields the slope $x_{r_2} = 0.32689(7)$, with $\chi^2/\text{dof} \approx 0.9$, which implies $z_M = 2.1767(5)$, consistent with the result obtained in Fig. 2.4 (a).

after taking log-log in the f_2 scaling of $r = 2$ quench, we obtain the slope $x_{r_2} = 0.32689(7)$, which implies $z_M = 2.1767(5)$. Remarkably, the statistical precision of this result is higher than the best results based on the $r = 1$ quenches discussed above, although the system sizes there were considerably larger. It is then interesting to ask what the optimal r is for extracting z_M, but we have not investigated this systematically. The applicability of the dual scaling for arbitrary r also opens an interesting opportunity to independently extract all of the exponents β, ν, and z, as we will discuss in Sec. 2.3.1.

Combining results from different quenches

As shown in the previous section, the f_1 and f_2 dual scaling behaviors are clearly observed in both linear and non-linear quenches. The f_2 scaling scheme is particularly interesting in practice. As we mentioned in Sec. 2.2, f_2 scaling does not involve the prior knowledge or optimization of the critical exponents, while the power in the universal scaling regime still carries the information of the critical exponents through Eq. (2.18). The power x can be measured easily by linear log-log fit of the data. This property of dual scaling and the convenient way of extracting the power x from f_2 scaling for any arbitrary r open an interesting opportunity to extract the exponents z, ν, and β in a completely independent way.

We first point out some important aspects of the applications of f_2 scaling. One important aspect of f_2 scaling is that it corresponds to the regime in which the correlation length ξ_v Eq. (2.5) is growing as v decreases, while ξ_v is still much smaller than the system size, i.e., $\xi_v \ll L$. Effectively, in this regime the rescaled quantity $\langle m^2 \rangle L^2$ is size-independent. This property provides a simple way to do the linear fit in practice: one can simply follow the largest available sizes, when the data points from these sizes become indistinguishable in the f_2 plot and the system sizes, thus, are large enough to be effectively free of finite-size effects. This L convergence aspect is seen in Figs. 2.5 (a) and 2.6 (b). Quantitatively, one can again use χ^2/dof to quantify the result. If small sizes that potentially carry finite-size

effect are included in the linear fit, they will certainly ruin the goodness of the statistics. The same principle can also be used for selecting the region for linear fit. The ideal region for the linear fit should be in the power-law regime. If the data points from either the quasi-adiabatic or diabatic regime are included, they will also ruin the goodness of the fit quantified by χ^2/dof.

In the following we use $r = 1$ and $r = 2$ quenches to demonstrate the idea outlined above. For $r = 1$ quench as shown in Fig. 2.5 (a), we consider sizes $L \geq 192$ since the data points from these sizes already show indistinguishable behavior in the power-law regime. The region in which linear fit is performed is indicated by the line with arrows. The selection of the region is determined by the minimization of χ^2/dof. We obtain $x_{r_1} = 0.550(3)$ with $\chi^2/\text{dof} \approx 1.0$. For $r = 2$ quench shown in the bottom panel of Fig. 2.6 (b), using the same principle for selecting the system sizes (with $L \geq 48$) and the region for linear fit (indicated by the line with arrows), we obtain $x_{r_2} = 0.32689(7)$ with $\chi^2/\text{dof} \approx 0.9$. Given two values x_{r_1} and x_{r_2}, the exponents can be easily computed as :

$$\begin{aligned} z\nu &= \frac{x_{r_2} - x_{r_1}}{r_1 x_{r_1} - r_2 x_{r_2}} \equiv a, \\ d\nu - 2\beta &= \frac{(r_2 - r_1) x_{r_1} x_{r_2}}{r_2 x_{r_2} - r_1 x_{r_1}} \equiv b. \end{aligned} \tag{2.25}$$

According to the above expressions, we obtain $a = 2.17(8)$ and $b = 1.75(5)$. Furthermore, with either the r_1- or the r_2-quench, one can use f_1 scaling with 2-parameter fitting to obtain β/ν and $z + 1/\nu$, as indicated by Figs. 2.4 (a) and 2.6 (a). We use the f_1 scaling from the $r = 1$ quench, treating all exponents as unknown and performing a 2-parameter fitting for $p_1 = z + 1/\nu$ and $p_2 = \beta/\nu$ and we obtain $p_1 = 3.16(5)$, $p_2 = 0.13(1)$ with $\chi^2/\text{dof} \approx 1.0$. Combining with the results from Eq. (2.25), one can then solve for z, ν, and β:

$$\begin{cases} z+1/\nu &= p_1, \\ z\nu &= a, \\ \beta/\nu &= p_2, \end{cases} \Rightarrow \begin{cases} z &= 2.16(4), \\ \nu &= 1.00(3), \\ \beta &= 0.13(1). \end{cases} \tag{2.26}$$

These exponents all agree with their known or expected (in the case of z) values within the error bars, which were estimated by introducing Gaussian noises to the fit parameters a, p_1, and p_2 and solving the equations repeatedly.

This method should be particularly useful in cases where it is difficult to reach the adiabatic limit and carry out standard finite-size scaling techniques around T_c, e.g., for frustrated systems such as spin glasses. [64]

2.3.2 Swendsen-Wang dynamics

Due to the rather large dynamic exponent, the Metropolis algorithm suffers significantly from critical slowing down. Physically, the slow dynamics originates from the inability of single-spin (or any local) updates to quickly change the structure of configurations with large clusters. In the SW algorithm, [9] a spin configuration is decomposed into clusters using bond variables introduced through the Fortuin-Kasteleyn transformation. [13] A broad range of cluster sizes appear according to Coniglio-Klein droplet theory, [65] and the algorithm is therefore much more efficient (has a much smaller dynamic exponent) than the Metropolis scheme.

In the SW algorithm, one unit of time is defined as decomposing the all spins in a configuration into clusters, using bonds set between same-oriented spins with probability $P = 1 - \mathrm{e}^{-2J/T}$. Each spin uniquely belongs to one of the clusters (with spins having no connected bonds treated as clusters of size 1) and each cluster is flipped independently with probability 1/2. In the quench process we again start at $T_i = 1.5T_c$ and stop exactly at the known T_c, repeating the procedure thousands of times for averaging.

Fig. 2.7 illustrates a linear quench process on 2D Ising model with Swendsen-Wang dy-

namics. As in the Metropolis case, when reaching T_c, a percolating cluster is also clearly observed in the SW scenario. However, in the Metropolis case single-spin flip updating scheme results in a rather severe critical slowing-down with $z_M \approx 2.17$, SW is designed to alleviate this problem by flipping a cluster of spins at once, for example, the largest percolating cluster marked by red color in Fig. 2.7 (d) can be easily flipped by SW algorithm. Therefore one can expect to see a smaller z, as we will show in the following.

The dynamic scaling, summarized as Eq. (2.22), is independent of the underlying updating scheme, except for the value of z. We can therefore carry out the same kind of non-equilibrium quench process as in the previous subsection to study SW dynamics. Here we will focus on the linear quench ($r = 1$) of the 2D Ising model.

We again observe scaling collapse onto a scaling function f_1 according to the first line of Eq. (2.22), as shown in Fig. 2.8 (a) (where we have not shown the diabatic data points, which deviate from the common scaling function—they will be analyzed further below). Here the dynamic exponent was again optimized to give the best fit. Due to the rather small value of the exponent in this case, $z_{\rm SW} \approx 0.3$, the universal power-law scaling regime is less accessible than in the Metropolis case. We therefore use a polynomial fit (to log-log data) in the whole region of the scaling variable in the figure, instead of dividing it into two velocity regimes. Nonetheless, given the predicted power x, Eq. (2.18), one can still test the consistency with the power-law behavior expected in the universal scaling regime after the optimized z_{SW} has been obtained. The result for the dynamic exponent is $z_{\rm SW} = 0.297(3)$, which is consistent with Ref. [51] (but with a smaller error bar). The dashed line in Fig. 2.8 (a) shows the predicted power-law given the above value of the dynamic exponent. The agreement is indeed good for the right-most points. This behavior strongly supports the conventional critical dynamics with $z_{\rm SW} > 0$, instead of a logarithmic divergence of the time scale. [53]

Note again that, for clarity, in Fig. 2.8 (a) we have not shown the diabatic points deviating from the common scaling function. These data points are included in Fig. 2.8 (b), which

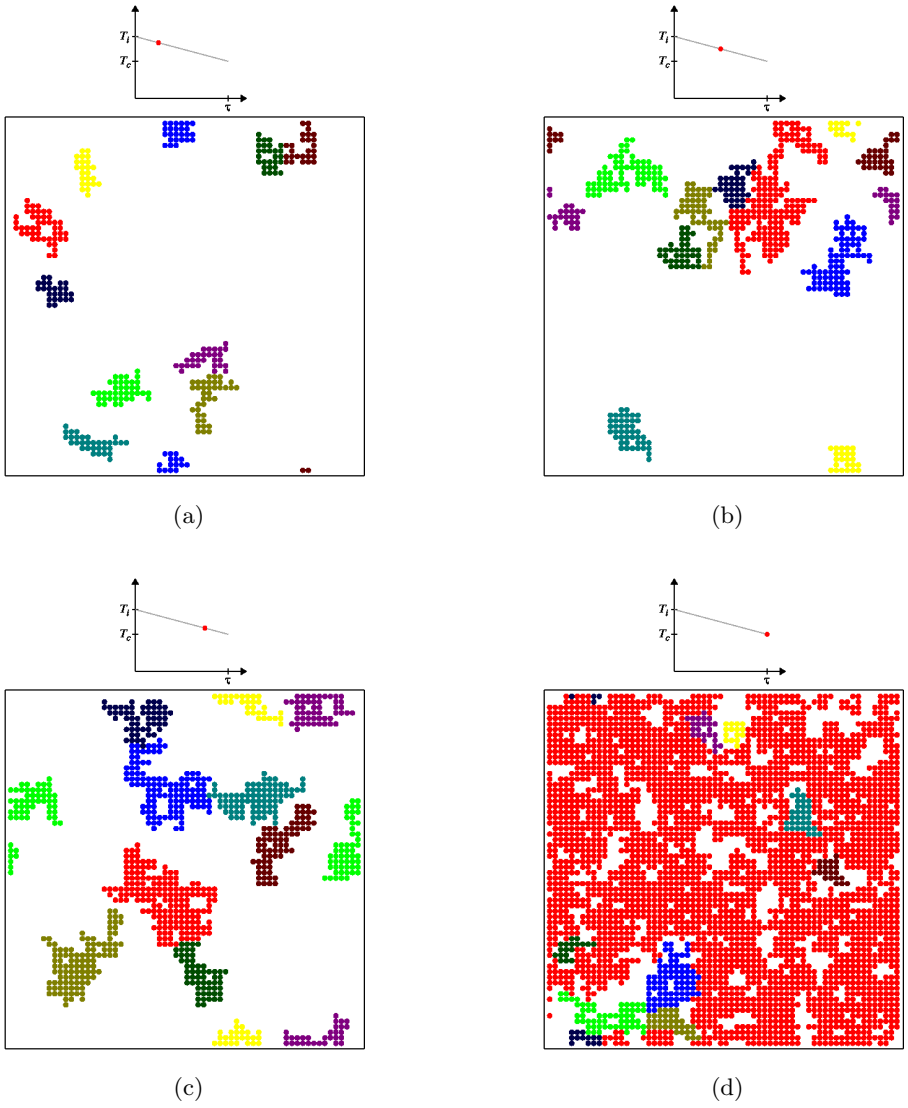

Figure 2.7: Illustration of a linear quench process on 2D Ising model with Swendsen-Wang dynamics. Shown are 25% (a), 50% (b), 75% (c), and 100% (d), through the quench process. For simplicity, only the largest 10 clusters are shown with the largest cluster always being marked by the red color. Same as in the Metropolis dynamics, at T_c (d), a percolating cluster spanning the entire system is clearly observed. In this demonstration, a total quench time $\tau_q = 3000$ Monte Carlo steps is used on a 64×64 square lattice.

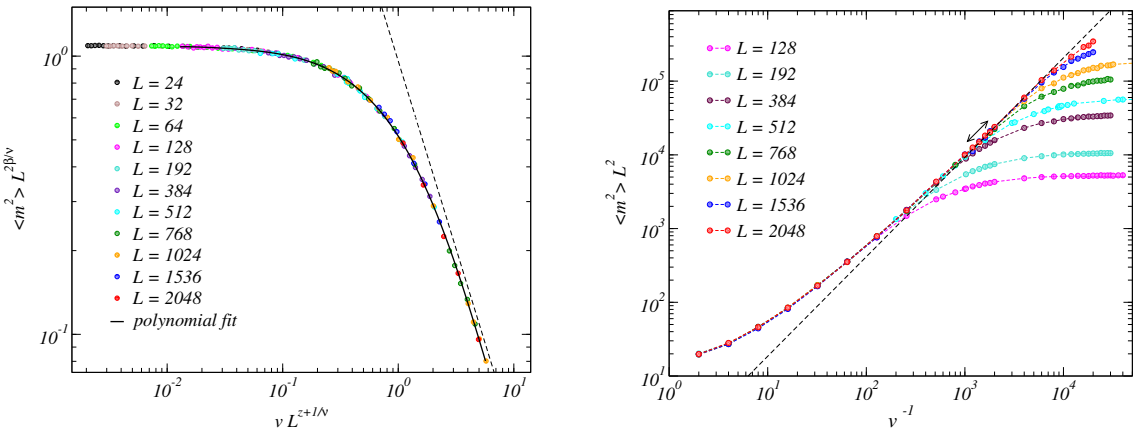

Figure 2.8: (a) Results of linear quenches with SW dynamics of the 2D Ising model. The magnetization squared and the quench velocity are rescaled according to the first line in Eq. (2.22), resulting in data collapsing onto the scaling function f_1. A high-order polynomial was fitted to the data and the dynamic exponent was adjusted to optimize this fit, giving the optimal exponent $z_{\rm SW} = 0.297(3)$ with $\chi^2/{\rm dof} \approx 1.0$. The dashed line indicates the predicted power-law behavior according to Eq. (2.18) in the universal scaling regime given the optimized value of $z_{\rm SW}$. (b) Scaling collapse using the second line of Eq. (2.22) to obtain the diabatic to power-law scaling function f_2 in the case of SW dynamics. The dashed line shows the slope expected with the dynamic exponent extracted in panel (a). As in the case of Metropolis, one can also independently obtain z by measuring the slope in the power-law regime. The line with arrow indicates the region in which linear fit is performed after taking log-log, we obtain $x = 1.35(4)$ with $\chi^2/{\rm dof} \approx 0.9$, which implies $z_{\rm SW} = 0.29(4)$.

shows a scaling collapse according to the second line of Eq. (2.22). We can observe that the universal power-law regime is reached in a window of $1/v$ where the data is collapsed for the system sizes we have used. As demonstrated in Metropolis case, one can independently estimate z_{SW} by performing linear fit in the f_2 scaling after taking log-log, this procedure yields $x = 1.35(4)$ with $\chi^2/\mathrm{dof} \approx 0.9$, which implies $z_{\mathrm{SW}} = 0.29(4)$. As in the Metropolis case, the z_{SW} extracted by f_1 and f_2 scalings are completely consistent.

2.3.3 Wolff dynamics

The Wolff algorithm [48] is an improvement of the SW algorithm. It is based on constructing single clusters according to the same bond rule as in the SW algorithm, but each time starting from a random seed site (instead of one not previously visited when decomposing the whole system into non-overlapping clusters in the SW algorithm) and flipping the clusters with probability one. The clusters are then on average larger than in the SW algorithm, and the dynamic exponent is therefore normally smaller. [54]

Fig. 2.9 shows a typical scenario for a linear quench on 2D Ising model with Wolff dynamics. Same as the Metropolis and SW dynamics, a percolation cluster is seen at T_c. Notice that in Wolff scenario a spin is randomly selected as the "seed" which will be used to grow a Wolff cluster. Since the selection is purely random, in some occasions the cluster may only have small sizes even when the temperature is close to T_c. However, one can imagine that the chances of hitting the large clusters will become higher and higher as the temperature moves toward T_c.

In order to compare the dynamics of the SW and Wolff algorithms it is important to treat the time-step in the latter in such a way that the number of spins flipped is proportional to N. Clearly, above T_c this is not the case for a single cluster, but one can still define the elementary unit of time as the flipping of one cluster and subsequently rescale the time based on the average cluster size, so that an extensive number of spins are flipped in the

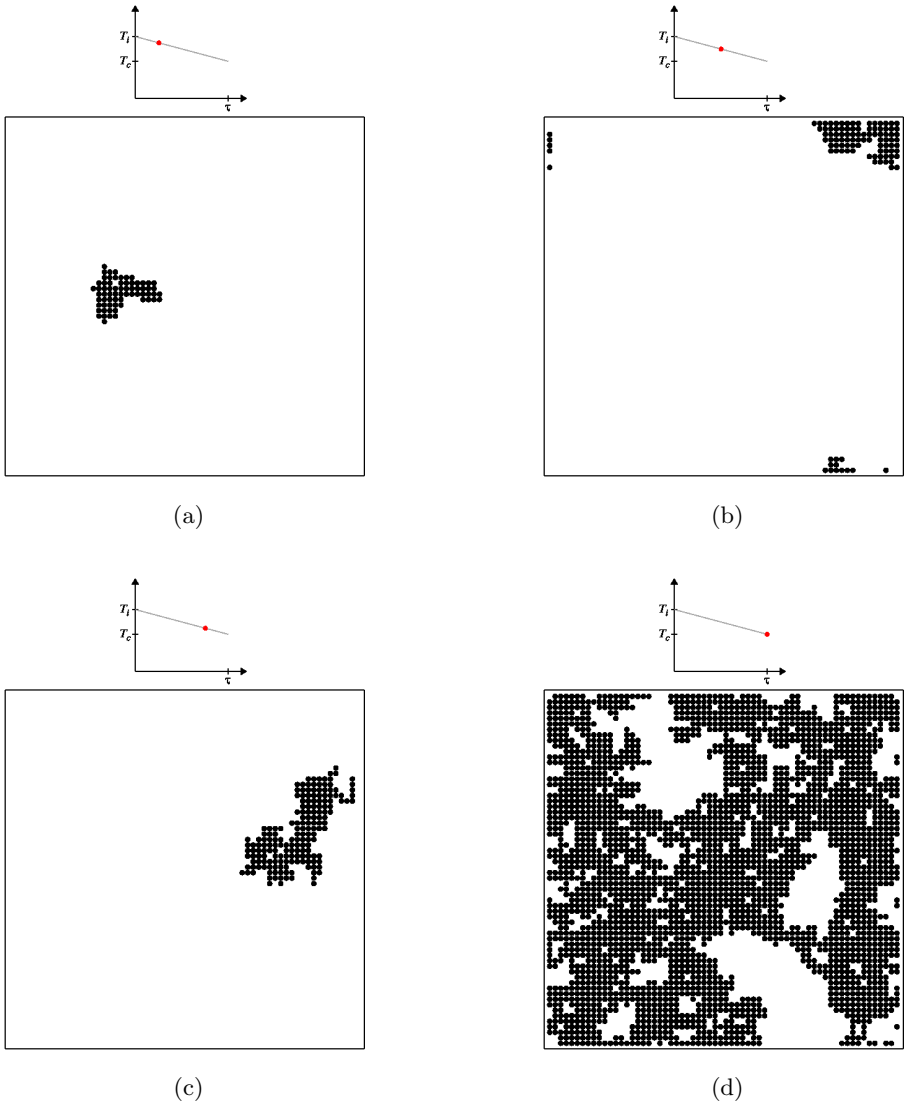

Figure 2.9: Illustration of a linear quench process on 2D Ising model with Wolff dynamics. Shown are 25% (a), 50% (b), 75% (c), and 100% (d), through the quench process. Wolff algorithm only constructs one cluster and flips it with probability 1, regardless of the size of the cluster. Same as in the Metropolis and SW dynamics, at T_c (d), a percolating cluster spanning the entire system is clearly observed in Wolff scenario. In this demonstration, a total quench time $\tau_q = 3000$ Monte Carlo steps is used on a 64×64 square lattice.

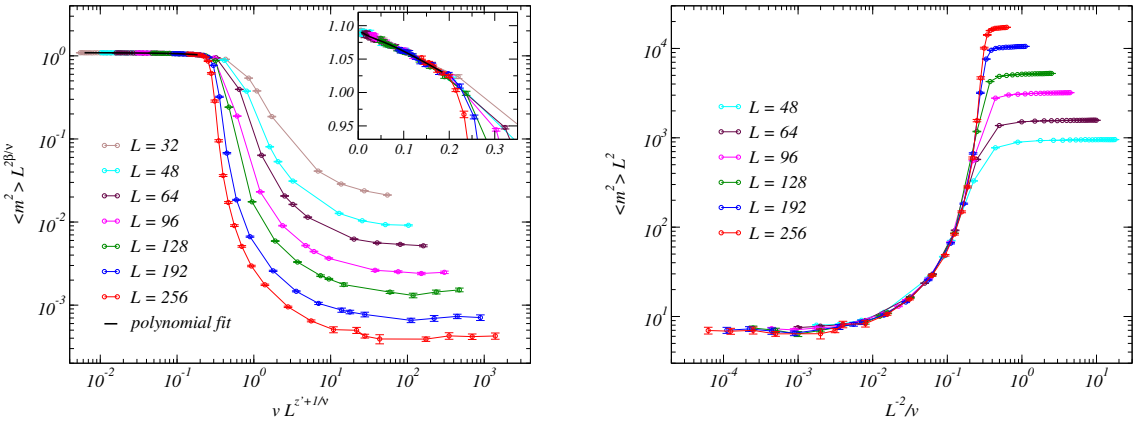

Figure 2.10: (a) Scaling collapse in the quasi-adiabatic regime (giving the scaling function f_1) for Wolff cluster dynamics with the time unit defined as the flipping of a single cluster. Here the scaling collapse appears to break down at a singular point, as shown in greater detail in the inset. In the regime where scaling collapse can be achieved, the optimized value of the dynamic exponent is $z'_W = 0.55(2)$ with $\chi^2/\text{dof} \approx 1.0$. (b) Scaled squared magnetization in the diabatic regime, using a velocity rescaling of the form expected in this regime (accounting for the size of the Wolff-clusters decreasing with the system size as L^{-2} for fixed v).

rescaled time unit. This is straight-forward in the equilibrium, where the scaling of the average cluster size is known in terms of critical exponents and the Fourtuin-Kasteleyn mapping. [65] The critical Wolff cluster size scales as the magnetic susceptibility, $\chi \sim L^{\gamma/\nu}$. This implies that on average $\sim L^d/L^{\gamma/\nu}$ Wolff updates correspond to one MC step as defined in SW or Metropolis dynamics. Denoting by z'_W the dynamic exponent measured using the single-cluster time unit and by z_W the exponent corresponding to properly rescaled time, the relationship between these exponents is therefore [54]

$$z_W = z'_W - (d - \gamma/\nu). \tag{2.27}$$

In non-equilibrium simulations the situation is more complicated, as we will see below.

We here perform the same kind of linear quench with Wolff dynamics at different velocities

as in the previous subsections for Metropolis and SW dynamics. We consider the elementary time unit as a single cluster flip and later discuss the subtleties involved in this definition.

The scaling procedure of the squared magnetization expected to yield the function f_1 is shown in Fig. 2.10 (a). Here we observe a feature distinctively different from the Metropolis and SW cases: There is no universal scaling regime with power-law behavior. There is still a quasi-adiabatic regime where the data collapse well. We discuss this regime first and will return later to the lack of universal power-law scaling regime.

In the quasi-adiabatic regime the rescaled squared magnetization is rather flat in Fig. 2.10 (a). Upon closer examination, as shown in the inset, there is still a clear drop when the scaled velocity approaches the region where the data-collapse breaks down. Interestingly, that break-down appears to take place at a single well defined point. Using a polynomial fit to the data before this point and optimizing the collapse by adjusting the dynamic exponent as in the previous cases, we obtain $z'_W = 0.55(2)$. This again is the dynamic exponent measured according to the single-cluster definition of time, and to compare with Metropolis and SW dynamics the exponent should be shifted according to Eq. (2.27)—provided that the quench is sufficiently adiabatic throughout this regime. Since for the 2D Ising model $\gamma = 7/4$ and $\nu = 1$, we obtain $z_W = 0.30(2)$. This value is in good agreement with previous results, e.g., Ref. [54], providing further confirmation of the quench process being effectively adiabatic in the regime where the scaling collapse occurs in Fig. 2.10 (a).

Let us now discuss the break-down of scaling collapse and absence of a power-law regime at higher rescaled velocity. It seems clear that the break-down should be related to the single-cluster definition of the time unit. The typical size of the cluster is naturally associated with the temperature and the corresponding KZ correlation length, ξ_v, reached at a given time step. This implies that at the early stage of the quench most of the system is left untouched by the Wolff construction, due to the small ξ_v and cluster size. The growth of the cluster size versus T as T is decreased is of course slower than in the equilibrium. The left panel of Fig. 2.11 shows the average cluster size for different quench times as a fraction

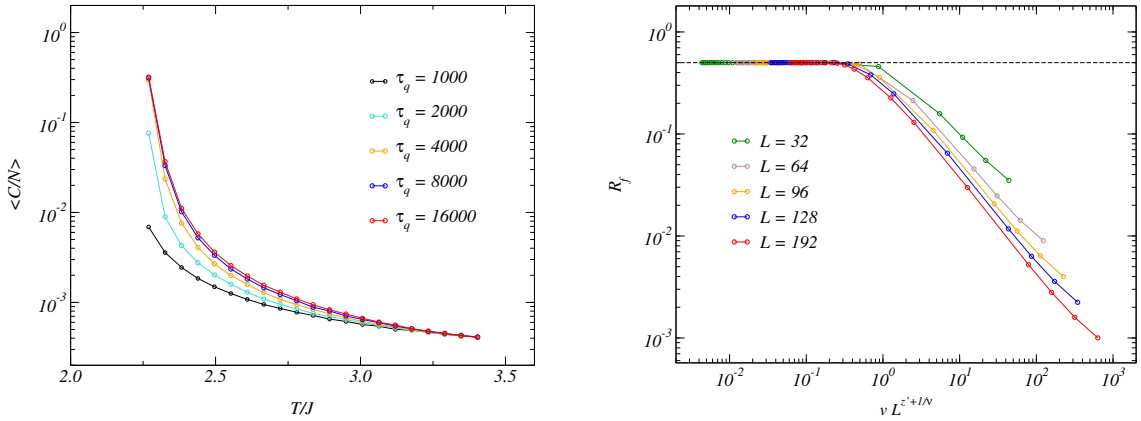

(a) (b)

Figure 2.11: (a) Temperature dependence of the average cluster size C relative to the system size N in Wolff-quenches at different velocities on a 128×128 lattice. (b) The fraction of spins that are actually flipped with respect to the initial configuration after the entire quench process, graphed as a function of the rescaled velocity with the dynamic exponent $z'_W = 0.55$ as obtained in Fig. 2.10 (a). The fraction of flipped spins should approach $1/2$ if the system at the initial and final times are completely decorrelated.

of the total system size for a system of size 128^2. It is also illuminating to examine the fraction R_f of spins actually flipped with respect to the initial configuration during the *entire* quench, i.e., counting the number of spins that are different in the initial and final configurations. If the simulation is ergodic within the total quench time, so that the initial and final configurations can become completely decorrelated, this fraction should be very close to 1/2 (strictly speaking, $R_f \to 1/2$ exponentially fast for quench times much longer than the autocorrelation time). Furthermore, with any definition of the time unit where all spins are visited, the fraction approaches some L-independent constant, $R_f \in (0, 1/2)$, when $v \to \infty$ (in practice, with our definitions, at $v = (T_i - T_c)/\tau_q$ with $\tau_q = 1$; the minimum quench time of one MC step). However, as shown in the right panel of Fig. 2.11, with the single-cluster definition the flipped fraction decays sharply with increasing velocity and size. Interestingly, it reaches 1/2 at a scaled velocity very close to the special point where the scaling collapse breaks down in Fig. 2.10 (a). It is clear that no quasi-adiabatic evolution, or even critical scaling, can take place if the scheme effectively is non-ergodic, as the $R_f \to 0$ behavior indicates.

There is still of course a diabatic regime where in the high-velocity limit the magnetization squared approaches its equilibrium value at the initial temperature. In this case, since the effect of the single-cluster flips in one unit of time changes with T, the velocity is not constant if one rescales to a time unit in which an extensive number of spins is flipped. Therefore, effectively, the procedure corresponds to a nonlinear quench protocol leading to an effectively much faster approach to the diabatic limit with increasing v than in schemes based on usual definitions of the time unit with an extensive number of spin flips. With usual time definitions, for any system size L one can reach any configuration, in principle, in a single time steps, while with the Wolff algorithm, in the diabatic regime, the number of steps (flipped clusters) needed for ergodic sampling increases with the system size and also with the velocity (since the clusters increase in size with decreasing velocity).

Despite the peculiarities of the Wolff time unit, we can still attempt to rescale the data

in Fig. 2.10 (a) using the same diabatic approach as in the SW and Metropolis cases, to obtain the scaling function f_2 in Eq. (2.22) for Wolff dynamics. However, in this case we have to modify the argument $a^{-(zr+1/\nu)}/v = v^a_{KZ}/v$ of the scaling function, because the effective velocity is normalized up by a factor, the inverse average fraction of flipped spins in a time step, which, as we have seen above, vanishes with increasing L for fixed v. Since we are analyzing the diabatic regime, where the cluster size should be L-independent for sufficiently large L, the flipped fraction of spins in one step should scale as L^{-d}, and, thus, we should let $v \to vL^d$ in the scaling analysis. Setting the lattice scale parameter $a = 1$ as before, we therefore expect scaling collapse with $f_2(L^{-d}/v)$, here with $d = 2$. Indeed, as shown in Fig. 2.10 (b), graphing $\langle m^2 \rangle L^2$ versus L^{-2}/v, the data collapse almost perfectly, down to a velocity where the scaling function appears to diverge in the thermodynamic limit (with the quasi-adiabatic plateaus splitting off later as L grows).

The above analysis shows that, even with the subtleties of the single-cluster time unit in the Wolff algorithm, there are still two well defined slow and fast regimes, where essentially perfect data collapse onto functions f_1 and f_2 can be achieved. Unlike the cases of Metropolis and SW dynamics, these scaling functions do not have any universal power-law parts connecting them in cross-overs, but instead they both break down in a singular manner with one type of scaling replaced by a completely different kind of scaling. In terms of rescaling of the time unit of the single-cluster Wolff steps, we have demonstrated that on the adiabatic side it is with the standard factor (same as in the equilibrium), $t \to tL^{-(d-\gamma/\nu)}$, while on the diabatic side it is just $t \to tL^{-d}$. The failures of these time rescalings at singular points leads us to conclude that Wolff dynamics is associated with a *dynamic phase transition*, and this transition is related to a sudden effective loss of ergodicity as a function of the velocity in fast quenches.

2.4 Higher-dimensional models

Despite the similar dynamic exponents of the SW and Wolff algorithms when applied to the 2D Ising model, $z_{SW} \approx z_W \approx 0.3$, the degree of critical slowing-down with these algorithms can be very different in higher dimensions. To demonstrate that the scaling schemes developed and tested in the bulk of the chapter also apply beyond the simple 2D Ising model, and to further examine the peculiarities of the Wolff algorithm discovered in Sec. 2.3.3, we here present results of linear SW and Wolff quenches of Ising models in higher dimensions. The resulting dynamic exponents are listed in Table 2.1.

For the 3D Ising model, with the Hamiltonian (2.7) defined with nearest-neighbor interactions on the simple cubic lattice, numerical estimates for the critical point T_c and the exponents are known to rather high precision; [66] $J/T_c = 0.22169(2)$, $\nu = 0.6298(5)$, and $\eta = 0.0366(8)$. Given these exponents, we use the exponent relation $2\beta/\nu = 1 + \eta$ in the $r = 1$ dynamic scaling relation (2.15).

We write the Hamiltonian for the fully-connected (or infinite-dimensional) Ising model as

$$H = -\frac{J}{N-1} \sum_{i=1}^{N} \sum_{j>i} \sigma_i \sigma_j, \tag{2.28}$$

where the coupling is normalized by the system size. Since mean-field theory becomes exact for this model when $N \to \infty$, we have $T_c/J = 1$, and the critical exponents are $\nu = 1/2$, $\beta = 1/2$. To apply scaling forms such as Eq. (2.22) in this case we have to use the upper critical dimension of the Ising model, $d_c = 4$, to define the effective system length as $L_{\text{eff}} = N^{1/d_c}$ and use $d = d_c$.

2.4.1 Swendsen-Wang dynamics

Data collapse for SW dynamics on the 3D model is shown in Fig. 2.12 (a). Fitting a polynomial to the quasi-adiabatic region and adjusting the exponent to optimize the collapse

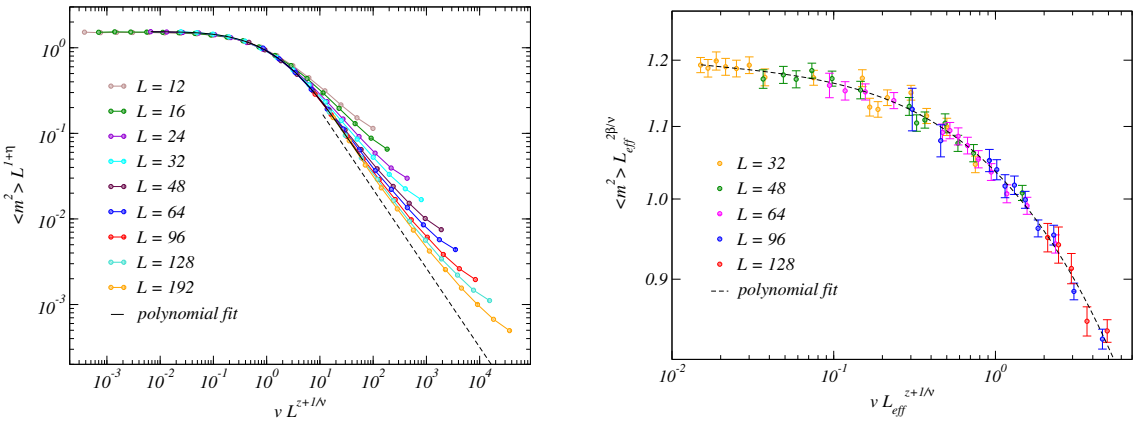

(a) (b)

Figure 2.12: (a) Optimized scaling collapse for linear SW quenches of the 3D Ising model, giving $z_{SW} = 0.53(1)$ with $\chi^2/\text{dof} \approx 1.1$. The dashed line shows the anticipated power-law asymptotic behavior in the universal scaling regime, with the above value of the dynamic exponent and the slope x given by Eq. (2.18). (b) Optimized log-log scaling collapse for linear SW quenches of the fully-connected Ising model, giving $z_{SW} = 1.2(2)$ with $\chi^2/\text{dof} \approx 0.8$.

as before gives $z_{SW} = 0.53(1)$, this is in good agreement with Ref. [52]. The collapsed region where this fitting procedure was carried out corresponds mainly to the quasi-adiabatic regime, but a cross-over to a power-law regime, with the slope consistent with the expected exponent, is also clear for the larger system sizes.

The same kind of scaling collapse for the fully-connected Ising model is shown in Fig. 2.12 (b). Here we have much less data, but, focusing on the quasi-adiabatic regime, we can observe scaling collapse with a dynamic exponent $z_{SW} = 1.2(2)$. This in good agreement with mean-field calculation, [54] according to which $z_{MF} = 1$.

2.4.2 Wolff dynamics

As we saw in the Sec. 2.3.3, Wolff dynamics on the 2D Ising model exhibits scaling collapse in the quasi-adiabatic and diabatic regimes, but the smooth cross-over with power-law scaling in Eq. (2.24) is lacking. It is interesting to investigate how this behavior evolves as the dimensionality is increased, which we do here by studying the 3D and fully connected models.

The analysis of the data in the quasi-adiabatic regime is presented in Fig. 2.13 (a). Here, again, the data collapse appears to break down essentially at a point, with no apparent signs of any emergent power-law scaling behavior (although the point at which the curves split off from the scaling function appears to show somewhat more finite-size drift than in Fig. 2.10 (a), where almost no drift can be seen). The dynamic exponent is $z'_W = 1.27(2)$. To compare this with the exponent in SW dynamics, one again has has to shift the value according to Eq. (2.27), which gives $z_W = 0.24(2)$.

Turning now to the fully connected Ising model, Fig. 2.13 (b) shows the outcome of an optimized data collapse yielding $z'_W = 2.04(4)$, or, after shifting the value according to Eq. (2.27), $z_W = 0.04(4)$. This confirms the expectation that the Wolff algorithm should be completely free from critical slowing down in this case. [54] The figure also shows an

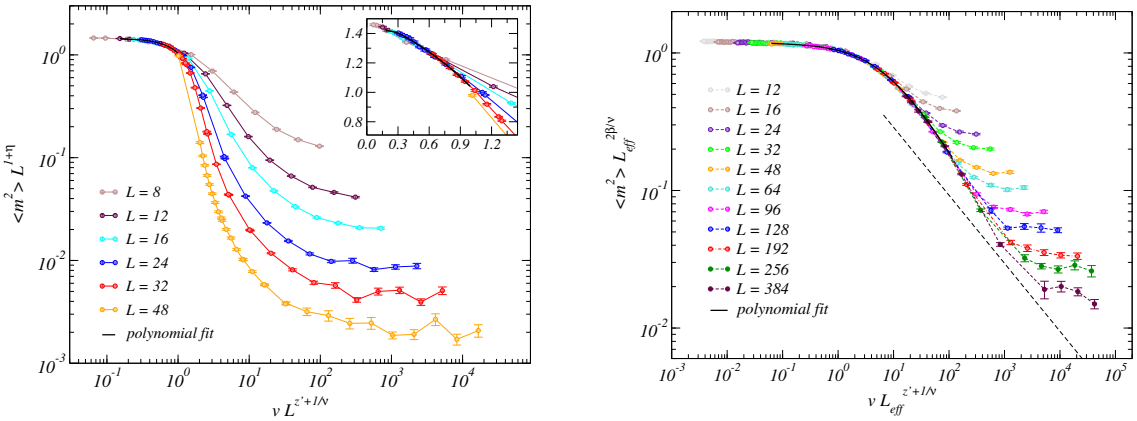

(a) (b)

Figure 2.13: (a) Optimized scaling collapse in the quasi-adiabatic regime of the 3D Ising model with Wolff dynamics. The optimal dynamic exponent with the single-cluster time unit is $z'_W = 1.27(2)$ with $\chi^2/\text{dof} \approx 1.0$. The shifted value according to Eq. (2.27) is $z_W = 0.24(2)$. The inset shows more details of the data (but on a lin-lin plot) around the point where the data collapse breaks down. (b) Optimized scaling collapse in the quasi-adiabatic regime of the fully connected Ising model subject to Wolff dynamics. The optimal dynamic exponent is $z'_W = 2.04(4)$, or $z_W = 0.04(4)$, with $\chi^2/\text{dof} \approx 0.9$. The dashed line shows the expected behavior with $z' = 2$ and mean-field static exponents ($\nu = \beta = 1/2$) if the exponent relation (2.18) is valid (which does not appear to be the case).

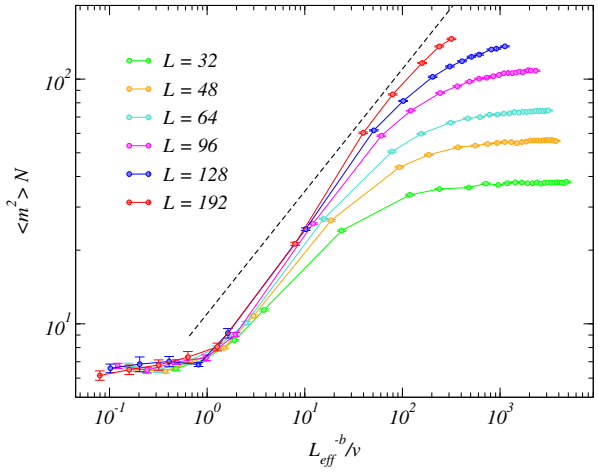

Figure 2.14: The same data as in Fig. 2.13 (b), analyzed using diabatic scaling. Here the exponent $b \approx 1.2$ accounts for the growth of the Wolff-cluster size with L_{eff}. It was optimized for the best data collapse. The dashed line shows the expected behavior with the exponent (2.18) with $z' = 2$, that does not appear to apply here.

interesting feature different from any of the other cases we have considered: While the data collapse now does also extend to (apparently) arbitrarily high scaled velocities and the behavior does look like a power law, the slope on the log-log plot is not what would be expected based on the relationship (2.18) with the dynamic exponent extracted in the optimization of the data collapse (i.e., with $z' = 2$ in place of z in the expression for the exponent x). While we do not know the exact reason for this, one can suspect that it has to do with the non-locality of the model invalidating the arguments leading to the exponent relation (2.18), perhaps similar to violation of hyperscaling relations above the upper critical dimension.

In Sec. 2.3.3, when analyzing the the diabatic regime for the 2D model, we had to rescale the velocity by a factor L^d to account for the fact that the Wolff clusters stay constant in size for fixed v when the system grows. In the fully-connected model, however, since the number of interacting bonds per site increases as N, the Wolff clusters should be expected to grow as well, as some power of the size. We have not investigated this behavior explicitly and

therefore just assume that it is power law and graph $\langle m^2 \rangle L_{\text{eff}}^{d_c}$ versus L_{eff}^{-b}/v $(= N^{-b/4}/v)$, where b is optimized and should be expected to be less than $d_u = 4$ (since the clusters cannot grow faster than N). As shown in Fig. 2.14, we can indeed achieve data collapse this way, with $b \approx 1.2$, although the subleading finite size corrections are very strong. This value of b indicates that the Wolff clusters grow approximately as $\sim N^{0.3}$.

Beyond the clearly diabatic behavior in Fig. 2.14 we cannot yet, for the range of system sizes considered, observe a clear power-law scaling regime, although the convergence of the data is certainty consistent with a power law. Again, as in Fig. 2.13 (b) the behavior does not appear to be consistent with the expected exponent given by Eq. (2.18), shown with the dashed line in Fig. 2.14.

2.5 Summary of results on 2D Ising model

We have demonstrated a non-equilibrium quench approach and associated dynamic scaling scheme for studying the scale-invariant universal behavior and various cross-over behaviors when approaching critical points of classical phase transitions. Using three different variants of MC dynamics—Metropolis, SW, and Wolff—we demonstrated that the order parameter (the squared magnetization) is governed by two different scaling functions describing quasi-adiabatic (including fully adiabatic) and diabatic (including extreme diabatic) evolution from an initial paramagnetic state to the critical point. In all cases we have studied, the two scaling functions capture the dynamic behavior for the entire range of velocities $v \in [0, \infty)$ for all system sizes (up to very small subleading finite-size corrections also present in the equilibrium). This complete characterization of the non-equilibrium scaling for several dynamic schedules was the main result of the chapter. In addition, we showed that the quench scheme can also be used to extract accurate values of the dynamic exponent for given combinations of models and dynamics. In the main part of the chapter we used the standard 2D Ising model, but we have also investigated the 3D and fully-connected

Dynamics	Model	z
Metropolis	2D	2.1767(5)
Swendsen-Wang	2D	0.297(3)
	3D	0.53(1)
	fc	1.2(2)
Wolff	2D	0.30(2)
	3D	0.24(2)
	fc	0.04(4)

Table 2.1: Dynamic exponents obtained using either f_1 or f_2 scaling for Ising models in two and three dimensions, as well as the fully-connected (fc) model (infinite-dimensional). The Metropolis dynamic exponent for 2D case quoted above is from f_2 scaling of $r = 2$ quench, which yields the best estimate so far. The exponents for Wolff dynamics have been shifted using Eq. (2.27) to account for the single-cluster definition of the time unit of the simulations.

(infinite-dimensional) variants and report results for them in Sec. 2.4. We summarize our results for the dynamic exponents in Table. 2.1.

In this chapter we performed linear and non-linear quenches to exactly the critical point T_c and observed excellent scaling in both cases. The quasi-adiabatic and diabatic scaling functions can be described perturbatively in v and $1/v$, respectively, for small values of these parameters. These regimes are normally (for SW and Metropolis dynamics) smoothly connected to each other via cross-overs to a universal, non-perturbative power-law scaling regime that can be described by either function. However, with Wolff dynamics, the two scaling regimes are separated in a singular manner and there is no power-law regime. This can be traced to the single-cluster definition of the time unit in the Wolff algorithm, which for a linear quench leads to an effectively non-linear, ultrafast approach to the diabatic limit, where the scheme becomes effectively non-ergodic. It is remarkable that the loss of ergodicity takes place in such a singular way, and not through a smooth cross-over. The

singular change in the scaling function can be interpreted as a dynamic phase transition.

An issue with the non-linear quenches of the form (2.13) is that the critical point has to be known exactly for the protocol to be asymptotically non-linear. If the critical point is not precisely known and the final point of the quench is therefore off the targeted critical value, the quench ultimately becomes linear (if one stops below the true T_c) [67] or doesn't reach T_c at all (if one stops above the true T_c). In this situation, assume that the final point of the non-linear quench is T^*, the offset from the critical point $|T_c - T^*|L^{1/\nu}$ enters as another argument of the scaling function (2.10). As usual in the scaling theory, the shorter length scale dominates, and, provided T^* is below T_c and not too far off T_c, one should be able to observe non-linear scaling $r \neq 1$ for some range of velocities before a cross-over to $r = 1$ scaling. If $T^* > T_c$ there should instead be a cross-over into high-T behavior with a finite correlation length. These cross-overs will be interesting targets for future studies.

Non-equilibrium relaxation from an ordered state has been widely used in the past to extract the dynamic exponents for ordered systems as well as spin glasses. [20, 44] In our language, this corresponds to a sudden quench to the critical point, $r = 0$ in Eq. (2.13), starting from the ordered state (instead of starting from the disordered state, as we did in the present work). The "velocity" in this case is the inverse waiting time [unlike our definition (2.13) where for $r \to 0$ there is effectively waiting before a sudden quench and no waiting after], and the order parameter asymptotically decays as a power of the time. Normally the decay is studied for systems sufficiently large to effectively be in the thermodynamic limit for the time windows considered. We have not compared these approaches in terms of their abilities to extract high-precision values for the dynamic exponent, but at least naively it appears to us that it should be better to take advantage of finite-size and finite velocity scaling. In addition, for a linear quench one can also easily, without much additional computational effort, obtain results not only at a known (or approximately known) final critical point, but one can collect data also before the critical point is reached and continue past the critical point as well. This opens opportunities for other types of scaling studies in the vicinity of

T_c, using Eq. (2.9) and its generalizations to incorporate both adiabatic and diabatic scaling functions.

Our value for the dynamic exponent for Metropolis updates of the 2D Ising model is in good agreement with the best known value. [45] As we mentioned in Sec. 2.1.2, for cluster dynamics the value of z has been a matter of debate for some time. For SW dynamics, it was claimed in Ref. [53] that $z_{\rm SW} = 0$ for the 2D Ising model. However, based on our approach, a nonzero $z_{\rm SW}$ is clearly shown, not only in the scaling collapse of Fig. 2.8 (a) but also as indicated by the consistent power-law behavior in the universal scaling regime. For Wolff dynamics of the 2D Ising model, it was reported in Ref. [53] that $z_W = 1.19(2)$, which is significantly higher than the value obtained in Ref. [54]. The latter is consistent with our result in Table 2.1. As pointed out in Ref. [53], z_W computed with standard relaxation from an ordered state may in practice be sensitive to the initial state, unless extremely long times are considered. Furthermore, the result may also depend on the targeted observable. [68] In this sense we think our approach is more stable in practice and has useful features for self-consistency checks, e.g., the same power laws appearing in all three dynamical regimes in Eq. (2.24).

We have demonstrated that the dynamic exponent in principle can be extracted by two different kinds of scaling collapses, especially when the static exponents are already known, given either the quasi-adiabatic function f_1 or the diabatic function f_2 in Eq. (2.22). Throughout the demonstration we show that the results of z obtained by f_1 and f_2 are completely consistent. Since the diabatic quenches are very fast in comparison to the quasi-adiabatic ones, it is more tempting to focus on the universal power-law scaling before the cross-over into the quasi-adiabatic behavior. Apart from the savings in raw computer resources, the data-collapsing procedure for f_2 in the universal scaling regime requires no knowledge or optimization of critical exponents; one simply plots $\langle m^2 \rangle N$ versus v^{-1}, in the style of Fig. 2.5 (a), Fig. 2.6 (b), or Fig. 2.8 (b), and uses linear fit to extract the slope x of the collapsed data on the log-log plot. The resulting x of course still is a combination of

the critical exponents (2.18) and one needs some further steps to disentangle them.

It is very interesting to note that all the static exponents can be extracted along with z by combining results from two different quench protocols characterized by two different values of r in Eq. (2.13), as we demonstrated in Sec. 2.3.1. This may potentially be very beneficial to systems such as spin glasses, where the large dynamic exponent makes it very difficult to carry out equilibrium calculations for large systems. [64] In our proposed method above, the need to equilibrate configurations at and close to the glass transition is completely circumvented, as one can start from some elevated temperature, where the equilibration is fast, and any slowing down "problem" just reflects the underlying dynamic exponent and manifests itself in the form of the desired exponent x.

We also point out that the non-equilibrium scheme discussed here is not restricted only to classical phase transitions, but also applies to quantum phase transitions, which can be studied, e.g., with the quantum MC simulation schemes recently developed in Refs. [33,37] for evolution in imaginary time. Some results for transverse-field Ising models were already reported in the above references.

Chapter 3

Quantum phase transitions approached through quasi-adiabatic quench

3.1 Introduction

Quantum Monte Carlo (QMC) methods [63] have become indispensable tools for ground-state and finite-temperature studies of many classes of interacting quantum systems, in particular those for which the infamous "sign problem" can be circumvented. [69] In ground-state projector methods, an operator $P(\beta)$ is applied to a "trial state" $|\Psi_0\rangle$, such that $|\Psi_\beta\rangle = P(\beta)|\Psi_0\rangle$ approaches the ground state of the Hamiltonian $\mathcal{H}$ when $\beta \to \infty$ and an expectation value $\langle A\rangle = \langle\Psi_\beta|A|\Psi_\beta\rangle/Z$, with the norm $Z = \langle\Psi_\beta|\Psi_\beta\rangle$, approaches its true ground-state value, $\langle A\rangle \to \langle 0|A|0\rangle$. For the projector, one can use $P(\beta) = \exp(-\beta\mathcal{H})$ or a high power of the Hamiltonian, $P(M) = (-\mathcal{H})^M$. Here we will discuss a modification of the latter projector for studies of dynamical properties of systems out of equilibrium.

Real-time dynamics for interacting quantum systems is difficult to deal with computationally. Solving the Schrödinger equation directly, computations are restricted to very small system sizes by the limits of exact diagonalization. Despite progress with the Density-Matrix Renormalization Group (DMRG) [70, 71] and related methods based on matrix-product states, this approach is in practice limited to one-dimensional systems and relatively short times. Efficiently studying long-time dynamics of generic interacting quantum systems in higher dimensions is still an elusive goal. However, recently, in Ref. [33], it was demonstrated that real-time and imaginary-time dynamics bear considerable similarities, and in the latter case, powerful and high-precision QMC calculations can be carried out on large

system sizes for the class of systems where sign problems can be avoided.

Our work reported here is a further development of the method introduced in Ref. [33], where it was realized that a modification of the ground-state projector Monte Carlo approach with $P(\beta) = \exp(-\beta\mathcal{H})$ can be used to study non-equilibrium set-ups in quantum quenches (or ramps), where a parameter of the Hamiltonian depends on time according to an arbitrary protocol. By performing a standard Wick rotation of the time axis, a wave function is governed by the Shrödinger equation in imaginary time $t = -i\tau$ (τ being real),

$$\partial_\tau |\psi(\tau)\rangle = -\mathcal{H}[\lambda(\tau)]|\psi(\tau)\rangle. \tag{3.1}$$

Here the Hamiltonian depends on the parameter λ through time, e.g.,

$$\mathcal{H} = \mathcal{H}_0 + \lambda(\tau)V, \tag{3.2}$$

where V and H_0 typically do not commute. The method is not limited to this form, however, and any evolution of $\mathcal{H}$ can be considered. The Schrödinger equation has the formal solution

$$|\psi(\tau)\rangle = U(\tau)|\psi(\tau_0)\rangle, \tag{3.3}$$

where the imaginary-time evolution operator is given by

$$U(\tau) = T_\tau \exp\left[-\int_{\tau_0}^{\tau} d\tau' \mathcal{H}[\lambda(\tau')]\right], \tag{3.4}$$

where T_τ indicates time ordering. A time-evolved state $U(\tau)|\Psi(\tau_0)\rangle$ and associated expectation values can be sampled using a generalized projector QMC algorithm. In Ref. [33] it was demonstrated that this non-equilibrium QMC (NEQMC) approach can be applied to study dynamic scaling at quantum phase transitions, and there are many other potential applications as well, e.g., when going beyond studies of finite-size gaps in "glassy" quantum dynamics and the quantum-adiabatic paradigm for quantum computing.

Here we introduce a different approach to QMC studies of quantum quenches, which gives results for a whole range of parameters $\lambda \in [\lambda(\tau_0), \lambda(\tau)]$ in a single run (instead of just the final time), at a computational effort comparable to the previous approach. Instead

of using the conventional time-evolution operator Eq. (3.4), we consider a generalization of the equilibrium QMC scheme based on projection with $(-\mathcal{H})^M$, acting on the initial ground state of $\mathcal{H}[\lambda(\tau_0)]$ with a product of evolving Hamiltonians:

$$P_{M,1} = [-\mathcal{H}(\lambda_M)]....[-\mathcal{H}(\lambda_2)][-\mathcal{H}(\lambda_1)], \tag{3.5}$$

where

$$\lambda_t = \lambda_0 + t\Delta_\lambda, \tag{3.6}$$

and $\Delta_\lambda = [\lambda_M - \lambda_0]/M$ is the single-step change in the tuning parameter.[1] Here we will consider a case where the ground state $|\Psi(\lambda_0)\rangle$ of $\mathcal{H}(\lambda_0)$ is known and easy to generate (stochastically or otherwise) and the ground states for other λ-values of interest are non-trivial. The stochastic sampling used to compute the evolution then takes place in a space representing path-integral-like terms contributing to the matrix element (the norm) $\langle\Psi(\lambda_0)|P_{1,M}P_{M,1}|\Psi(\lambda_0)\rangle$. We will also later consider a modification of the method in which the ground state at the final point λ_M is known as well, in which case contributions to $\langle\Psi(\lambda_M)|P_{M,1}|\Psi(\lambda_0)\rangle$ are sampled.

Staying with the doubly-evolved situation for now, we evaluate generalized expectation values after t out of the M operators in the product (3.5) have acted:

$$\langle A\rangle_t = \frac{\langle\Psi(\lambda_0)|P_{1,M}P_{M,t+1}AP_{t,1}|\Psi(\lambda_0)\rangle}{\langle\Psi(\lambda_0)|P_{1,M}P_{M,1}|\Psi(\lambda_0)\rangle}. \tag{3.7}$$

We will refer to this matrix element as an *asymmetric expectation value*, with the special case $t = M$ corresponding to a true quantum-mechanical expectation value taken with respect to an evolved wave function,

$$|\psi_M\rangle = \frac{P_{M,1}|\Psi(\lambda_0)\rangle}{\sqrt{\langle\Psi(\lambda_0)|P_{1,M}P_{M,1}|\Psi(\lambda_0)\rangle}}, \tag{3.8}$$

which approaches the ground state $|\Psi[\lambda(\tau_M)]\rangle$ of the Hamiltonian $H[\lambda(\tau_M)]$ for $M \to \infty$.

[1] In principle, one can also consider a nonlinear grid of "time" points, but here, we will consider the simplest case of a uniform grid.

Away from the adiabatic limit, the evolved wave function Eq. (3.8) is, generally speaking, not the ground state of the equilibrium system. Nevertheless, as we demonstrate in detail in Ref. [37], a quench velocity $v \propto \Delta_\lambda N$ can be defined such that the symmetric expectation value $\langle A\rangle_{t=M}$ in Eq. (3.7) approaches the expectation value $\langle A(\tau = t)\rangle$ after a conventional linear imaginary-time quantum quench with Eq. (3.4) done with the same velocity v, if v is low enough. In fact, the two quantities are the same to leading (linear) order in v, not only in the strict adiabatic limit $v \to 0$. We therefore name this scheme the *quasi-adiabatic* QMC (QAQMC) algorithm. Importantly, the leading corrections to the adiabatic evolution of the asymmetric expectation values for any t contain important information about non-equal time correlation functions, very similar to the imaginary-time evolution.

The principal advantage of QAQMC over the NEQMC approach is that expectation values of diagonal operators in the basis used can be obtained simultaneously for the whole evolution path $\lambda_0 \ldots \lambda_M$, by measuring $\langle A\rangle_t$ in Eq. (3.7) at arbitrary t points [2] (and one can also extend this to general off-diagonal operators, along the lines of Ref. [72], but we here limit studies to diagonal operators). The QAQMC scheme is also easier to implement in practice than the NEQMC method because there are no time integrals to sample.

As mentioned above, we will here have in mind a situation where the initial state $|\Psi(\lambda_0)\rangle$ is in some practical sense "simple," but this is not necessary for the method to work—any state that can be simulated with standard equilibrium QMC methods can be used as the initial state for the dynamical evolution. The final evolved state $|\psi_M\rangle$ can be very complex, e.g., for a system in the vicinity of a quantum-critical point or in a "quantum glass" (loosely speaking, a system with slow intrinsic dynamics due to spatial disorder and frustration effects). Here, as a demonstration of the correctness and utility of the QAQMC approach, we study generalized dynamic scaling in the neighborhood of the quantum phase transitions in the standard one-dimensional (1D) and 2D transverse-field Ising models (TFIMs).

[2] Eq. 3.7 has been defined for $t \leq M$, but we can also define the asymmetric expectation value for $2M \geq t > M$ by placing the operator within the product $P_{M,1}$. Clearly, we have the symmetry $\langle A\rangle_{2M-t} = \langle A\rangle_t$.

As noted first in Ref. [33], the NEQMC method can be used to extract the components of the quantum metric tensor, [73] the diagonal elements of which are the more familiar fidelity susceptibilities. Thanks to its ability to capture the leading non-adiabatic corrections to physical observables, the QAQMC approach can also be used for this purpose, and, as we will discuss briefly here and in more detail in Ref. [41], one can also extract the Berry curvature through the imaginary antisymmetric components of the geometric tensor

The rest of this chapter is organized in the following way. In Sec. 3.3, we summarize the result of adiabatic perturbation theory (APT) for quantum critical scaling formalism that had been discussed in detail in Ref. [37]. In Sec. 3.4, we discuss tests of the QAQMC scheme on 1D and 2D TFIMs, and also present a high-precision result for the critical field in the 2D model. In Sec. 3.5, we summarize our main conclusions and discuss future potential applications of the algorithm.

3.2 Adiabatic perturbation theory

The key question we address in this section is whether the matrix element $\langle A\rangle_t$ in Eq. (3.7) can give useful dynamical information for arbitrary "time" points t in the sequence of $2M$ operators. The expression only reduces to a conventional expectation value at the symmetric point $t = M$, and even there it is not clear from the outset how $\langle A\rangle_{t=M}$ computed for different M relates to the velocity dependence of the expectation value $\langle\Psi(0)|U^*(\tau)\,A\,U(\tau)|\Psi(0)\rangle$ based on the Schrödinger time-evolution operator in Eq. (3.4). Going away from the symmetric point brings in further issues to be addressed. For instance, there is no variational property of the asymmetric expectation value $\langle\mathcal{H}\rangle_t$ of the Hamiltonian for $t \neq M$. Nevertheless, the approach to the adiabatic limit is well behaved and we can associate the leading deviations from adiabaticity with well defined dynamical correlation functions that appear as physical response in real time protocols. We show here, for the linear evolution Eq. (3.6), that one can identify a velocity $v \propto N/M$ such that a linear imaginary-time quench with

$\lambda_t = vt$ in Eq. (3.6) gives the same results in the two approaches when $t = M$, including the leading (linear) corrections in v. For $t \neq M$, the relevant susceptibilities in QAQMC defining non-adiabatic response are different than at $t = M$ but still well defined, contain useful information, and obey generic scaling properties.

In order to facilitate the discussion of the QAQMC method, we here first review the previous APT approach for Schrödinger imaginary-time dynamics [33, 41] and then derive analogous expressions for the product-evolution. After this, we discuss some properties of the symmetric and asymmetric expectation values.

3.2.1 Imaginary-time Schrödinger dynamics

The NEQMC method [33] uses a path-integral-like Monte Carlo sampling to solve the imaginary-time Shcrödinger equation Eq. (3.1) for a Hamiltonian $\mathcal{H}[\lambda(\tau)]$ with a time-dependent coupling. The formal solution at time τ is given by the evolution operator Eq. (3.4). In the strict adiabatic limit, the system will follow the instantaneous ground state, while in the slow limit one can anticipate deviations from adiabaticity, which will become more severe in gapless systems and, in particular, near phase transitions. Let us discuss the leading non-adiabatic correction to this imaginary-time evolution. The natural way to address this question is to use APT, similar to that developed in Refs. [40, 74] in real time. We here follow closely the discussion of the generalization to imaginary time in Ref. [33].

We first write the wave function in the instantaneous eigenbasis $\{|n(\lambda)\rangle\}$ of the time-dependent Hamiltonian $\mathcal{H}[\lambda(\tau)]$:

$$|\psi(\tau)\rangle = \sum_n a_n(\tau)|n(\lambda(\tau))\rangle. \tag{3.9}$$

We then substitute this expansion into Eq. (3.1),

$$\frac{da_n}{d\tau} + \sum_m a_m(\tau)\langle n|\partial_\tau|m\rangle = -\mathcal{E}_n(\lambda)\, a_n(\tau), \tag{3.10}$$

where $\mathcal{E}_n(\lambda)$ are the eigenenergies of the Hamiltonian $\mathcal{H}(\lambda)$ corresponding to the states $|n\rangle$ for this value of λ. Making the transformation

$$a_n(\tau) = \alpha_n(\tau) \exp\left[\int_\tau^0 \mathcal{E}_n(\tau')d\tau'\right], \tag{3.11}$$

we can rewrite Eq. (3.1) as an integral equation;

$$\alpha_n(\tau) = \alpha_n(0) + \sum_m \int_\tau^0 d\tau' \, \langle n|\partial_{\tau'}|m\rangle \alpha_m(\tau') \times \exp\left[-\int_{\tau'}^0 d\tau'' \left(\mathcal{E}_n(\tau'') - \mathcal{E}_m(\tau'')\right)\right], \tag{3.12}$$

where it should be noted that $\alpha_n(0) = a_n(0)$. In principle we should supply this equation with initial conditions at $\tau = \tau_0$, but this is not necessary if $|\tau_0|$ is sufficiently large, since the sensitivity to the initial condition will then be exponentially suppressed. Instead, we can impose the asymptotic condition $\alpha_n(\tau \to -\infty) \to \delta_{n0}$, which implies that in the distant past the system was in its ground state.

Eq. (3.12) is ideally suited for an analysis with the APT. In particular, if the rate of change is very small, $\dot{\lambda}(\tau) \to 0$, then to leading order in $\dot{\lambda}$ the system remains in its ground state; $\alpha_m(\tau) \approx \delta_{m0}$ (except during the initial transient, which is not important because we are interested in large $|\tau_0|$). In the next higher order, the transition amplitudes to the states $n \neq 0$ are given by;

$$\alpha_n(0) \approx -\int_{-\infty}^0 d\tau \, \langle n|\partial_\tau|0\rangle \exp\left[-\int_\tau^0 d\tau' \, \Delta_{n0}(\tau')\right], \tag{3.13}$$

where $\Delta_{n0}(\tau) = \mathcal{E}_n(\tau) - \mathcal{E}_0(\tau)$. The matrix element above for non-degenerate states can also be written as

$$\langle n|\partial_\tau|0\rangle = -\langle n|\partial_\tau \mathcal{H}(\tau)|0\rangle / \Delta_{n0}(\tau). \tag{3.14}$$

In what follows we will assume that we are dealing with a non-degenerate ground state.

To make further progress in analyzing the transition amplitudes Eq. (3.13), we consider the very slow asymptotic limit $\dot{\lambda} \to 0$. To be specific, we assume that near $\tau = 0$ the tuning

parameter has the form (see also Ref. [74])

$$\lambda(\tau) \approx \lambda(0) + \frac{v_\lambda |\tau^r|}{r!}\Theta(-\tau). \tag{3.15}$$

The parameter v_λ, which controls the adiabaticity, plays the role of the quench amplitude if $r = 0$, the velocity for $r = 1$, the acceleration for $r = 2$, etc. It is easy to check that in the asymptotic limit $v_\lambda \to 0$, Eq. (3.13) gives

$$\alpha_n \approx v_\lambda \frac{\langle n|\partial_\lambda|0\rangle}{(\mathcal{E}_n - \mathcal{E}_0)^r} = -v_\lambda \frac{\langle n|\partial_\lambda \mathcal{H}|0\rangle}{(\mathcal{E}_n - \mathcal{E}_0)^{r+1}}, \tag{3.16}$$

where all matrix elements and energies are evaluated at $\tau = 0$. From this perturbative result we can in principle evaluate the leading non-adiabatic response of various observables and define the corresponding susceptibilities. For the purposes of comparing with the QAQMC approach, Eq. (3.16) suffices.

3.2.2 Operator-product evolution

The quasi-adiabatic QMC method may appear very different from NEQMC but has a similar underlying idea. Instead of imaginary time propagation with Eq. (3.4), we apply a simple operator product to evolve the initial state. We first examine the state propagated with the first t operators in the sequence $P_{t,1}$ in Eq. (3.5),

$$|\psi_t\rangle = [-\mathcal{H}(\lambda_t)] \dots [-\mathcal{H}(\lambda_2)][-\mathcal{H}(\lambda_1)]|\psi_0\rangle, \tag{3.17}$$

and after that we will consider symmetric expectation values of the standard form $\langle\psi_M|A|\psi_M\rangle$ as well as the asymmetric expectation values in Eq. (3.7). We assume that the spectrum of $-\mathcal{H}$ is strictly positive, which is accomplished with a suitable constant offset to $\mathcal{H}$ if needed.

Linear protocols

The coupling λ can depend on the index t in an arbitrary way. It is convenient to define

$$\tau_i = \frac{i}{T}, \tag{3.18}$$

where T is the overall time scale, which can be set to unity. The leading non-adiabatic corrections will be determined by the system properties and by the behavior of $\lambda(\tau_i)$ near the point of measurement t. The most generic is the linear dependence $\lambda(\tau_i) \approx \lambda(t) + \tilde{v}_\lambda(t - \tau_i)$, where $\tilde{v}_\lambda$ is related to the quench velocity (see below). In the end of this section we will briefly consider also more general nonlinear quench protocols.

Our strategy to analyze Eq. (3.17) in the adiabatic limit will be the same as in the preceding subsection. We first go to the instantaneous basis and rewrite

$$|\psi(\tau_i)\rangle \equiv |\psi_i\rangle = \sum_n a_n(\tau_i)|n(\lambda_i)\rangle \equiv \sum_n a_n^i |n^i\rangle. \tag{3.19}$$

In the instantaneous basis, the discrete Schrödinger-like equation $|\psi^{i+1}\rangle = -\mathcal{H}(\tau_{i+1})|\psi^i\rangle$ reads

$$a_n^{i+1} = -\sum_m a_m^i \mathcal{E}_n^{i+1} \langle n^{i+1}|m^i\rangle, \tag{3.20}$$

and it is instructive to compare this with Eq. (3.10). It is convenient to first make a transformation

$$a_n^i = \prod_{j=i+1}^{t} \frac{1}{(-\mathcal{E}_n^j)} \alpha_n^i. \tag{3.21}$$

This transformation does not affect the transition amplitude at the time of measurement t: $a_n^t = \alpha_n^t$. Then the equation above becomes

$$\alpha_n^{i+1} = \sum_m \alpha_m^i \left[\prod_{j=i+1}^{t} \frac{\mathcal{E}_n^j}{\mathcal{E}_m^j} \right] \langle n^{i+1}|m^i\rangle. \tag{3.22}$$

Let us introduce a discrete derivative

$$\langle n^i|\overleftarrow{\Delta} \equiv \langle n^{i+1}| - \langle n^i|, \tag{3.23}$$

and write the Schrödinger-like equation as

$$\alpha_n^{i+1} = \alpha_n^i + \sum_m \alpha_m^i \left[\prod_{j=i+1}^{t} \frac{\mathcal{E}_n^j}{\mathcal{E}_m^j} \right] \langle n^i|\overleftarrow{\Delta}|m^i\rangle. \tag{3.24}$$

In the adiabatic limit, the solution of this equation is $\alpha_n^i = \delta_{n0}$, i.e., the instantaneous ground state. To leading order of deviations from adiabaticity we find

$$\alpha_n^{i+1} = C_n + \sum_{k=0}^{i} \left[\prod_{j=k+1}^{t} \frac{\mathcal{E}_n^j}{\mathcal{E}_0^j} \right] \langle n^k | \overleftarrow{\Delta} | 0^k \rangle, \tag{3.25}$$

where C_n can be determined from the initial condition. In the limit of sufficiently large t the initial state is not important so we should have $\alpha_n^{t-i} \to 0$ for $i \gg 1$, so that $C_n = 0$. Therefore we find that the amplitude of the transition to the excited state is approximately

$$\alpha_n^t \approx \sum_{k=0}^{t-1} \left[\prod_{j=k+1}^{t} \frac{\mathcal{E}_n^j}{\mathcal{E}_0^j} \right] \langle n^k | \overleftarrow{\Delta} | 0^k \rangle. \tag{3.26}$$

Changing the summation index k to $p = t - k$ we have

$$\alpha_n^t \approx \sum_{p=1}^{t} \left[\prod_{j=t+1-p}^{t} \frac{\mathcal{E}_n^j}{\mathcal{E}_0^j} \right] \langle n^{t-p} | \overleftarrow{\Delta} | 0^{t-p} \rangle. \tag{3.27}$$

It is clear that for large t only $p \ll t$ terms contribute to the sum. In the extreme adiabatic limit one can thus move the matrix element outside of the summation and use the spectrum of the final Hamiltonian. In this case we find

$$\begin{aligned} \alpha_n^t &\approx \frac{\mathcal{E}_n}{\mathcal{E}_0} \frac{\langle n | \overleftarrow{\Delta} | 0 \rangle}{1 - \mathcal{E}_n/\mathcal{E}_0} \\ &= -\mathcal{E}_n \Delta_\lambda \frac{\langle n | \overleftarrow{\partial_\lambda} | 0 \rangle}{\mathcal{E}_n - \mathcal{E}_0} = \mathcal{E}_n \Delta_\lambda \frac{\langle n | \partial_\lambda | 0 \rangle}{\mathcal{E}_n - \mathcal{E}_0}, \end{aligned} \tag{3.28}$$

where $\Delta_\lambda = \lambda(t) - \lambda(t-1)$. By comparing Eqs. (3.16) and (3.28) we see that near the adiabatic limit QAQMC and NEQMC are very similar if $\mathcal{E}_n/\mathcal{E}_0 \approx$ const. This can in principle always be ensured by having a sufficiently large energy offset, but even with a small offset we expect the ratio to be essentially constant for the range of n contributing significantly when the spectrum becomes gapless close to a quantum-critical point. If the condition indeed is properly satisfied, then from Eqs. (3.16) and (3.28), we identify the quench velocity as

$$v_\lambda = \mathcal{E}_0 \Delta_\lambda. \tag{3.29}$$

This is the main result of this section. We will confirm its validity explicitly in numerical studies with the QAQMC method in Sec. 3.4. Since $\mathcal{E}_0 \propto N$, where N is the system size, we can also see that $v_\lambda \propto N\Delta_\lambda \propto N/M$ for a given total change in λ over the M operators in the product.

Let us point out that Eq. (3.28) can be also rewritten as

$$\alpha_n^t \approx -\mathcal{E}_0\Delta_\lambda \frac{\langle n|\overleftarrow{\partial_\lambda}|0\rangle}{\mathcal{E}_n - \mathcal{E}_0} - \Delta_\lambda \langle n|\overleftarrow{\partial_\lambda}|0\rangle. \tag{3.30}$$

The first contribution here exactly matches that of Eq. (3.16) while the second term is an additional contribution corresponding to a sudden quench.

3.2.3 Expectation values

While asymptotically Eq. (3.7) gives the ground state of the observable A in the adiabatic limit for all values of t, the approach to this limit as $t \to \infty$ is qualitatively different depending on whether t is equal to M or not. More precisely, if $t = \eta M$ where $\eta \in (0, 2)$ as $M \to \infty$, we encounter two different asymptotic regimes for $\eta \neq 1$ and $\eta = 1$.

Symmetric expectation values; $t = M$

In this limit the expectation value of the observable A in the leading order of the adiabatic perturbation theory reduces to

$$\langle A\rangle_{t=M} \approx \langle\psi(v_\lambda)|A|\psi(v_\lambda)\rangle, \tag{3.31}$$

where $v_\lambda \approx \mathcal{E}_0\Delta_\lambda$ is the imaginary time velocity identified earlier. For generic observables not commuting with the Hamiltonian, we find

$$\langle A\rangle_{t=M} \approx \langle A\rangle_0 + v_\lambda \chi'_{A\lambda}, \tag{3.32}$$

where

$$\chi'_{A\lambda} = \sum_{n\neq 0} \langle 0|A|n\rangle \frac{\langle n|\partial_\lambda|0\rangle}{\mathcal{E}_n - \mathcal{E}_0} + c.c. \tag{3.33}$$

is the susceptibility. All energies and matrix elements are evaluated at "time" $t = M$.

For diagonal observables A, like the energy or energy fluctuations, we have

$$\langle A\rangle_{t=M} \approx \langle A\rangle_0 + v_\lambda^2 \sum_{n\neq 0} \frac{|\langle n|\partial_\lambda|0\rangle|^2}{(\mathcal{E}_n - \mathcal{E}_0)^2}\langle n|A|n\rangle. \tag{3.34}$$

In particular, the correction to the energy is always positive as it should be for any choice of wave function deviating from the ground state. Let us emphasize that for diagonal observables the leading non-adiabatic response at the symmetric point in imaginary time coincides with that in real time, and, thus QAQMC or NEQMC can be used to analyze real time deviations from adiabaticity, as was pointed out in the case of NEQMC in Ref. [33].

Asymmetric expectation value, $t \neq M$

It turns out that the asymptotic approach to the adiabatic limit is quite different for non-symmetric points $t = \eta M$ with $\eta \neq 1$. Without loss of generality we can focus on $0 < \eta < 1$ (since all expectation values are symmetric with respect to $\eta \to 2 - \eta$ for the symmetric protocol we consider [**?**]). Then the expectation value of A is evaluated with respect to different eigenstates

$$\langle A\rangle_t = \frac{\langle\psi_L|A|\psi_R\rangle}{\langle\psi_L|\psi_R\rangle}, \tag{3.35}$$

where

$$\begin{aligned} |\psi_R\rangle &= \mathcal{H}(\lambda_t)\cdots\mathcal{H}(\lambda_2)\mathcal{H}(\lambda_1)|\psi_0\rangle, \\ |\psi_L\rangle &= \mathcal{H}(\lambda_{t+1})\cdots\mathcal{H}(\lambda_{M-1})\mathcal{H}(\lambda_M)P_{M,1}|\psi_0\rangle. \end{aligned} \tag{3.36}$$

Note that the overlap $\langle\psi_L|\psi_R\rangle$ is independent of t by construction and is real.

It is easy to see that for diagonal observables we obtain a leading asymptotic as in Eq. (3.34) but with the opposite sign in the second term

$$\langle A\rangle_{t\neq M} \approx \langle A\rangle_0 - v_\lambda^2 \sum_{n\neq 0} \frac{|\langle n|\partial_\lambda|0\rangle|^2}{(\mathcal{E}_n - \mathcal{E}_0)^2}\langle n|A|n\rangle. \tag{3.37}$$

In particular, the leading correction to the ground state energy is negative when t deviates sufficiently from the symmetric point, i.e., $|\lambda_t - \lambda_1|/v_\lambda \ll M$. There is no contradiction here since the left and right states are different (i.e., we are not evaluating a true expectation value and there is no variational principle). Both Eqs. (3.34) and (3.37) recover the exact result in the adiabatic limit. Since the correction up to the sign exactly matches the real time result, we can still use the non-symmetric expectation value for diagonal observables to extract the real time non-adiabatic response. For $t \to M$, the sign of the correction should change, to connect smoothly to the variational $t = M$ expectation value. The crossover between positive and negative corrections to the energy takes place around a point that asymptotically converges to $t = M$ in the adiabatic limit (where the deviation from the ground-state energy at $t = M$ vanishes). We will illustrate this with numerical results in Sec. 3.3.1 (see Fig. 3.2).

As in the symmetric case, using the APT discussed in the previous section the results derived here easily extend to other values of the exponent r.

3.3 Formalism and quantum-critical scaling

As a demonstration of the utility of QAQMC and the behaviors derived in the previous section we here study the TFIM, defined by the Hamiltonian

$$\mathcal{H} = -s \sum_{\langle i,j \rangle} \sigma_i^z \sigma_j^z - (1-s) \sum_i \sigma_i^x, \tag{3.38}$$

where $\langle i, j \rangle$ are nearest-neighbor sites, and σ_z and σ_x are Pauli matrices. Here, s plays the role of the tuning parameter, which in the simulations reported below will vary between 0 (where the ground state is trivial) to a value exceeding the quantum-critical point; $s_c = 1/2$ in a 1D chain and $s_c \approx 0.247$ in the 2D square lattice. [75]

Fig. 3.1 demonstrates a typical linear quench in imaginary time on a 2D transverse-field Ising model. An obvious transition around $s \approx 0.247$ is clearly seen, as we will discuss in

more detail in Sec. 3.4.2. Since the quench is carried in imaginary time, the entire transition curve m^2 vs. s is obtained in a single simulation.

We work in the standard basis of eigenstates of all S_i^z. The simulation algorithm samples strings of $2M$ diagonal and off-diagonal terms in Eq. (3.38), in a way very similar to the $T > 0$ stochastic series expansion (SSE) method, which has been discussed in detail in the case of the TFIM in Ref. [13]. The modifications for the QAQMC primarily concern the sampling of the initial state, here $|\Psi(0)\rangle = \prod_i |\uparrow_i + \downarrow_i\rangle$, which essentially amounts to a particular boundary condition replacing the periodic boundaries in finite-temperature simulations. An SSE-like scheme with such modified boundaries was also implemented for the NEQMC method in Ref. [33], and recently also in a study of combinatorial optimization problems in Ref. [30]. We here follow the same scheme, using cluster updates in which clusters can be terminated at the boundaries. The implementation for the product with varying coupling s is even simpler than SSE or NEQMC, with the fixed-length product replacing the series expansion of Eq. (3.4). The changes relative to Refs. [13, 33] are straightforward and we therefore do not discuss the sampling scheme further here.

3.3.1 Cross-over of the energy correction

As we discussed in Ref. [37], the asymmetric expectation value (3.7) of the Hamiltonian has a negative correction to the ground-state energy when t is sufficiently away from the symmetric point $t = M$. In Fig. 3.2 we illustrate this property and the convergence to the ground-state energy for all t with increasing M with simulation data for a small 1D TFIM system. We here plot the results versus the rescaled propagation power $\eta = t/M$. The region of negative deviations move toward the symmetric point with increasing M. Note that the deviations here are not strongly influenced by the critical point (which is within the parameter s simulated but away from the symmetric point), although the rate of convergence should also be slow due to criticality. The rate of convergence to the ground state can be expected to be (and is here seen to be) most rapid for $\eta < \eta_{c1}$ and $\eta > \eta_{c2}$.

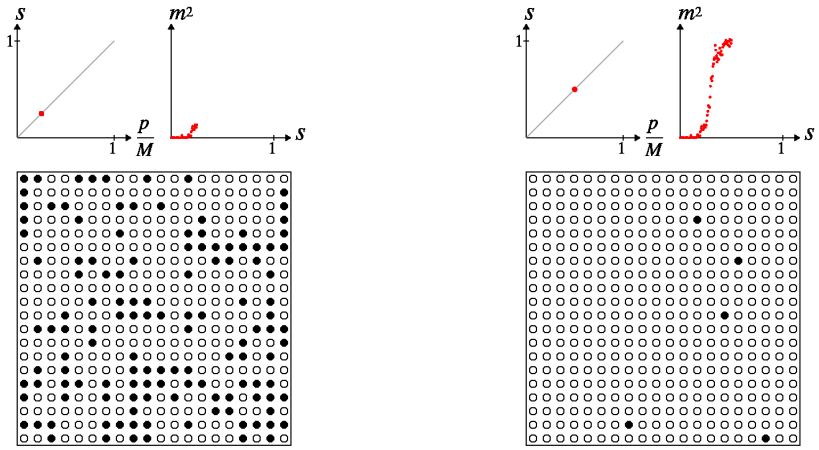

(a)

(b)

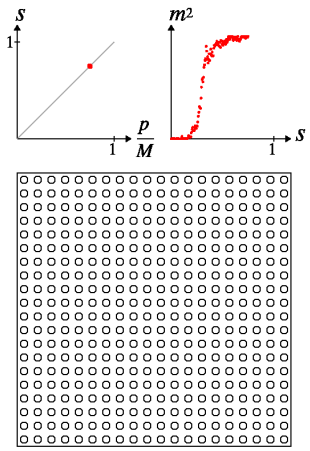

(c)

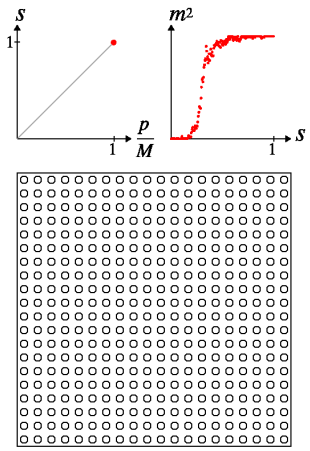

(d)

Figure 3.1: Illustration of a linear quench in imaginary time on 2D transverse-field Ising model. Shown are 25% (a), 50% (b), 75% (c), and 100% (d), through the quench process. For each panel, the top-left sub-panel shows the tuning parameter s as a function of the imaginary-time index p, the top-right sub-panel shows the order parameter, the z-component magnetization-squared, as a function of the tuning parameter s, and the bottom sub-panel shows the system. In this demonstration, a normalized string length $M/N = 100$ is used on a 20×20 square lattice. Notice that the entire m^2 vs. s curve can be obtained in a single run.

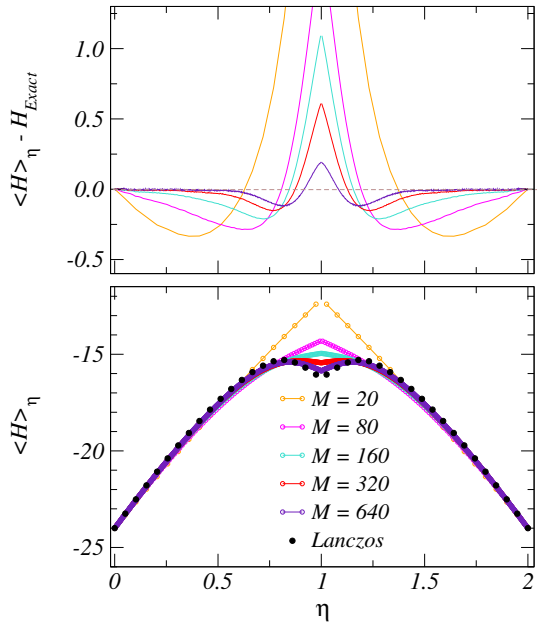

Figure 3.2: Symmetric and asymmetric expectation values of the Hamiltonian in QAQMC calculations for 1D TFIM Eq. (3.38) with $N = 24$. Here, the evolution was from $s = 0$ to 0.6 and, thus, $s = 0.6$ is the symmetric point here labeled by $\eta = t/2M = 1$. For $\eta \leq 1$, $s = 0.6\eta$ and for $\eta \geq 1$, $s = 1.2 - 0.6\eta$, and the critical point $s = 1/2$ hence corresponds to $\eta_{c1} \approx 0.833$ and $\eta_{c2} \approx 1.167$. (Bottom) Expectation value and (top) deviation from the true ground-state energy (obtained using Lanczos exact diagonalization).

3.3.2 Quantum-critical dynamic scaling

The idea of dynamic scaling at a critical point dates back to Kibble and Zurek for quenches (also called ramps, since the parameter does not have to change suddenly, but linearly with arbitrary velocity as a function of time) of systems through classical phase transitions. [14, 15] Here, the focus was on the density of defects. The ideas were later generalized also to quantities more easily accessible in experiments, such as order parameters, and the scaling arguments were also extended to quantum systems. [16, 31, 38, 39] The basic notion is that the system has a relaxation time $t_{\rm rel}$, and if some parameter (here a parameter of the Hamiltonian) is changed such that a critical point is approached, the system can stay adiabatic (or in equilibrium) only if the remaining time t to reach the critical point is much larger than the relaxation time, $t \gg t_{\rm rel}$. In general, one expects $t_{\rm rel} \sim \xi^z \sim \epsilon^{-z\nu}$, where ξ is the correlation length, ν the exponent governing its divergence with the distance ϵ to the critical point, and z the dynamic exponent. For a system of finite size (length) L, ξ is maximally of order L and, thus, for a linear quench the critical velocity $v_{\rm crit}$ separating slow and fast power-law quenches according to Eq. (3.15) should heuristically be given by $v_{crit} \sim L^{-(z+1/\nu)}$, and for a power-law quench with exponent r according to Eq. (3.15) this generalizes to [74]

$$v_{crit} \sim L^{-(zr+1/\nu)}. \tag{3.39}$$

One then also expects a generalized finite-size scaling form for singular quantities A,

$$A(L,\epsilon) = L^{\kappa} f(\epsilon L^{1/\nu}, v L^{zr+1/\nu}), \tag{3.40}$$

where κ characterizes the leading size-dependence at the critical point of the quantity considered. For $v \to 0$, Eq. (3.40) reduces to the standard equilibrium finite-size scaling hypothesis. This scaling was recently suggested and tested in different systems, both quantum [40, 74] and classical [32].

The above expression Eq. (3.40) combined with the product-evolution Eq. (3.5) allows us to study a phase transition based on different combinations of scaling in the system size

and the velocity in non-equilibrium setups. For example, if one wants to find the critical point for the phase transition and the exponent ν is known, one can carry out the evolution under the critical-velocity condition:

$$vL^{z+1/\nu} = c, \tag{3.41}$$

where c is a constant. In this paper, we focus on linear quench protocols and set $r = 1$ henceforth. As we discussed in Sec. 3.2.2, the QAQMC method applied to a system of size (volume) N based on evolution with M operators in the sequence and change Δ_λ between each successive operator corresponds to a velocity $v \propto N\Delta_\lambda \propto N/M$, with the prefactor depending on the ground state energy (at the critical point). The exact prefactor will not be important for the calculations reported below, and for convenience in this section, we define

$$v = s_{\rm f}\frac{N}{M}, \tag{3.42}$$

where $s_{\rm f}$ is the final value of the parameter s in Eq. (3.38) over the evolution (which is also the total change in s, since we start with the eigenstate at $s = 0$). The critical product-length M is, thus, given by

$$M = \frac{1}{c}NL^{z+1/\nu} = \frac{1}{c}L^{d+z+1/\nu}, \tag{3.43}$$

where we have also for simplicity absorbed $s_{\rm f}$ into c.

Using an arbitrary c of order 1 in Eq. (3.41), the critical point s_c can be obtained based on a scaling function with the single argument $\epsilon L^{1/\nu}$ in Eq. (3.40). We will test this approach here, in Secs. 3.4.1 and 3.4.2, and later, in Sec. 3.4.3, we will show that exact knowledge of the exponents in Eq. (3.41) is actually not needed. First, we discuss the quantities we consider in these studies.

3.3.3 Quantities studied

We will focus our studies here on the squared z-component magnetization (order parameter),

$$m_z^2 = \Big\langle \frac{1}{N^2}\Big(\sum_i^N \sigma_i^z\Big)^2 \Big\rangle, \tag{3.44}$$

We can also define a susceptibility-like quantity (which we will henceforth refer to as the susceptibility) measuring the magnetization fluctuations:

$$\chi = N(\langle m_z^2\rangle - \langle|m_z|\rangle^2). \tag{3.45}$$

Here both terms have the same critical size-scaling as the equal-time correlation function;

$$\langle m_z\rangle^2 \sim \langle|m_z|\rangle^2 \sim L^{-(d+z-2+\eta)}, \tag{3.46}$$

where d is the spatial dimensionality. The prefactors for the two quantities are different, however, a divergent peak remains in Eq. (3.45) at the transition. Away from the critical point $\chi \to 0$ with increasing system size.

To clarify our use of χ, we point out that we could also just study the scaling of $\langle m_z^2\rangle$, but the peak produced when subtracting off the second term in Eq. (3.45) is helpful in the scaling analysis. According to Eq. (3.40) and using $z = 1$ in Eq. (3.46), the full scaling behavior of the fluctuation around the critical point should follow the form

$$\chi \sim L^{1-\eta}\, f\big((s-s_c)L^{1/\nu}, vL^{1+1/\nu}\big), \tag{3.47}$$

for any dimensionality d.

We should point out here that the true thermodynamic susceptibility based on the Kubo formula [76] (imaginary-time integral) yields a stronger divergence $L^{2-\eta}$. This quantity is, however, more difficult to study with the QAQMC algorithm, because, unlike in standard finite-T QMC methods, the time integration cannot simply be carried out within the space of time-evolving Hamiltonians in Eq. (3.5) and Eq. (3.7). The standard Feynman-Suzuki

correspondence between the d-dimensional quantum and $(d+1)$-dimensional classical systems is not realized in our scheme. The configuration space of time-evolving Hamiltonians builds in the relaxation time, $t_{\rm rel}$, in a different way, not just in terms of equilibrium fluctuations in the time direction, but in terms of evolution as a function of a time-dependent parameter.

A useful quantity to consider for extracting the critical point is the Binder cumulant, [62],

$$U = \frac{3}{2}\left(1 - \frac{1}{3}\frac{\langle m_z^4 \rangle}{\langle m_z^2 \rangle^2}\right). \tag{3.48}$$

For a continuous phase transition, U converges to a step function as $L \to \infty$. The standard way to analyze this quantity for finite L is to graph it versus the argument s for different L and extract crossing points, which approach the critical point with increasing L. Normally, this is done in the equilibrium, either by taking the limit of the temperature $T \to 0$ for each L first, or by fixing $\beta = 1/T \propto L^z$ if z is known. Here, the latter condition is replaced by Eq. (3.41), but, as we will discuss further below, the condition can be relaxed and the exponents do not have to be known accurately *a priori*. Our approach can also be used to determine the exponents, either in a combined procedure of simultaneously determining the critical point and the exponents, or with a simpler analysis after first determining the critical point.

We have up until now only considered calculations of equal-time observables, but, in principle, it is also possible and interesting to study correlations in the evolution direction, which also can be used to define susceptibilities.

In the following we will illustrate various scaling procedures using results for the 1D and 2D TFIMs. The dynamic exponent $z = 1$ is known for both cases, and in the 1D case all the exponents are rigorously known since they coincide with those of the classical 2D Ising model. For the 2D TFIM, the exponents are know rather accurately based on numerics for the 3D classical model.

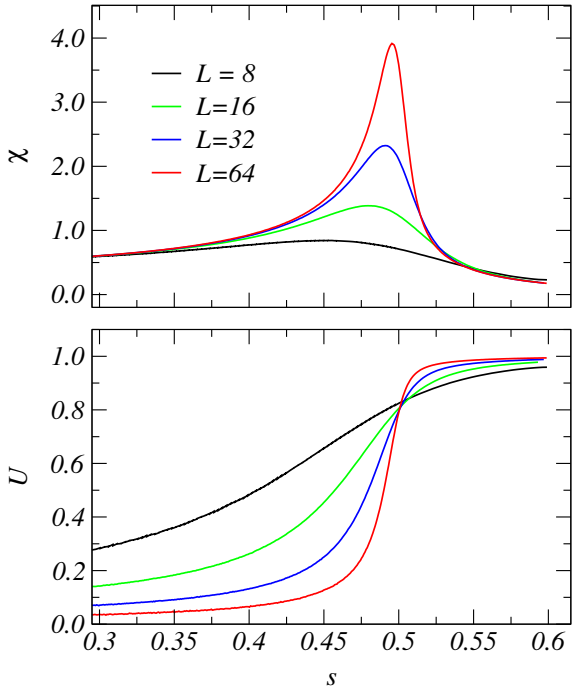

Figure 3.3: Results of typical QAQMC runs for the 1D TFIM, Eq. (3.38). The binder cumulant Eq. (6.16) (bottom) and the susceptibility χ Eq. (3.45) (top) are graphed versus s for several system sizes L. In these simulations, which spanned the range $s \in [0, 0.6]$, the length of the index sequence was of the form Eq. (3.43), i.e., with the exponents applicable in this case $M = L^3/c$ with the arbitrary constant chosen to be $c = 4^3/240$.

3.4 Numerical results

3.4.1 1D transverse-field Ising model.

The 1D TFIM provides a rigorous testing ground for the new algorithm and scaling procedures since it can be solved exactly. [6] The critical point corresponds to the ratio between the transverse field and the spin-spin coupling equaling 1, i.e., $s = 1/2$ in the Hamiltonian Eq. (3.38). The critical exponents, known through the mapping to the 2D Ising model, [10] are $\nu = 1$ and $\eta = 1/4$.

The results presented here were obtained in simulations with the parameter s spanning the

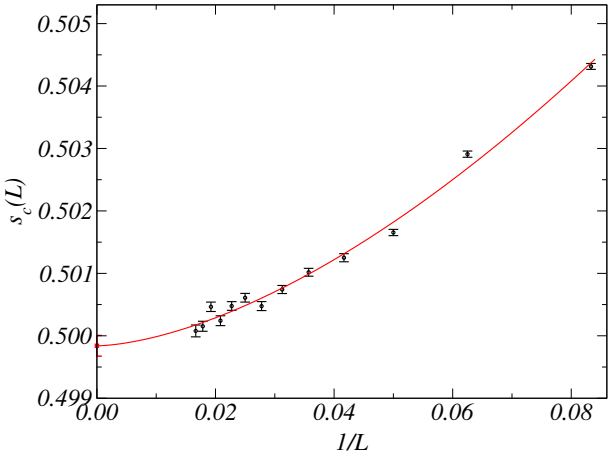

Figure 3.4: Results of a Binder-crossing scaling analysis of the 1D TFIM data in Fig. 3.3 (including also other system sizes not shown there). Crossing points were extracted based on system sizes L and $L+4$, with $L = 4, 8, \ldots, 60$. The curve is a fit to the form [62] $s_c(L) = s_c + a/L^b$, $s_c = 0.49984(16)$ and $b = 1.6(1)$.

range $[0, s_{\rm f}]$ with $s_{\rm f} = 0.6$, i.e., going from the trivial ground state of the field term to well above the critical point. Fig. 3.3 shows examples of results for the susceptibility and the Binder cumulant. The operator-sequence length M, Eq. (3.5), was scaled with the system size in order to stay at the critical velocity according to Eq. (3.43). We emphasize again that a single run produces a full curve within the s-range used. In order to focus on the behavior close to criticality, we have left out the results for small s in Fig. 3.3. Since M is very large (up to $\approx 10^6$ for the largest L in the cases shown in the figure), we also do not compute expectation values for each t in Eq. (3.7), but typically spacing measurements by $\propto N$ operators.

Extracting Binder curve-crossings using system-size pairs L and L+4, with $L = 4, 8, 12, \ldots 60$, and extrapolating the results to $L \to \infty$, we find $s_c = 0.49984(16)$, as illustrated in Fig.(3.4). Thus, the procedure produces results in full agreement with the known critical point.

The dynamical scaling of the susceptibility is illustrated in Fig. 3.5. Here, there are no adjustable parameters at all, since all exponents and the critical coupling are known (and

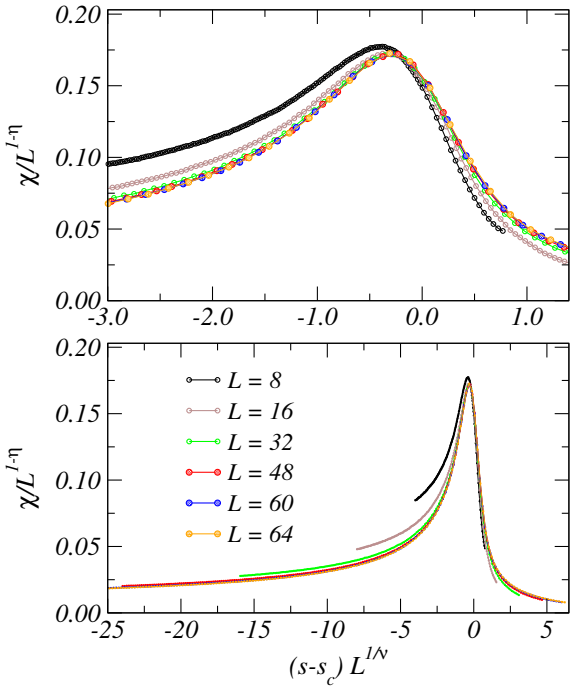

Figure 3.5: Scaled susceptibility of the 1D TFIM. The axes have been scaled according to the form Eq. (3.47) with the second argument constant and using the exact critical point $s_c = 1/2$. The results are shown on two different scales to make visible deviations (due to subleading size and velocity corrections) from the common scaling function far away from criticality as well as the good data collapse close to the critical point.

we use the exact critical coupling $s_c = 1/2$, although the numerical result extracted below is very close to this value and produces an almost identical scaling collapse). While some deviations from a common scaling function are seen for the smaller systems and far away from the scaled critical point $(s - s_c)L$, the results for larger sizes and close to the peak rapidly approach a common scaling function. This behavior confirms in practice our discussion of the definition of the velocity and the ability of the QAQMC method to correctly take into account at least the first corrections to the adiabatic evolution.

3.4.2 2D transverse-field Ising model

The 2D transverse-field Ising model provides a more serious test for our algorithm since it cannot be solved exactly. Among many previous numerical studies, [75, 77] Ref. [75] arguably has the highest precision so far for the value of the critical coupling ratio. Exact diagonalization was there carried out for up to 6×6 lattice size. In terms of the critical field $h_c = 1 - s$ in units of the coupling $J = s$, the critical point was determined to $h_c/J = 1/0.32841(2) = 3.04497(18)$, where the error bar reflects estimated uncertainties in finite-size extrapolations. Results based on QMC simulations [77] are in agreement with this value, but the statistical errors are larger than the above extrapolation uncertainty. One might worry that the system sizes $L \leq 6$ are very small and the extrapolations may not reflect the true asymptotic $L \to \infty$ size behavior. However, the data points do follow the functional forms expected based on the corresponding low-energy field theory, and there is therefore no *a priory* reason to question the results. It is still useful to try to reach similar or higher precision with other approaches, as we will do here with the QAQMC method combined with dynamic scaling.

In this case we simulate the linear quench in the window of $s \in [0, 0.3]$, which contains the previous estimates for the critical value $s_c \approx 0.247$ as discussed above. Although we could also carry out an independent scaling analysis to extract the critical exponents, we here choose to just use their values based on previous work on the classical 3D Ising model; $1/\nu \approx 1.59$, and $\eta \approx 0.036$. [66] Our goal here is to extract a high-precision estimate of the critical coupling, and, at the same time, to further test the ability of QAQMC to capture the correct critical scaling behavior. We again scale M with L according to Eq. (3.43), with the constant $c = 4^{4.59}/32$.

As in the 1D case, we extract Binder-cumulant crossing points based on linear system sizes L and $L + 4$ with $L = 4, 8, \ldots, 56$. Fig. 3.6 shows the results versus $1/L$ along with a fit to a power-law correction [62] for $s_c(L)$. Extrapolating to infinite size gives $s_c = 0.247244(4)$,

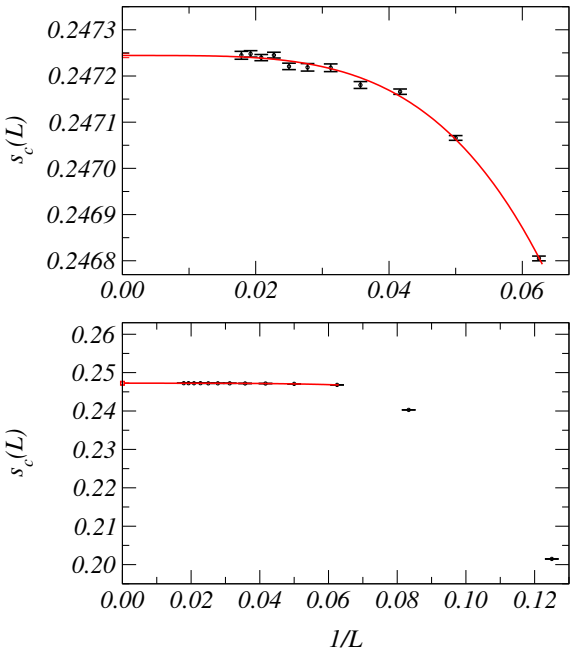

Figure 3.6: Binder crossings for the 2D TFIM extracted using L and $L+4$ systems with $L = 4, 8, \ldots, 56$. The crossing points have been fitted to the standard form [62] $s_c(L) = s_c + a/L^b$, for which the optimal values are $s_c = 0.247244(4)$ and $b = 4.0(1)$. The results are shown on two different scales to illustrate large deviations from the fitted form for the smaller systems, followed by a rapid convergence for larger sizes.

which corresponds to a critical field (in unit of J) $h_c/J = 3.04458(7)$. This is in reasonable good agreement with the value obtained in Ref. [75] and quoted above, with our (statistical) error bar being somewhat smaller. To our knowledge, this is the most precise value for the critical coupling of this model obtained to date. We emphasize that we here relied on the non-equilibrium scaling ansatz to extract the equilibrium critical point. Allowing for deviations from adiabaticity in a controlled way and utilizing the advantage of the QAQMC algorithm allowed us to extract observables in the whole range of couplings in a single run. This requires considerably less computational resources than standard equilibrium simulations, which must be repeated for several different couplings in order to carry out the crossing-point analysis.

Fig. 3.7 shows the susceptibility scaled according to the behavior expected with Eq. (3.40) when the second argument is held constant. As in the 1D case, the data converge rapidly with increasing size toward a common scaling function in the neighborhood of the transition point, again confirming the correct quasi-adiabatic nature of the QAQMC method.

3.4.3 Further tests

The results discussed in the preceding subsections were obtained with the KZ velocity condition Eq. (3.41), applied in the form of Eq. (3.43) tailored to the QAQMC approach, with specific values for the constant c. In principle, the constant is arbitrary, but the non-universal details of the scaling behavior depend on it. This is in analogy with a dependence on the shape, e.g., an aspect ratio, of a system in equilibrium simulations at finite temperature, or to the way the inverse temperature $\beta = 1/T$ is scaled as aL^z with arbitrary a in studies of quantum phase transitions (as an alternative to taking the limit $\beta \to \infty$ for each lattice size). The critical point and the critical exponents should not depend on the choices of such shape factors or limiting procedures.

To extract the critical coupling, in the preceding subsections, we fixed the exponents ν

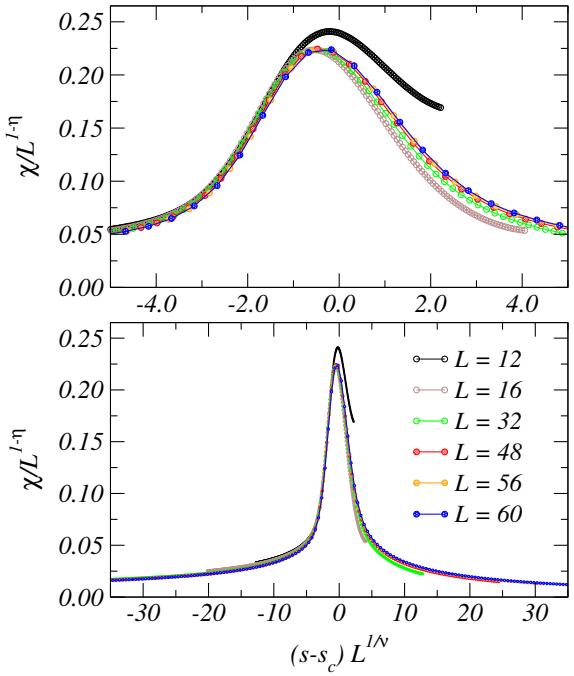

Figure 3.7: Scaled susceptibility of the 2D TFIM, based on Eq. (3.47) with a constant second argument. Here we have used $1/\nu = 1.59$ and $\eta = 0.036$ for the classical 3D Ising model [66].

and z at their (approximately) known values, and one may at first sight assume that it is necessary to use their correct values. It is certainly some times convenient to do so, in order to set the second argument of the scaling function Eq. (3.40) to a constant and, thus, obtain a simpler scaling function depending on a single argument. However, one can study critical properties based on the scaling approach discussed above as long as the velocity approaches zero as the system size increases. This observation can be important in cases where the critical exponents are not known and one would like to obtain an accurate estimate of the critical coupling before carrying out a scaling analysis to study exponents. We will test this in practice here. As we will discuss further below, one should use a different power κ in the scaling ansatz Eq. (3.40) if the velocity is brought to zero slower than the critical form.

In cases where we use the "wrong" values of the exponents, we formally replace $z + 1/\nu$ by a free parameter α,

$$v \sim L^{-\alpha}/c, \tag{3.49}$$

and the corresponding substitution in Eq. (3.43). To understand the scaling of the observables for arbitrary α, we return to the general scaling form given by Eq. (3.40). In the case of the Binder cumulant and for linear quench protocol, this form reads

$$U = f\big((s - s_c)L^{1/\nu}, vL^{z+1/\nu}\big). \tag{3.50}$$

As we pointed out above, when the velocity scales exactly as $L^{-(z+1/\nu)}$, the dependence on the second argument in the scaling function drops out and we can find the crossing point in a standard way as we did in Figs. 3.4 and 3.6. Suppose that we do not know the exponents ν and z *a priory* and instead scale v as in Eq. (3.49). Then there are three possible situations: (i) $\alpha = z + 1/\nu$, (ii) $\alpha > z + 1/\nu$, and (iii) $\alpha < z + 1/\nu$, where we already have analyzed scenario (i). In scenario (ii), where velocity scales to zero faster than the critical KZ velocity, the second argument of the scaling function $L^{z+1/\nu}/L^{\alpha}$ approaches zero as the system size increases and, thus, the scaling function effectively approaches the equilibrium velocity-independent form. We can then extract the crossing point as in the first scenario, and this

gives the correct critical coupling in the limit of large system sizes. Finally, in case (iii) the velocity scales zero slower than the critical KZ value and the second argument in Eq. (3.50) diverges, which implies that the system enters a strongly non-equilibrium regime. This scenario effectively corresponds to taking the thermodynamic limit first and the adiabatic limit second. Then, if the system is initially on the disordered side of the transition, the Binder cumulant vanishes in the thermodynamic limit. At finite but large system sizes its approach to zero should be given by the standard Gaussian theory:

$$U \approx \frac{C}{L^d}. \tag{3.51}$$

Combining this with the scaling ansatz Eq. (3.50) we find that for $\alpha < z+1/\nu$, the expected asymptotic of the Binder cumulant is

$$U \approx L^{-d} v^{-d/(z+1/\nu)} \tilde{f}\big((s-s_c)L^{1/\nu}\big), \tag{3.52}$$

where $\tilde{f}$ is some other velocity independent scaling function. Thus we can find the correct transition point by finding crossing points of $UL^d v^{d/(z+1/\nu)}$. Similar considerations apply to the ordered side of the transition, where the Binder cumulant approaches one as the inverse volume.

The three cases are illustrated in the lower panel of Fig. 3.8, which shows Binder-cumulant crossings extracted from appropriately scaled data in cases (i), (ii), and (iii) above. Additionally, to illustrate the insensitivity to the choice of the constant c in the scaled sequence length in Eq. (3.43), results based on two different constants are shown for case (i). In all cases, the extrapolated critical couplings agree with each other to within statistical errors. Note that, on the one hand, if the exponent α gets very large, then the time of simulations, which scales as M, rapidly increases with the system size and the algorithm becomes inefficient. On the other hand, if α is very small, our results indicate that the size dependence is larger and it is more difficult to carry out the extrapolation to infinite size. The optimal value of α should be as close as possible to the critical KZ power, but to be on the safe side when scaling according to the standard KZ critical form, case (i), one may choose a

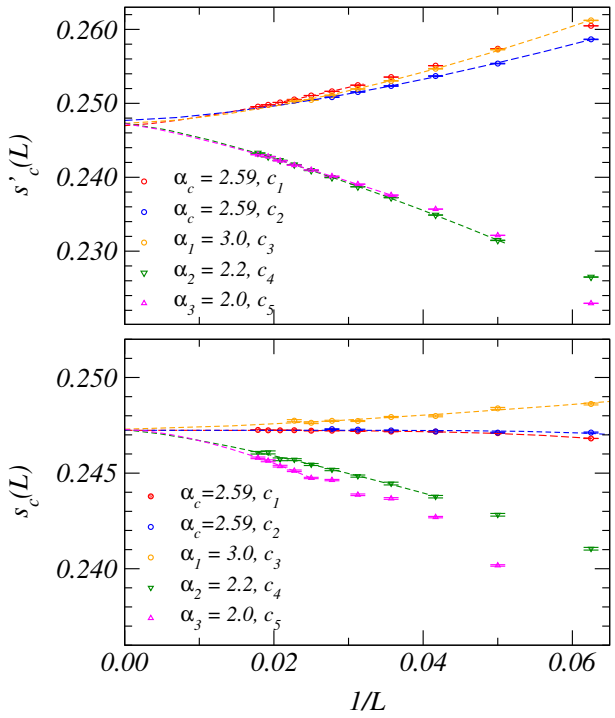

Figure 3.8: Critical-point estimates based on curve crossings of appropriately scaled quantities for scenarios (i)-(iii) discussed in the text. The Binder cumulant (bottom) and the squared magnetization (top) give estimates $s_c(L)$ and $s'_c(L)$, respectively, based on system sizes L and $L+4$. The red and blue curves correspond to runs in which the velocity was kept at the critical value, scenario (i), but with different constants of proportionality c in Eq. (3.43); $c_1 = 4^{4.59}/32$ and $c_2 = 4^{4.59}/48$. The yellow curves were obtained with the velocity decreasing faster than v_{crit} with L, scenario (ii), with the proportionality constant $c_3 = 4^5/32$. The green and pink curves correspond to cases where the velocity is sub-critical, scenario (iii), with constants $c_4 = 4^{4.2}/32$, $c_5 = 4^4/32$. In all cases, power-law corrections were fit in order to extrapolate to infinite size (with small sizes excluded until statistically sound fits were obtained).

somewhat larger value, since the subcritical velocity in case (ii) has the same scaling form.

Next we illustrate how the same idea works in the case of the order parameter. Around the critical point (s_c, $v_{\rm crit}$), the squared magnetization [see Eq. (3.44)] can be written as

$$m_z^2 \;=\; L^{-2\beta/\nu} f\big((s-s_c)L^{1/\nu}, vL^{z+1/\nu}\big). \tag{3.53}$$

As in the previous discussion we scale $v \sim L^{-\alpha}$ and depending on the exponent α there are two different asymptotics of the scaling function. For $\alpha \geq z + 1/\nu$ the second argument vanishes or approaches constant so we effectively get the equilibrium scaling

$$m_z^2 \;=\; L^{-2\beta/\nu} f\big((s-s_c)L^{1/\nu}\big) \tag{3.54}$$

If, conversely, $\alpha < z + 1/\nu$ then on the disordered side of the transition m_z^2 scales as L^{-d}. This immediately determines the asymptotic of the scaling function in Eq. (3.53):

$$m_z^2 = L^{-d} v^{\frac{(2\beta/\nu)-d}{z+1/\nu}} \tilde{f}\big((s-s_c)L^{1/\nu}\big). \tag{3.55}$$

Equation (3.55) can be used in the same way as the Binder cumulant to extrapolate the critical point, using the standard form [62] $s_c'(L) = s_c' + a/L^b$ for the rescaled m_z^2. As shown in the top panel of Fig. (3.8), after rescaling the order parameter and extrapolating the crossing points between the appropriately rescaled m_z^2 curves to the thermodynamics limit, all curves, obtained from below or above the adiabatic limit Eq. (3.39), converge to the same value $s_c' \approx 0.247$. This approach also suggests a way to determine the transition point in experiment, since one can sweep through the critical point at different velocities, the crossing point can then be extracted through the measurement of the order parameter. It is also worth mentioning that since one can extrapolate the critical point independently without knowing the actual exponent ν prior to the simulation, an optimization procedure can be carried out to determine the exponents posterior to the simulation. [17]

For completeness we also briefly discuss the role of the final point $s_{\rm f}$ of the evolution. Fig. 3.9 shows 2D results for the squared magnetization Eq. (3.44) and susceptibility Eq. (3.45) obtained for a range of final points above the critical value. Here the velocity was kept

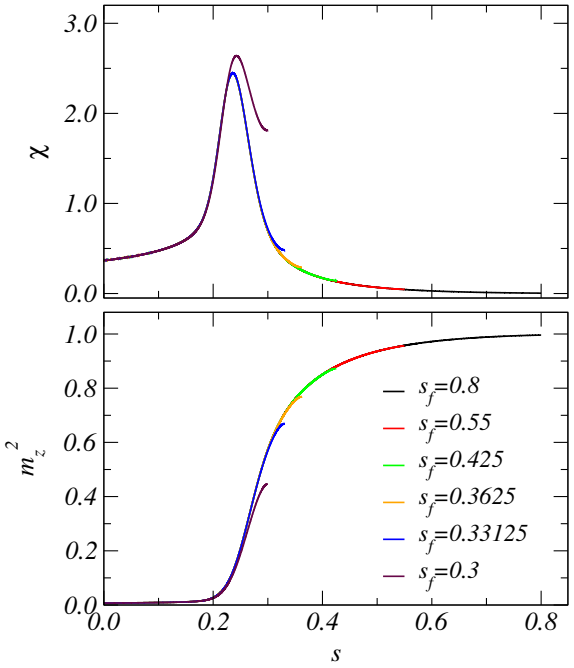

Figure 3.9: Squared magnetization (bottom) and susceptibility (top) vs s of the 2D TFIM with $L = 12$. In these runs, different curves correspond to different end points s_f of the evolution, with the velocity $v \propto s_{\rm f}N/M$ kept constant. The $s_f = 0.3$ curve is from the simulation shown in Sec. 3.4.2.

constant for all the cases. The values of the computed quantities at some fixed s, e.g., at s_c, show a weak dependence on $s_{\rm f}$ for the lowest-$s_{\rm f}$ runs. The deviations are caused by contributions of order v^2 and higher, which are non-universal as discussed in Sec. 3.2.2. For very high velocities the dependence on $s_{\rm f}$ can be much more dramatic than in Fig. 3.9, but this is not the regime in which the QAQMC should be applied to study universal physics.

3.5 Summary and Discussion

We have presented a nonequilibrium QAQMC approach to study quantum dynamics, with a simple product of operators with evolving coupling replacing the standard Schrödinger time evolution. We showed that this approach captures the leading non-adiabatic corrections

to the adiabatic limit, both by analytical calculations based on the APT and by explicit simulations of quantum-critical systems with the QAQMC algorithm. The simulation results obey the expected generalized dynamic scaling with known static and dynamic critical exponents. We also extended the scaling formalism beyond results obtained previously in Ref. [33]. We analyzed the leading non-adiabatic corrections within this method and showed that they can be used to extract various non-equal time correlation functions, in particular, the Berry curvature and the components of the metric tensor. A clear advantage of the QAQMC approach is that one can access the whole range of couplings in a single run. Being a simple modification of projector QMC, the QAQMC method is applicable to the same class of models as this conventional class of QMC schemes—essentially models for which "sign problems" can be avoided.

As an illustration of the utility of QAQMC, we applied the algorithm and the scaling procedures to the 1D and 2D TFIMs. The expected scaling behaviors are observed very clearly. In the 1D case we extracted a critical coupling in full agreement with the known value, and in 2D we obtained an estimate with unprecedented (to our knowledge) precision (small error bars); $(h/J)_c = 3.04458(7)$. Based on repeating the fitting procedures with different subsets of the data, we believe that any systematical errors due to subleading corrections neglected in the extrapolations should be much smaller than the statistical errors, and, thus, we consider the above result as unbiased.

The QAQMC approach bears some similarities to previous implementations of *quantum annealing* within QMC algorithms. [78, 79] However, the previous works have mainly considered standard equilibrium QMC approaches in which some system parameter is changed as a function of the *simulation time*. This evolution is not directly related to true quantum dynamics (and, thus, is not really quantum annealing), but is dependent on the particular method used to update the configurations. In contrast, in our scheme, as in the NEQMC method introduced in Ref. [33], the evolution takes place *within* the individual configurations, and there is a direct relationship to true Schrödinger evolution in imaginary time.

In Green's function (GF) QMC simulations the gradual change of a system parameter with the simulation time is rather closely related to the QAQMC scheme (since also there one applies a series of terms of the Hamiltonian to a state), with the difference being that QAQMC uses true importance sampling of configurations, with no need for guiding wave functions and no potential problems related to mixed estimators. Our asymmetric expectation values could be considered as a kind of mixed estimator as well, but we have completely characterized them within the APT. In addition, the previous uses of GFQMC with time-evolving Hamiltonians have, to our knowledge, never addressed the exact meaning of the velocity of the parameter evolution. The correct definition of the velocity is of paramount importance when applying quantum-critical scaling methods, as we have discussed here. We have here computed the velocity within APT for the QAQMC scheme. The same relationship with Schrödinger dynamics may possibly hold for GFQMC as well, but, we have not applied the APT to this case and it is therefore not yet clear whether GFQMC can capture correctly the same universal non-equilibrium susceptibilities as the QAQMC and NEQMC methods. We expect QAQMC to be superior to time-evolving GFQMC, because of its better control over measured symmetric and asymmetric expectation values and fully realized importance sampling.

Some variants of GFQMC use true importance sampling, e.g., the Reptation QMC (RQMC) method, [80] which also avoids mixed estimators. The configuration space and sampling in the QAQMC method bears some similarities with RQMC, recent lattice versions of which also use SSE-inspired updating schemes. [81] However, to our knowledge, imaginary-time evolving Hamiltonians have not been considered in RQMC and in other related variants of GFQMC, nor has the role played by the velocity when crossing the quantum critical point been stressed. This has so far been our focus in applications of the QAQMC and NEQMC methods. In principle one could also implement the ideas of time-evolution similar to QAQMC within the RQMC approach.

We also stress that we have here not focused on optimization. Previous works on quantum

annealing within QMC schemes have typically focused on their abilities to optimize difficult classical problems. While the QAQMC may potentially also offer some opportunities in this direction, our primary interest in the method is to use it to extract challenging dynamical information under various circumstances.

The QAQMC and NEQMC methods provide correct realizations of quantum annealing in imaginary time. Besides their ability to study dynamic scaling, with exponents identical to those in real-time Schrödinger dynamics, [33] it will be interesting to explore what other aspects of real-time dynamics can be extracted with these methods. In particular, their applicability to quantum glasses, of interest in the context of quantum adiabatic computing [30] as well as in condensed matter physics, deserves further studies.

The ability of the QAQMC to produce results for a whole evolution path in a single run can in principle also be carried over to the conventional Schrödinger imaginary-time evolution with $U(\tau)$ in Eq. (3.4). By "slicing" the time evolution into K successive evolutions over a time-segment Δ_τ,

$$U(\tau) = \prod_{n=1}^{K} T_\tau \exp\left[-\int_{\tau_{n-1}}^{\tau_n} d\tau \mathcal{H}[\lambda(\tau)]\right], \tag{3.56}$$

where $\tau_n = n\Delta_\tau$, one can evaluate matrix elements analogous to Eq. (3.7) by inserting the operator of interest at any point within the product of time-slice operators in $\langle\Psi(\lambda_0)|U^*(\tau)U(\tau)|\Psi(\lambda_0)\rangle$. In this case, the symmetric expectation value, evaluated at the mid-point, is identical to the NEQMC method, [33] and the asymmetric expectation values will exhibit properties similar to those discussed in Sec. 3.2.3. We have not yet explored this approach, and it is not clear whether it would have any other advantage besides the exact reduction to Schrödinger dynamics of the symmetric expectation values. In practice the simulations will be more complex than the QAQMC approach because of the need to sample integrals, but not much more so than the NEQMC method. It should be relatively easy to adapt the RQMC method with an evolving Hamiltonian in this formulation of the time-evolution.

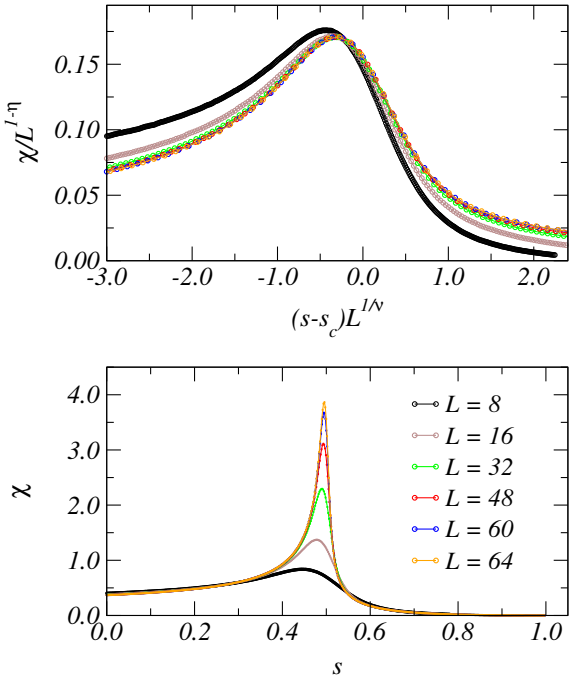

Figure 3.10: One-way evolution $s \in [0, 1]$ with QAQMC for the 1D TFIM. (Bottom) The susceptibility Eq. (3.45). (Top) The rescaled susceptibility Eq. (3.47). Each full curve corresponding to a given chain length L was obtained in a single run. The constant for the critical-velocity condition Eq. (3.41) was held at $4^3/80$.

Finally, we point out that, in principle, one can also carry out a *one-way evolutions* with the QAQMC algorithm. Instead of starting with the $\lambda = \lambda_0$ eigenstate at both $\langle\psi_L|$ and $|\psi_R\rangle$ and then projecting them to the $\lambda = \lambda_M$ eigenstate using two sequences of the form Eq. (3.5), one can make $\langle\psi_L|$ correspond to λ_0 and let it evolve to $|\psi_R\rangle$ corresponding to λ_M with only a single operator sequence of length M. In the case of the TFIM Eq. (3.38), the obvious choice is then to evolve from $s = 0$ to $s = 1$ (the classical Ising model), so that both edge states are trivial. All our conclusions regarding the definition of the velocity and applicability of scaling form remain valid in this one-way QAQMC. Results demonstrating this in the case of the 1D TFIM are sown in Fig. 3.10. We anticipate that this approach may be better than the two-way evolution in some cases, but we have not yet compared the two approaches extensively.

Chapter 4

Comparison between simulation-time quantum annealing and imaginary-time quantum annealing

4.1 Introduction

In Refs. [33,37], two quantum Monte Carlo algorithms have been developed, non-equilibrium quantum Monte Carlo (NEQMC) and quasi-adiabatic quantum Monte Carlo (QAQMC), both algorithms carried out quantum evolution in imaginary time. This feature of imaginary-time evolution is reminiscent of quantum annealing [78, 82, 83] , however, so far, quantum annealing is typically carried out in *simulation time*. In this Chapter, we discuss the striking difference between the simulation-time quantum annealing and imaginary-time quantum-annealing in detail.

In this Chapter, we will use one-dimensional (1D) transverse-field Ising model (TFIM) to do the demonstration. The Hamiltonian reads as :

$$\mathcal{H} = -s \sum_{\langle i,j \rangle} \sigma_i^z \sigma_j^z - (1-s) \sum_i \sigma_i^x, \tag{4.1}$$

where $\langle i, j \rangle$ stands for the nearest-neighbor pairs and σ_i^z and σ_i^x are Pauli matrices. We are

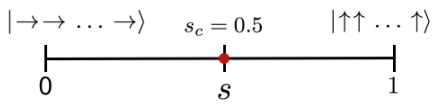

Figure 4.1: $T = 0$ phase diagram of the one-dimensional transverse-field Ising model with the Hamiltonian Eq. 4.1. A QCP at $s_c = 1/2$ is known exactly for the 1D TFIM [6].

interested in the zero-temperature quantum phase transition as the tuning parameter s is tuned $s : 0 \to 1$. Since 1D TFIM can be solved analytically [6] and also through a mapping to the two-dimensional classical Ising model [5, 10], the quantum critical point (QCP) and critical exponents are known exactly as the following: QCP $s_c = 1/2$, correlation length exponent $\nu = 1$, order parameter exponent $\beta = 1/8$, and dynamic exponent $z = 1$. The phase diagram is illustrated in Fig. 4.1.

4.2 Simulation schemes and updating schemes

Simulation-time quantum annealing [78,82,83] is motivated by simulated-annealing [55], the latter used the decrease of the thermal fluctuation to find the minimum of a cost function, while the former used quantum tunneling and the decrease of quantum fluctuation to achieve the goal. Many problems that quantum annealing tried to solve are incorporated in the same form of Eq. (4.1). The starting Hamiltonian with $\mathcal{H}(s = 0)$ has a ground state that is easy to prepare, for example, in Eq. (4.1) $s = 0$ corresponds to an equal superposition ground state:

$$|\Psi(0)\rangle = \prod_i \frac{|\uparrow\rangle_i + |\downarrow\rangle_i}{\sqrt{2}}. \tag{4.2}$$

And the system evolves through some protocol $s : 0 \to 1$ to eventually $\mathcal{H}(s = 1)$ that has a complicated ground state configuration. As long as the evolution is slow, the wave function $|\Psi(s)\rangle$ should keep staying in the ground state, and therefore the hard problem embedded in $\mathcal{H}(s = 1)$ is solved automatically when the evolution reaches $s = 1$, this is the idea of quantum adiabatic algorithm [84].

Next we use stochastic-series expansion (SSE)-based projector quantum Monte Carlo (PQMC) [11–13, 63] on transverse-field Ising model to demonstrate the implementation. A typical projector quantum Monte Carlo applies on a trial state $|\Psi_0\rangle$ many times, say M times, the Hamiltonian $\mathcal{H}(s)$ to project out the ground state:

$$
\begin{aligned}
|\Psi_{\mathrm{GS}}\rangle &= \big[-\mathcal{H}(s)\big]^{M}|\Psi_0\rangle \\
&= \sum_{[i_M,\ldots,i_1]} H_{i_M}(s)\ldots H_{i_1}(s)|\Psi_0\rangle
\end{aligned}
\tag{4.3}
$$

where the Hamiltonian $\mathcal{H}$ depends on a particular tuning parameter s and H_i is one of the many local operators which $\mathcal{H}$ consists of. In the case of TFIM, there are only three types of local operators, the single-site spin-flipping operator that is off-diagonal, the Ising interaction operator that is diagonal and acting on a nearest-neighbor pair of spins, and a single-site constant operator [1]. The second line of Eq. (4.3) lays out the formalism for quantum Monte Carlo simulations, which carries out importance sampling scheme by stochastically generating operator-spin configurations. Fig. 4.3 (a) illustrates the SSE configuration of Eq. (4.3) when applied on a 8-spin transverse-field Ising chain with $M = 8$. The operator product $H_{i_M}(s)\ldots H_{i_1}(s)$ forms the imaginary-time dimension [7].

The QAQMC algorithm [37], which is a successor of NEQMC [33], modifies Eq. (4.3) in the following way: instead fixing the tuning parameter s for all the operators in the operator product, we change s from $s:0\rightarrow s_f$ as we move along the imaginary-time direction:

$$
\begin{aligned}
|\Psi_{s_f}\rangle &= \big[-\mathcal{H}(s_{_M})\big]\ldots\big[-\mathcal{H}(s_1)\big]|\Psi_0\rangle \\
&= \sum_{[i_M,\ldots,i_1]} H_{i_M}(s_{_M})\ldots H_{i_1}(s_1)|\Psi_0\rangle
\end{aligned}
\tag{4.4}
$$

where $s_0 = 0$ and $s_{_M} = s_f$. The same SSE configuration in Fig. 4.3 (a) can also be used to visualize Eq. (4.4). The caution when interpreting Eq. (4.3) and Eq. (4.4) respectively using Fig. 4.3 (a) is that in the PQMC picture, the tuning parameter s is fixed in the imaginary-time direction, i.e., all operators correspond to the same magnitude of s; one the other hand, in the QAQMC picture, the parameter s is evolving $s:0\rightarrow s_f$ along the imaginary-time direction, i.e., each operator in the imaginary-time takes different values of s.

[1] Strictly speaking, the constant operator is not necessary, it is introduced to facilitate the off-diagonal update. [11–13, 63]

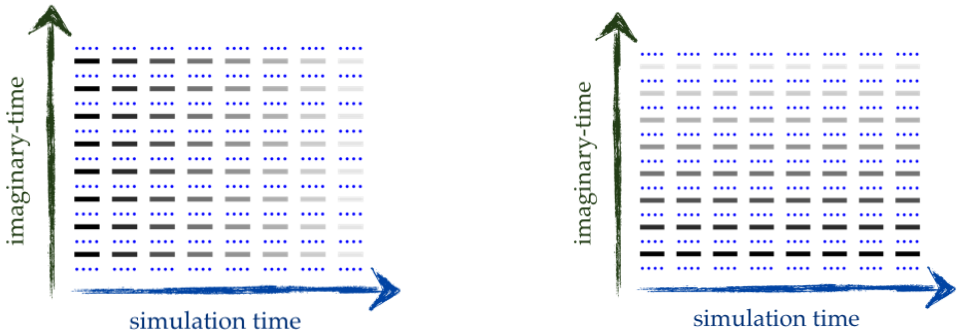

(a) (b)

Figure 4.2: Simulation-time quantum annealing (a) versus imaginary-time quantum annealing (b). In the simulation-time annealing scheme, at each instance of simulation time, the parameter s is fixed along the imaginary-time direction. Therefore, one has to change s in simulation time. In imaginary-time annealing scheme, the change of the parameter s has been incorporated into the algorithm through Eq. (4.4). Each simulation time instance is simply an independent evolution path of $s : 0 \to s_f$. In both plots, the colors of the bars are used to represent the operators taking different magnitude of the tuning parameter s. In Sec. 4.3, it will be revealed that these two types of annealing scheme will lead to two dramatically different consequences.

The approaches discussed above therefore lead to two distinct quantum annealing schemes. In PQMC, the tuning parameter s is fixed in the imaginary-time, to perform annealing, one has to change s in *simulation time*, as illustrated in Fig. 4.2 (a); at each time instance, the snapshot of the configuration (each column in Fig. 4.2 (a)) gives an operator product in which all operators take the same value of s. On the other hand, in QAQMC, the tuning of s is naturally incorporated into the algorithm, therefore, at any instance of the simulation time, the operator product corresponds to an evolution path of $s : 0 \rightarrow s_f$. Each simulation time instance in QAQMC (each column in Fig. 4.2 (b)) is simply an independent evolution path.

SSE-type quantum Monte Carlo (QMC) importance sampling scheme [7], generally involves two stages of updates: diagonal update and off-diagonal-update. Diagonal updates involve exchanges between the constant single-site operators and the Ising interaction operators. Off-diagonal updates involve exchange between the constant single-site operators and the single-site spin-flipping operators. Different QMC algorithms have different updating schemes. Roughly speaking, diagonal update is more universal among different QMC algorithms, therefore will not be the focus here. The off-diagonal update, which has variations leading to different efficiencies in terms of both relaxation time as well as computer performance, will be the focus here. Generally speaking, there are two types of off-diagonal updates: local updates and cluster updates. Below we discuss these two updating schemes.

In classical Ising model with Metropolis [42] dynamics, one performs single-site (local) spin-flipping updates on the individual spins one by one. However, in QMC, one can not simply flip a single spin in the extended spatial-temporal dimension without violating a given configuration, since in this extended space every spin is linked to another spin (either the spin itself in the next imaginary-time instance or another spin in the next imaginary-time instance). Therefore, the minimal local update corresponds to updating a pair of spins in the space-time dimension, as illustrated in Fig. 4.3 (b). Although it is not exactly the same as the Metropolis local update as in the classical Monte Carlo simulation, one can

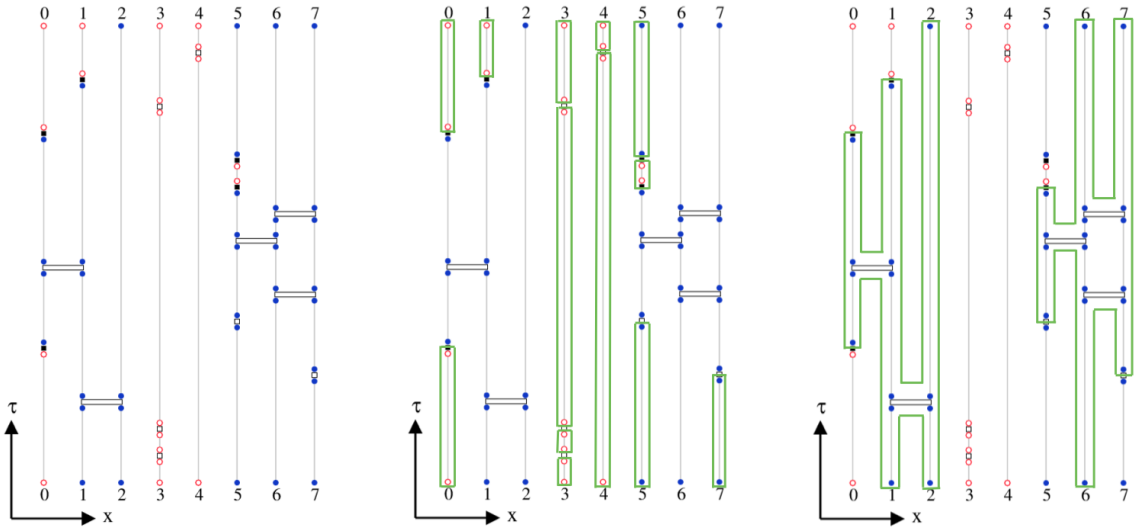

Figure 4.3: (a) SSE representation for Eq. (4.3) and Eq. (4.4) on a 8-spin 1D TFIM with $M = 8$. The horizontal direction is the spatial dimension, the vertical direction is the imaginary-time dimension, which scales as ξ^z with ξ being the spatial correlation length and z the dynamic exponent. The open square denotes a constant single-site operator, the filled square stands for the single-site spin-flipping (off-diagonal) operator, and the bar represents a Ising-interaction (diagonal) operator. (b) Local updates on the SSE configuration are shown in (a). The minimal local update in QMC corresponds to updating a pair of spins in the extended spatial-temporal dimension. When the spins are flipped, the operators connected to the spins are also updated. The green rectangles identify the pairs of spins that will be updated in the local update scheme. (c) Cluster update on the same configuration shown in (a) and (b). In addition to the "local clusters" that consist only a pair of spins shown in (b), cluster update also identifies "global clusters" then can extend the entire spatial-temporal dimension, as highlighted by the green color. The construction of the cluster starts with a single-site operator, continuing the construction through the Ising type operators, and terminates when encountering another single-site operator or the boundary.

imagine that in the thermodynamic limit, the span of the link that connects a pair of spin will be much shorter than the scale of the imaginary-time dimension, therefore becomes effectively "local." Local update that attempts to flip a pair of spins in the extended space is easy to implement, however, it is not efficient enough. Cluster updates try to improve this drawback. Currently, the SSE-based cluster update [11–13] is the most state-of-the-art and a widely used algorithm. In terms of TFIM, the SSE-based cluster update constructs a "cluster" in the spatial-temporal dimension, starting from a single-site operator (either a constant operator or an off-diagonal spin-flipping operator), continuing the construction of cluster when encountering Ising type operators, and terminates the construction when arriving at a single-site operator or the boundary. The process is illustrated in Fig. 4.3 (c).

It is interesting to note that, due to the mapping from a d-dimensional quantum spin system to a $(d+1)$-dimensional classical spin system [10], the local update QMC on a 1D TFIM is reminiscent of the Metropolis local update in 2D classical Ising model, and the cluster update QMC on a 1D TFIM is similar to the Swendsen-Wang/Wolff cluster update on 2D classical Ising model. In the next section, we will show that this qualitatively described correspondence of the dynamic can be also proved quantitatively.

When implementing PQMC, one needs to use the operator product that is long enough in order to project out the ground state. For the 1D TFIM with the Hamiltonian Eq. (4.1), a set of equilibrium runs have been tested at $s = s_c = 1/2$. As shown in Fig. 4.4, $M = 4L^2$ is enough to obtain convergence.

4.3 Numerical results

In this section, we use both simulation-time quantum annealing and imaginary-time quantum annealing outlined in the previous section to perform critical quenches on 1D TFIM with the Hamiltonian Eq. (4.1), whose QCP and critical exponents are all well known [6]. The simulation starts from $s = 0$ with the initial configuration Eq. (4.2), and the annealing

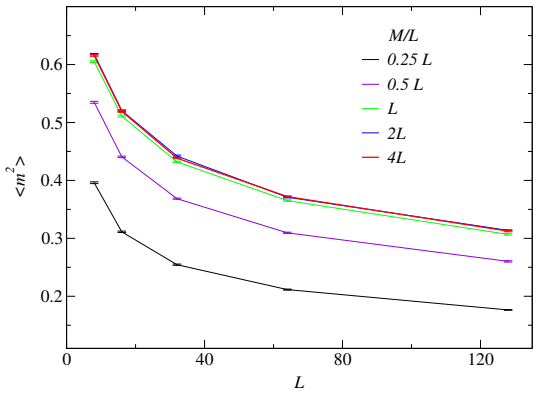

Figure 4.4: Equilibrium runs for PQMC on 1D TFIM with difference sizes at $s = s_c = 1/2$. We use the order parameter $\langle m^2 \rangle$ as an indicator to observe how it converges as the length of the operator product M increases. As the figure shows, $M = 4L^2$ can achieve convincing convergence.

process of $s : 0 \to s_c$ is carried out with linear and non-linear quench protocols that can be described by the following form:

$$\begin{aligned} s(t) &= s_c - \frac{s_c}{(\tau N_0)^r}(\tau N_0 - t)^r, \\ v &= s_c/\tau^r, \end{aligned} \tag{4.5}$$

where N_0 is the normalization constant, τ the total quench time, v the generalized quench velocity, and $r \in \mathbb{R}$ the parameter that controls the quench protocol, for example $r = 1$ for constant velocity linear quench, $r = 2$ for constant acceleration quadratic quench, and $r = 1/2$ for non-linear square-root quench, etc. In terms of simulation-time quantum annealing, τ is the duration of the simulation, therefore the normalization constant is trivial: $N_0 = 1$. In terms of imaginary-time quantum annealing, the quench time is controlled by the length of the operator product M, which should scale as the system size: $M \propto N$, therefore the normalization constant should be $N_0 = N$. When quenching exactly to QCP, we will expect to see a dynamic finite-size scaling that has been discussed in detail in Refs. [17,37]:

$$\langle m_z^2 \rangle = L^{-2\beta/\nu} f(vL^{zr+1/\nu}), \tag{4.6}$$

where m_z is the z-component magnetization, L is the linear size of the system. Furthermore, based on the dynamic finite-size scaling behavior, one can expect to see a power-law behavior in the high-velocity regime:

$$\langle m_z^2 \rangle = L^{-2\beta/\nu}(vL^{z+1/\nu})^{-x}, \tag{4.7}$$

with the power x related to the critical exponents

$$x = \frac{d - 2\beta/\nu}{zr + 1/\nu}, \tag{4.8}$$

where d is the dimensionality.

In simulation-time quantum annealing, the parameter s is changed at each iteration, i.e., each simulation time instance, while keeping s fixed along the imaginary-time direction, as illustrated in Fig. 4.2 (a). When carrying out the QMC updates, one can consider local updates and cluster updates, respectively, as described in the previous section. For either case, the scaling Eq. (4.6) is expected to hold, while the only difference being the dynamic exponent z that appears in the expression. Fig. 4.5 shows the result of scaling collapse from the simulation-time annealing to the QCP. Panel (a) of Fig. 4.5 shows the result from the annealing with local update, and panel (b) of Fig. 4.5 shows the result from the annealing with cluster update. Since the static exponents ν and β are already known, one can carry out a fitting procedure as described in Ref. [17] to estimate the dynamic exponent z. From the local update, we obtain $z \approx 2.17$, which is the Metropolis dynamics exponent of the 2D classical Ising mode. From the cluster update, we obtain $z \approx 0.3$, which is the Swendsen-Wang/Wolff dynamic exponent of the 2D classical Ising model, neither of these two schemes could render Hamiltonian dynamic that has $z = 1$ for TFIM.

Next we discuss the scenario of imaginary-time quantum annealing. As explained in detail in Refs. [33,37], one important scaling to follow when implementing QAQMC and NEQMC is that the length of the operator product M in Eq. (4.4) should scale as $M \propto N$. As discussed

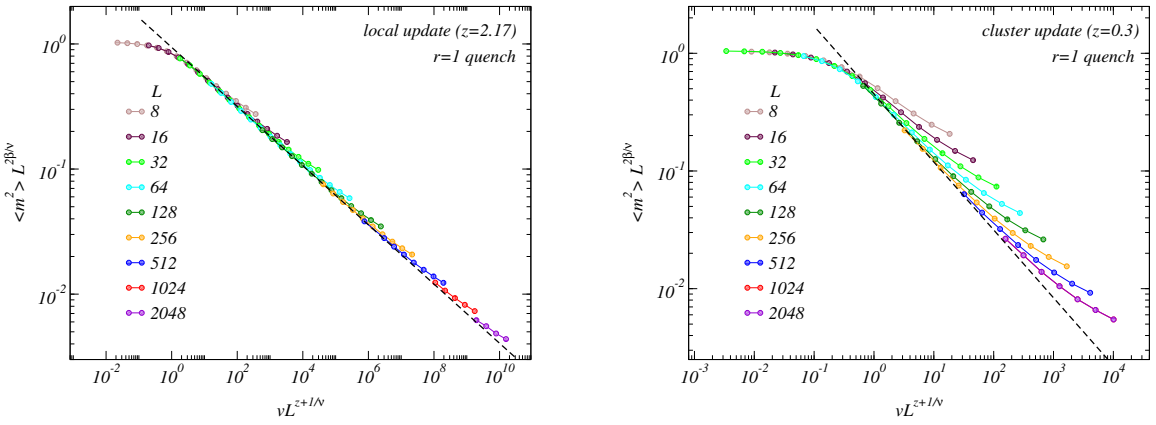

(a) (b)

Figure 4.5: Critical quench on the 1D TFIM with simulation-time quantum annealing in a linear quench protocol $s : 0 \to s_c$ implemented with local updates (a) and cluster updates (b), respectively. At the QCP $s_c = 1/2$, the scaling collapse of the form Eq. (4.6) allows one to carry out a fitting procedure to determine the value of the dynamic exponent z. Here $z \approx 2.17$ for the local update, which is the same as the Metropolis dynamic as in the 2D classical Ising model [17], and $z \approx 0.3$ for the global update, the same as the Swendsen-Wang/Wolff dynamics as in the 2D classical Ising model [17]. The dashed lines in both figures indicate the power-law behavior with the power x predicted by Eq. (4.8). One issue that should be highlighted here is that, the TFIM is known to have dynamic exponent $z = 1$ of Hamiltonian dynamics [6], however, simulation-time quantum annealing fails to reproduce this result. Instead, depending on the dynamics employed (local update or cluster update), it renders either Metropolis dynamics with $z = 2.17$ or Swendsen-Wang/Wolff dynamics with $z = 0.3$. In either case, simulation-time quantum annealing falls into exactly the classical scenario.

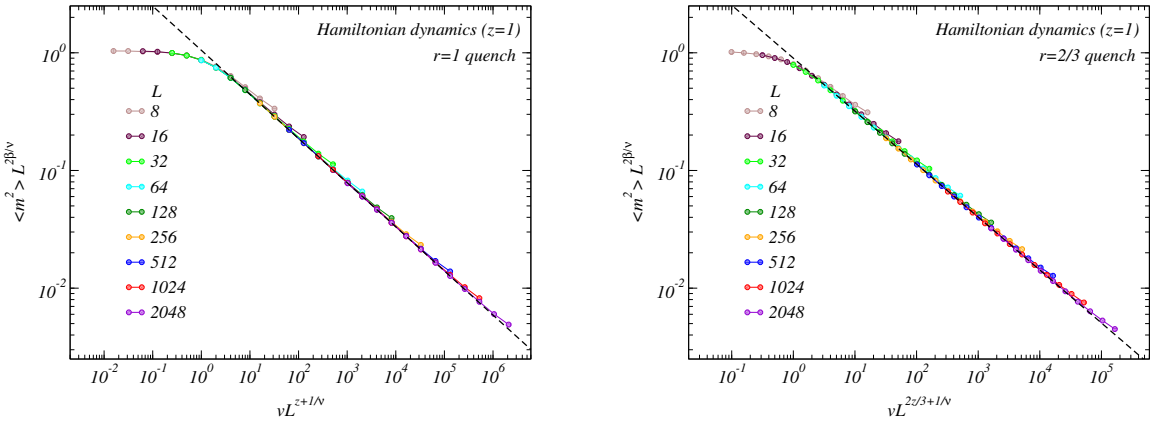

(a) (b)

Figure 4.6: Critical quench on 1D TFIM with imaginary-time quantum annealing of s : $0 \to s_c$ implemented with $r = 1$ linear quench protocol (a) and $r = 2/3$ non-linear quench protocol (b). Cluster updates are used for both scenarios. A fitting procedure for the scaling collapse of Eq. (4.6) can be carried out to determine the value of the dynamic exponent z. For both $r = 1$ and $r = 2/3$ quenches, $z = 1$ is obtained. The dashed line in both panels indicate the power-law behavior with the power x predicted by Eq. (4.8). The upshot is that, as opposed to simulation-time annealing that falls into classical scenarios, imaginary-time annealing successfully generates Hamiltonian dynamics and is robust to different quench protocols.

in the previous section, imaginary-time annealing carries out quench in the imaginary-time direction, as illustrated in Fig. 4.2 (b). Therefore M plays the role of the total quench time τ in Eq. (4.5). We perform imaginary-time annealing with linear quench $r = 1$ and non-linear quench $r = 2/3$, respectively, to QCP s_c. The scaling collapse of Eq. (4.6) is expected to hold and is shown in Fig. 4.6. Once again, given the scaling form, one can carry out the same fitting procedure discussed in Ref. [17] to determine the dynamic exponent z. Panel (a) of Fig. 4.6 shows the scaling collapse for the $r = 1$ linear quench protocol, which gives $z = 1$, exactly the Hamiltonian dynamics for the TFIM. Panel (b) of Fig. 4.6 shows the scaling collapse for the $r = 2/3$ non-linear quench protocol, which also yields $z = 1$. This result has drawn a clear distinction between simulation-time quantum annealing and imaginary-time quantum annealing: the former only corresponds to the stochastic dynamics of the simulation (updating) algorithm, while the latter successfully renders Hamiltonian dynamics and is robust to various quench protocols and details of the QMC updates, i.e., local and cluster updates give the same z as the Hamiltonian dynamics does not depend on the QMC method used.

Chapter 5

Non-equilibrium quench on classical and quantum 3-regular ferromagnetic random graphs

5.1 Introduction

The non-equilibrium quench (NEQ) method for studying continuous transitions has been thoroughly demonstrated on Ising model in terms of both classical (thermal) transition [17] and (zero-temperature) quantum phase transition [33, 37] in the preceding chapters. To further extend the applicability of the NEQ approach, in this Chapter we apply this method to a 3-regular random graph with ferromagnetic (FM) interactions, which is a disordered system but still shows ferromagnetic order at low-temperature [85]. In this system, each spin is individually interacting with three other spins through the FM interactions. A typical 3-regular random graph is depicted in Fig. 5.1. The randomness comes from the fact that for a given number of spins (vertices) N, there will be numerous ways of arranging the vertices such that they have different connectivities that are unable to transform from one to another simply by relabeling the vertex numbers, i.e., the graphs are not isomorphic. An efficient algorithm called Steger-Wormald algorithm [86] is used to generate the realizations of 3-regular graphs. Below, we will use $\langle \dots \rangle$ to denote a standard statistical average and $[\dots]$ for the average over realizations.

Despite the disorderedness, one can still expect an Ising-like ordered state at low temperature due to the ferromagnetic interaction. In fact, the 3-regular random graph can be though of as a special case of "scale-free" network in which the connectivities of the nodes have a power-law distribution. The scale-free network has been investigated in detail and

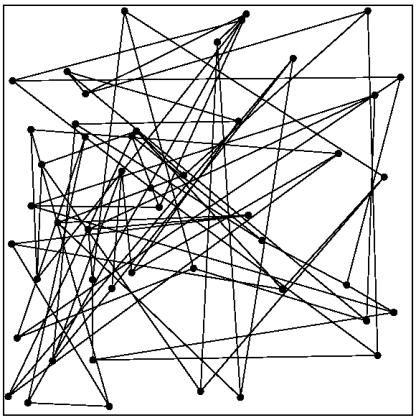

Figure 5.1: A typical 3-regular random graph in which each spin is individually interacting with three other spins.

show continuous transition in some ranges of the power [85].

The rest of this Chapter is organized in the following way: In Sec. 5.2, we describe the quench protocols and dynamic finite-size scaling underlying the NEQ approach. In Sec. 5.3, we apply the NEQ approach to study the thermal transition of the 3-regular FM random graphs. In Sec. 5.4, we study the zero-temperature quantum phase transition of the same system in the framework of imaginary-time quantum quench.

5.2 Quench protocols and Dynamic finite-size scaling

The basic idea of NEQ is to approach the transition λ_c [1] through some quench protocol that can be formulated as:

$$\begin{aligned} \lambda(t) &= \lambda_c + v(\tau - t)^r, \\ v &= (\lambda(0) - \lambda_c)/\tau^r, \end{aligned} \tag{5.1}$$

[1] λ plays the role of the source of fluctuation. In thermal transition, λ corresponds to the temperature T and in quantum phase transition corresponds to the tuning parameter of the Hamiltonian.

where τ is the total quench time, v a generalized velocity whose physical interpretation depends on the quench protocol, and $r \in \mathbb{R}$ is the parameter controlling the quench protocol, for example, $r = 0$ generates a sudden quench with quench amplitude v, $r = 1$ corresponds to a linear quench with constant velocity v, $r = 2$ stands for a quadratic quench with constant acceleration v, etc. For continuous transitions, the correlation length $\xi_\lambda \sim \varepsilon^{-\nu}$ and relaxation time $\tau_{\text{rel}} \sim \xi_\lambda^z$ diverge at λ_c, where $\varepsilon \equiv |\lambda - \lambda_c|/\lambda_c$ is the reduced distance from the critical point, ν the correlation length exponent and z the dynamic exponent. The divergence of ξ_λ and τ_{rel} result in the critical slowing down phenomenon [8]. To incorporate these critical phenomena, the quench velocity should scale as:

$$v_c(N) \sim L^{-(zr+1/\nu)} \sim N^{-(z'r+1/\nu')} \tag{5.2}$$

in order to be in the quasi-adiabatic regime [14, 15, 17, 33, 37]. In the above expression, we normalize the exponents by the dimensionality d: $z' \equiv z/d$ and $\nu' \equiv \nu d$, since in the random graph system the linear size L is not well-defined.

When approaching the critical point λ_c through the above protocol, a dual-scaling behavior for the order parameter m_z^2, the z-component magnetization squared, as a function of the quench velocity v is expected [17]:

$$\langle m_z^2 \rangle = \begin{cases} N^{-2\beta/\nu'} f_1(vN^{z'r+1/\nu'}), & v \lesssim v_c(N) \\ N^{-1} \left(\frac{1}{v}\right)^x, & v_c(N) \ll v \ll 1 \\ N^{-1} f_2(1/v), & v \gtrsim 1. \end{cases} \tag{5.3}$$

The first scaling function f_1 governs the low-velocity regime, and the second scaling function f_2 describes the high-velocity regime. The intermediate velocity regime $v_c(N) \ll v \ll 1$ is where both functions are applicable and reduce to a pure power-law behavior. Moreover, the power x of the power-law is closely related to the critical exponents:

$$x = \frac{d - 2\beta/\nu}{zr + 1/\nu} = \frac{1 - 2\beta/\nu'}{z'r + 1/\nu'}. \tag{5.4}$$

As discussed in Ref. [17], given two different quench protocols r_1 and r_2 and their corresponding powers x_1 and x_2, one can obtain:

$$z'\nu' = \frac{x_2 - x_1}{r_1 x_1 - r_2 x_2}. \tag{5.5}$$

This expression combined with the optimization result from the scaling collapse of Eq. (5.3) allows us to disentangle all exponents z', ν', and β, as we will demonstrate in the following sections.

5.3 Classical quench on 3-regular ferromagnetic random graphs

In this section, we study the thermal transition of the 3-regular ferromagnetic random graphs. The Hamiltonian is the same as the Ising model:

$$\mathcal{H} = -J \sum_{\langle i,j \rangle} \sigma_i \sigma_j, \tag{5.6}$$

where $J > 0$ is homogeneous. At high temperature, thermal fluctuation destroys the order of the system. However, due to the ferromagnetic interaction, one can expect to see a non-zero magnetization at low temperature. Since the system is Ising-like, we can expect a continuous transition.

5.3.1 Locating the transition temperature T_c

In the framework of equilibrium phase transition, one can use the crossings of the finite-size Binder cumulant [62] to locate the transition temperature T_c:

$$U(N,T) = \frac{3}{2}\Big(1 - \frac{1}{3}\frac{\big[\langle m^4 \rangle\big]}{\big[\langle m^2 \rangle\big]^2}\Big). \tag{5.7}$$

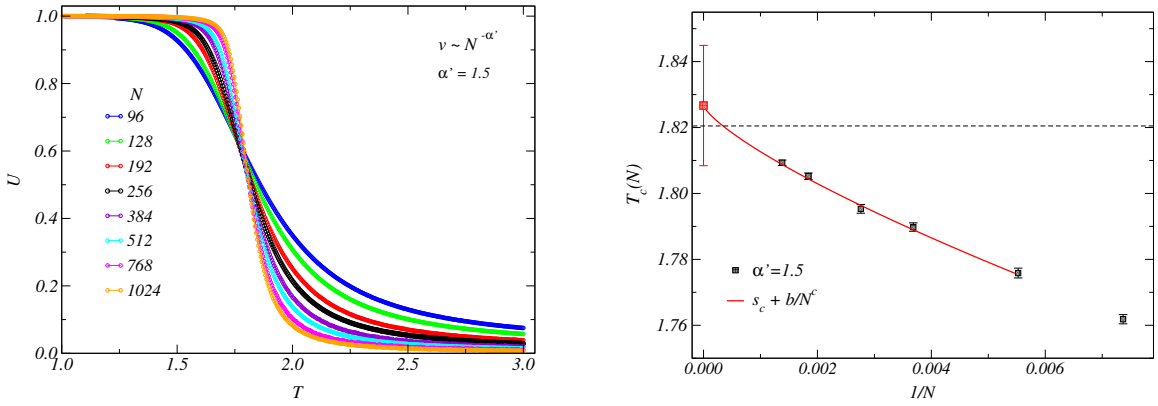

(a) (b)

Figure 5.2: (a) Some typical Binder cumulants calculated using different system sizes with a linear quench from an initial temperature $T_i = 3.0$ to a final temperature $T_f = 1.0$ with the quench velocity $v = 2.0/\tau$ scaling as $v \sim N^{-\alpha'}$, here with $\alpha' = 1.5$. (b) The crossings of the Binder cumulants from panel (a). The crossing points are expected to show power-law behavior, which can be described by $T_c(N) = a + b/N^c$. The intercept a corresponds to the transition temperature in the thermodynamic limit T_c. We obtain $a = 1.827 \pm 0.018$, $b = -2.67 \pm 0.96$, and $c = 0.76 \pm 0.18$. This implies $T_c \approx 1.83(2)$, in good agreement with the analytic solution [85] that yields $T_c = 2/\ln 3$, which is marked by the dashed horizontal line in the figure.

Notice that the realization averages are taken first before the construction of the Binder cumulant. In the non-equilibrium scenario with a quench velocity v, one can expect the following scaling around the transition:

$$U(v, N, T) = f\big((T - T_c)N^{1/\nu'}, vN^{z'+1/\nu'}\big). \tag{5.8}$$

If one can scale the velocity $v \sim N^{-\alpha'}$ such that $\alpha' > z' + 1/\nu'$, the second argument in the above equation vanishes in the thermodynamic limit. Therefore the same procedure of extracting Binder crossings used in the equilibrium scenario can be applied here. Fig. 5.2 illustrates this procedure.

In Fig. 5.2, $\alpha' = 1.5$ is used to scale the velocity (the value can be justified posterior to the simulations). For all the sizes considered, we use the value of α' to scale the velocity $v \sim N^{-\alpha'}$. Some typical curves of the Binder cumulants are shown in Fig. 5.2 (a). The finite-size effect causes the shift of the crossings of the cumulants, these crossings can then be fitted by a power-law form [7], since the order parameter and the physical quantities constructed through it scale as a power-law at the transition:

$$T_c(N) = a + b/N^c,$$

where a corresponds to the transition temperature in the thermodynamic limit as $N \to \infty$. As shown in Fig. 5.2, the extrapolation of the crossing points give $T_c \approx 1.83(2)$. This is in good agreement with the analytic result for the T_c of the scale-free network [85].

5.3.2 Critical quenches to T_c

Given the known transition temperature, one can perform critical quenches to T_c and expect the scaling behavior Eq. (5.3) [2]. Here we start from an initial temperature $T_i = 1.5T_c$ and quench to $T_f = T_c$ with the protocols Eq. (5.1) of $r = 1$ and $r = 2/3$, respectively. The rescaled order parameter $\langle m^2 \rangle N^{2\beta/\nu'}$ versus the rescaled velocity $vN^{z'r+1/\nu'}$ is shown in Fig. 5.3.

On both panels of Fig. 5.3, one can clearly see a power-law behavior in the middle region, and a plateau on the left corresponding to the quasi-adiabatic limit. One can perform a 2-parameter fitting to determine the values of $z'r + 1/\nu'$ and β/ν' that yield the optimized scaling collapse, with the optimization quantified by χ^2 per degree of freedom (dof). The numerical results also implies the power of the power-law.

For $r = 1$ quench, we obtain $z' + 1/\nu' = 1.09(2)$, and $\beta/\nu' = 0.243(3)$ with $\chi^2/\text{dof} = 0.80$, which implies $x_1 \approx 0.472(11)$. For $r = 2/3$ quench, we obtain $2z'/3 + 1/\nu' = 0.90(2)$,

[2] In this Chapter, we will only focus on the first scaling function f_1.

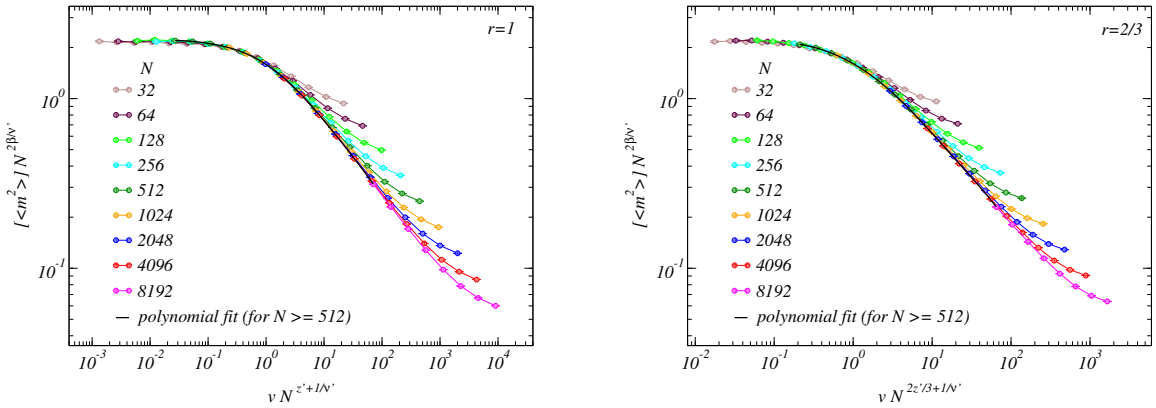

(a) (b)

Figure 5.3: Critical quenches to $T_c = 2/\ln 3$ with $r = 1$ (linear quenches) (a) and $r = 2/3$ (non-linear quenches) (b), respectively. A 2-parameter fitting is carried out to find the optimized parameters $p_1 = z'r + 1/\nu'$ and $p_2 = \beta/\nu'$ that yield the best scaling collapse for the f_1 function. For the $r = 1$ quench, we obtain $z' + 1/\nu' = 1.09(2)$, and $\beta/\nu' = 0.243(3)$ with $\chi^2/\text{dof} = 0.80$. For $r = 2/3$ quench, we obtain $2z'/3 + 1/\nu' = 0.90(2)$, and $\beta/\nu' = 0.246(4)$ with $\chi^2/\text{dof} = 1.05$. Notice that in both panels, the tails corresponding to the high-velocity quenches are not included in the fitting.

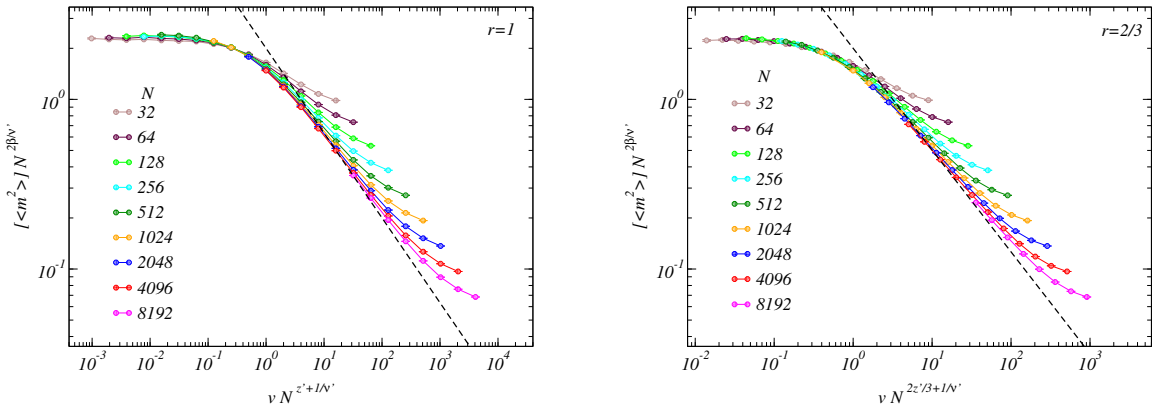

(a) (b)

Figure 5.4: f_1 scaling collapse for the $r = 1$ linear quench (a) and $r = 2/3$ non-linear quench (b). Here the mean-field exponents $z' = 1/2$, $\nu' = 2$, and $\beta = 1/2$ are used directly. The dashed lines on both panels indicate the expected power of the power-law, given Eq. (5.4).

and $\beta/\nu' = 0.246(4)$ with $\chi^2/\text{dof} = 1.05$, which implies $x_{2/3} \approx 0.564(14)$. The numerical result for $z' + 1/\nu' \approx 1$ also justifies the choice of α' in the extraction of T_c. Since the choice of $\alpha' = 1.5 > z' + 1/\nu'$, the quench will converge to the quasi-adiabatic limit in the thermodynamic limit. It should be noted that the same power x can be obtained by analyzing another scaling function f_2, which will yield the same result quoted above. Combining all the fit results, the exponents can be extracted as follows:

$$\begin{cases} z' + 1/\nu' &= 1.09(2), \\ 2z'/3 + 1/\nu' &= 0.90(2), \\ \beta/\nu' &= 0.245(5), \end{cases} \Rightarrow \begin{cases} z' &= 0.57(9), \\ \nu' &= 1.92(3), \\ \beta &= 0.47(1). \end{cases} \tag{5.9}$$

Since the 3-regular random FM graph is reminiscent of the mean-filed Ising model, one would expect to see mean-field exponents: $z = 2$, $\nu = 1/2$, $\beta = 1/2$, at the upper critical dimension $d_u = 4$, which translate to $z' = 1/2$ and $\nu' = 2$. It can be argued that the numerical results obtained in Eq. (5.9) still have some finite-size effects which lead to deviations of 2-3 error bars from the true exponents in the case of ν' and β. If one uses the mean-filed exponents to rescale the data, as shown in Fig. (5.4), a clear scaling collapse can be observed.

5.4 Quantum quench on 3-regular ferromagnetic random graphs

In this section we study the zero-temperature ($T = 0$) quantum phase transition of the 3-regular random FM graphs. The Hamiltonian can be written as

$$\mathcal{H}(s) = -s \sum_{\langle i,j \rangle} \sigma_i^z \sigma_j^z - (1-s) \sum_i \sigma_i^x. \tag{5.10}$$

The transition is expected to take place when the parameter s is tuned from $s : 0 \to s_f$.

A clear distinction between the simulation-time quantum annealing and imaginary-time

quantum annealing has been made in Ch. 4, here we will focus on the latter, which allows to study Hamiltonian dynamics. We will use quasi-adiabatic quantum Monte Carlo (QAQMC) algorithm [37] to perform the quench in imaginary-time. The algorithm applies a series of operators (product evolution) on a trial state $|\Psi_0\rangle$:

$$\begin{aligned} |\Psi_{s_f}\rangle &= \big[-\mathcal{H}(s_{_M})\big]\ldots\big[-\mathcal{H}(s_1)\big]|\Psi_0\rangle \\ &= \sum_{[i_M,\ldots,i_1]} H_{i_M}(s_{_M})\ldots H_{i_1}(s_1)|\Psi_0\rangle \end{aligned} \tag{5.11}$$

where $|\Psi_0\rangle$ corresponds to an equal superposition state:

$$|\Psi_0\rangle = \prod_i \frac{|\uparrow\rangle_i + |\downarrow\rangle_i}{\sqrt{2}}. \tag{5.12}$$

The quantum Monte Carlo importance sampling with cluster update [7, 11–13] provides an efficient way to stochastically sample the operator product in Eq. (5.11). The length of the operator product, M, plays the role of total quench time τ in QAQMC scheme. In Ref. [37], it has been shown that the length of the operator product should scale as the total number of spins, i.e., $M \propto N$. The quench protocol for the Hamiltonian Eq. (5.10) with $s : 0 \to s_f$ can then be defined as :

$$\begin{aligned} s(t) &= s_c - \frac{s_c}{M^r}(M-t)^r, \\ v &= s_c/\tilde{M}^r, \end{aligned} \tag{5.13}$$

where $\tilde{M} = M/N$ is the normalized length of the operator product.

5.4.1 Locating the quantum critical point s_c

Despite the exact solution for the classical 3-regular FM graphs [85], to our knowledge there is no counterpart in the $T = 0$ quantum system. In this subsection, we treat all critical exponents as unknown and perform the same technique used in Sec. 5.3 to extract the

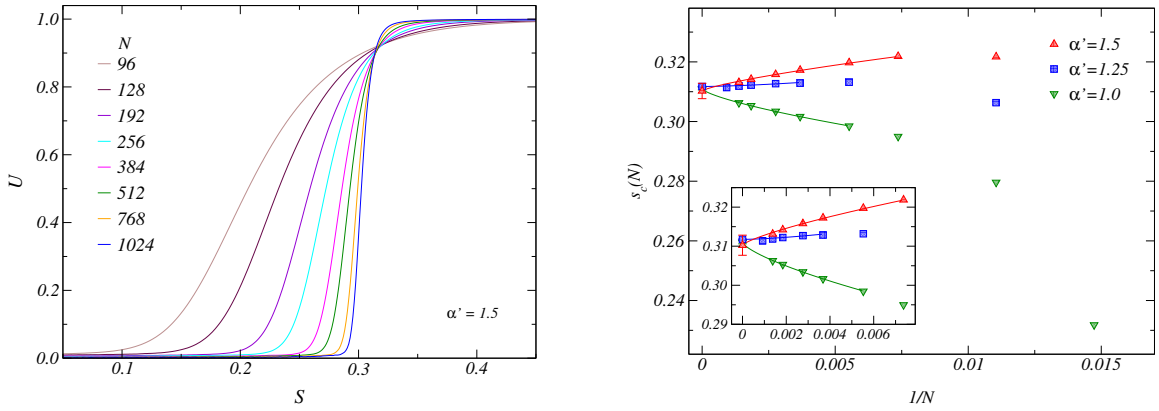

(a) (b)

Figure 5.5: (a) Examples of Binder cumulants from different system sizes with linear quench $s : 0 \to 0.6$. All the curves from different sizes satisfy the same scaling $v \sim N^{-\alpha'}$, with α chosen to be 1.5. (b) The crossings of the Binder cumulants from $\alpha' = 1.0$, $\alpha' = 1.25$, and α'=1.5, respectively. The crossing points are expected to show power-law behavior as described in Eq. (5.15). The extrapolations of the crossing points yield $s_c = 0.3110(4)$ for $\alpha' = 1.0$, $s_c = 0.3117(1)$ for $\alpha' = 1.25$, and $s_c = 0.310(2)$ for $\alpha' = 1.5$. All the extrapolations give consistent results. The inset shows a more focused window in the region $1/N \to 0$.

quantum critical point (QCP) of the Hamiltonian Eq. (5.10) and the relevant exponents associated with the transition.

With the quench protocol Eq. (5.13), we scale the velocity as $v \sim N^{-\alpha'}$. As $\alpha' > z' + 1/\nu'$, the quench scenario will be quasi-adiabatic in the thermodynamic limit, therefore one can again use the Binder cumulant defined below to locate the QCP:

$$U = \frac{3}{2}\Big(1 - \frac{1}{3}\Big[\frac{\langle m^4\rangle}{\langle m^2\rangle^2}\Big]\Big). \tag{5.14}$$

Here the realization average $[\dots]$ is taken after the ratio $\langle m^4\rangle/\langle m^2\rangle^2$ is computed for each realization [87].

Here we perform linear quenches for $s : 0 \to 0.6$ with three different choices of α', $\alpha' =$

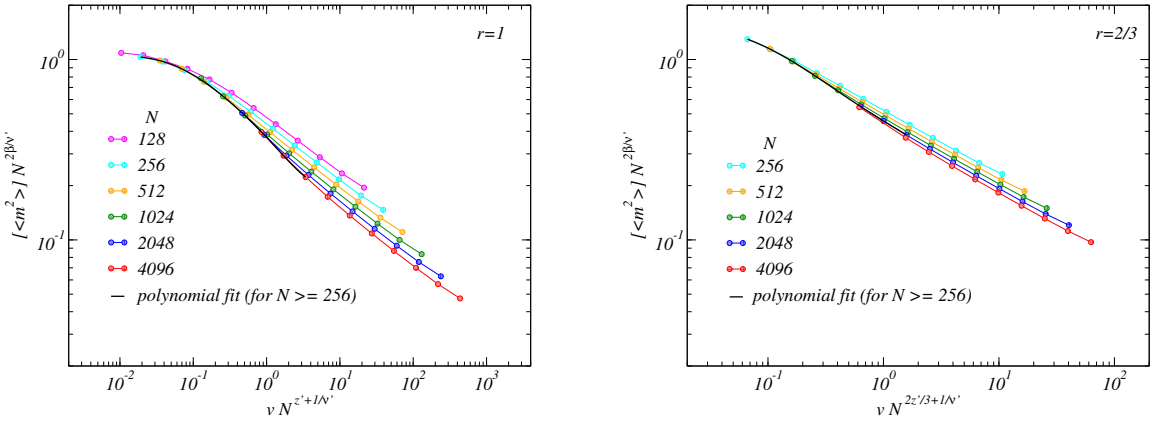

(a) (b)

Figure 5.6: Critical quenches to the QCP, $s_c = 0.311$, and the resulting f_1 scaling collapse for the $r = 1$ linear quench (a) and $r = 2/3$ non-linear quench (b), respectively. The exponents can be extracted as discussed in the text. In both $r = 1$ and $r = 2/3$ quenches, only sizes $N \geq 256$ are included in the fitting.

$1.0, 1.25$ and $\alpha' = 1.5$, respectively. The values of α' can later be examined by a consistency check. Since the order parameter $\langle m^2 \rangle$ will show power-law behavior at the transition s_c, the Binder cumulant, which is constructed through the order parameter, is expected to show the same behavior. Therefore the crossing points can be fitted by a power-law form [7]:

$$s_c(N) = s_c + b/N^c. \tag{5.15}$$

The extrapolations of the Binder crossings are illustrated in Fig. 5.5. All the choices of α' extrapolated to consistent values corresponding to a QCP $s_c \approx 0.311$.

5.4.2 Critical quenches to the QCP s_c

Once the QCP has been extrapolated, one can perform critical quenches to s_c with the protocol described in Eq. (5.13) and expect the scaling behavior Eq. (5.3). Here we perform two different quench protocols, $r = 1$ and $r = 2/3$, respectively. For $r = 1$, the scaling

collapse shown on Fig. 5.6 (a) for the f_1 scaling results in $z' + 1/\nu' = 0.87(2)$ and $\beta/\nu' = 0.296(4)$. For $r = 2/3$, another scaling collapse for the f_1 scaling shown on Fig. 5.6 (b) yields $2z'/3 + 1/\nu' = 0.64(8)$ and $\beta/\nu' = 0.34(1)$. It can be seen that β/ν' shows a finite difference between the $r = 1$ quench and $r = 2/3$ quench, due to finite-size effect. A similar behavior was also observed in Fig. 1.4, in which quantum FM model would show a strong finite-size effect.

Chapter 6

Non-equilibrium quench on classical and quantum 3-regular anti-ferromagnetic random graphs

6.1 Introduction

The spin-glass transition has been an important topic in the development of statistical physics, not only because of its diverse and complex phases, but also its applications in different areas such as biology, networks, and combinatorial optimizations. Extensive works have been done during the past few decades, [23] but still many challenges are yet to be overcome, e.g, a more efficient simulation method that could alleviate the critical slowing-down. Currently there are only two types of exactly solvable spin-glass models, both are under mean-field description. The first type is the Sherrington-Kirkpatrick model which considers fully connected interactions. [24] The second type, which employs the cavity method with replica symmetry breaking (RSB) [1, 25], is antiferromagnetic Potts model on a random graph with finite connectivity. [28, 29] The latter has attracted more attention in the past decade due to its relationship to algorithm design and NP problems (NP stands for non-deterministic polynomial time) in information science. [30] Since theoretical works are subject to limited cases, numerical simulations, especially unbiased Monte Carlo simulations, have been a major tools to investigate spin-glass systems.

As discussed in the previous chapters, a non-equilibrium approach in the framework of Monte Carlo (MC) simulations and generalized dynamic finite-size scaling have been developed for studying thermal phase transitions. [17] In this framework, the transition temperature is approached through a non-equilibrium quench process, formally known as the

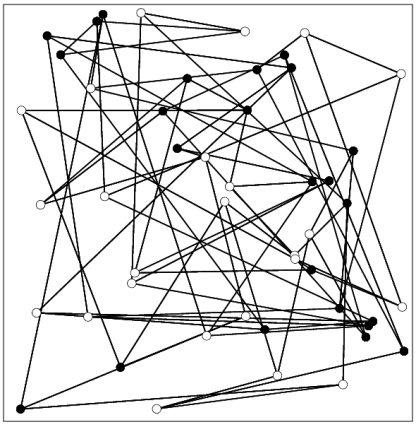

Figure 6.1: A typical example of 3-regular graph with 48 spins. "3-regular" stands for the fact that every spin is connecting to three other spins through the antiferromagnetic interactions. Although the interaction strength is isotropic, however, due to loops of odd number of edges, the system is geometrically frustrated. The graph is generated using the efficient Steger-Wormald algorithm. [86]

Kibble-Zurek mechanism (KZ). [14–16, 38] It has been realized that this approach is especially suitable for studying spin-glass transitions since the quench velocity is a quantity one can control, as opposed to the traditional equilibrium approach that suffers seriously from the divergence of the relaxation time and the critical slowing-down. The same framework was also established in terms of quantum phase transition [33, 37, 38] approached through KZ. In the quantum case, it has been demonstrated [37] that one can extract quantum critical point to high numerical precision even when the critical exponents are not known prior to the simulation, this advantage has been demonstrated in this chapter to be valuable when exploring the spin-glass systems.

In this chapter, we apply the non-equilibrium approach to investigate both classical and quantum spin-glass transitions. We explicitly use antiferromagnetic Ising model on 3-regular random graph as our benchmark system, since it is highly frustrated and shows spin-glass phase below some finite temperature $T_g > 0$ while remarkably can be exactly solved in the classical case using RSB. [28, 29] A typical example of 3-regular graph with $N = 48$ is illus-

trated in Fig. 6.1. The randomness comes into play when generating the realizations. Since for a given number of spins (vertices), there are many realizations that are not isomorphic, namely, for two realizations one can not transform one graph to the other graph by simply relabeling the vertex numbers, an efficient algorithm called Steger-Wormald [86] is used to generate the underlying graphs. This model is also interesting in terms of quantum case, because of its connections to the Max Cut problem in graph theory and the complexity of the Quantum Adiabatic Algorithm (QAA) for quantum computing [30]. Finding a Max Cut of the graph is equivalent to finding the maximum number of satisfying boolean constraints, or in the language of physics a ground state configuration of the given Hamiltonian. However, in previous studies not so much has been addressed in the context of KZ, therefore we provide another perspective for the class of problems that have been studied by the QAA.

The rest of the chapter is organized in the following way: In Sec. 6.2 we summarize the major results from Refs. [17,37] about the dynamic finite-size scaling around the transition. In Sec. 6.3 we demonstrate the non-equilibrium approach of quenching temperature to the transition point of the 3-regular random graph, through this process we show scaling behaviors around the transition and extract critical exponents. In Sec. 6.4 we apply *quasi-adiabatic quantum Monte Carlo* algorithm [37] to achieve quantum quench for the same model and extract quantum critical point for the spin-glass transition, then we also show scaling behaviors around the transition and estimate critical exponents. In Sec. 6.5 we summarize our main result and discuss possible applications.

6.2 Dynamic finite-size scaling

We consider a system with Hamiltonian $\mathcal{H}$ and a parameter λ that characterizes the continuous transition. For a classical system, λ is the temperature; for a quantum system at zero temperature, λ is the tuning parameter of the Hamiltonian. The initial value of λ sets the initial state of the system that is either easy or trivial to prepare. We are interested in

the behavior of the system when λ is tuned according to some power-law protocol from an initial value to its critical value λ_c that corresponds to the transition of the system: [18]

$$\lambda(t) = \lambda_c + v(\tau - t)^r, \tag{6.1}$$

where τ is the total time period during this process and v is interpreted as amplitude for sudden quench ($r = 0$), velocity for linear quench ($r = 1$), acceleration for quadratic quench ($r = 2$), etc. When the transition point λ_c is approached, the relaxation time will diverge as $\tau_{\text{rel}} \sim \xi_\lambda^z \sim \varepsilon^{-z\nu}$, where ξ_λ is the correlation length, ν the correlation length exponent, z the dynamic exponent, and $\varepsilon = |\lambda - \lambda_c|/\lambda_c$ the reduced distance from the critical point. When the system is tuned into the regime in which τ_{rel} grows exponentially, the system effectively enters into a "freeze-out" period since the fast-growing relaxation time prevents the system from relaxing back to the equilibrium state. In addition, the velocity also comes into play in the non-equilibrium scenario: When the velocity is low, the process is nearly equilibrium, or quasi-adiabatic, and the response of the system can be described by the adiabatic perturbation theory. [16] On the other hand, when the quench velocity is high, the excitation defects lead to the breakdown of the adiabaticity. Obviously, the survival of the adiabaticity depends on the interplay between two time scales: the quench time and the relaxation time. It was first qualitatively purposed by Kibble and Zurek [14, 15] that the time to reach the critical point should scale as the relaxation time in order to keep adiabaticity, this mechanism was initially purposed to explain defect formations in cosmology and classical phase transitions. Later the same has been applied to quantum phase transition. [38] For a review, see Refs. [16,67]. Interestingly, the classical counterpart has not been rigorously discussed until recently. [17, 32]

As illustrated in Fig 6.1, we are discussing a system which does not have a well-defined length scale. We than use the following conventions to characterize the finite-size scaling: $N = L^d$ is the system size, where L is the effective linear size and d is the dimension of the system defined with finite dimension. The define the normalized dynamic exponent

$z' = z/d$, and the normalized domain size exponent $\nu' = \nu d$.

From the original qualitative argument of KZ, [14, 15] KZ for quantum phase transitions [18, 38, 67], or rigorous derivation for classical phase transitions [17, 32], one obtains that there is a size-dependent characteristic velocity threshold $v_c(N)$ which characterizes the cross-over behavior between the quasi-adiabatic and non-adiabatic regimes

$$v_c(N) \sim L^{-(zr+1/\nu)} \sim N^{-(z'r+1/\nu')}, \tag{6.2}$$

where the physical interpretation of $v_c(N)$ depends on the quench protocol as we discussed above. Alternatively, Eq. (6.2) also implies a characteristic domain size $\mathcal{V}_v$ associated with a given v:

$$\mathcal{V}_v \sim \xi_v^d \sim v^{-\frac{1}{z'r+1/\nu'}}, \tag{6.3}$$

which implies that a fast quench that introduces a high density of excitation defects will result in a small domain size. Or, equivalently, a small-r quench also result in a similar behavior. More importantly, the characteristic threshold Eq. (6.2) implies a generalization of the finite-size scaling ansatz for a physical quantity A: [17, 33, 37]

$$\begin{aligned} A(N, \lambda, v) &= L^{\kappa/\nu} \tilde{F}(L/\xi_\lambda, v/v_c) \\ &= N^{\kappa/\nu'} F[(\lambda - \lambda_c) N^{1/\nu'}, v N^{z'r+1/\nu'}], \end{aligned} \tag{6.4}$$

where κ is the exponent that describes how the quantity A grows in terms of the power-law in the reduced distance from λ_c, and F is an universal function for a given quantity A. We also use the Edwards-Anderson (EA) order parameter [22] to capture the spin-glass transition when approaching λ_c:

$$q = \frac{1}{N}\sum_{i=1}^{N}\sigma_i^{(1)}\sigma_i^{(2)}, \tag{6.5}$$

where $\sigma^{(1)}$ and $\sigma^{(2)}$ are spin configurations from two independent simulations, or two independent "replica" for a given realization. Exactly at the transition λ_c, the expression Eq. (6.4) for the order parameter can be written as:

$$\big[\langle q^2\rangle\big] = N^{-2\beta/\nu'} F(vN^{z'r+1/\nu'}), \tag{6.6}$$

where $\langle \dots \rangle$ stands for the ensemble average for a given realization and $[\dots]$ stands for the averages over realizations.

In recent study [17], it has been shown that at λ_c the order parameter shows a dual scaling behavior described by two scaling functions f_1 and f_2:

$$\big[\langle q^2\rangle\big] = \begin{cases} N^{-2\beta/\nu'} f_1\big(vN^{z'r+1/\nu'}\big), & v < v_c(N) \\ N^{-1}v^{-x}, & v_c(N) < v < 1 \\ N^{-1} f_2(v^{-1}), & v \gtrsim 1 \end{cases} \tag{6.7}$$

Here the first scaling function f_1 is applicable from $v = 0$ up to a size-independent cut-off which is of order $O(1)$. The second scaling function f_2 applies from $v = \infty$ down to the size-dependent lower bound $v_c(L)$ Eq. (6.2). The middle region $v_c(N) < v < 1$ is where both functions apply. Following the same terminology established in Ref. [17], we will call the regime $v < v_c(N)$ quasi-adiabatic regime, $v_c(N) < v < 1$ the power-law regime, and $v \gtrsim 1$ diabatic regime. Physically speaking, f_1 describes the quasi-adiabatic regime where v is perturbatively small compared to $v_c(N)$ and the regime in which perturbation breaks down such that the behavior turns to a power-law; on the other hand, f_2 describes the diabatic regime where $1/v$ is perturbatively small and $\mathcal{V}_v$ is of the order of 1 lattice space and the regime where $\mathcal{V}_v$ begins to grow while still much smaller than the system size. In Ref. [17], it is also shown that the middle region, the power-law regime, is of great interest

since it corresponds to the regime in which both perturbation in v and $1/v$ break down and f_1 and f_2 overlap and smoothly connect to each other through the power-law. This universal power-law regime is also important in the sense that in this regime the domain size, $\mathcal{V}_v$ of Eq. (6.3), is growing when v is decreasing, while the size is still much smaller than the system size: $\mathcal{V}_v \ll N$. More importantly, the power x governing the power-law contains the information of the critical exponent:

$$x = \frac{1 - 2\beta/\nu'}{z'r + 1/\nu'}. \tag{6.8}$$

As demonstrated in Ref. [17], the f_2 scaling function and Eq. (6.8) combined has an interesting application: by performing two different quenches characterized by two parameters r_1 and r_2, respectively, one can compute the following by measuring the associated powers x_{r_1} and x_{r_2}:

$$\begin{aligned} z'\nu' &= \frac{x_{r_2} - x_{r_1}}{r_1 x_{r_1} - r_2 x_{r_2}}, \\ \nu' - 2\beta &= \frac{(r_2 - r_1) x_{r_1} x_{r_2}}{r_2 x_{r_2} - r_1 x_{r_1}}. \end{aligned} \tag{6.9}$$

The above expressions along with the knowledge from f_1 scaling function of a given quench (either r_1 or r_2) allows one to independently extract all exponents z', ν', and β, as we will demonstrate in Sec. 6.4.

The dynamic finite-size scaling Eq. (6.4) has been studied extensively in ferromagnetic systems, such as classical Ising model [17] as well as quantum Ising model in imaginary time, [33, 37] however, to our knowledge, it has not been investigated in either classical or quantum spin-glass transition. Therefore, in this chapter we extend this framework to the studies of spin-glass transitions.

6.3 Thermal spin-glass transition

In this section we demonstrate the applications of the dynamic finite-size scaling under the framework of non-equilibrium quenches. The Hamiltonian of the antiferromagnetic Ising model on 3-regular random graph can be written as

$$\mathcal{H} = J \sum_{\langle i,j \rangle} \sigma_i \sigma_j, \tag{6.10}$$

where $J > 0$, $\sigma_i = \pm 1$, and $\langle i, j \rangle$ stands for nearest-neighbor spin pairs. A typical example of the 3-regular graph has been illustrated in Fig. 6.1. The presence if odd-length loops in the system results in frustration and highly degenerate ground states. Remarkable, using RSB, when the temperature T is higher than the spin-glass transition T_c, the loops can be ignored since the lengths are typically of order $O(\ln(N))$, therefore it has been argued that a mea-field description can be used to describe the system before the RSB local instability sets in when $T < T_c$, where $T_c/J = -2/\ln(1 - 2/(1 + \sqrt{2}))$ [28, 29]. In the case of thermal transition, the parameter λ discussed in Sec. 6.2 corresponds to the temperature T.

The simulation scheme is as following: For each realization we do equilibration at the initial temperature $T_i = 1.5T_c$, and then quench the system to the final temperature $T_f = T_c$ with different protocols Eq. (6.1). One unit of time is defined as one Monte Carlo step in which N attempts of single spin-flip are performed according to the Metropolis algorithm [42]. Some typical examples of linear quenches are shown in Fig. 6.2. We use 64-bit multi-spin coding, which allows us to do average over 64 independent runs for a given simulation. Since the system has a spin-glass phase when $T \leq T_c$, we expect the fluctuation over different realizations to be much greater than the fluctuation over different MC sampling paths for a given realization, therefore the näive motive of improving the statistical precision by repeatedly running the simulations (at least several thousands of times) for a given realization will become only marginal when the ensemble average is taken to the realization

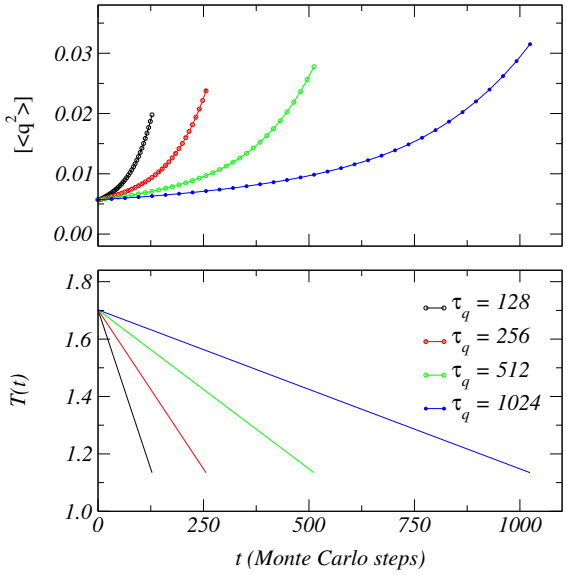

Figure 6.2: Illustrations of linear quenches of the 3-regular random graphs with $N = 512$ spins. The system is first equilibrated at the initial temperature $T_i = 1.5T_c$ and then quenched to the final temperature $T_f = T_c$ with different quench velocities. Shown are the temperature as a function of time (bottom) and order parameter $[\langle q^2 \rangle]$ as a function of time, for different velocities defined as $v = 0.5/\tau_q$ (in unit of T_c). The error bars are smaller than the symbol size.

average. We therefore only do one quench (which gives average over 64 independent runs) for a given realization, repeating the procedures for, typically, thousands of realizations.

Furthermore, since the system is equivalent to a mean-field spin-glass of upper critical dimension $d = 6$, critical exponents can be computed analytically, $\beta = 1$, $\nu = 1/2$, and $z = 4$ [1]. In terms of our normalized notations, the mean field values read $\beta = 1$, $\nu' = \nu d = 3$, and $z' = z/d = 2/3$. We would like to point out that knowing the transition point T_c or the critical exponents is not a necessary condition for our approach o work, however, the full knowledge of the spin-glass transition serves as a good test ground for the non-equilibrium approach we are demonstrating. Later we will show that how to numerically extract the transition point independently and then extract critical exponents independently.

The most distinct feature from the traditional equilibrium approach is that, this non-equilibrium process starts from a temperature away from T_c, and then quenches to T_c. This has allowed one to completely avoid critical slowing-down at T_c, which traditional equilibrium techniques have always suffered from. In this non-equilibrium approach, any critical slowing-down phenomena only reflect on the scaling behavior Eq. (6.7). In fact, in Sec. 6.3.2, we will further discuss that how a potentially serious critical slowing-down problem with a large z could turn to facilitate the scaling under this framework.

The duality of f_1 and f_2 has been demonstrated extensively in Ref. [17] for ferromagnetic system, below in Sec. 6.3.1 we use linear quench to show the same behavior of dual scaling in the spin-glass system. In Sec. 6.3.2 we show an approach to extract critical exponents by combining results from different quench protocols. This approach is an efficient application of the power-law behavior.

6.3.1 Linear quench to T_c

Some typical examples of linear quenches to T_c are shown in Fig. 6.2. For linear quenches r=1 in Eq. (6.1). The velocity is defined as $v = 0.5/\tau_q$ (in unit of T_c) for a given quench time τ_q. Fig. 6.3 shows the first scaling function f_1 described by the dual scaling Eq. (6.7). It is expected that in the adiabatic limit as $v \to 0$, the scaling will reduce to the equilibrium one, as the plateau to the left shows; the curves then make a cross-over to the power-law regime as v increases. The power-law would extend to infinitely large v as $N \to \infty$, however, in terms of finite-size systems, the f_1 scaling eventually breaks down at some high-velocity cut-off. More importantly, the dashed line in Fig. 6.3 shows the power-law behavior with the power given by Eq. (6.8), one can see a very good agreement between simulations and prediction.

It is worth mentioning that, the power-law regime corresponds to the regime when $\mathcal{V}_v$ of Eq. (6.3) is growing as v is decreasing while $\mathcal{V}_v$ is still much smaller than the system size,

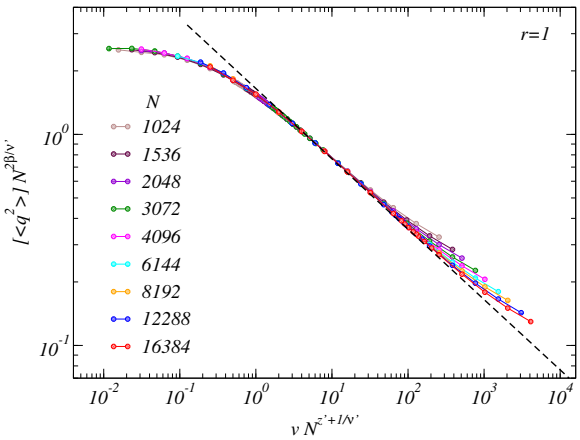

Figure 6.3: f_1 scaling for linear quenches to T_c. The mean-field values of the exponents $\beta = 1$, $\nu' = 3$, $z' = 2/3$ are used. The linear quenches are performed at velocities $v = 0.5/\tau_q$ for different quench times τ_q. The error bars are at most of the symbol size. Three different scaling regimes described in Eq. (6.7) can be clearly observed. The plateau to the left corresponds to the quasi-adiabatic regime, in which the scaling reduces to the equilibrium one as $v \to 0$. The middle region corresponds to the power-law regime in which the the order parameter $[\langle q^2 \rangle]$ shows a power-law in v with the power x described by Eq. (6.8). The power-law could extend to infinitely large velocity in the thermodynamic limit, however, for finite-size systems the curves to the right eventually begin to deviate from the scaling as $v \to \infty$. The dashed line shows the power-law with the power given by Eq. (6.8).

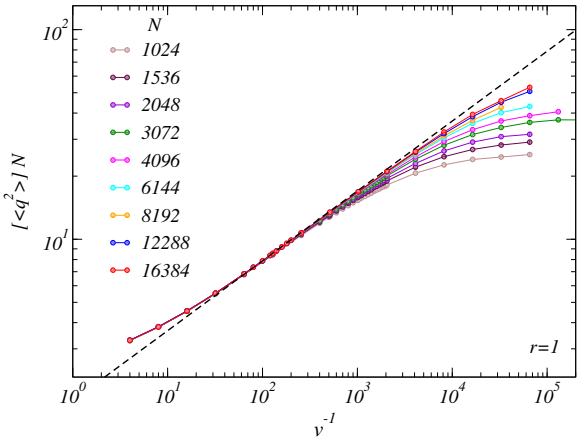

Figure 6.4: f_2 scaling for linear quenches to T_c. The left region corresponds to the diabatic regime. Those tails of the curves that showed deviations in the f_1 scaling of Fig. 6.3 now collapse into a scaling form in this diabatic regime. The middle region corresponds to the power-law regime. The dashed line shows the power-law with the power given by Eq. (6.8). The right region corresponds to the adiabatic regime in which the curves begin to show deviations, since the f_2 scaling applies from $v = \infty$ down to a low-velocity cut-off. Note that the data sets come from the same ones used in Fig. 6.3. It is also worth pointing out that f_2 scaling requires no knowledge of the the critical exponents, while the power-law still intrinsically contains the information of the critical exponents as described by Eq. (6.8).

i.e., $\mathcal{V}_v \ll N$, this is when the behavior becomes effectively size-independent. However, the effective high dimensionality, $d = 6$, of the system results in an equivalently small system size, therefore $\mathcal{V}_v$ becomes comparable to N at considerable high velocity. This is indicated by the limited range of the power-law as shown in Fig. 6.3. In some situations, when the power-law is more favorable over other scalings, one can explicitly implement different quench protocols that effectively suppress $\mathcal{V}_v$ such that the power-law behavior becomes enhanced, as we will demonstrate in Sec. 6.3.2.

We now turn to the second scaling function f_2, as demonstrated in Fig. 6.4. The left region of Fig. 6.4 corresponds to the diabatic regime, the right region corresponds to the adiabatic regime. Note that Figs. 6.3 and 6.4 are simply different scaling behaviors realized by the same data sets. It is also worth pointing out that the deviating tails of the curves in Fig. 6.3 now show perfect scaling in Fig. 6.4. One the other hand, since f_2 is applicable from $v = \infty$ down to a low-velocity cut-off, the plateau from f_1 in the quasi-adiabatic regime in Fig. 6.3 now splits into deviations in the f_2 scaling. Remarkably, the power-law still strongly holds in f_2 scaling, as the agreement between the prediction (dashed line) and the simulations is clearly observed. The f_2 scaling is remarkable in the sense that, the applicable range corresponds to the regime where the domain size $\mathcal{V}_v$ is still much smaller than the system size, and the fact that rendering f_2 scaling requires no knowledge of the critical exponents, however, the power governing the power-law implicitly carries the information of the exponents. In Sec. 6.3.2 we further discuss more applications of this property.

6.3.2 Non-linear quenches to T_c

In Sec. 6.3.1, we demonstrate the duality of scaling behaviors described by f_1 and f_2. This scaling behavior has suggested a straightforward way to extract critical exponents: one can simply carry out a fitting procedure to determine the values of β, ν', and z' that yield the optimized scaling collapse of f_1, and then one can perform f_2 scaling for a consistency check. In Ref. [17], this procedure has been extensively employed to extract dynamic exponents

of several types of dynamics to high precision. In practice, however, 2-parameter or 3-parameter optimization is not easy to achieve high accuracy, needless to say one has to know roughly the values of the parameters in order to find correct ranges to optimize.

The second scaling behavior f_2 has actually suggested another convenient way to extract critical exponents. The key observation is that, as we mentioned in Sec. 6.3.1, rendering f_2 requires no knowledge of the critical exponents, but remarkably, the power x associated with the power-law corresponds to the combinations of exponents. The power x_r associated with a given r-quench protocol can be directly obtained by a linear fit after taking log-log of the f_2 scaling. Since the linear fit is practically easier to carry out than f_1 optimization, which generally involves high-order polynomial fitting, this procedure is more favorable. In addition, since f_2 describes the diabatic and power-law regimes that involve higher velocities, computationally it means shorter runs are sufficient to determine the exponents. Furthermore, by performing two different quench protocols, one can obtain two values x_{r_1} and x_{r_2} corresponding to two different combinations of exponents, therefore one can solve the equations of two systems to disentangle the exponents.

As we pointed out earlier, the power-law regime corresponds to the regime in which the domain size $\mathcal{V}_v$ is growing as v is decreasing but $\mathcal{V}_v$ is still much less than the system size, in this regime the behavior becomes effectively size-independent and the curves should collapse on top of each other in the power-law regime for considerable large sizes, as is clearly observed in Fig. 6.4. This also suggests a systematic way of determining the system sizes to be used for linear fit: one can simply observe when do the largest and the second largest sizes begin to merge together in the f_2 scaling, this is when the system sizes become much larger than $\mathcal{V}_v$ and the power-law completely dominates the scaling. Since in a linear fit, selecting the correct region for fitting is more important, as opposed to a high-order polynomial fit in which more data points are required in order to improve the statistics, this systematic method provides an easy way to select the correct region for the linear fit.

Apparently the applicability of the procedure through f_2 scaling relies on the existence of

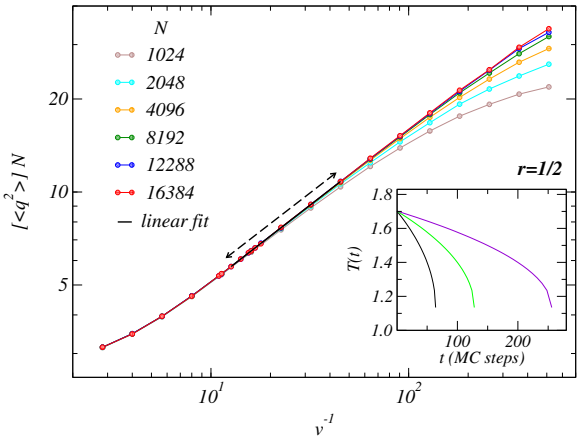

Figure 6.5: f_2 scaling from $r = 1/2$ quench. The inset shows some typical examples of $r = 1/2$ quenches. As discussed in the text, we include $N = 12288$ and $N = 16384$ for linear fit. The dashed line with arrows indicates the region selected for linear fit. The region is determined by statistical χ^2/dof as data points outside this region correspond to cross-over to either diabatic regime (to the left) or quasi-adiabatic regime (to the right) and therefore will ruin the χ^2/dof. Linear fit after taking log-log yields the power $x_{1/2} = 0.497(2)$ with $\chi^2/\text{dof} \approx 0.90$, where $\text{dof} = 13$.

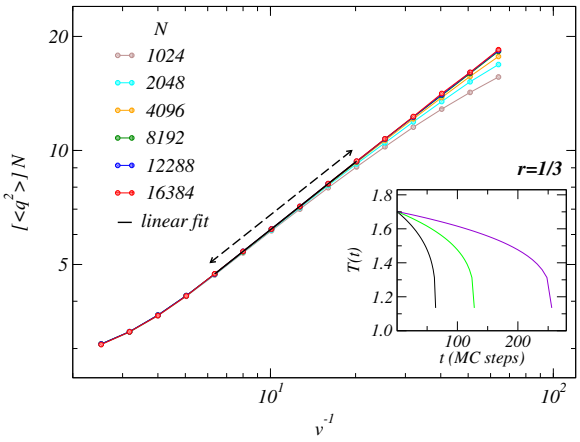

Figure 6.6: The same kind of plot as in Fig. 6.5 for an $r = 1/3$ quench. The dashed line with arrows indicates the region selected for the linear fit. The linear fit one the log-log scale gives the power $x_{1/3} = 0.593(1)$ with $\chi^2/\text{dof} \approx 0.83$, where $\text{dof} = 10$.

the power-law regime, the size of which is determined by the size of the range $v_c(N) < v < 1$. The wider the range, the more accessible the power-law regime. This property leads to an interesting advantage that traditional equilibrium approaches view as a disadvantage: a large z that results in a serious critical slowing-down will naturally create a wide power-law regime. Because of this advantage, many spin-glass systems that have serious critical slowing-down could be investigated efficiently through this approach.

In addition, in this procedure small $\mathcal{V}_v$ is favorable in order to observe a size-independent power-law behavior. As intuitively suggested by Eq. (6.3), a quench protocol with smaller r could suppress the growth of $\mathcal{V}_v$. Of course there should exist a lower limit for the choice of r since when $r \to 0$ the process becomes effectively a sudden quench. In principle one could rigorously find an optimal quench protocol for this purpose, which requires details of the system under study, but we empirically find that $r = 1/2$ and $r = 1/3$ suffice for this 3-regular random graph system. We next use these two non-linear quenches to demonstrate the procedure we have outlined.

In Figs. 6.5 and 6.6, we perform two types of non-linear quenches with $r = 1/2$ and $r = 1/3$, respectively, with v defined as $v = 0.5/\tau_q^r$ (in unit of T_c) according to Eq. (6.1). The focus will be using linear fit to extract critical exponents from the power-law regime in the f_2 scaling. As indicated by both figures, the largest two curves from $N = 12288$ and $N = 16384$ have already shown clear size-independent behavior in the power-law regime, we therefore include these two sizes in the linear fit. Furthermore, one can then use statistical χ^2 per degree of freedom (dof) to determine the correct region that yields the optimized linear fit result, since the points outside the power-law regime $v_c(N) < v < 1$ will ruin the χ^2/dof if being included in the linear fit.

For the $r = 1/2$ quench, we obtain $x_{1/2} = 0.497(2)$ with $\chi^2/\text{dof} \approx 0.90$, and dof = 13. For the $r = 1/3$ quench, we have $x_{1/3} = 0.593(1)$ with $\chi^2/\text{dof} = 0.83$, where dof = 10. Using equations Eq. (6.9), we obtain $z'\nu' = 1.9(1)$, and $\nu' - 2\beta = 0.97(2)$, which is consistent with the mean-field calculations [1]. In this demonstration we only considered the largest two

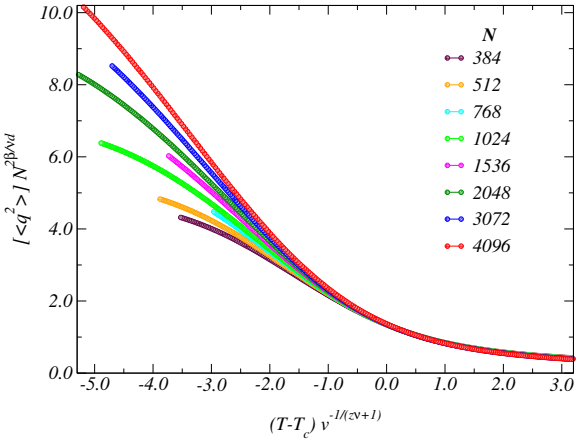

Figure 6.7: Results for a linear quench through the spin-glass transition. The quench starts from $T_i = 1.5T_c$ and goes down to $T_f = 0.5T_c$. The quench velocity is defined as $v = 1/\tau_q$ (in units of T_c.) For different sizes, the factor $vN^{z'+1/\nu'}$ is kept constant. When $T \geq T_c$, the scaling Eq. (6.12) works very well. In the spin-glass phase when $T < T_c$, the scaling begins to break down.

sizes, but in practice, especially when corrections to scaling are called for, one can further include more data points, as long as they show size-independent scaling, to improve the statistics.

6.3.3 Linear quench through the spin-glass transition

So far we have talked about the scaling behavior at T_c. It would be interesting to see whether the scaling survives in the spin-glass phase, since the correlation length ξ_T may begin to grow exponentially when $T < T_c$. Eq. (6.4) has suggested a way to probe the scaling behavior in the spin-glass phase: For a given quench protocol r, one can perform a set of simulations with different system sizes for which the factor $vN^{z'r+1/\nu'}$ is kept constant. Explicitly, in a linear quench, the order parameter $[\langle q^2 \rangle]$ can be written as:

$$\left[\langle q^2\rangle\right] = N^{-2\beta/\nu'} F\left[(T-T_c)N^{1/\nu'}, \text{const.}\right] \tag{6.11}$$

$$= N^{-2\beta/\nu'} \tilde{F}\left[(T-T_c)v^{-1/(z'\nu'+1)}\right]. \tag{6.12}$$

The above scaling Eq. (6.12) should work when $T \geq T_c$ before the spin-glass phase, it will then be interesting to see how will this scaling extend when quenching through the critical point. As Fig. 6.7 shows, the scaling works very well when $T \geq T_c$, but, presumably due to some special property of the glass phase, below T_c the scaling seems to break down. This indicates that the scaling does not work for $T < T_c$.

It is worth pointing out that keeping the factor $vN^{z'r+1/\nu'}$ constant amounts to scaling the velocity v (or generalized velocity when $r \neq 1$) exactly as the characteristic velocity $v_c(N)$, Eq. (6.2). For a set of sizes that are quenched according to the condition $v/v_c(N) = \text{const.}$, the scenario is equivalent to the equilibrium case. Therefore, if one did not rescale data in the style of Fig. 6.7, the curves would cross rather than collapse. More importantly, the extrapolation of the crossing points corresponds to the transition point T_c in the thermodynamic limit. This has been extensively studied in quantum Ising model [37]. We will further discuss this application in Sec. 6.4.1.

6.4 Quantum spin-glass transition

In this section we study the same 3-regular random graph as illustrated in Fig. 6.1, but instead of thermal transition, now we consider a $T = 0$ quantum Hamiltonian:

$$\mathcal{H} = s\sum_{\langle i,j\rangle} \sigma_i^z \sigma_j^z - (1-s)\sum_i \sigma_i^x, \tag{6.13}$$

where σ_i^z and σ_i^x are Pauli matrices and $s \in [0,1]$. The goal is to quench the quantum fluctuation by tuning the parameter s such that $s : 0 \to s_f$ at some finite velocity. We use

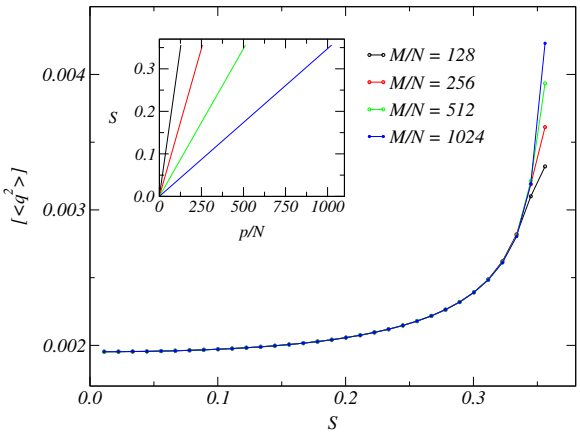

Figure 6.8: Some typical examples of linear quenches for a system size $N = 512$. The inset shows the tuning parameter s as a function of the imaginary time index normalized by the system size N. The main frame shows the corresponding EA order parameter (overaged over realizations) as a function of s.

the qausi-adiabatic quantum Monte Carlo algorithm (QAQMC) to achieve the evolution *in a single simulation*, the details of the algorithm will be referred to Ref. [37] and we only summarize the main idea as follows:

The evolution of the Hamiltonian Eq. (6.13) with $s : 0 \to s_f$ can be achieved by applying a product of evolving Hamiltonians $\mathcal{P}_{M,1}$ on an initial state $|\Psi_0\rangle = \prod_i |\uparrow_i + \downarrow_i\rangle$:

$$\begin{aligned} |\Psi_M\rangle &= \mathcal{P}_{M,1}\,|\Psi_0\rangle \\ &= \big[-\mathcal{H}(s_{_M})\big]\ldots\big[-\mathcal{H}(s_2)\big]\big[-\mathcal{H}(s_1)\big]\,|\Psi_0\rangle \\ &= \sum_{[p_{_M},\ldots,p_1]} H_{p_{_M}}(s_{_M}) \;\ldots\; H_{p_2}(s_2) \quad H_{p_1}(s_1) \;\; |\Psi_0\rangle \\ &\equiv \sum_{[p_{_M},\ldots,p_1]} P_{M,1}\,|\Psi_0\rangle\,, \end{aligned} \tag{6.14}$$

where $\sum_{[p_{_M},\ldots,p_1]}$ corresponds to sum over all possible combinations of the indices. The above expression can be described as performing a Wick rotation to the imaginary time axis such that the evolution is carried out in imaginary time. The tuning parameter s plays the role of λ in Eq. (6.1) and the way which specifies how the values s_i are discretized

determines a protocol. Some typical examples of linear quenches are shown in Fig. 6.8. An important result from Ref. [37] is that the length of the operator product $P_{M,1}$ in Eq. (6.14) should scale as the number of spins, i.e., $M \propto N$ and the velocity (or generalized velocity when the protocol is non-linear) can be defined as $v \propto (N/M)^r$. The physical observables A during the evolution can then be computed by the *asymmetric expectation value*:

$$\langle A\rangle_t = \frac{\langle\Psi_0|\mathcal{P}_{1,M}\mathcal{P}_{M,t+1}\, A\, \mathcal{P}_{t,1}|\Psi_0\rangle}{\langle\Psi_0|\mathcal{P}_{1,M}\mathcal{P}_{M,1}|\Psi_0\rangle}. \tag{6.15}$$

The quantum Monte Carlo importance sampling scheme for computing the observables Eq. (6.15) is achieved by the Stochastic Series Expansion updating scheme, [11–13] which consists of *diagonal update* and *cluster update*. We are interested in the EA order parameter defined as in Eq. (6.5) with σ replaced by σ^z and the dimensionless Binder cumulant constructed through the EA order parameter:

$$U = \frac{1}{2}\Big[3 - \frac{\langle q^4\rangle}{\langle q^2\rangle^2}\Big], \tag{6.16}$$

where $\langle\ldots\rangle$ stands for the ensemble average for a given realization and $[\ldots]$ stands for the average over realizations. Following directly from Eq. (6.4), the scaling form of U around the quantum critical point (QCP) s_c can be written as:

$$U = F\big[(s - s_c)N^{1/\nu'}, vN^{z'r+1/\nu'}\big]. \tag{6.17}$$

The Hamiltonian Eq. (6.13) has been studied recently [30] in the context of QAA, in which the relation between QAA and combinatorial optimization has been discussed in detail. Here we look at the problem in terms of non-equilibrium quench and focus on the spin-glass transition. In Sec. 6.4.1 we extract QCP corresponding to the spin-glass transition. In Sec. 6.4.2 we demonstrate the dual scaling behavior at QCP.

6.4.1 Extracting the critical point s_c

As we mentioned in Sec. 6.3, the thermal transition of the 3-regular random graph can be analytically solved by the RSB solution [1, 28, 29], consequently the critical exponents are known exactly. However, to our knowledge there is no exact solution for the quantum case despite the development of quantum cavity method [88, 89]. Furthermore, although there is a correspondence between d-dimensional quantum system and $(d+1)$-dimensional classical system, it is not fully clear that if this correspondence still holds in spin-glass system when the classical counterpart is already at the upper critical dimension. Therefore to be unbiased, we treat all exponents associated with the quantum spin-glass transitions as unknown. In this section, we use a technique developed in Ref. [37] to demonstrate that one can still extract s_c without knowing the exact values of the critical exponents.

Recall the original KZ argument and Eq. (6.2): to be quasi-adiabatic, the velocity should scale as $v_c(N) \sim N^{-(z'r+1/\nu')}$. If the exponents are not known prior to the simulation, one can formally assume that

$$v(N) \sim N^{-\alpha'}. \tag{6.18}$$

We are interested in two scenarios: (i) $\alpha' = z'r + 1/\nu'$, (ii) $\alpha' > z'r + 1/\nu'$. The first scenario follows directly from the KZ argument and Eq. (6.2). When the exponents are already known, one can keep the second argument in Eq. (6.17) constant and use the standard equilibrium approach of extracting Binder crossings [62] to find s_c. In the second scenario when $\alpha' > z'r + 1/\nu'$, it implies that the velocity scales to zero faster than the velocity threshold $v_c(N)$, which means that the second argument of the scaling function Eq. (6.17), $N^{z'r+1/\nu'}/N^{\alpha'}$, goes to zero in the thermodynamic limit. This scenario amounts to taking the adiabatic limit first and taking the thermodynamic limit second, consequently, this is equivalent to equilibrium situation in the thermodynamic limit when $N \to \infty$. This suggests that for a given trial of α' that potentially satisfies $\alpha' > z'r + 1/\nu'$, one can still

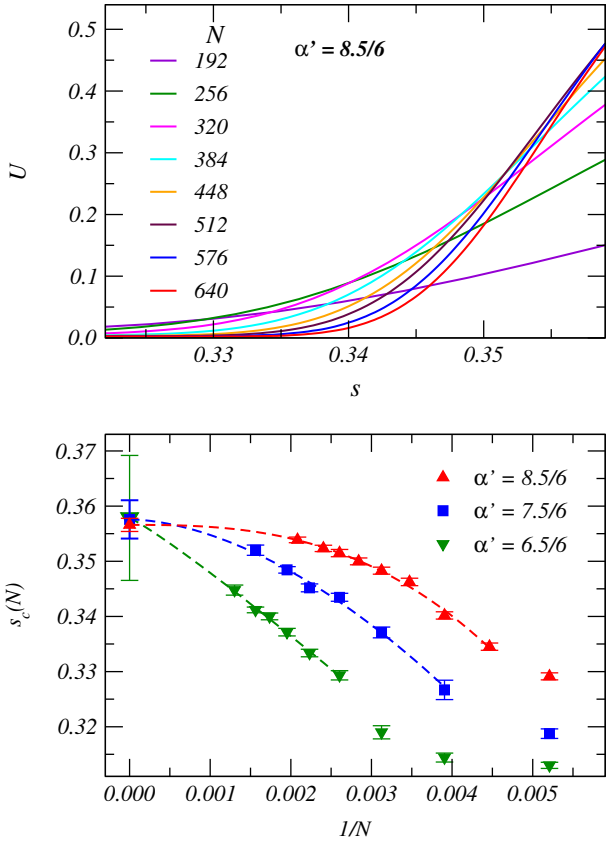

Figure 6.9: Binder cumulants Eq. (6.16) for different system sizes that obey Eq. (6.18) with $\alpha' = 8.5/6$ (top). Extrapolations of the crossings of Binder cumulants for different choices of α' (bottom). For $\alpha' = 6.5/6$, the extrapolation is obtained by looking at the crossings between N and $N + 64$ curves with $N = 192, \ldots, 640$. For $\alpha' = 7.5/6$, the extrapolation is from the crossings between N and $N + 64$ curves with $N = 192, \ldots, 576$. For $\alpha' = 8.5/6$, the extrapolation is from the crossings between N and $N + 32$ curves with $N = 192, \ldots, 448$. A larger value of α' implies that the velocity converges to zero faster, therefore the extrapolation will converge to equilibrium earlier. Indeed, using the standard form Eq. (6.19), the extrapolation from $\alpha' = 8.5/6$ scaling gives the smallest error bar with $s_c \approx 0.3565(12)$.

look at the Binder crossings based on different system sizes on which Eq. (6.18) is imposed, the extrapolation of the Binder crossings corresponds to the equilibrium transition point. This procedure has been thoroughly tested in Ref. [37], below we apply this technique to the quantum spin-glass transition.

We use linear quench protocol ($r = 1$), therefore α' will be compared to $z' + 1/\nu'$. In light of the knowledge from the classical system, in which the quantity $z' + 1/\nu'$ is 1, we intuitively take this as the lower bound in the quantum case and empirically select $\alpha' = 6.5/6 \approx 1.083$, $\alpha' = 7.5/6 = 1.25$, and $\alpha' = 8.5/6 \approx 1.417$. Later these choices can be justified after the exponents are extracted. For a given choice of α', one can look at the crossings between Binder cumulants from different sizes that satisfy the condition Eq. (6.18). Some typical examples are illustrated in the top panel of Fig. 6.9. Since close to the transition point any quantities related to the order parameter can be written as a power-law, the standard form [63] is used to fit the crossings of the Binder cumulant:

$$s_c(N) = s_c + a/N^b, \tag{6.19}$$

where a and b are fit parameters.

As the above argument implies, if the chosen α' corresponds to scenario (ii), the extrapolation of the crossings to the thermodynamic limit should correspond to the equilibrium transition point. One can further make different choices for consistency check, since the correct trials of α' should all lead to the same extrapolation. As indicated by the bottom panel of Fig. 6.9, indeed different choices of α' all lead to the same extrapolation result. Furthermore, a larger α' implies that the scenario will reduce to the adiabatic limit faster, this is also indicated by the smaller error bar on the extrapolation of $\alpha' = 8.5/6$ curve, from which we obtain $s_c \approx 0.3565(12)$, this is in good agreement with Ref. [30].

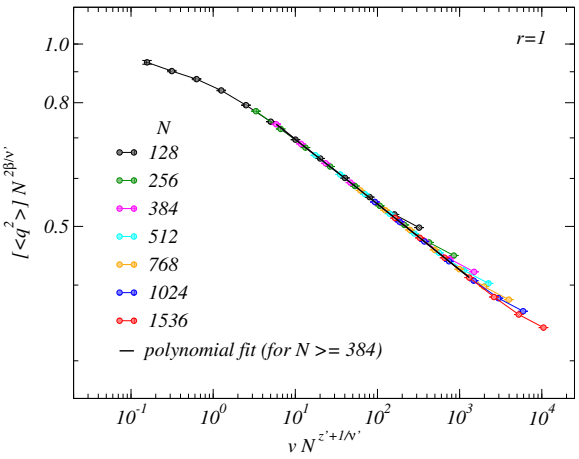

Figure 6.10: f_1 scaling of results obtained in a linear quench to s_c. The velocity is defined as $v = s_c/\tilde{M}$, where $\tilde{M} = M/N$ and M is the total length of the operator product $P_{M,1}$ in Eq. (6.14) and should scale as $M \propto N$. The scaling indicates that the velocities yield scaling in the power-law regime, while the quasi-adiabatic regime in the region $v < N^{-(z'+1/\nu')}$ is not accessible due to the requirement of long runs, and the out-of-scaling "tail" of each curve corresponds to the diabatic regime. A fitting procedure is carried out to determine the exponents that yield the optimized scaling collapse, we obtain $z' + 1/\nu' = 1.31(17)$ and $\beta/\nu' = 0.428(9)$, with $\chi^2/\text{dof} \approx 0.90$. The solid line indicates the polynomial fit of the fitting procedure.

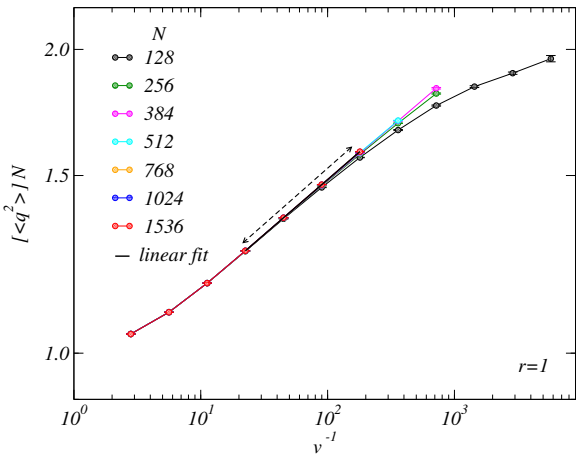

Figure 6.11: f_2 scaling procedure of $r = 1$ linear quenches to s_c. The data set is the same as the one used in Fig. 6.10, but scaled according to the second scaling form in Eq. (6.7). The left region corresponds to the diabatic regime and the right region is the adiabatic regime, while the middle corresponds to the power-law regime. The tails that do not collapse in Fig. 6.10 now show scaling collapse. Furthermore, one can use linear fit after taking log-log to find the power x governing the power-law. The dashed line with arrows indicates the region selected for the linear fit, the selection of the region is guided by what region minimizes the χ^2/dof. In addition, the power-law should be a size-independent behavior, therefore we include sizes with $N \geq 768$ in the fitting procedure, the selection of sizes is also systematically guided by the minimization of χ^2/dof. The solid line indicates the fit result. The linear fit yields $x_1 = 0.1089(1)$ with $\chi^2/\text{dof} \approx 0.90$, in full agreement with the result predicted by f_1 scaling.

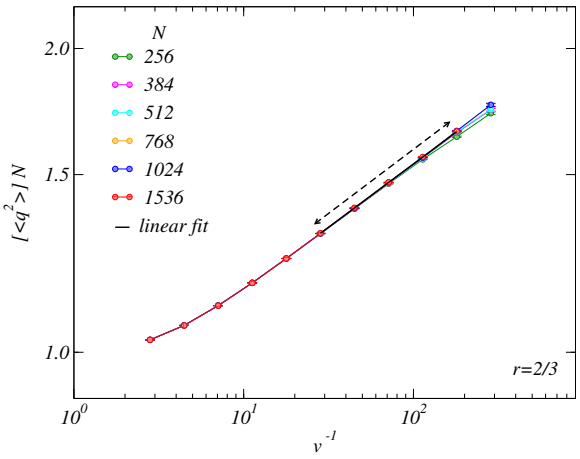

Figure 6.12: f_2 scaling for non-linear $r = 2/3$ quenches to s_c, in the same style as Fig. 6.11. One can again use linear fit after taking log-log to find the power x governing the power-law regime. The dashed line with arrows indicates the region selected for the linear fit. We include sizes $N \geq 768$ for linear fit, which gives $x_{2/3} = 0.1255(4)$ with $\chi^2/\text{dof} \approx 1.6$.

6.4.2 Scalings at the critical point

After the critical point is obtained, $s_c \approx 0.3565(12)$, we perform another set of linear quenches with the aim of approaching s_c with different velocities. The velocity can be defined as $v = s_c/\tilde{M}$, where $\tilde{M} = M/N$ and M is the total length of the operator product $P_{M,1}$ in Eq. (6.14). At s_c the dual scaling behavior Eq. (6.7) will again be expected. So far the exact values of the exponents appeared in Eq. (6.7) are not yet known, however the scaling behavior allows us to numerically extract the values.

Fig. 6.10 shows the f_1 scaling from linear quenches with different velocities. Since the exponents β, ν', and z' are unknown, a 2-parameter fitting procedure is performed to determine the values of $z' + 1/\nu'$ and β/ν'. We obtain $z' + 1/\nu' = 1.31(17)$ and $\beta/\nu' = 0.428(9)$, with $\chi^2/\text{dof} = 0.9$. The fitting result for $z' + 1/\nu'$ also justifies the choices of α' used for Binder crossings as we discussed in Sec. 6.4.1. A legitimate choice of α' should be greater than $z' + 1/\nu'$, therefore, it implies that $\alpha' = 8.5/6$ are indeed corresponding to the scenario (ii). As indicated by Fig. 6.10, the available velocities result in the f_1 scaling in

the power-law regime. The power associated with the power law can be predicted by the fitted exponents according to Eq. (6.8). The fitted results for $z' + 1/\nu'$ and β/ν' predict that $x \approx 0.109$. One can independently check this prediction by looking at the f_2 scaling, as we discuss next.

Fig. 6.11 shows the f_2 scaling from the same data set used in Fig. 6.10. As we discussed in Sec. 6.3, f_1 and f_2 are equivalent, or more precisely speaking, they are complimentary since f_1 covers the scaling in the quasi-adiabatic and power-law regimes and f_2 covers the scaling in the power-law and diabatic regimes, one can see a clear power-law behavior in both Figs. 6.10 and 6.11. Also, having the same situation as in the classical case, in the f_1 plot the tails that do not show scaling in the diabatic regime turn into scaling collapse in the f_2 plot.

Furthermore, f_2 is easier to render in practice since it requires no knowledge of the critical exponents. As we pointed out in Sec. 6.3, one can use a linear fit after taking log-log of the data to find the power x, which governs the power-law and contains the information of critical exponents. Ideally, the power-law regime should show a size-independent behavior. In practice small sizes will show deviation due to finite-size effect. One then can use χ^2/dof to quantify the selections of the region in which linear fit is carried out and sizes included in the fit, since region outside the power-law regime or small sizes will ruin the χ^2/dof if being included. As shown in Fig. 6.11, we obtain $x_1 = 0.1089(1)$ with $\chi^2/\text{dof} = 0.9$, this is completely consistent with the prediction from f_1 scaling.

To fully extract the exponents, we perform another set of non-linear quenches to s_c with $r = 2/3$. The goal is to obtain the power $x_{2/3}$ in order to apply Eq. (6.9), therefore we only focus on the f_2 scaling. As shown in Fig. 6.12, the scaling is still clearly observed in non-linear quench. Using linear fit for the region indicated by the dashed line with arrow, we obtain $x_{2/3} = 0.1255(4)$ with $\chi^2/\text{dof} \approx 1.6$.

The results of x_1 and $x_{2/3}$ allow one to compute $z'\nu'$, according to Eq. (6.9). We obtain

$z'\nu' = 0.656(25)$. Combine the numerical results obtained so far, one can easily solve for the exponents z', ν', and β:

$$\begin{cases} z' + 1/\nu' &= 1.31(17), \\ z'\nu' &= 0.656(25), \\ \beta/\nu' &= 0.428(9), \end{cases} \Rightarrow \begin{cases} z' &= 0.52(7), \\ \nu' &= 1.26(16), \\ \beta &= 0.54(7). \end{cases} \tag{6.20}$$

The results obtained above strongly indicate that the exponents in the quantum case are very different from the classical counterparts. We would like to point out that although the classical system is at the upper critical dimension d_{cl}, the dimensionality of the quantum case should be effectively $d_q = d_{cl} + z_q$, where z_q is the dynamic exponent of the quantum system, therefore the exponents in the quantum case are not expected to be in the mean-field description.[1] Furthermore the mean-field description can not fully capture the quantum case since the system is anisotropic in the spatial dimension but isotropic in the imaginary time dimension.

6.4.3 Comparison with previous results

The same Hamiltonian Eq. (6.13) has been extensively studied in the context of the performance of QAA on the Max Cut of random 3-regular graphs. [30] One of the major issues being discussed is that whether the energy gap decreases polynomially or exponentially with the system size N. In Ref. [30], Farhi *et al.* looked at the median of the minimum gap (taken from the median among realizations for a given system size) and found that close to the critical point s_c, a power-law better explains the vanishing of the energy gap than the exponential form does. The power-law form extracted therein reads as $\Delta E_{\min} \propto N^{-0.78}$. This corresponds to a $z' = 0.78$ in our notation. Despite the difference in the value of z', it is qualitatively consistent with our conclusion that at s_c a power-law scaling is clearly

[1] We also found that, for either $r = 1$ or $r = 2/3$ quench, if one tries to rescale the raw data in the style of Fig. 6.10 with the classical exponents, no scaling collapse is observed.

observed. It should also be noted that in Ref. [30], only instances of the 3-regular random graphs satisfying certain additional conditional conditions were considered, while in our case we consider many randomly generated realizations. Also, the power-law form extracted in Ref. [30] is from the medians of the instances considered, while in our case we consider average over realizations.

In the classical phase transition, the 3-regular AFM random graphs and the SK model are known to be in the same universality class, as discussed in Sec. 6.3. However, in the quantum scenario the situation is not clear yet. Read, Sachdev, and Ye looked at the quantum SK model [111] and found the exponents to be $z = 2$, $\nu = 1/4$, and $\beta = 1$, at an effective upper critical dimension $d = 8$. Translated to our notation, it corresponds to $z' = 1/4$ and $\nu' = 2$. It is possible that in the quantum case these two models are not in the same universality class, or the QMC results are still affected by finite-size effects. However, we would like to point out that, as will be discussed in Appendix A, the values $z' + 1/\nu'$ and β/ν' obtained in the $r = 1$ linear quenches (see Fig. 6.10) are consistent with the QAQMC result for the quantum SK model.

6.5 Summary and Discussion

We have presented a non-equilibrium approach for studying both classical and quantum spin-glass transitions. This approach is a further extension of KZ mechanism and generalized dynamic finite-size scaling.

In terms of classical transition, this framework shows advantages over the traditional equilibrium methods, since the critical slowing-down can be completely avoided. Furthermore, there is no any "waiting time" associated with the relaxation process that generally used in the equilibrium approaches. In this non-equilibrium quench, one has the freedom of choosing quench velocities (or generalized velocities for non-linear quenches). Remarkably, as we showed in terms of the dual scaling behavior, different quench velocities will result in either

	z'	ν'	β	β/ν'	$p(r)$	$p(1)$	$p(0^+)$	$p(\infty)$
C	2/3	3	1	1/3	2/3+1/3r	1	1/3r	2/3
Q	0.52(7)	1.26(16)	0.54(7)	0.428	$0.52 + 1/1.26r$	1.31	$1/1.26r$	0.52

Table 6.1: Comparison between the critical exponents for the classical (C) and quantum (Q) 3-regular AFM random graphs. The classical exponents are equivalent to the fully-connected SK model with $d = 6$ [1]. The exponent $p(r) \equiv z' + 1/\nu' r$ governs the time scale required for approaching the critical point without losing the adiabaticity.

f_1 or f_2 scaling, depending on the range the velocity falls into. Since these two scalings are equivalent, one can solely work with one scaling function and perform consistency check with the other. However, in practice, f_2 is more favorable for the following three major reasons: First, rendering f_2 scaling requires no knowledge of the critical exponents, while the power associated with the power-law regime contains the information of critical exponents. Second, the f_2 scaling describes higher velocity regime, which translates to computationally shorter simulations. One can achieve scaling with relatively shorter runs than the traditional equilibrium methods. Third, the power governing the power-law in f_2 scaling can be measured easily, one simply performs linear fit after taking log-log. Furthermore, one can carry out this procedure for two different quench protocols and then solve the system of two equations to determine the critical exponents. The advantages will become more significant when the critical slowing-down affects the performance of traditional equilibrium simulation methods. A serious critical slowing-down problem generally is associated with a large dynamic exponent z. However, in this non-equilibrium quench approach, critical slowing-down has no effect on the procedure and a large z only creates a wide power-law regime, which can be taken advantage by the f_2 scaling.

As for the quantum phase transition, we use the QAQMC algorithm to demonstrate this non-equilibrium approach. The advantage of using QAQMC is that it can take measurements for the entire evolution in a single simulation when the Hamiltonian is evolving as

a function of the tuning parameter. We demonstrate that, without any knowledge prior to the simulation, one can extract information such as transition point and critical exponents associated with the transition. At the first stage one can first determine the transition point by choosing the correct velocity scaling. At the second stage after the transition point is determined, one then uses the scaling behavior at the transition point to determine the critical exponents. The exponents obtained are summarized in Table 6.1. The knowledge of the critical exponents for both the classical and quantum systems also allow us to make a systematic comparison between simulated annealing (SA) and quantum annealing (QA), the former is a classical optimization algorithm and the later uses the idea of quantum computing. Given the expression Eq. (6.2), one can write down the time scale to reach the critical point as:

$$\tau \sim v^{-1/r} \sim N^{z'+1/\nu' r}. \tag{6.21}$$

Therefore $p(r) \equiv z' + 1/\nu' r$ defines this time scale. Also, at the spin-glass transition point the order parameter scales as $\langle q^2 \rangle \sim N^{-2\beta/\nu'}$, the typical size of the order parameter is related to β/ν'. For linear quench, as shown in Table. 6.1, QA takes longer to reach the critical point and also gets smaller order parameter. In other words, QA has worse performance than SA. In the scenario when $r \to 0^+$, the time scale associated with QA is still longer. In another limit when $r \to \infty$, QA shows better scaling than SA. It is therefore plausible that one can devise a non-linear quench protocol such that SA and QA show comparable results. Nevertheless, linear quench seems to be the most approachable protocol. Furthermore, since many optimization problems can be either reduced to the 3-regular AFM (e.g., MaxCut of a 3-regular graph) or be shown to be in the same NP-class as the model [30], the numerical results obtain here imply that quantum algorithms can not do better than classical algorithms for this class of problems.

Chapter 7

Non-equilibrium quench in classical 3D spin-glasses

7.1 Introduction

Spin-glasses, a type of magnetic system that has disordered interactions, have been an important and challenging topic in the development of statistical physics and condensed matter physics [1,23] . In the early development, the interests in spin-glasses arose because of the complex spin-glass phases and the complexity of finding the ground state. Later on, it was found that many problem in other areas such as biology, computer science, combinatorial optimization, and even social networks, can be mapped onto a spin-glass problem. Therefore, a deeper understanding of the spin-glasses, the establishment of the underlying mathematical framework, and the development of analytical and computational techniques can have divers applications and impact.

A typical spin-glass Hamiltonian can be written as

$$\mathcal{H} = \sum_{ij} J_{i,j}\sigma_i\sigma_j, \tag{7.1}$$

which is a modification of the Ising model. Depending on the specific cases under study, the interaction strength J_{ij} will be different. But generally speaking, the randomness and disorder come into play through the interaction strength or the geometrical arrangement. The frustration and highly degenerate ground state will result in a rough energy landscape in the configuration space, as demonstrated in Fig. 7.1 (a).

Roughly speaking, we can categorize spin-glasses into two types, finite dimension Fig. 7.1 (b) and infinite dimension Fig. 7.1 (c) and (d). A fully-connected spin-glass with interaction being Gaussian distributed $J_{ij} \sim \mathcal{N}(0, \frac{1}{N})$ is known as the Sherrington-Kirkpatrick (SK)

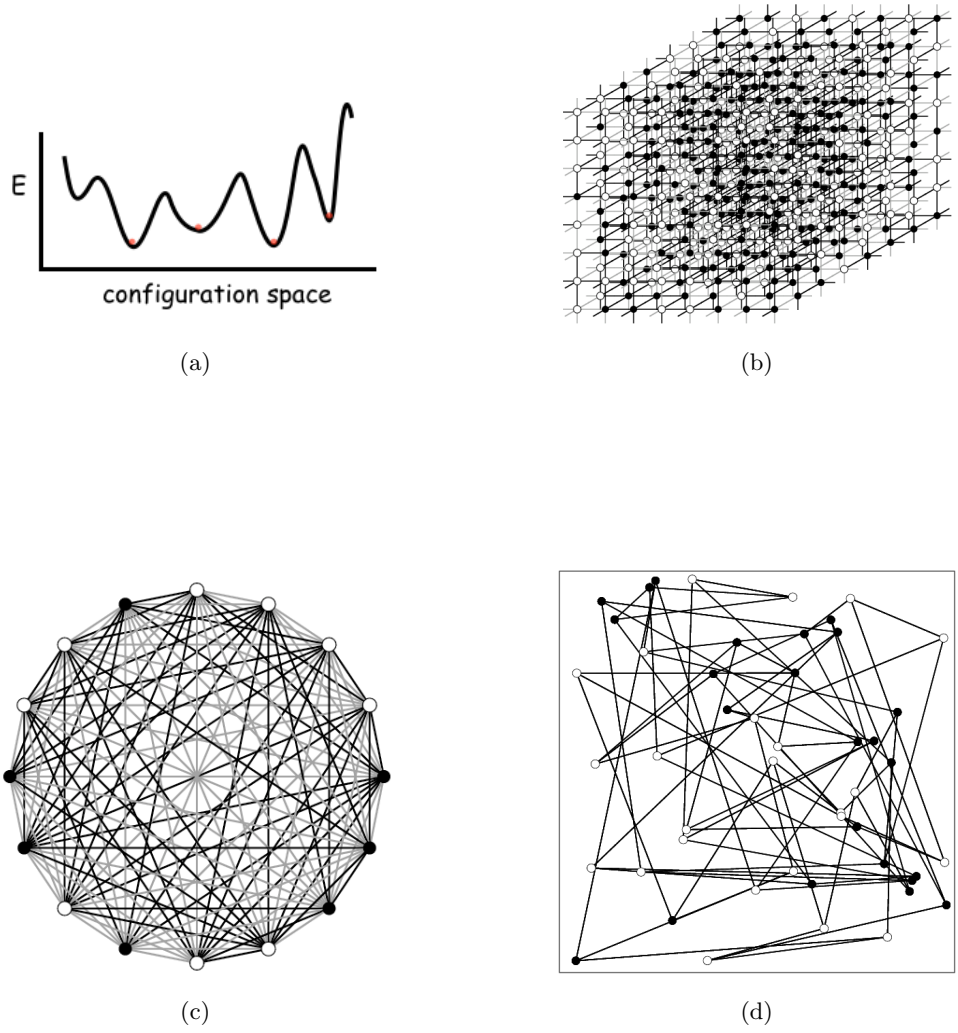

(a) (b)

(c) (d)

Figure 7.1: Illustration of spin-glasses. (a) A rough energy landscape in the configuration space. (b) A three dimensional (3D) spin-glass. (c) A fully-connected spin-glass, also known as Sherrington-Kirkpatrick (SK) model. (d) A 3-regular random graph with anti-ferromagnetic interactions. In cases (c) and (d), the dimensionality is regarded as infinitely dimensional.

model Fig. 7.1 (c), which can be solved exactly by mean-field description [24]. A k-regular random graph with nearest-neighbor anti-ferromagnetic interactions $J_{ij} = -1$, Fig. 7.1 (d), is a special case of Potts spin-glass, can also be solved using cavity method with replica symmetry breaking (RSB) [1]. For finite dimension spin-glasses, a two-dimensional spin-glass is known to have $T = 0$ transition. However, a three-dimensional spin-glass has a non-trivial transition and there is no analytical solutions to this date.

Due to the lack of analytical solutions, numerical simulations, especially unbiased Monte Carlo simulation has become the major tool to investigate the problem. However, an challenging issue that makes spin-glass study difficult is the critical slowing-down near the spin-glass transition T_c [8, 23]. The serious critical slowing-down arises due to the nature of the continuous phase transition exacerbated by the rough energy landscape in which the configuration gets stuck in local minima and the importance sampling becomes rather ineffective. Despite some development of numerical approaches such as simulated annealing [55] and replica exchange [90], a more efficient method to deal with the critical slowing down near the spin-glass transition is still called for.

Recently, we have developed a non-equilibrium approach to study second order phase transitions [17, 33, 37]. The idea is based on approaching the transition point through a quench protocol, also known as Kibble-Zurek mechanism [14, 15], and the dynamic finite-size scaling ansatz. As it returns out, this non-equilibrium approach can completely avoid critical slowing-down problem and allows one to study spin-glass transition rather efficiently. In this Chapter we demonstrate this non-equilibrium approach on three-dimensional spin-glass (3DSG) systems.

The most widely studied 3DSG models are of Bimodal model and Gaussian model, both cases consider nearest-neighbor interactions, and in the former case the interaction is discrete $J_{ij} = -1$ or $+1$, while in the later the interaction is Gaussian distributed $J_{ij} \sim \mathcal{N}(0, 1)$. In terms of the static properties of the spin-glass transitions, extensive studies [64, 91–106] have shown that these two systems belong to the same university class, although the tran-

sition temperatures are different:

$$\begin{aligned} T_c &= 1.102(3) \qquad \text{Bimodal} \\ T_c &= 0.94(2) \qquad \text{Gaussian} \\ \nu &= 2.562(42) \\ \eta &= -0.3900(36) \end{aligned} \tag{7.2}$$

The most precise measurements (smallest error bars) for the critical exponents and T_c are from Ref. [104], which carried out large-scale simulation on Bimodal 3DSG with a dedicated field-programmable gate array (FPGA) cluster called "Janus" located in Spain.

Despite the well-established universality class of the equilibrium property, the dynamic aspect of the Bimodal and Gaussian 3DSG is still controversial. Different studies have been carried out over a span of more than a decade [64, 91–106], to try to identify the dynamic universality class. However, the serious critical slowing-down poses a severe challenge for studying dynamics around the transition. The typical values of the dynamic exponents for these two systems generally fall into the range $5 \sim 7$, with no consensus reached yet. We will use the efficient non-equilibrium approach to tackle this problem and show that Bimodal and Gaussian are actually in the same dynamic universality class.

The rest of this Chapter is organized in the following way. In Sec. 7.2, we briefly summarize the dynamic finite-size scaling formalism established in Refs. [17]. In Sec. 7.3, we present the simulation scheme and numerical results. in Sec. 7.4 we discuss the conclusion obtained in this Chapter.

7.2 Dynamic critical scaling formalism

In this Chapter, we are interested in 3D spin-glasses with the geometry illustrated in Fig. 7.1 (b) and Hamiltonian of the form of Eq. 7.1. Therefore, for a cube of size length L, the number of spins is $N = L^3$. In [17], we developed a dynamic finite-size scaling formalism when

a continuous transition temperature T_c is approached through a non-equilibrium quench protocol:

$$T(t) = T_c + v(\tau_q - t)^r, \tag{7.3}$$

where τ_q is total quench time, r the quench parameter that controls the linear quench (constant velocity) with $r = 1$, constant acceleration quench with $r = 2$, quadratic quench with $r = 1/2$, etc, and v is the generalized velocity defined as:

$$v = (T_i - T_c)/\tau^r, \tag{7.4}$$

where $T_i > T_c$ is the initial temperature.

Based on the KZ mechanism [14, 15] and the generalized dynamic finite-size scaling [17], we found a dual scaling behavior of the order parameter(in the case of the spin-glasses, the Edward-Anderson order parameter Eq. (1.37), as a function of the quench velocity

$$\langle q^2 \rangle = \begin{cases} L^{-(1+\eta)} f_1(vL^{zr+1/\nu}), & v \lesssim v_{KZ}(L) \\ L^{-d} \left(\frac{1}{v}\right)^x, & v_{KZ}(L) \ll v \ll 1 \\ L^{-d} f_2(1/v), & v \gtrsim 1 \end{cases} \tag{7.5}$$

where d is the dimensionality and $v_{KZ}(L)$ is a size-dependent characteristic velocity that separates a quasi-adiabatic and high-velocity regimes:

$$v_{KZ} \sim L^{-(zr+1/\nu)}. \tag{7.6}$$

The dual functions f_1 and f_2 describe the quasi-adiabatic and high-velocity regimes, respectively. Interestingly, there is a wide region $v_{KZ}(L) \ll v \ll 1$ in which both functions apply and both functions reduce to an universal power-law, with the power being related to the critical exponents:

$$x = \frac{d - 2\beta/\nu}{zr + 1/\nu} = \frac{2 - \eta}{zr + 1/\nu} \tag{7.7}$$

where the second equality is obtained by simply using the scaling relation [7].

7.3 Numerical simulations

In this section, we demonstrate the application of the dynamic finite-size scaling outlined in Sec. 7.2 on 3D spin-glass systems. We will consider two types of spin-glasses, Bimodal and Gaussian, whose static critical quantities have been well studied, as summarized in Eq. 7.2.

7.3.1 Simulation scheme

We work in the framework of Monte Carlo simulation. We start from an initial temperature $T_i = 2.0$ and linearly quench to a final temperature $T_f = 0.5$, with different quench times $\tau_q = 150 \times 2^n$ Monte Carlo steps, where $n = 0, 1, 2, \ldots$. The quench velocity is therefore defined as $v = 1.5/\tau_q$. The simulation carries out an equilibration run at T_i to ensure thermalization before the quench process starts, then linearly quenches to T_f, the simulation stops immediately once T_f is reached, therefore there is no "waiting time" in this simulation scheme. We also put 150 uniformly divided grids on the quench path $T_i \to T_f$ as our measurement points. Some typical examples of the quench processes are illustrated in Fig. 7.2 (a).

In terms of the simulation techniques, we use multi-spin coding with 64-bit long integer, therefore we can simulate 64 independent "replica" in a single run. As a general rule in the numerical study of disordered systems, for a given quantity under study, one has to do average over many (typically, hundreds or thousands) realizations. Since spin-glasses have large fluctuation over different realizations, the fluctuation of the ensemble average in a given realization is expected to be much smaller than the fluctuation over different realizations.

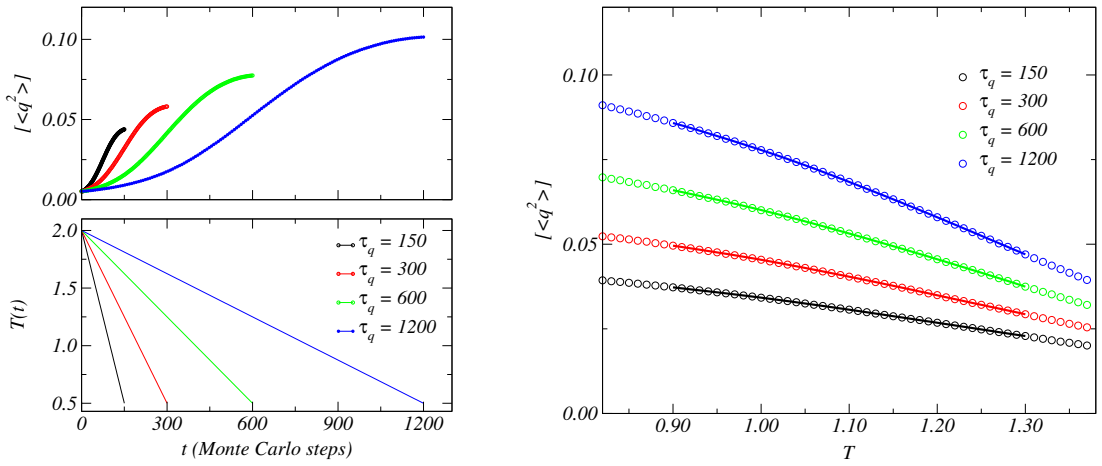

Figure 7.2: (a) Typical examples of linear quenches of the Bimodal 3DSG. A system of size $N = 12^3$ was equilibrated at the initial temperature $T_i = 2.0$ and was then linearly quenched to $T_c = 1.10$. The quench velocity is $v = 1.5/\tau_q$, where τ_q is the total quench time. Here one unit of time is defined as one MC step consisting N attempts to flip randomly selected spins using the standard Metropolis probability. Shown are the temperature (bottom panel) and the Edward-Anderson order parameter squared (top panel) versus time for different total quench times, where $[\ldots]$ stands for realization average. We are interested in the scaling of $[\langle q^2 \rangle]$ at T_c. (b) The same data as (a), but plotted as $[\langle q^2 \rangle]$ versus temperature T. The symbols are numerical data, and the lines are polynomial fit in the region around $T_c \approx 1.10$.

Therefore, for each realization, we only do one single quench run, which yields an average of 64 independent replicas. The number of realizations for each size also depends on the quench times: for short quench times we can obtain $\mathcal{O}(10^4)$ realizations, and for longer quenches we will have at least $\mathcal{O}(10^2)$ realizations. In the following we will use $[\langle q^2 \rangle]$ to denote the realization average of $\langle q^2 \rangle$.

The goal in the next subsection is to compare the dynamic exponents z for the Bimodal and Gaussian 3DSGs, and therefore, identify their dynamic universality class(es). The dual scaling behavior Eq. (7.6) requires the knowledge of the transition temperature T_c and critical exponents ν and η. In principle one can also use the technique developed in Refs. [17, 37] to extract all the critical quantities independently, for simplicity we use the currently known values quoted in Eq. (7.2). However, to take into account the fact that the numerical results quoted in Eq. (7.2) all carry statistical errors, we take the following procedure to facilitate the data analysis that will be discussed in detail in the next subsection. For each quench curve, we use polynomial fit for $[\langle q^2 \rangle]$ vs. T around T_c, therefore we can know the value of $[\langle q^2 \rangle]$ at any temperature in the region of interest. The procedure is illustrated in Fig. 7.2 (b). Later, when estimating the error bars of the dynamic exponent z, we will do so by introducing noises to T_c and see how the fluctuation in T_c affect $[\langle q^2 \rangle]$ and consequently how this fluctuation propagates to affect the scaling behavior Eq. (7.5).

7.3.2 Results: Bimodal and Gaussian 3D spin-glasses

In this section, we use the dual scaling behavior Eq. (7.5) with the critical exponents quoted in Eq. (7.2) at the respective spin-glass transition temperature T_c of the Bimodal and Gaussian 3DSG to extract the dynamic exponent z. The procedure is as follows: Given the scaling form of f_1 or f_2 in Eq. (7.5) and knowns values of the critical exponents ν and η, the only unknown parameter is z, therefore one can easily carry out a fitting procedure to determine the optimized value of z that yields the least squared error. This procedure has been demonstrated and used extensively in Ref. [17] for classical Ising models to obtain

several high-precision numerical estimate of the dynamic exponents. Here we apply the same technique to illustrate the advantage of this method on spin-glass systems. In the later part of the section we also discuss the correction to scaling.

As mentioned in the previous section, we perform quenches with different quench velocities $v = 1.5/\tau_q$ from $T_i = 2.0$ to $T_f = 0.5$, and then perform polynomial fit for $[\langle q^2 \rangle]$ as a function of T in the region around T_c. Then we can obtain the value of $[\langle q^2 \rangle]$ at T_c for all the quenches being carried out. A simpler procedure would be simply performing quenches to exactly T_c, however, as we will do later, we also introduce noises to T_c to estimate how the fluctuation affects the scaling and the values of z, this procedure is more general and preferable.

First, according to the first scaling function f_1 in Eq. (7.5), which governs the scaling around a characteristic velocity $v_{KZ}(L) \sim L^{-(z+1/\nu)}$ and covers the quasi-adiabatic regime and universal power-law regime, we graph the rescaled order parameter, $[\langle q^2 \rangle] L^{1+\eta}$ versus the rescaled velocity $v/v_{KZ}(L) = vL^{z+1/\nu}$, for both cases of Bimodal 3DSG and Gaussian 3DSG, a clear scaling collapse os observed in Fig. 7.3 (a) and (b), respectively. We use the fitting procedure outlined previously to obtain the best fit for the scaling function, which also yields the optimized z for the scaling collapse. After the optimized z is determined, we then introduce 1-σ noise to T_c, this results in a new set of $[\langle q^2 \rangle]$ due to the change of T_c, we also introduce 1-σ noises to ν and η. These new data sets and critical exponents are then used to determine the value of z. This procedure is carried out repeatedly to estimate the error of z. For the Bimodal case, we obtain $z = 5.852(55)$ with $\chi^2/\text{dof} = 1.07$. For the Gaussian case, we obtain $z = 6.005(96)$ with $\chi^2/\text{dof} = 1.00$. This numerical result strongly supports the idea that these two models belong to the same dynamic university class. Note that with the help of introducing 1-σ noises to all possible errors, we take all sources of uncertainties into account.

In both panels of Fig. 7.3, it can be clearly seen that in the low velocity limit, i.e. the plateau on the left region, the rescaled order parameter saturates. This is in good agreement with

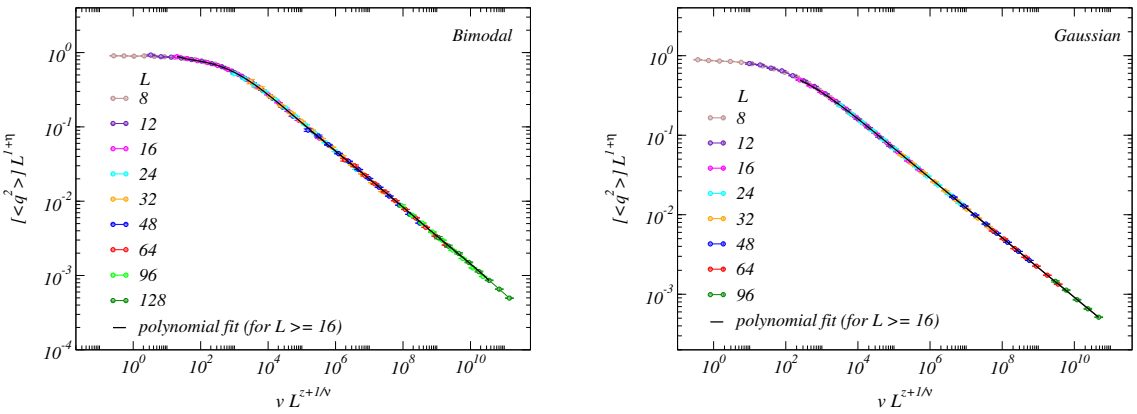

(a) (b)

Figure 7.3: Log-log plot for the f_1-scaling for Bimodal 3DSG (a) and Gaussian 3DSG (b), respectively. An optimization is carried out to determine the value of the dynamic exponent z. In the Bimodal case, we obtain $z = 5.852(55)$ with $\chi^2/\text{dof} = 1.07$. In the Gaussian case, the result is $z = 6.005(96)$ with $\chi^2/\text{dof} = 1.00$. In both cases, we exclude small sizes to avoid finite-size effects. The exclusion of the sizes is determined by the minimization of the χ^2 and the stability of the fitted result. For these two cases, sizes of $L < 16$ are excluded. The solid line in both panels indicate the polynomial fit. As the scaling suggests, in both panels, the plateau on the left region corresponds to the quasi-adiabatic regime, the middle region corresponds to the universal power-law regime, in which a straight line is clearly observed. This power-law regime can be analyzed in another way, as will be discussed below and in Fig. 7.4.

the equilibrium scaling, since in the static case we have $[\langle q^2 \rangle] \sim L^{-(1+\eta)}$. To the right down the plateau is the universal power-law regime, which exhibits a clear straight line in the log-log plot. This power-law can be analyzed in another way, as we discuss next.

According to the second scaling function f_2 of Eq. 7.5, one simply graphs the overall order parameter $[\langle q^2 \rangle]N$ versus $1/v$, the scaling will emerge, as shown in Fig. 7.4. The high-velocity scaling f_2 corresponds to a physical situation where the correlation length associated with the velocity $\xi_v \sim v^{-1/(z+1/\nu)}$ is much smaller than the correlation length of the phase transition $\xi_T \sim (T - T_c)^{-\nu}$, i.e., $\xi_v \ll \xi_T$. As a manner of fact, a typical length scale ξ is determined by $\xi = min(\xi_v, \xi_T)$, the high-velocity regime results in small isolated clusters, $[\langle q^2 \rangle]N$ captures the overall contributions from these small domains.

In addition, as mentioned earlier, there is an universal power-law regime which both f_1 and f_2 reduce to. We can clearly see this power-law regime again in the middle region of both panels in Fig. 7.4. Since f_2 only covers high-velocity regime, one can see the curves begin to split in the low-velocity region on the right. These splitting curves are exactly those forming plateaus in the f_1 scaling of Fig. 7.3. We note that Figs 7.3 and 7.4 are from exactly the same raw data, only being graphed differently according to f_1 and f_2 scalings, respectively, while both scalings show a clear universal power-law in the middle region of $v_{KZ}(L) \ll v \ll 1$.

More interestingly, while rendering f_2 does not require the knowledge of critical exponents, the power x is related to the critical exponents through Eq. (7.7). With the static exponents being known, one can easily extract the dynamic exponent z. In Fig. 7.4, the data sets $[\langle q^2 \rangle]$ at T_c are plotted versus $1/v$ in a log-log plot, and a linear fit is carried out to determine the slope of the straight line, which corresponds to the power x of the power-law. The same procedure of introducing 1-σ noises as used in the f_1 scaling is again employed here. We repeatedly introduce 1-σ noises to T_c (and therefore the data set $[\langle q^2 \rangle]$), ν, and η, to estimate the error of x.

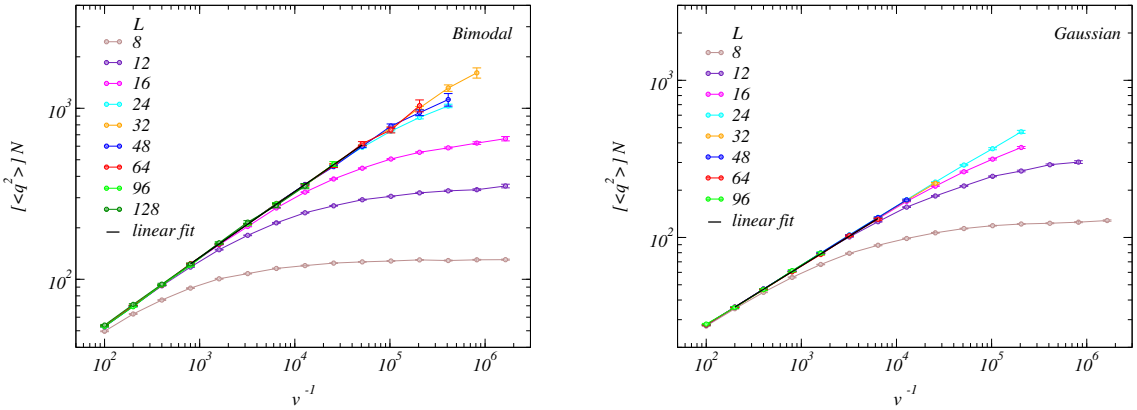

(a) (b)

Figure 7.4: Log-log plot for the f_2-scaling for Bimodal 3DSG (a) and Gaussian 3DSG (b), respectively. For both cases, the same raw data sets used in Fig. 7.3 are used for this figure, only being graphed differently according to the high-velocity f_2-scaling rather than the f_1-scaling. It should be noted that f_2-scaling does not require the knowledge of the critical exponents, one simply plots the overall order parameter $[\langle q^2 \rangle]N$ versus $1/v$ and the scaling emerges. The middle region that shows linear behavior in the log-log plot is exactly the power-law regime (which also shows linear behavior in the log-log plot) in the f_1-scaling of Fig. 7.3. The power-law region has an anticipated form $[\langle q^2 \rangle]N \sim av^{-x}$, with the power x related to the dynamic exponent z through Eq. 7.7. Using linear fit, we obtain $x = 0.3851(45)$, $a = 2.24(3)$, with $\chi^2/\text{dof} = 1.04$ for the Bimodal case, and $x = 0.3745(66)$, $a = 1.60(4)$, with $\chi^2/\text{dof} = 0.70$ for the Gaussian case. This translates to $z = 5.816(74)$ for the Bimodal and $z = 5.99(11)$ for the Gaussian. f_2-scaling corresponds to a situation when $\xi_v \ll \xi_T$, in terms of finite size this means the system size has to be large enough to be approximately in the thermodynamic limit. Therefore, in both cases, we include sizes of $L \geq 64$. The selection of sizes is determined by the minimization of the χ^2. The solid lines in both panels show the fit region and the result of linear fit.

For Bimodal 3DSG, we obtain $x = 0.3851(45)$, with $\chi^2/\text{dof} = 1.04$. For the Gaussian 3DSG, we obtain $x = 0.3745(66)$, with $\chi^2/\text{dof} = 0.70$. The numerical results of the power x can be translated to obtain the dynamic exponent z, which yields $z = 5.816(74)$ for the Bimodal case and $z = 5.99(11)$ for the Gaussian case. This result again supports the conclusion drawn from the f_1 scaling that the Bimodal and Gaussian 3DSGs are in the same dynamic universality class, and the conclusion is drawn by taking all possible sources of uncertainties into account.

Strictly speaking, any finite-size scaling will need correction due to finite-size effect [7, 21, 107]. Even though in Figs. 7.3 and 7.4, we have used f_1 and f_2 scaling respectively to demonstrate that Bimodal 3DSG and Gaussian 3DSG should be in the same dynamic universality class, to further verify this conclusion, we do correction to scaling to clear any concern of finite-size effect. Since f_2 scaling has a simpler form than f_1 scaling, and as shown above, the universal power-law regime observed in f_1 and f_2 scaling are completely equivalent, we use the following form to take into account the correction to f_2 scaling in the power-law regime:

$$[\langle q^2 \rangle] N \sim a(v^{-1})^{x_1} \left[1 + b\,(v^{-1})^{-x_2}\right], \tag{7.8}$$

where the power x_1 plays the role of the naïve power x Eq. (7.7) that determines of the dynamic exponent z. With the scaling form, we expect that the fitting function can incorporate a wider range of velocity and smaller sizes, as shown in Fig. 7.5.

In Fig. 7.5, the figures are plotted in the same style as Fig. 7.4, but the correction to f_2 scaling Eq. 7.8 is used to fit the data rather than the pure f_2 scaling form written in Eq. 7.5. An optimization procedure [1] is then carried out to determine the optimized

[1] Since the fit function Eq. 7.8 is non-linear, the optimization involved more complicated procedures. There definitely exists comprehensive optimization routines in several programming languages and software packages that can achieve the goal, but here we simply divide the parameter space (x_1, x_2, a, b) into fine grids and use exhaustive searching to find the best parameter set. We find this approach achieve better χ^2.

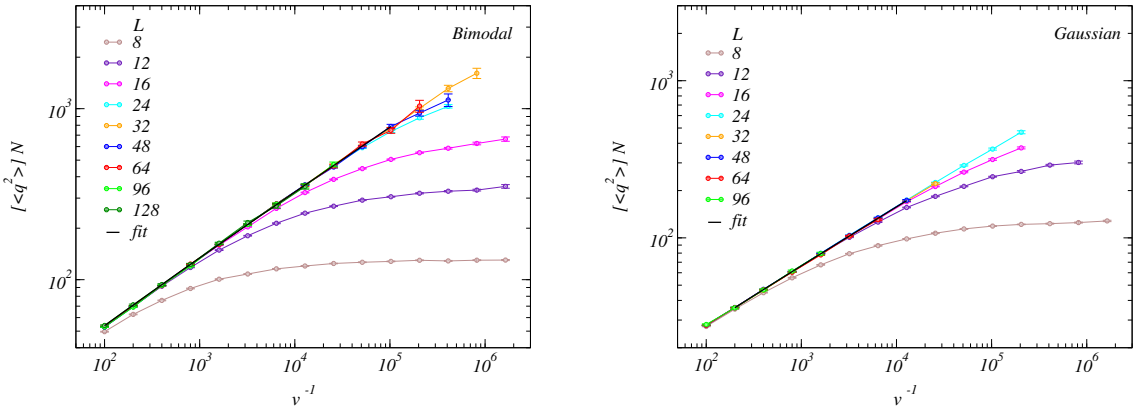

(a) (b)

Figure 7.5: Log-log plot for the f_2-scaling with correction for Bimodal 3DSG (a) and Gaussian 3DSG (b), respectively. For both cases, the same raw data sets used in Figs. 7.3 and 7.4 are used here. The figures are graphed according to the high-velocity f_2-scaling, in the same style as in Fig. 7.4. A correction to scaling form Eq. (7.8) is used to fit the power-law regime in the middle. For the Bimodal case, sizes of $L \geq 32$ are included in the fit. For the Gaussian case, sizes of $L \geq 48$ are included. In both panels, compared to the pure f_2 scaling shown in Fig. 7.4, the correction form can include smaller sizes and a larger velocity range, as indicated by the solid lines that show the fit result and fit region. The fit result yields $x_1 = 0.376(11)$ with $\chi^2/\text{dof} = 1.05$ for the Bimodal case, and $x_1 = 0.373(25)$ with $\chi^2/\text{dof} = 1.1$ for the Gaussian case, implying that $z = 5.97(29)$ for the Bimodal case and $z = 6.02(43)$ for the Gaussian case. This again concludes that Bimodal and Gaussian 3DSG are in the same dynamic universality class.

parameters (x_1, x_2, a, b) that yields the minimized χ^2. For the Bimodal 3DSG, we obtain $x_1 = 0.376(11)$, $x_2 = 0.34(11)$, $a = 10.40(77)$, and $b = -0.4(2)$, with $\chi^2/\text{dof} = 1.05$. For the Gaussian 3DSG, we obtain $x_1 = 0.373(25)$, $x_2 = 0.74(34)$, $a = 5.08 \pm 1.38$, and $b = -1.0 \pm 2.8$, with $\chi^2/\text{dof} = 1.1$. We use the same technique of introducing 1-σ noises to estimate the error bars of the parameters (x_1, x_2, a, b). Focusing on the leading exponent x_1, which can be translated to obtain the dynamic exponent z, we obtain $z = 5.97(29)$ for the Bimodal case and $z = 6.02(43)$ for the Gaussian case. This again verifies the previously established conclusion that the Bimodal and Gaussian 3DSGs belong to the same dynamic universality class.

Comparing Fig. 7.5 with Fig. 7.4, we note that the correction to f_2 scaling does include more smaller sizes and a wider velocity range, even though the error bars of the relevant exponents inevitably increase. Furthermore, the numerical result of the parameters implies that the correction terms are statistically zero, this is also evidenced by the goodness of fit in the pure f_2 scaling.

7.4 Summary and Discussion

In this chapter, we demonstrate the application of a non-equilibrium quench techniques developed in Ref. [17] on 3D spin-glasses. The advantage of the technique is that it does not suffer from any critical slowing down effects. Any critical slowing down phenomena only reflect itself in terms of the scaling behavior Eq. (7.5). Especially, the range of the universal power-law regime is determined by $L^{-(z+1/\nu)} \ll v \ll 1$, this implies that the more serious the critical slowing problem, the wider the power-law regime and the easier one can make use of this technique to measure the power of the power-law (the slope in the log-log plot) either in the f_1 or f_2 scaling.

The dual scaling behavior Eq. (7.5) also shows some advantages over the traditional single scaling function in the equilibrium scenarios. One can use one function to perform fitting

procedure and another one to perform consistency check. The second scaling function f_2 in some cases may be more favorable since it governs high-velocity quenches that correspond to shorter simulations, and also its convenience of not requiring the knowledge of critical exponents. In Ref. [17], we also demonstrate how to use f_2 scaling and combine different quench protocols to extract all the exponents. However, as explained in Sec. 7.3, f_2 scaling works best when $\xi_v \ll L$, that means the system size has to be large enough to be approximately be in the thermodynamic limit. Since in practice one does not know the size cut-off prior to the simulation, one has to gradually increase the system size in order to observe the finite-size effect vanish. f_1 scaling on the other hand has milder finite-size effect. These features therefore suggest some trade-off and optimized protocols in order to achieve the best performances for both f_1 and f_2 scalings.

Most importantly, we use the dual dynamic finite-size scaling behavior Eq. (7.5) to extract the dynamic exponents of the Bimodal and Gaussian 3DSG, the numerical results are summarized in Table. 7.1. All the results bring us to the same conclusion that these two spin-glass models are in the same dynamic universality class.

	f_1	pure f_2	correction to f_2
Gaussian	6.005(96)	5.99(11)	6.02(43)
Bimodal	5.852(88)	5.816(74)	5.97(29)

Table 7.1: Summary of the dynamic exponent z obtained for Bimodal and Gaussian 3DSG, using different scaling schemes discussed in Sec. 7.3. These results are plotted in Fig. 7.6. All the numerical results strongly support the conclusion that these two models belong to the same dynamic universality class.

There were also other numerical techniques being developed that can be used to obtain the dynamic exponents, mostly known is the relaxation method [44, 108, 109]. However, the advantage of the non-equilibrium approach demonstrated here over other numerical methods is that critical slowing down is no longer an issue. In the relaxation method, one

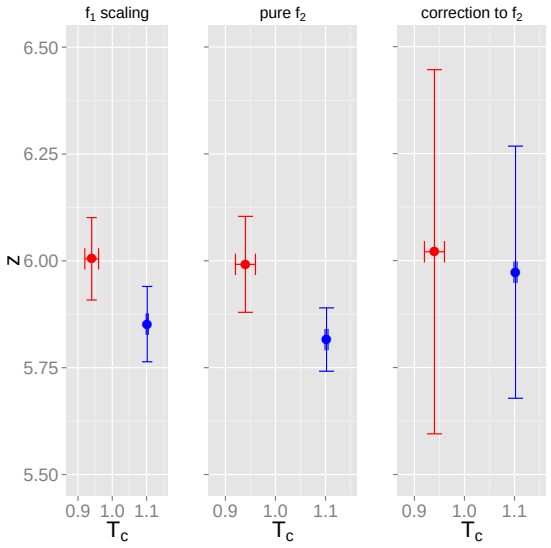

Figure 7.6: Visualization of Table 7.1, with the blue color stands for the Bimodal case and red one for the Gaussian case.

usually starts with an perfectly ordered state at T_c and observes how the order parameter vanishes, the time scale over which the order parameter goes to zero is proportional to the relaxation time, which shows a power-law $\tau_{\text{rel}} \sim \xi^z$, and z can then be determined through this relation. This power-law decay will become more noticeable at later time. However, very often, statistical fluctuations will pick up quickly at later time, this implies that the relaxation method becomes less accurate right at the moment when the power-law decay dominates, therefore the overall procedure is not as effective as it seems to be. In addition, the obtained z will also depend on the targeted quantities [68] used to observe the relaxation process. In light of these issues, we think the non-equilibrium quench will be a more desirable approach, especially for spin-glass systems.

Appendices

Appendix A

QAQMC performance for the quantum Sherrington Kirkpatrick model

A.1 Introduction

Throughout this thesis, the quasi-adiabatic quantum Monte Carlo (QAQMC) algorithm has been used extensively on different types of systems, from quantum Ising model in Ch. 3, disordered 3-regular FM random graphs in Ch. 5, to spin-glasses in Ch .6. Despite that now it has been well tested on several benchmark system [17, 33, 37], it is worthwhile to further check its utility on disordered on frustrated systems. Here we perform QAQMC on the fully-connected quantum Sherrington-Kirkpatrick (SK) model [24], whose Hamiltonian can be written as

$$\mathcal{H}(s) = s\sum_{i=1}^{N}\sum_{j=1}^{N} J_{ij}\sigma_i^z\sigma_j^z - (1-s)\sum_{i=1}^{N}\sigma_i^x, \tag{A.1}$$

where $J_{ij} \sim \mathcal{N}(0, 1/N)$ is the normal random variable with mean 0 and variance $1/N$. Fig. A.1 illustrates a typical example of SK model with $N = 16$ spins.

For spin-glass systems, a suitable order parameter is the Edwards-Anderson spin-glass order parameter [22]:

$$q = \frac{1}{N}\sum_{i}\sigma_i^{(1)}\sigma_i^{(2)}, \tag{A.2}$$

where (1) and (2) stand for two independent spin configurations ("replicas") for a given realization of $\{J_{ij}\}$.

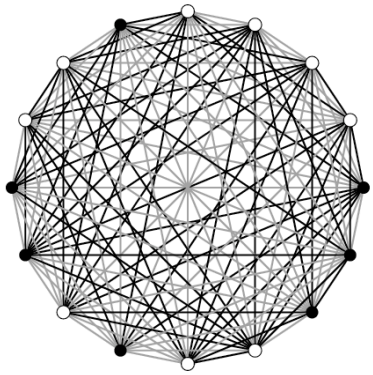

Figure A.1: An example of fully-connected SK model with $N = 16$ spins. The interaction strength J_{ij} is a random normal variable $J_{ij} \sim \mathcal{N}(0, 1/N)$.

A.2 Numerical result

We perform QAQMC imaginary-time quenches on the quantum SK model to extract the quantum critical point (QCP) s_c. We use the Binder cumulant defined below to locate s_c:

$$U = \frac{3}{2}\Big(1 - \frac{1}{3}\Big[\frac{\langle q^4\rangle}{\langle q^2\rangle^2}\Big]\Big), \tag{A.3}$$

where $\langle \dots \rangle$ stands for the ensemble average for a given realization of $\{J_{ij}\}$ and $[\dots]$ represents an average over realizations.

Around the transition, based on the dynamic finite-size scaling ansatz [17, 37], physical quantities can be written as a size-dependent pre-factor multiplied by a scaling function that takes two arguments: the reduced distance from the QCP and the quench velocity normalized by a characteristic velocity $v_c \sim N^{-(z'+1/\nu')}$, where $z' \equiv z/d$ is the normalized dynamic exponent and $\nu' \equiv \nu d$ is the normalized correlation length exponent, and d is the dimension of the system. For example, the Binder cumulant Eq. (A.3), which is dimensionless, can be written as:

$$U = U\big((s - s_c)N^{1/\nu'}, vN^{z'+1/\nu'}\big). \tag{A.4}$$

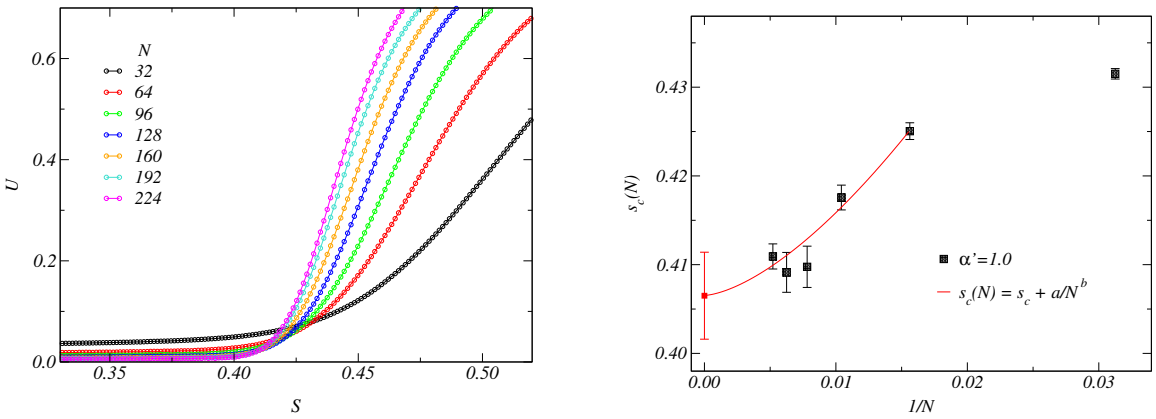

(a) (b)

Figure A.2: (a) Binder cumulants for different sizes and quench velocities that satisfy the scaling $v \sim N^{-\alpha'}$ with α' chosen to be $\alpha' = 1$. (b) Crossing points from the Binder cumulant shown in panel (a). The crossing points can be fitted using a power-law form, Eq. (A.5), which gives extrapolation of $s_c = 0.4065(49)$, in good agreement with Ref. [87].

Linear quench with $s : 0 \to s_f$ is carried out at velocity $v \sim N^{-\alpha'}$. The quench path presumably covers the QCP s_c, therefore $s_f > s_c$, and the parameter α' is a parameter that controls the magnitude of the velocity. To be quasi-adiabatic, α' should satisfy the requirement: $\alpha' > (z' + 1/\nu')$ [37]. When the criterion is met, the second argument in the scaling function Eq. (A.4) vanishes in the thermodynamic limit $N \to \infty$ and the quench becomes effectively quasi-adiabatic. Therefore, the Binder crossing technique used to determined the QCP in the equilibrium scenario can also be used in this non-equilibrium framework.

Here we choose $\alpha' = 1.0$ and perform linear quenches for different sizes, the resulted Binder cumulant are shown in Fig A.2 (a). At QCP, the order parameter will show power-law decay, therefore the Binder crossing is also expected to have the same behavior. One can then use the power-law form to fit the crossing points, which drift due to finite-size effect:

$$s_c(N) = s_c + a/N^b, \tag{A.5}$$

which gives $s_c = 0.4065 \pm 0.0049$, $a = 11.6 \pm 3.8$, and $b = 1.55 \pm 0.85$. The s_c extracted here

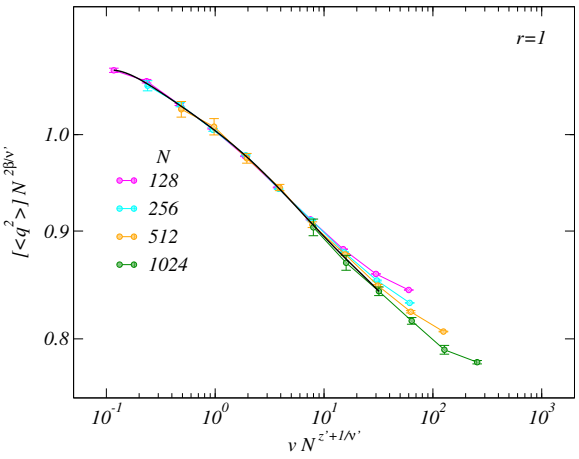

Figure A.3: f_1 scaling for the $r = 1$ linear quench to s_c. A 2-parameter fitting for $z' + 1/\nu'$ and β/ν' is carried out to obtain the scaling collapse.

is in good agreement with Ref. [110].

Once the QCP is extracted, one can perform critical quenches to s_c and expect the dynamic scaling behavior Eq. 6.7. Fig. A.3 shows the result of the f_1 scaling for the $r = 1$ linear quench. The optimization for the scaling collapse with a 2-parameter fitting gives $z'+1/\nu' = 1.0(2)$ and $\beta/\nu' = 0.48(1)$. This is in good agreement with Refs. [87, 111].

Appendix B

Performance of high-velocity quenches on 3D Ising spin-glasses

B.1 Introduction

In Ch. 7, we have demonstrated the advantage of the non-equilibrium quenching method on spin-glass systems over the traditional equilibrium approaches. This method allows us to efficiently study the spin-glass transition and extract the critical exponents associated with the transition to high numerical precision. However, the dynamic finite-size scaling, Eq. (7.5), takes place at the transition point T_c. Therefore one has to have the knowledge of T_c in order to take advantage of the dual scaling behavior. A typical way to extract T_c, in the framework of the non-equilibrium quench, is to perform linear quench with the velocity satisfying the condition:

$$v \sim L^{-\alpha}, \tag{B.1}$$

where v is the quench velocity associated with the quench protocol Eq. (7.3), and L is the linear size of the system. As long as $\alpha \geq z + 1/\nu$, the quench velocity can be kept below or at most equal to the Kibble-Zurek velocity, Eq. (7.6), such that the system can stay quasi-adiabatic. Consequently, for different sizes that satisfy the same condition of Eq. (B.1), they can be analyzed in terms of the equilibrium procedure, for example, one can keep track of the Binder cumulant to extract the transition point. This method has been demonstrated in Chapters 3, 5, and 6. In practice, spin-glass systems typically have large dynamic exponent z that will result in a serious critical slowing-down, as we have seen in Ch. 7, therefore the condition $\alpha \geq z + 1/\nu$ corresponds to long quench simulations. The

computational effort will eventually become unaffordable for large sizes.

In this Appendix section, we explore another way of extracting T_c. This approach is also under the same framework of non-equilibrium quenching we have been demonstrating through the thesis, nonetheless, we will focus on the high-velocity scaling regime rather than the quasi-adiabatic one. We will use classical 3D bimodal Ising spin-glass for the demonstration.

B.2 Extracting T_c and x from the high-velocity scaling regime

In Chapters. 1, 2, and 7, it has been demonstrated in detail that at T_c there is a dual scaling behavior as a function of the quench velocity v. In the intermediate velocity regime, the order parameter, e.g. the Edwards-Anderson order parameter Eq. (1.37) for the spin-glass system, shows a power-law behavior:

$$\begin{aligned} \langle q^2 \rangle &\sim L^{-2\beta/\nu} f\big((T-T_c)L^{1/\nu}, vL^{z+1/\nu}\big), \\ &\sim L^{-2\beta/\nu}(vL^{z+1/\nu})^{-x}\tilde{f}\big((T-T_c)L^{1/\nu}\big), \\ &\sim N^{-1}v^{-x}\tilde{f}\big((T-T_c)L^{1/\nu}\big), \end{aligned} \tag{B.2}$$

where $N = L^d$ is the total number of spins. The above expression is simply the power-law form that has been shown previously. Nevertheless, it has suggested another way of exploiting the scaling form to find T_c, as we discuss in the following.

For a given system sizes, we perform different linear quenches from $T_i = 2.0$ to $T_f = 0.5$, the quench velocity therefore is defined as $v = 1.5/\tau$, where τ is the total quench time. Same as the procedure discussed in Ch. 7, for each quench path, we use a polynomial to fit the data points in the range $T \in [0.9, 1.2]$, the range should presumably include the T_c. After the polynomial is obtained, for a given system size N and quench velocity v, one can obtain the order parameter at any given temperature within the temperature range of interest.

If the exponent x and T_c were known, Eq. (B.2) simply provides a way to collapse the data in the high-velocity regime. If one only rescales the order parameter and graphs it

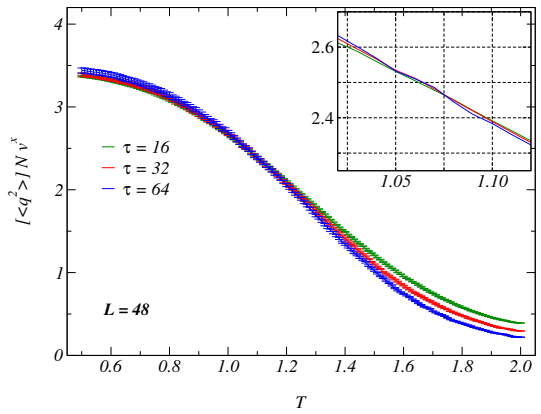

Figure B.1: For classical 3D bimodal Ising spin-glass of system size $L = 48$. Linear quenches with three different quench times $\tau = 16, 32$, and 64 from initial temperature $T_i = 2.0$ to final temperature $T_f = 0.5$ are performed. Plotted are the rescaled order parameter as a function of temperature (in original scale). Given a value of x, one can determine a centroid resulted from the three crossing points of these three curves. The centroid then defines the sum of distances to these three crossing points. The parameters (x, T_c) are then determined by the minimization of SOD. The insect shows the crossing of these three curves in a more focused window around T_c.

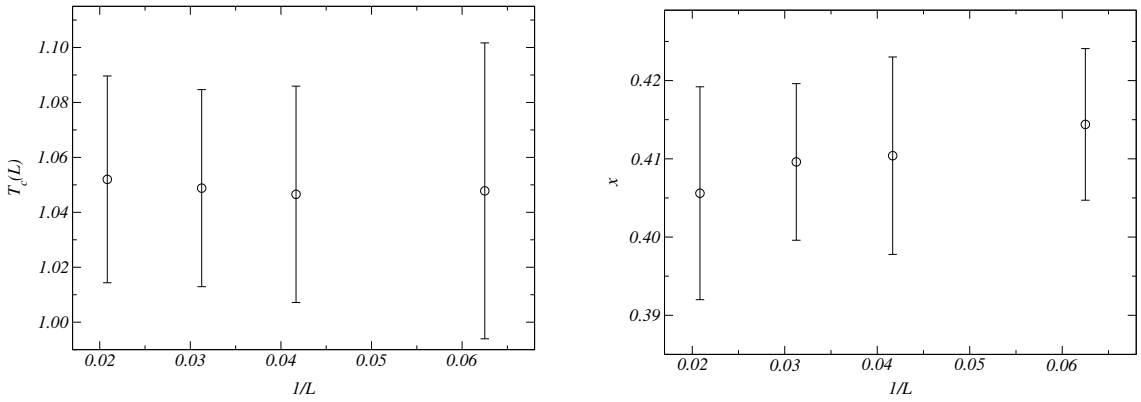

(a) (b)

Figure B.2: Using high-velocity three-curve crossing technique to extract T_c and x simultaneously. For a given system size, the procedure outlined in the text is carried out to determine the values of T_c and x. It is indicated from the plots that this procedure has very little finite-size effect.

as the original scale of the temperature, the curves would cross rather than collapse. The crossings of the curves could be used to extract T_c. Furthermore, if the exponent x is also unknown, the following approach provides a way to determine T_c and x simultaneously: for a given system size N and three different quench paths corresponding to three different quench velocities, one can choose a value of x such that after the order parameter is rescaled according to Eq. (B.2) with the given x, the three curves should nearly cross at a presumable T_c. A correct choice of x results in three curves crossing at exactly the same point, which corresponds to the actual T_c. In practice, due to finite grid of the parameters, the three curves will form three crossing points that center at a centroid, which in turns defines a sum of distances (SOD) to these three points. The optimal value of x thus corresponds to the one that has the lowest SOD, the corresponding centroid consequently corresponds to T_c. [1] A typical example is illustrated in Fig. B.1.

Note that this approach focuses on the high-velocity scaling regime, which is the straight

[1] A similar technique that uses three-curve crossing has also been discussed in Ref. [112].

line in the log-log scale of the f_1 graph such as Fig. 7.3. The data points from temperatures other than T_c would not collapse onto the curve, only those (from different quench velocities) that are at T_c will form scaling collapse. The procedure outline above is therefore designed to find the value of T_c that would result in these collapsing points.

We perform the high-velocity three-curve crossing technique on different sizes. For a given system size the procedure is carried out to determine the values of T_c and x simultaneously, the results are shown in Fig. B.2. We have seen very little finite-size effect, and the main source of uncertainties on T_c and x is from the procedure of determining the centroid of the three crossing points. The extracted values are consistent withe the known ones, $T_c \approx 1.102(3)$ and $x \approx 0.385(5)$.

List of Journal Abbreviations

AIP Conf. Proc.	American Institute of Physics Conference Proceedings
Ann. Rev. Cond. Mat. Phys.	Annual Review of Condensed Matter Physics
Comb. Prob. Comp.	Combinatorics, Probability, and Computing
Comm. Math. Phys.	Communication in Mathematical Physics
Eur. Phys. J. B	European Physical Journal B
Euro. Phys. Lett.	Europhysics Letters
J. Chem. Phys.	Journal of Chemical Physics
J. Phys. A	Journal of Physics A
J. Phys. A: Math. Gen.	Journal of Physics A: Mathematical and General
J. Phys. A: Math. Theo.	Journal of Physics A: Mathematical and Theoretical
J. Phys. C: Sol. Stat. Phys.	Journal of Physics C: Solid State Physics
J. Phys.: Cond. Mat.	Journal of Physics: Condensed Matter
J. Stat. Mech.	Journal of Statistical Mechanics
J. Stat. Mech.: Theor. Exp.	Journal of Statistical Mechanics: Theory and Experiment
J. Stat. Phys.	Journal of Statistical Physics
J. Phys. Soc. Jpn.	Journal of the Physical Society of Japan
Phys. Rep.	Physics Reports
Phys. Rev. A	Physical Review A
Phys. Rev. B	Physical Review B
Phys. Rev. E	Physical Review E
Phys. Rev. Lett.	Physical Review Letters
Physica A: Stat. Mech. App.	Physica A: Statistical Mechanics and Applications
Prog. Theor. Phys.	Progress of Theoretical Physics
Rev. Mod. Phys.	Reviews of Modern Physics

Bibliography

[1] M. Mézard, G. Parisi, and M. A. Virasoro, *Spin Glass Theory and Beyond* (1987).

[2] K. G. Wilson, Rev. Mod. Phys. **47**, 773 (1975).

[3] M. N. Barber, *Phase Transitions and Critical Phenomena*, Vol. 8, edited by C. Domb and J. Lebowitz .

[4] P. C. Hohenberg and B. I. Halperin, Rev. Mod. Phys. **49**, 435 (1977).

[5] L. Onsager, Phys. Rev. **65**, 117 (1944).

[6] S. Sachdev, *Quantum Phase Transitions, Second Edition* (2011).

[7] A. W. Sandvik, AIP Conf. Proc. **1297**, 135 (2010).

[8] H. Yahata and M. Suzuki, J. Phys. Soc. Jpn. **27**, 1421 (1969).

[9] R. H. Swendsen and J.-S. Wang, Phys. Rev. Lett. **58**, 86 (1987).

[10] M. Suzuki, Prog. Theor. Phys. **56**, 1454 (1976).

[11] A. W. Sandvik, Phys. Rev. B **59**, R14157 (1999).

[12] O. F. Syljuåsen and A. W. Sandvik, Phys. Rev. E **66**, 046701 (2002).

[13] A. W. Sandvik, Phys. Rev. E **68**, 056701 (2003).

[14] T. W. B. Kibble, J. Phys. A: Math. Gen. **9**, 1387 (1976).

[15] W. H. Zurek, Nature **317**, 505 (1985).

[16] A. Polkovnikov, K. Sengupta, A. Silva, and M. Vengalattore, Rev. Mod. Phys. **83**, 863 (2011).

[17] C.-W. Liu, A. Polkovnikov, and A. W. Sandvik, Phys. Rev. B **89**, 054307 (2014).

[18] C. De Grandi, V. Gritsev, and A. Polkovnikov, Phys. Rev. B **81**, 012303 (2010).

[19] C. Dekker, A. F. M. Arts, H. W. de Wijn, A. J. van Duyneveldt, and J. A. Mydosh, Phys. Rev. Lett. **61**, 1780 (1988).

[20] G. Parisi, J. J. Ruiz-Lorenzo, and D. A. Stariolo, J. Phys. A: Math. Gen. **31**, 4657 (1998).

[21] M. Hasenbusch, A. Pelissetto, and E. Vicari, Phys. Rev. B **78**, 214205 (2008).

[22] G. Parisi, Phys. Rev. Lett. **50**, 1946 (1983).

[23] K. Binder and A. P. Young, Rev. Mod. Phys. **58**, 801 (1986).

[24] D. Sherrington and S. Kirkpatrick, Phys. Rev. Lett. **35**, 1792 (1975).

[25] M. Mézard and G. Parisi, Eur. Phys. J. B **20**, 217 (2001).

[26] M. Mézard, G. Parisi, and R. Zecchina, Science **297**, 812 (2002).

[27] M. Mézard and R. Zecchina, Phys. Rev. E **66**, 056126 (2002).

[28] L. Zdeborová and F. Krzkała, Phys. Rev. E **76**, 031131 (2007).

[29] F. Krzakała and L. Zdeborová, Euro. Phys. Lett. **81**, 57005 (2008).

[30] E. Farhi *et al.*, Phys. Rev. A **86**, 052334 (2012).

[31] J. Dziarmaga, Phys. Rev. Lett. **95**, 245701 (2005).

[32] A. Chandran, A. Erez, S. S. Gubser, and S. L. Sondhi, Phys. Rev. B **86**, 064304 (2012).

[33] C. De Grandi, A. Polkovnikov, and A. W. Sandvik, Phys. Rev. B **84**, 224303 (2011).

[34] M. Kolodrubetz, B. K. Clark, and D. A. Huse, Phys. Rev. Lett. **109**, 015701 (2012).

[35] A. Chandran, F. J. Burnell, V. Khemani, and S. L. Sondhi, J. Phys.: Cond. Mat. **25**, 404214 (2013).

[36] M. Kolodrubetz, D. Pekker, B. K. Clark, and K. Sengupta, Phys. Rev. B **85**, 100505 (2012).

[37] C.-W. Liu, A. Polkovnikov, and A. W. Sandvik, Phys. Rev. B **87**, 174302 (2013).

[38] A. Polkovnikov, Phys. Rev. B **72**, 161201 (2005).

[39] W. H. Zurek, U. Dorner, and P. Zoller, Phys. Rev. Lett. **95**, 105701 (2005).

[40] S. Deng, G. Ortiz, and L. Viola, Euro. Phys. Lett. **84**, 67008 (2008).

[41] C. D. Grandi, A. Polkovnikov, and A. W. Sandvik, J. Phys.: Cond. Mat. **25**, 404216 (2013).

[42] N. Metropolis, A. W. Rosenbluth, M. N. Rosenbluth, A. H. Teller, and E. Teller, J. Chem. Phys. **21**, 1087 (1953).

[43] K. tai Leung, J. Phys. A: Math. and Gen. **26**, 6691 (1993).

[44] F.-G. Wang and C.-K. Hu, Phys. Rev. E **56**, 2310 (1997).

[45] M. P. Nightingale and H. W. J. Blöte, Phys. Rev. B **62**, 1089 (2000).

[46] Y. Ozeki and N. Ito, J. Phys. A: Math. and Theor. **40**, R149 (2007).

[47] M. J. Dunlavy and D. Venus, Phys. Rev. B **71**, 144406 (2005).

[48] U. Wolff, Phys. Rev. Lett. **62**, 361 (1989).

[49] C. F. Baillie and P. D. Coddington, Phys. Rev. B **43**, 10617 (1991).

[50] Z. B. Li, L. Schülke, and B. Zheng, Phys. Rev. Lett. **74**, 3396 (1995).

[51] W. Klein, T. Ray, and P. Tamayo, Phys. Rev. Lett. **62**, 163 (1989).

[52] P. D. Coddington and C. F. Baillie, Phys. Rev. Lett. **68**, 962 (1992).

[53] J. Du, B. Zheng, and J.-S. Wang, J. Stat. Mech.: Theor. and Exp. **2006**, P05004 (2006).

[54] P. Tamayo, R. Brower, and W. Klein, J. Stat. Phys. **58**, 1083 (1990).

[55] S. Kirkpatrick, C. D. Gelatt, and M. P. Vecchi, Science **220**, 671 (1983).

[56] S. Suzuki, J. Stat. Mech.: Theor. Exp. **2009**, P03032 (2009).

[57] S. Suzuki, J. Phys.: Conf. Ser. **302**, 012046 (2011).

[58] Y. Nourani and B. Andresen, J. Phys. A: Math. Gen. **31**, 8373 (1998).

[59] G. Biroli, L. F. Cugliandolo, and A. Sicilia, Phys. Rev. E **81**, 050101 (2010).

[60] P. L. Krapivsky, J. Stat. Mech.: Theor. and Exp. **2010**, P02014 (2010).

[61] F. Zhong and Z. Xu, Phys. Rev. B **71**, 132402 (2005).

[62] K. Binder, Phys. Rev. Lett. **47**, 693 (1981).

[63] A. W. Sandvik, AIP Conference Proceedings **1297**, 135 (2010).

[64] H. G. Katzgraber, M. Körner, and A. P. Young, Phys. Rev. B **73**, 224432 (2006).

[65] A. Coniglio and W. Klein, J. Phys. A: Math. Gen. **13**, 2775 (1980).

[66] M. Hasenbusch, K. Pinn, and S. Vinti, Phys. Rev. B **59**, 11471 (1999).

[67] J. Dziarmaga, Advances in Physics **59**, 1063 (2010).

[68] G. Ossola and A. D. Sokal, Nuclear Physics B **691**, 259 (2004).

[69] R. K. Kaul, R. G. Melko, and A. W. Sandvik, Ann. Rev. Cond. Mat. Phys. **4**, 179 (2013).

[70] S. R. White, Phys. Rev. Lett. **69**, 2863 (1992).

[71] U. Schollwöck, Rev. Mod. Phys. **77**, 259 (2005).

[72] A. Dorneich and M. Troyer, Phys. Rev. E **64**, 066701 (2001).

[73] J. P. Provost and G. Vallee, Comm. Math. Phys. **76**, 289 (1980).

[74] C. De Grandi, V. Gritsev, and A. Polkovnikov, Phys. Rev. B **81**, 224301 (2010).

[75] C. J. Hamer, J. Phys. A: Math. and Gen. **33**, 6683 (2000).

[76] A. W. Sandvik and J. Kurkijärvi, Phys. Rev. B **43**, 5950 (1991).

[77] M. S. L. du Croo de Jongh and J. M. J. van Leeuwen, Phys. Rev. B **57**, 8494 (1998).

[78] G. E. Santoro and E. Tosatti, J. Phys. A: Math. Gen. **39**, R393 (2006).

[79] V. Bapst, L. Foini, F. Krzakala, G. Semerjian, and F. Zamponi, Phys. Rep. **523**, 127 (2013).

[80] S. Baroni and S. Moroni, Phys. Rev. Lett. **82**, 4745 (1999).

[81] G. Carleo, F. Becca, S. Moroni, and S. Baroni, Phys. Rev. E **82**, 046710 (2010).

[82] T. Kadowaki and H. Nishimori, Phys. Rev. E **58**, 5355 (1998).

[83] G. E. Santoro, R. Martonák, E. Tosatti, and R. Car, Science **295**, 2427 (2002).

[84] E. Farhi *et al.*, Science **292**, 472 (2001).

[85] A. V. M. Leone, A. Vzquez1 and R. Zecchina, Eur. Phys. J. B **28**, 191 (2002).

[86] A. Steger and N. C. Wormald, Comb. Prob. Comp. **8**, 377 (1999).

[87] J. V. Alvarez and F. Ritort, J. Phys. A: Math. Gen. **29**, 7355 (1996).

[88] C. Laumann, A. Scardicchio, and S. L. Sondhi, Phys. Rev. B **78**, 134424 (2008).

[89] F. Krzakala, A. Rosso, G. Semerjian, and F. Zamponi, Phys. Rev. B **78**, 134428 (2008).

[90] K. Hukushima and K. Nemoto, J. Phys. Soc. Jpn. **65**, 1604 (1996).

[91] R. E. Blundell, K. Humayun, and A. J. Bray, J. Phys. A: Math. Gen. **25**, L733 (1992).

[92] E. Marinari, G. Parisi, and F. Ritort, J. Phys. A: Math. Gen. **27**, 2687 (1994).

[93] G. Parisi, P. Ranieri, F. Ricci-Tersenghi, and J. J. Ruiz-Lorenzo, J. Phys. A: Math. Gen. **30**, 7115 (1997).

[94] A. P. Young, J. Phys. C: Sol. Stat. Phys. **17**, L517 (1984).

[95] R. E. Hetzel, R. N. Bhatt, and R. R. P. Singh, Euro. Phys. Lett. **22**, 383 (1993).

[96] M. Henkel and M. Pleimling, Euro. Phys. Lett. **69**, 524 (2005).

[97] M. Palassini and A. P. Young, Phys. Rev. B **63**, 140408 (2001).

[98] A. T. Ogielski, Phys. Rev. B **32**, 7384 (1985).

[99] K. Binder and A. P. Young, Phys. Rev. B **29**, 2864 (1984).

[100] H. G. Katzgraber and I. A. Campbell, Phys. Rev. B **72**, 014462 (2005).

[101] H. G. Katzgraber and I. A. Campbell, Phys. Rev. B **69**, 094413 (2004).

[102] T. Olson and A. P. Young, Phys. Rev. B **61**, 12467 (2000).

[103] E. Marinari, G. Parisi, and J. J. Ruiz-Lorenzo, Phys. Rev. B **58**, 14852 (1998).

[104] Janus Collaboration, M. Baity-Jesi *et al.*, Phys. Rev. B **88**, 224416 (2013).

[105] A. T. Ogielski and I. Morgenstern, Phys. Rev. Lett. **54**, 928 (1985).

[106] R. R. P. Singh and S. Chakravarty, Phys. Rev. Lett. **57**, 245 (1986).

[107] R. A. Baños, L. A. Fernandez, V. Martin-Mayor, and A. P. Young, Phys. Rev. B **86**, 134416 (2012).

[108] N. Ito, Physica A: Stat. Mech. App. **196**, 591 (1993).

[109] N. Ito, Physica A: Stat. Mech. App. **192**, 604 (1993).

[110] D. Lancaster and F. Ritort, J. Phys. A: Math. Gen. **30**, L41 (1997).

[111] N. Read, S. Sachdev, and J. Ye, Phys. Rev. B **52**, 384 (1995).

[112] Y.-D. Hsieh, Y.-J. Kao, and A. W. Sandvik, J. Stat. Mech.: Theor. Exp. **2013**, P09001 (2013).

Curriculum Vitae

Cheng-Wei Liu

Boston University, Physics Department
590 Commonwealth Avenue
Boston, Massachusetts 02215 USA

Phone: (617) 353-4916
http://people.bu.edu/cwliu/
E-mail: cwliu@buphy.bu.edu

EDUCATION

• Sep '10 – Dec '14, Ph.D. in Physics, Boston University, Boston, MA, USA

Advisor: Professor Anders W. Sandvik

Thesis: *Computational studies of thermal and quantum phase transitions approached through non-equilibrium quenching*

RESEARCH AND TEACHING EXPERIENCE

- Aug '12 – present, Research assistant, Boston University.
- July '11 – July '12, Teaching assistant, Boston University.

AWARDS

- Boston University Dean's Fellowship, Sep '10 – June '11.

SKILLS

- Computation: numerical algorithms, scientific computing, large-scale simulations, Monte Carlo simulations, quantum Monte Carlo algorithms, data analysis, statistical analysis.
- Programming languages: C, C++ (STL), Python (NumPy, SciPy), R, CUDA GPU, Fortran, Octave, Matlab
- Scripting: Python, Perl, regular expression
- Data visualization: R, PostScript, Xmgrace, Matplotlib, LaTeX
- Operating system: Linux, Macintosh
- Version control: Git

TALKS

- **Quantum annealing on spin-glass system and its implication for quantum computing**, Oct 1 '14, CMT seminar, Boston University.
- **Efficient simulation scheme for studying spin-glass transition**, Mar 5 '14, APS March Meeting, Denver, CO.
- **Computational studies of thermal and quantum phase transitions approached through non-equilibrium quenching**, Oct 2 '14, Departmental Seminar, Boston University.
- **Quasi-adiabatic quantum Monte Carlo algorithm for non-equilibrium quantum phase transition**, Mar 22 '13, APS March Meeting, Baltimore, MD.

PUBLICATIONS

1. *Quasi-adiabatic quantum Monte Carlo algorithm for quantum evolution in imaginary time*,
   C.-W. Liu, A. Polkovnikov, and A. W. Sandvik,
   Phys. Rev. B **87**, 174302 (2013).

2. *Dynamic scaling at classical phase transitions approached through non-equilibrium quenching*,
   C.-W. Liu, A. Polkovnikov, and A. W. Sandvik,
   Phys. Rev. B **89**, 054307 (2014).

3. *Quantum versus classical annealing - insights from scaling theory and results for spin glasses on 3-regular graphs*,
   C.-W. Liu, A. Polkovnikov, and A. W. Sandvik,
   arXiv:1409.7192.

4. *Universal dynamic scaling in three-dimensional Ising spin glasses*,
   C.-W. Liu, A. Polkkovnikov, A. W. Sandvik, and A. P. Young,
   arXiv:1411.6745.

5. *Classical and quantum phase transitions approached through non-equilibrium quench on 3-regular random graphs and the applications to quantum computing*,
   C.-W. Liu, A. Polkovnikov, and A. W. Sandvik,
   manuscript in preparation.